Volume 12| Issue 2| 2026

Journal
of Biomedical Photonics & Engineering

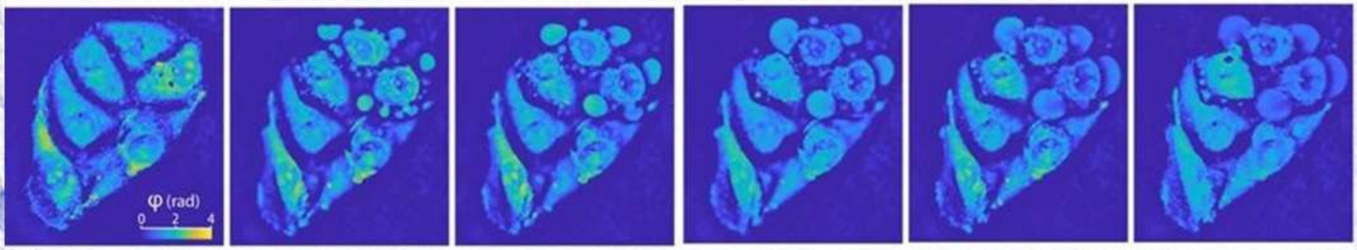

Special Issue Editors:

Oleg Vasyutinskii
Valery Tuchin
Junle Qu
Dongping Zhong
Aleksandra Mayorova
Elina Genina
Ivan Bratchenko

Journal of Biomedical Photonics & Engineering

Volume 12, Issue 2 (June 2026)

Special Section

International Russian-Chinese Workshop on Light for Life Sciences

Advanced Photonic Technologies in Biomedicine

Special Issue Editors

Prof. Oleg Vasyutinskii
Ioffe Institute, Russian Federation

Prof. Valery Tuchin
Saratov State University, Russia, Russian Federation

Prof. Junle Qu
Shenzhen University, China

Prof. Dongping Zhong
Shanghai Shang Jiao Tong University, China

Dr Aleksandra Mayorova
Lebedev Physical Institute, Russian Federation

Prof. Elina Genina
Saratov State University, Russian Federation

Prof. Ivan Bratchenko
Immanuel Kant Baltic Federal University, Russian Federation

Postal address:
39B Lukacheva st., room #301
Samara 443086, Russian Federation

Used Figures from this issue on the Cover

Andrey V. Belashov et al., SLM-Based System for Localized Targeted Irradiation of Cells and Noninvasive Monitoring of Cell Death, 020307, Fig. 3(c).

Contents

Articles

Determination of Carotenoids in the Ovaries of Healthy Cats and Cats with Leiomyosarcom 020301
Ekaterina I. Selifonova, Andrey M. Zakharevich, Iuliia S. Kruss, Andrey S. Rykhlov, Alexey A. Chernov, Tatyana Yu. Rusanova, and Valery V. Tuchin

A Problem of THz Endoscopy of Hard-to-Access Tissues 020302
Kirill I. Zaytsev, Gleb M. Katyba, Nikita V. Chernomyrdin, Kirill B. Dolganov, Irina N. Dolganova, Sergei V. Garnov, and Vladimir N. Kurlov

Development of Technology for Analysing X-Ray Images of Bone Tissue for Computer Diagnosis of Osteoporosis 020303
Daria V. Nekrasova, Nataly Yu. Ilyasova, Nikita S. Demin, and Sergey S. Pervushkin

Machine Learning Classification of Augmented Raman Serum Spectra for Chronic Heart Failure Detection 020304
Yulia A. Khristoforova, Ekaterina O. Salnikova, and Irina A. Matveeva

Variational and Numerical Analysis of Contour-Based Segmentation Methods in Cephalometry 020309
Yulia Zh. Pchelkina

The Effect of Riboflavin and Blue Laser Irradiation on B16-F10 Melanoma Cell Death 020312
Aigul K. Gilmutdinova, Elena V. Iurova, Evgeniya V. Pogodina, Anna V. Khokhlova, Dmitry E. Sugak, and Yury V. Saenko

Special Section

Detritylation by Self-Contained Photoacid Generators on the Base of Substituted Benzo[b]thiophene-2-Carboxanilides under UV-Laser and Lamp Irradiation 020305
Natalia V. Izmailova, Lubov G. Samsonova, and Ruslan M. Gadirov

Linear Dichroism and Birefringence in Polarization-Modulation Pump-Probe Spectroscopy 020306
Denis A. Volkov, Maxim V. Belashov, Maxim E. Sasin, and Oleg S. Vasyutinskii

SLM-Based System for Localized Targeted Irradiation of Cells and Noninvasive Monitoring of Cell Death 020307
Andrey V. Belashov, Anna A. Zhikhoreva, Maxim V. Belashov, Anna V. Salova, Tatiana N. Belyaeva, Ilia K. Litvinov, Elena S. Kornilova, and Irina V. Semenova

Alternating Magnetic Field Effect on Oxygen Transport Function of Red Blood Cells *in Vitro* 020308
Olga V. Slatinskaia, Alexander V. Priezzhev, Lizaveta V. Uzlova, Victor V. Zinchuk, and Andrei E. Lugovtsov

New Opportunities for Non-Invasive Assessment of Blood Microcirculation Parameters in Patients with Cardiac Pathology 020310
Yury Gurfinkel, Simon Matskeplishvili, Petr Ermolinskiy, Larisa Dyachuk, Andrei Lugovtsov, Andrei Yamaev, and Alexander Priezzhev

Numerical Modeling and Spectral Balancing of an LED-Based Reflectance Spectrophotometer (360–760 nm) 020311
Mikhail E. Parfyonov and Dmitry N. Artemyev

Optical Coherence Tomography Angiography for Monitoring Sublingual Microcirculatory Changes: a Prospective Tool for Investigation of Tissue Hypoperfusion in Critical Care Medicine 020401
Anton A. Plekhanov, Ivan A. Ryzhkov, Pavel A. Shilyagin, Elena B. Kiseleva, Konstantin N. Lapin, Lydia A. Varnakova, Yulia V. Korzhimanova, Anna I. Dementeva, Marina A. Sirotkina, Grigory V. Gelikonov, Evgeniy V. Grigoryev, and Natalia D. Gladkova

Determination of Carotenoids in the Ovaries of Healthy Cats and Cats with Leiomyosarcom

Ekaterina I. Selifonova[1*], Andrey M. Zakharevich[1], Iuliia S. Kruss[1], Andrey S. Rykhlov[2], Alexey A. Chernov[3], Tatyana Yu. Rusanova[1], and Valery V. Tuchin[1,4,5]
[1] Saratov State University, 83 Astrakhanskaya str., Saratov 410012, Russian Federation
[2] Saratov State University of Genetics, Biotechnology and Engineering named after N.I. Vavilov, 4 Pyotr Stolypin av., Saratov 410012, Russian Federation
[3] V.I. Razumovsky Saratov State Medical University, 112 Bolshaya Kazachya str., Saratov 410012, Russian Federation
[4] Institute of Precision Mechanics and Control, FRC "Saratov Scientific Centre of the RAS", 24 Rabochaya str., Saratov 410028, Russian Federation
[5] Tomsk State University, 36 Lenin av., Tomsk 634050, Russian Federation
*e-mail: selif-ei@yandex.ru

Abstract. The mortality rate of ovarian cancer remains the greatest among other oncological diseases of genital system worldwide. Using carotenoids as a preventive measure against ovarian cancer and a means to improve the state of genital system in general is a popular trend when determining the nutritive factors. In our study we have determined the total content of carotenoids in healthy feline ovaries and ovaries of cats diagnosed with leiomyosarcoma. We have found that total content of carotenoids varies between left and right ovaries of the same healthy cat. However, cats diagnosed with leiomyosarcoma had significantly lower carotenoid content in both left and right ovaries. As carotenoids can be used as chemotherapeutic agents, the study of their content in ovaries is a relevant problem that requires further study. Determination of the impact of carotenoids on oncological processes may find practical use in public healthcare.

Keywords: ovary tissues; leiomyosarcoma; oncology; carotenoids; spectroscopy.

Paper #9433 received 18 Nov 2025; revised manuscript received 1 Dec 2025; accepted for publication 1 Dec 2025; doi: 10.18287/JBPE26.12.020301.

1 Introduction

Ovarian cancer has the highest lethality rate out of all gynecological cancers as it usually is not detected until it has already progressed to its later stages, it tends to relapse and it still has a very narrow range of treatment options [1]. Some tumors that form from smooth muscle fibers of uterus, such as leiomyosarcoma, affect up to 70% of all women during their lifetime and their treatment requires significant financial expenditures [2, 3]. Currently, there is still relatively few information regarding the etiology of ovarian cancer. Certain nutritive factors and lifestyle choice may play a role in formation of ovarian cancer and can be used as a preventive measure to decrease the lethality of this disease. The role of carotenoids in prevention of ovarian cancer and other forms of genital system cancers is especially interesting. Carotenoids and retinyl ethers are sources of vitamin A and its natural derivatives in human body; they regulate replication and differentiation of cells in human endometrium. Carotenoids (a series of more than 800 of structurally different molecules) act as chemopreventive agents regardless of whether they transform into vitamin A, therefore, they can be potentially used as efficient replacement to existing chemotherapeutic agents used to treat ovarian cancer [4]. More than 50 types of carotenoids are present in common food products including a group of approximately 20 substances that, after consumed with food, can be found in human blood (plasma or serum). Primary components of that group (more than 90%) include β-carotene, α-carotene, lycopene, β-cryptoxanthin, lutein and zeaxanthin [5]. Currently, there are active discussions on functional activity of carotenoids related to their photochemical, structural, antioxidant, light absorbing and

This paper was presented at the Saratov Fall Meeting 2025 – International Symposium on Optics and Biophotonics, Saratov, Russian Federation, September 29 – October 3, 2025.

photoprotective properties [6]. There are studies dedicated to finding the correlations between the presence of carotenoids in blood serum and occurrence of breast cancer. It has been found that total content of circulating carotenoids, α-carotene, β-carotene, β-cryptoxanthin, lycopene and lutein may correlate with reduced risk of development of breast cancer, however, the reliability of provided evidence is estimated as low or very low [7, 8]. However, Czeczuga-Semeniuk and Wołczyński established that carotenoids may trigger the growth of leiomyoma and are involved in differentiation of endometrium adenocarcinoma [9]. Studies of carotenoid content in normal tissues of uterus and in samples of various tumors taken from human uterus showed that the highest total content of carotenoids were observed for endometrium adenocarcinoma group, thus, confirming certain enzyme defects in carotenoid metabolism or some kind of their metabolic modification as a result of neoplastic process [9]. Fourteen different carotenoids were identified in the sample of tissues taken from human ovaries. Total content of carotenoids was relatively low for the whole group of oncological samples, while the average content of provitamin A was comparable to that observed for samples of normal ovary tissues. It was only higher for group with endometriosis [10]. Other studies of tissues of malignant tumors in uterus reported statistically higher total content of carotenoids compared to samples of normal uterus tissues and samples of benign tumors taken from uterus. The observed discrepancies in the frequency of extraction of several carotenoids do not allow to reach a solid conclusion and require further studies [11]. Greater consumption of carotenoids may reduce epithelial ovarian cancer [12]. Other studies conducted in North America and Europe state that consumption of primary carotenoids by adults does not play any significant role in incidence of ovarian cancer [13]. Thus, currently there are no certain recommendations on carotenoid consumption as there is evidence of both positive and negative effects of carotenoid consumption on human health that require further studies [14]. It is known that cats can digest β-carotene rather well. Cats whose diet included increased β-carotene content had greater concentrations of β-carotene in blood plasma, lutein and endometrium tissues and estradiol, thus, support optimal functioning of ovaries and providing the best medium for embryos to survive and develop in the uterus [15]. Gunyeli et al. recommend astaxanthin, a carotenoid, as a potential nutrient that can be used to protect urogenital tissues from damage caused by chemotherapeutic and cytotoxic agents such as methotrexate [16].

Carotenoids, being powerful antioxidants, can interact with reactive oxygen species through oxidation, reduction, hydrogen extraction or addition reactions, reducing oxidative damage to tissue cells [17]. They may also reduce the risk of cancer by suppressing cell proliferation, inducing apoptosis, influencing intercellular communication, and strengthening immune function [18]. Most studies show that adequate consumption of fruits and vegetables containing carotenoids and other antioxidants significantly reduces the risk of cancer [19]. However, not all carotenoids are able to reduce the risk of cancer development and there are still controversies and discussions on this topic [20]. Recent studies have shown that carotenoids play a dual role, acting as both antioxidants and prooxidants, making it difficult to determine their role in cancer development [21]. Some studies suggest that conflicting results may be due to differences in phytochemical intake, regional differences, dietary and lifestyle factors, age and hereditary factors, limitations in sample size, and data collection methods. Further high-quality and well-designed experimental studies are needed to examine the relationship between carotenoids and cancer incidence [18].

Animal models are often used for research, in particular: ferrets [22], pigs [23], rats [24], cats [25], etc. The purpose of this study was to establish the content of carotenoids in normal feline ovaries and ovaries of cats diagnosed with leiomyosarcoma.

2 Methods and Materials

The *ex vivo* studies involved examination of ovaries of non-purebred cats aged 1.5 to 9 years obtained from veterinary clinic performing ovariectomy and ovariohysterectomy. We studied both healthy feline ovaries and ovaries of cats diagnosed with leiomyosarcoma. To confirm the diagnosis, we performed histologic examination of samples within 48 h after ovary extirpation using hematoxylin-eosin staining. Surface morphology and elementary composition of tissue samples was studied using MIRA 2 LMU scanning electron microscope (SEM) (TESCAN ORSAY HOLDING, Czechia) operating in secondary electron registration mode (with acceleration voltage of 30 kV) equipped with INCA Energy 350, a system of energy dispersive X-ray analysis (EDAX) (Oxford Instruments Analytical, Great Britain). INCA Energy microanalysis system allows quantitative determination of chemical elemental composition of sample within selected area. Surface images of samples were produced by fixing the samples on a special carbon substrate (carbon band) and tomographic scanning was performed after the samples were coated with gold. The surface layer of tissues with depth of effective signal generation being 1 μm. The scanning was performed using acceleration voltage of 20 kV in vacuum at pressure of approximately 10^{-2} Pa. For SEM analysis we prepared (0.90 ± 0.09) mm wide sections of ovary tissues that were placed between glass slides and dried at normal atmospheric pressure and room temperature (23 °C) for 10 days.

To determine the total content of carotenoids, ovaries were cut into pieces no greater than 1 mm in size and then dried in ULAB UT-4610 drying cabinet at 40 °C for 3 h. 0.1 g of dried up sample weight was weighted on GR-200 (A&D Companyassay, Japan) balance (extra-fine fit as classified by GOST (State Standard) 24104-20010. Weighted samples were placed into glass beakers, 5 ml of 95% ethanol was poured into the beakers and the resulting biomass was stirred for 15 min at 40 °C. The content of beaker was transferred to test tubes and centrifuged at 5000 rpm in Zenroe centrifuge (Cence, China) for 10 min. Supernatant was transferred to quartz cuvette with path length of 1 cm; absorption spectra were registered relative to compensation solution (95% ethanol) using Shimadzu UV-2550(PC) double-beam spectrophotometer (Shimadzu, Japan). Collection, processing and output of analysis results was performed by UVProbe for Windows 2.30 software package for PC. Spectral range: 200–500 nm; maximum permissible values of absolute accuracy of wavelength (λ) ± 0.3 nm.

Total quantitative content of carotenoids (in mg/100 g calculated to β-carotene) at the 450 nm wavelength was calculated as follows [26]:

$$C = \frac{A \cdot 5 \cdot 10}{m \cdot 2500} \cdot 100\ \%, \qquad (1)$$

where A is the absorbance of tested sample; m is the weight of sample, mg; 5 is the volume of ethanol, ml; 10 is the weight of β-carotene per 1 ml of 1% ethanol solution, mg; 2500 is the absorption coefficient of β-carotene in ethanol at 450 nm.

Statistical analysis of data was performed by comparing various samples using Mann-Whitney U-test. For that, we distributed the samples in ascending order for ovary 1 and ovary 2 for each diagnosed group. The resulting experimental value (U_{exp}) was compared to critical (tabular) value (U_{cr}).

$$U_{exp} = n_1 \cdot n_2 + \frac{n_1 \cdot (n_1 + 1)}{2} - \sum r_1, \qquad (2)$$

where U_{exp} is calculated value of Mann-Whitney U parameter; n_1 and n_2 are the sizes of firth and second samples, respectively; r_1 is the rank sum for the first (greater) sample. Initially, we assumed that the discrepancies between two samples were insignificant, while the following inequality was valid: $U_{cr} < U_{exp}$ (with $p = 0.05$). If $U_{cr} > U_{exp}$, then the discrepancy between samples is statistically significant.

3 Results

3.1 Histological Examination

Histological examination has revealed general characteristics of the structure of healthy ovary. The ovary's exterior is covered with a single-layer cubical epithelium followed by subepithelial white tissue. The ovary's interior consists of cortical and medullary substances that are not distinctly separated from each other. Cortical substance comprises the majority of ovary and contained follicles. The medullary substance comprises the smaller part of ovary's interior and contains many blood vessels (Fig. 1).

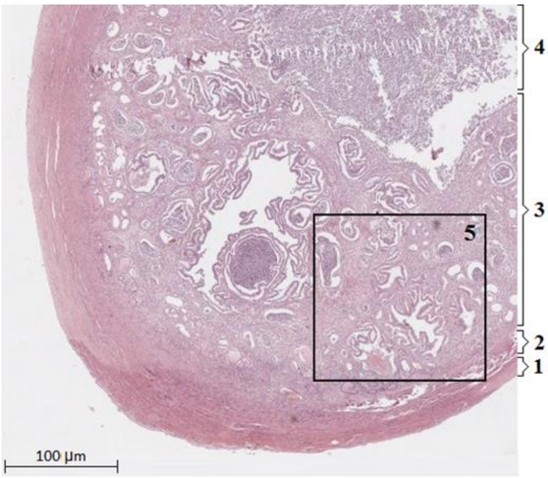

Fig. 1 Histological examination of feline ovary: 1 – single-layer cubical epithelium; 2 – subepithelial albugineous layer; 3 – ovary's cortical substance; 4 – ovary's medullary substance; 5 – area chosen for SEM examination.

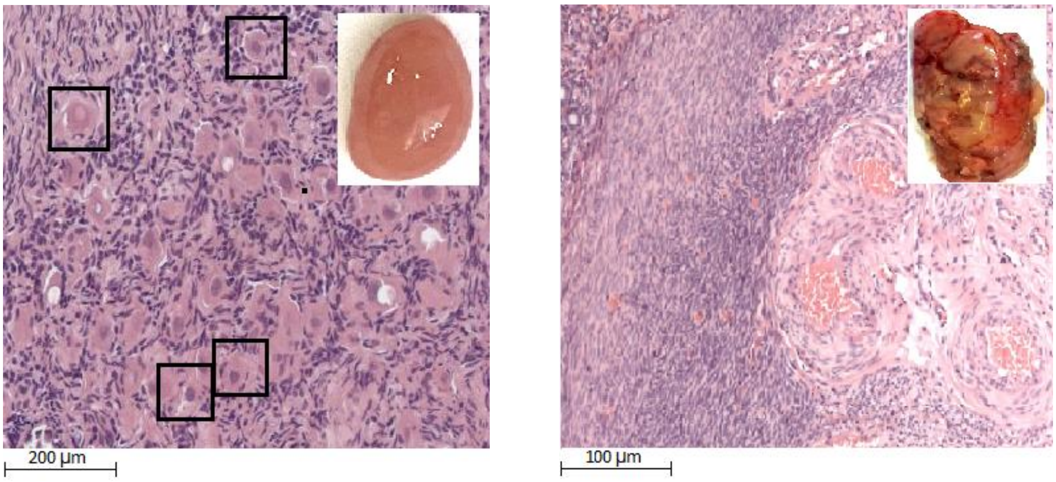

(a) (b)

Fig. 2 Images of histological sections of (a) healthy feline ovaries and (b) feline ovaries with leiomyosarcoma.

The images of histological sections of healthy and cancerous feline ovaries are provided in Fig. 2. Fig. 2a shows the histological examination of healthy ovaries. The histological structure of ovary is intact. The cortical substance is well-developed, the ratio of stroma to parenchyma is close to 1:1.5; the theca has a typical appearance. There are many visible follicles at various stages of maturation. There is no evidence of atypical development, necrosis, invasive growth, mitotic activity, inflammation, bacterial or fungal colonies. The histological pattern corresponds to ovary in follicular growth phase.

Ovaries with leiomyosarcoma is presented in Fig. 2(b). The examination revealed prominent atypical tissue changes with autolytic tumor fragments. Atypical fusiform tumor cells have high nucleocytoplasmic ratio with 1−2 eosinophilic nucleoli visible at magnification of 400; tumor necrosis fields with cell shadows are also visible. The degree of nuclear atypia is high, tumor cells form solid fields. Stroma is rather poorly developed; vascularization is badly visualized. Lymphovascular invasion is not determined in the sample of studied materials. Mitotic activity shows 20 mitoses per 10 fields of view at magnification of 400× (2.5 mm^2). Morphological pattern is mostly typical for leiomyosarcoma.

3.2 SEM Scanning of Ovary Tissue Sections

Dried sections of studied samples were studied using scanning electron microscopy (SEM images are shown in Fig. 3).

The extracellular matrix is formed by elastic collagen fibers whose packing density varied between studied samples. In healthy ovaries collagen fibers have approximately the same diameter without any breaks and are densely packed (Fig. 3(a)). The sample of ovary with leiomyosarcoma contains a specific intertwining of collagen fibers that form several regular compacted fusiform foci (Fig. 3(b)).

Elemental composition of studied samples found via energy dispersive analysis is provided in Table 1. The weight ratio of elements was determined for five points within four selected areas of SEM images of each of the studied samples and averaged. As we can see, the ratios of *N* and *O* in affected tissues is greater, while the ratio of *C* is lower.

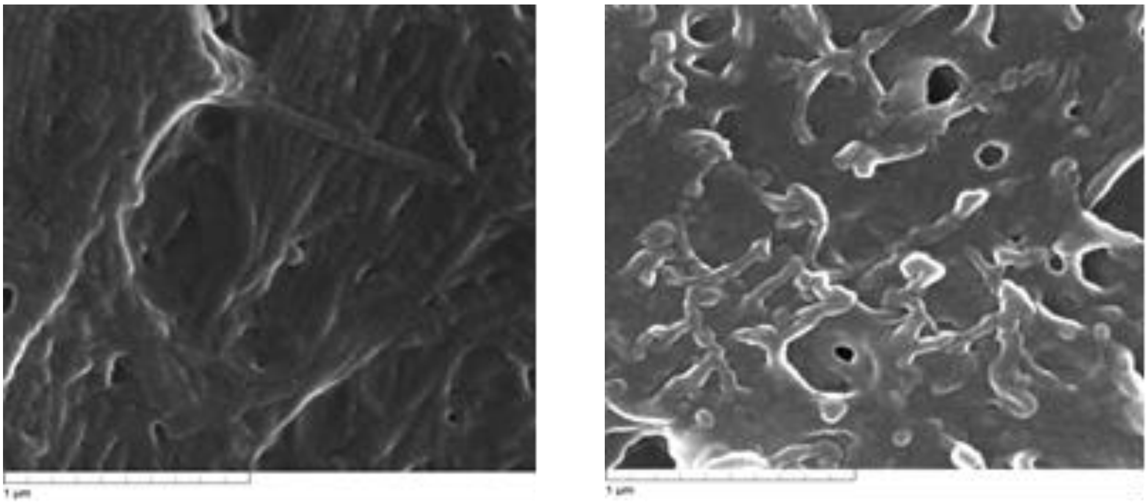

(a) (b)

Fig. 3 SEM images (magnification of 100 kx) of sections of cat's ovary tissue samples: (a) healthy ovary, (b) ovary with leiomyosarcoma.

Table 1 Elemental composition of studied samples.

Studied sample	**Element content, wt. %**									
	C	***N***	***O***	***Na***	***Mg***	***Al***	***P***	***S***	***Cl***	***K***
Healthy ovary	66.9	11.5	16.8	0.62	−	−	0.64	0.44	1.32	0.87
Leiomyosarcoma	52.9	18.5	22.7	0.72	0.09	0.12	0.21	0.85	1.63	1.62

Table 2 Parameters of soft tissue evaporation by continuous CO_2 laser radiation.

	***O*₁**	***O*₂**	***O*₁**	***O*₂**	***O*₁**	***O*₂**	***O*₁**	***O*₂**	***O*₁**	***O*₂**
Sample	**Sample 1**		**Sample 2**		**Sample 3**		**Sample 4**		**Sample 5**	
Healthy ovaries	1.25	0.85	1.95	0.64	1.12	0.34	1.54	0.42	2.14	0.73
Discrepancy between O_1 and O_2	0.40		1.31		0.78		1.12		1.41	
Sample	**Sample 6**		**Sample 7**		**Sample 8**		**Sample 9**		**Sample 10**	
Ovary with leiomyosarcoma	0.08	0.03	0.04	0.00	0.36	0.29	0.35	0.24	0.28	0.11
Discrepancy between O_1 and O_2	0.05		0.04		0.28		0.11		0.17	

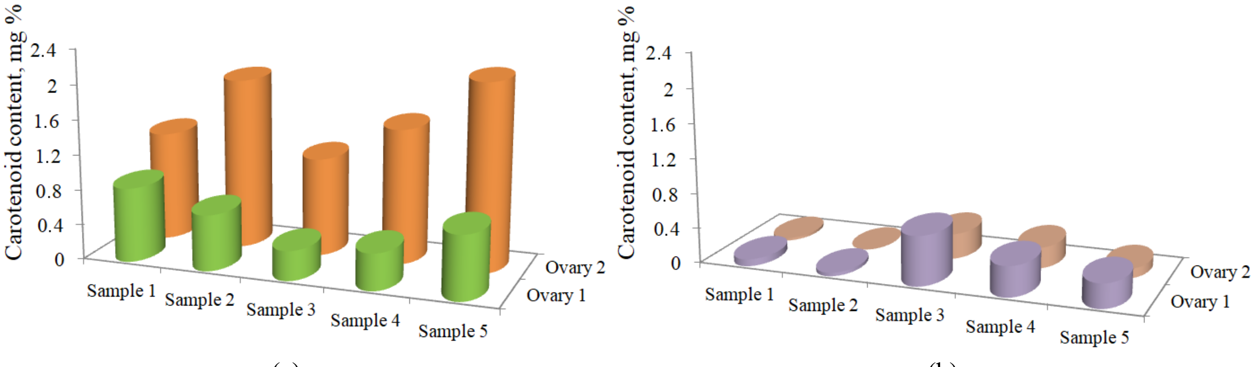

(a) (b)

Fig. 4 Total carotenoid content (calculated to *β*-carotene) in the samples of feline ovaries: (a) healthy ovary; (b) ovary with leiomyosarcoma.

3.3 Spectrophotometric Studies

Total carotenoid content calculated to β-carotene has been determined after extraction of these carotenoids from tissues by 95% ethanol solution. The results of spectrophotometric examination are provided in Table 2. We have studied five healthy animals (samples 1−5) and five animals with the same diagnosis (samples 6−10), and for reference we also have studied both ovaries for each cat (O_1 and O_2).

The highest content of carotenoids was observed in healthy ovaries and equaled 2.14 mg% with discrepancies between the pair of ovaries varying between 0.4 and 1.41 mg%. Total carotenoid content in ovaries with leiomyosarcoma ranged from 0 to 0.57 mg% with discrepancies between the pair of ovaries varying between 0.04 and 0.28 mg% (Fig. 4).

Mann-Whitney *U*-test was used to compare Sample 1 (values obtained for ovary 1, $n = 5$) and Sample 2 (values obtained for ovary 2, $n = 5$) for healthy ovaries and ovaries with leiomyosarcoma. The critical (tabular) values of U are 4 (if $p = 0.05$) and 1 (if $p = 0.01$). For experimental data, the found values of U were 0 and 7 for healthy ovaries and ovaries with leiomyosarcoma, respectively. Therefore, we can see that healthy ovaries significantly differ from each other ($U_{exp} < U_{cr}$). In the case of ovaries with leiomyosarcoma, $U_{exp} > U_{cr}$, thus, there is no significant difference between the ovaries.

The same approach was used to compare samples with different diagnoses, i.e. healthy feline ovaries with ovaries of cats diagnosed with leiomyosarcoma. To do that, we combined results for both cancerous ovaries into a separate sample ($n = 10$). The experimental value of U according to Mann-Whitney test equaled 2. Critical (tabular) values of U are 27 (if $p = 0.05$) and 16 (if $p = 0.01$). Thus, we can see that tested samples significantly differed from each other at both levels of significance.

According to our studies, left and right ovaries of a healthy cats have different total carotenoid content. For examples, total carotenoid content in left ovary ranged from 1.12 to 2.14 mg%. This results in significant discrepancies in total carotenoid content (calculated to β-carotene) between left and right ovaries of one animal that may vary from 0.40 to 1.41 mg%.

Total carotenoid content in left ovaries of cats diagnosed with leiomyosarcoma ranged from 0.04 to 0.57 mg%, while in right ovaries it ranged from 0.00 to 0.29 mg%. The discrepancies in content between left and right ovaries ranged from 0.04 to 0.28 mg%.

Looking ahead, it was interesting to establish a possible correlation between carotenoid levels in the skin and internal organs, including ovarian tissue. If such a correlation were found, it would be possible to monitor carotenoid levels in ovarian tissue in both normal and pathological conditions. Currently, noninvasive and rapid methods for determining carotenoid levels in living tissues *in vivo* are well developed and are used to monitor changes in their concentration in response to food intake or dietary supplements containing carotenoids. Reflectance spectroscopy is an accessible method used for the rapid, noninvasive, quantitative determination of carotenoids in living human skin [27]. The analyzed skin area is illuminated with white light in the range of 350 to 850 nm, and a compression method is used to reduce the effect of oxyhemoglobin on the reflectance spectra. Detection of carotenoids in skin *in vivo* is also possible using a simple spectroscopic optical setup developed by the authors [28] with a fiber probe without lenses, mirrors, or aperture, which reduces development costs. High correlation between resonance Raman spectroscopy and reflectance spectroscopy data was achieved in the noninvasive determination of carotenoids in human skin *in vivo* and cow udder *in vitro*. [29]. Thus, the introduction of noninvasive measurements of carotenoids in living tissues into clinical practice may improve dietary recommendations for disease prevention.

To improve the accuracy of determining the spectral absorption of beta-carotene within tissue using reflectance spectroscopy, it is possible to simultaneously use compression and immersion tissue optical clearing [30]. Studies on tissue phantoms have shown that the combination of analytical and experimental optical clearing methods expands the capabilities of diffuse reflectance spectroscopy for precise extracting the absorption coefficient of beta-carotene as one of the chromophores within tissue.

4 Conclusion

We found that total carotenoid content in healthy feline ovaries differs between left and right ovary of the same animal. However, both left and right ovaries of cats diagnosed with leiomyosarcoma contained significantly lower quantities of carotenoids. As carotenoids can be used as chemotherapeutic agents, the study of their total content in ovaries is relevant and requires further studies.

Author Contribution

T. Yu. Rusanova and V. V. Tuchin designed the concept of study; A. A. Chernov, E. I. Selifonova and A. M. Zakharevich conducted the experimental study; A. S. Rykhlov gathered clinical data and results of study and conducted histological examination of samples in a specialized laboratory; T. Yu. Rusanova, A. A. Chernov, E. I. Selifonova, A. M. Zakharevich, A. S. Rykhlov and V. V. Tuchin discussed the results of the study; A. A. Chernov, Yu. S. Kruss prepared the first draft of the article and performed statistical analysis of data; T. Yu. Rusanova and V. V. Tuchin edited the final draft of the article.

Disclosures

All authors declare that there is no conflict of interest in this paper.

Ethical Practices

This article does not describe any studies involving people or animals as research subjects.

Acknowledgements

This work was supported by the Russian Science Foundation (project No. 24-23-00519).

References

1. R. U. K, A. P. Elango, R. Subramanian, and S. Ks, "The evolving landscape of ovarian cancer: innovations in biotechnology and artificial intelligence- based screening and treatment," Current Treatment Options in Oncology 26(7), 622–637 (2025).
2. R. Sparić, M. Andjić, I. Babović, L. Nejković, M. Mitrović, J. Štulić, M. Pupovac, and A. Tinelli, "Molecular insights in uterine leiomyosarcoma: a systematic review," International Journal of Molecular Sciences 23(17), 9728 (2022).
3. M. Bosoteanu, M. Deacu, R. I. Voda, C. I. Orasanu, M. Aschie, S. E. Vlad, R. C. Penciu, and S. I. Chirila, "Five-year retrospective study of uterine stump and leiomyosarcoma," Clinics and Practice 12(6), 897–907 (2022).
4. N. Arslansoy and O. Fidan, "Carotenoids and Their Antioxidant Power," Biochemistry 60 (2024).
5. A. Nishino, T. Ichihara, T. Takaha, T. Kuriki, H. Nihei, K. Kawamoto, H. Yasui, and T. Maoka, "Accumulation of paprika carotenoids in human plasma and erythrocytes," Journal of Oleo Science 64(10), 1135–1142 (2015).
6. R. Srivastava, "Physicochemical, antioxidant properties of carotenoids and its optoelectronic and interaction studies with chlorophyll pigments," Scientific Reports 11(1), 18365 (2021).
7. M. K. Dehnavi, S. Ebrahimpour-Koujan, K. Lotfi, and L. Azadbakht, "The association between circulating carotenoids and risk of breast cancer: a systematic review and dose–response meta-analysis of prospective studies," Advances in Nutrition 15(1), 100135 (2024).
8. C. Peng, O. A. Zeleznik, K. H. Shutta, B. A. Rosner, P. Kraft, C. B. Clish, M. J. Stampfer, W. C. Willett, R. M. Tamimi, and A. H. Eliassen, "A metabolomics analysis of circulating carotenoids and breast cancer risk," Cancer Epidemiology, Biomarkers & Prevention 31(1), 85–96 (2022).
9. E. Czeczuga-Semeniuk and S. Wołczyński, "Dietary carotenoids in normal and pathological tissues of corpus uteri," Folia Histochemica et Cytobiologica 46(3), 283–290 (2008).

10. E. Czeczuga-Semeniuk and S. Wolczynski, “Identification of carotenoids in ovarian tissue in women,” Oncology Reports 14(5), 1385-1392 (2005).
11. E. Czeczuga-Semeniuk and S. Wołczyński, “Does variability in carotenoid composition and concentration in tissues of the breast and reproductive tract in women depend on type of lesion?,” Advances in Medical Sciences 53(2), 270-277 (2008).
12. M. Zhang, C. D. J. Holman, and C. W. Binns, “Intake of specific carotenoids and the risk of epithelial ovarian cancer,” British Journal of Nutrition 98(1), 187-193 (2007).
13. A. Koushik, D. J. Hunter, D. Spiegelman, K. E. Anderson, J. E. Buring, J. L. Freudenheim, R. A. Goldbohm, S. E. Hankinson, S. C. Larsson, M. Leitzmann, J. R. Marshall, M. L. McCullough, A. B. Miller, C. Rodriguez, T. E. Rohan, J. A. Ross, A. Schatzkin, L. J. Schouten, W. C. Willett, A. Wolk, S. M. Zhang, and S. A. Smith-Warner, “Intake of the major carotenoids and the risk of epithelial ovarian cancer in a pooled analysis of 10 cohort studies,” International Journal of Cancer 119(9), 2148–2154 (2006).
14. V. Böhm, G. Lietz, B. Olmedilla-Alonso, D. Phelan, E. Reboul, D. Bánati, P. Borel, J. Corte-Real, A. R. De Lera, C. Desmarchelier, J. Dulinska-Litewka, J.-F. Landrier, I. Milisav, J. Nolan, M. Porrini, P. Riso, J. M. Roob, E. Valanou, A. Wawrzyniak, B. M. Winklhofer-Roob, R. Rühl, and T. Bohn, “From carotenoid intake to carotenoid blood and tissue concentrations – implications for dietary intake recommendations,” Nutrition Reviews 79(5), 544–573 (2021).
15. B. P. Chew, B. B. C. Weng, H. W. Kim, T. S. Wong, J. S. Park, and A. J. Lepine, “Uptake of β-carotene by ovarian and uterine tissues and effects on steroidogenesis during the estrous cycle in cats,” American Journal of Veterinary Research 62(7), 1063–1067 (2001).
16. I. Gunyeli, M. Saygin, and O. Ozmen, “Methotrexate-induced toxic effects and the ameliorating effects of astaxanthin on genitourinary tissues in a female rat model,” Archives of Gynecology and Obstetrics 304(4), 985–997 (2021).
17. C.-S. Lei, Y.-C. Hou, M.-H. Pai, M.-T. Lin, and S.-L. Yeh, “Effects of quercetin combined with anticancer drugs on metastasis-associated factors of gastric cancer cells: *in vitro* and *in vivo* studies,” The Journal of Nutritional Biochemistry 51, 105–113 (2018).
18. N. I. Krinsky and E. J. Johnson, “Carotenoid actions and their relation to health and disease,” Molecular Aspects of Medicine 26(6), 459–516 (2005).
19. J. Shin, M.-H. Song, J.-W. Oh, Y.-S. Keum, and R. K. Saini, “Pro-oxidant actions of carotenoids in triggering apoptosis of cancer cells: a review of emerging evidence,” Antioxidants 9(6), 532 (2020).
20. C. Allemani, T. Matsuda, V. Di Carlo, R. Harewood, M. Matz, M. Nikšić, A. Bonaventure, M. Valkov, C. J. Johnson, J. Estève, O. J. Ogunbiyi, G. A. E Silva, W.-Q. Chen, S. Eser, G. Engholm, C. A. Stiller, A. Monnereau, R. R. Woods, O. Visser, G. H. Lim, J. Aitken, H. K. Weir, M. P. Coleman, CONCORD Working Group, “Global surveillance of trends in cancer survival 2000–14 (CONCORD-3): analysis of individual records for 37 513 025 patients diagnosed with one of 18 cancers from 322 population-based registries in 71 countries,” The Lancet 391(10125), 1023–1075 (2018).
21. G. L. Russo, S. Moccia, M. Russo, and C. Spagnuolo, “Redox regulation by carotenoids: Evidence and conflicts for their application in cancer,” Biochemical Pharmacology 194, 114838 (2021).
22. C. Liu, R. M. Russell, and X.-D. Wang, “Lycopene supplementation prevents smoke-induced changes in p53, p53 phosphorylation, cell proliferation, and apoptosis in the gastric mucosa of ferrets,” The Journal of Nutrition 136(1), 106–111 (2006).
23. A. A. Selifonov and V. V. Tuchin, “Optical properties of porcine oral mucosa at application of iodine preparation based on glycerol,” Photonic Diagnosis, Monitoring, Prevention, and Treatment of Infections and Inflammatory Diseases, 116260X (2021).
24. V. V. Tuchin, D. Zhu, and E. A. Genina, Handbook of Tissue Optical Clearing: New Prospects in Optical Imaging, 1st ed. (CRC Press, 2021).
25. N. N. Karkischenko, V. N. Karkischenko, Yu. V. Fokin, L. A. Taboyakova, O. V. Alimkina, and M. M. Borisova, “Between cognitivity and neuropathies: neuroimaging of the effects of gabaergic modulation of the hippocampus and prefrontal neocortexis by normalized brain electrograms,” Biomedicine (2), 12–38 (2020).
26. D.B. Rodriguez-Amaya, A guide to carotenoid analysis in foods. Printed in the United States of America, ILSI Press, 64 p. (2001). ISBN: 1578810728.
27. I. V. Ermakov and W. Gellermann, “Dermal carotenoid measurements via pressure mediated reflection spectroscopy,” Journal of Biophotonics 5(7), 559–570 (2012).
28. S. Andree, C. Reble, and J. Helfmann, “Spectral *in vivo* signature of carotenoids in visible light diffuse reflectance from skin in comparison to *ex vivo* absorption spectra,” Photonics & Lasers in Medicine 2(4), (2013).
29. M. E. Darvin, C. Sandhagen, W. Koecher, W. Sterry, J. Lademann, and M. C. Meinke, “Comparison of two methods for noninvasive determination of carotenoids in human and animal skin: Raman spectroscopy versus reflection spectroscopy,” Journal of Biophotonics 5(7), 550–558 (2012).

30. S. Masoumi, M. A. Ansari, E. Mohajerani, E. A. Genina, and V. V. Tuchin, "Combination of analytical and experimental optical clearing of rodent specimen for detecting beta-carotene: phantom study," Journal of Biomedical Optics 23(09), 1 (2018).

A Problem of THz Endoscopy of Hard-to-Access Tissues

Kirill I. Zaytsev[1]*, Gleb M. Katyba[2], Nikita V. Chernomyrdin[1], Kirill B. Dolganov[1], Irina N. Dolganova[2], Sergei V. Garnov[1], and Vladimir N. Kurlov[2]

[1] Prokhorov General Physics Institute of the Russian Academy of Sciences, 38 Vavilova str.,
Moscow 119991, Russian Federation

[2] Osipyan Institute of Solid State Physics of the Russian Academy of Sciences, 2 Academician Osipyan str.,
Moscow District, Chernogolovka 142432, Russian Federation

*e-mail: kirzay@gmail.com

Abstract. Despite terahertz (THz) technologies offer a number of applications in medical diagnosis and therapy, their translation into clinics is hampered by the lack of THz endoscopes capable of sensing THz response of hard-to-access tissues. In this paper, we focus on recent attempts to mitigate this difficulty. We consider the two existing principles of THz endoscopy. The first uses the fiber-coupled THz photoconductive antennas (PCAs) for the THz generation and detection in close proximity to an object. The second relies on the THz optical fibers to deliver THz waves to an analyte and then to detect the reflected THz signal. Most recent developments in the area of THz fiber optics pave the way to solve the challenging problem of THz endoscopy. Among them, we emphasize the THz fibers, fiber bundles, waveguides, and endoscopes developed by our research group based on the sapphire shaped crystals obtained by the edge-defined film-fed growth (EFG) technique.

Keywords: THz technology; THz fiber optics; THz endoscopy; THz medical diagnosis; THz spectroscopy and imaging.

Paper #9378 received 16 Oct 2025; revised manuscript received 31 Dec 2025; accepted for publication 31 Dec 2025; published online 10 Apr 2026. doi: 10.18287/JBPE26.12.020302.

1 Introduction

During the past decades, THz technology has been vigorously explored [1–4]. Nowadays, it has a potential in a number of applications, including the non-destructive testing [5], security task [6], label-free medical diagnostics of neoplasms [7, 8], cerebral ischemia, neurodegenerative diseases, traumatic injuries of the brain [9], diabetic foot syndrome [10], and even cancer therapy [11]. The majority of these applications involve measurements of the THz dielectric (optical) properties of an object. Despite the ubiquitous use of THz technologies, their translation into the aforementioned fields is hampered by the lack of THz endoscopes and methods to quantify the THz response of hard-to-access objects [7, 12]. In contrast to the visible–IR range with diverse fiber optics technologies, a lack of the THz fiber optics components and systems is evident, which leads to the nascent state of THz endoscopy [13, 14].

In this paper, recent attempts to address this challenging problem are considered. THz applications in medical diagnosis are overviewed, with an emphasis on neoplasms with the different nosologies and localizations [7]. Then, two distinct approaches of THz endoscopy are discussed [12]. The first uses the fiber-coupled THz PCAs to emit and detect THz waves in close proximity to a hard-to-access object [15, 16]. Such systems seem to be quite complex, cumbersome, and non-cost-efficient, which somewhat limits their practical utility. The second relies on the THz optical fibers / waveguides as key elements for delivering THz waves from an emitter to an object and then to detect the reflected THz signal. Although the THz optical fibers / waveguides still remain rare, expensive, and inefficient, recent developments in the THz fiber optics technologies pave the way to solve the demanding problem of THz endoscopy [12].

2 Results

We notice a few examples of THz waveguides and related endoscopic systems, which use the different material platforms, fabrication strategies, and guiding mechanisms, such as the reflection from walls in metal tubes [17], total internal reflection in step-index fibers [18], anti-resonant reflecting optical waveguiding

This paper was presented at the XI International Conference "Information Technology and Nanotechnology" (ITNT-2025), Samarkand, Uzbekistan, October 7 – 9, 2025.

(ARROW) [19] or photonic crystalline (PC) / Bragg waveguiding [20] in microstructured fibers, as well as plasmonic waveguiding [21].

Several THz fiber optics elements were developed by our research group relying on the EFG-grown sapphire shaped crystals [14]. A favorable combination of the unique physical and chemical properties of sapphire (high refractive index and low absorption in the THz range, high mechanical and radiation strength, chemical inertness, and biocompatibility) with the capabilities of the EFG technique to produce crystals of a delicate cross section directly from the Al_2O_3 melt, makes the EFG-grown sapphire shaped crystals an attractive material platform of THz fiber optics.

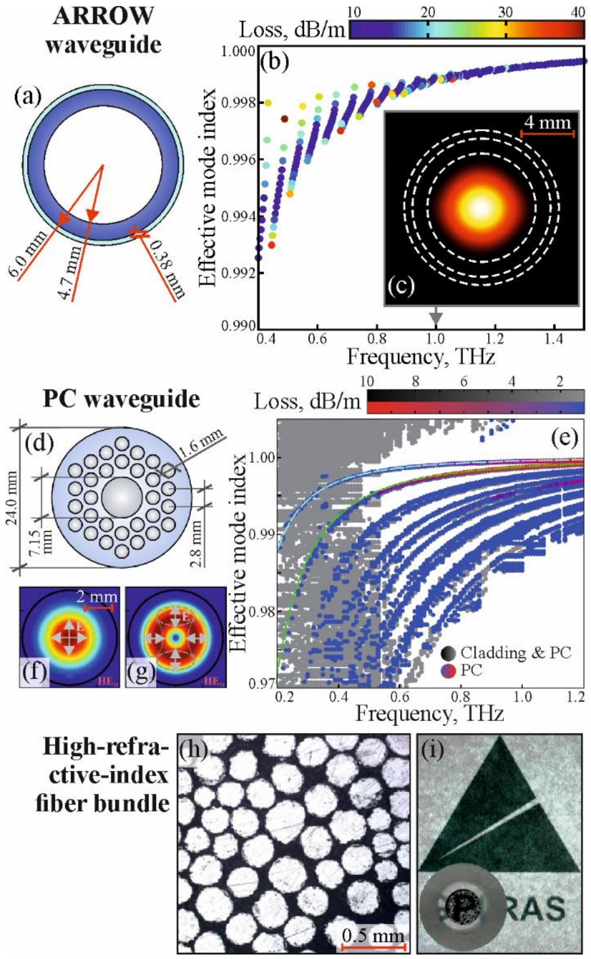

Fig. 1 A few examples of the EFG-grown THz fiber optics elements. (a–c) Scheme of the cross-section of the ARROW THz waveguide based on a PTFE-coated sapphire tube, along with the guiding properties (effective mode index and propagation loss) and intensity distribution (over the cross-section) for the fundamental mode in such waveguide. (d–g) Similar data set for the sapphire PC THz waveguide with two core-guided effective modes. (h),(i) Microscopy and photo of the THz optical fiber bundle formed by the sub-millimeter-diameter step-index sapphire fibers suspended in epoxy resin. Courtesy of K.I. Zaytsev.

In this way, the EFG technique was applied to produce:

- the hollow-core ARROW (Figs. 1 (a–c)) or PC (Figs. 1 (d–g)) waveguides for the THz-wave delivery and intrawaveguide sensing [22–25];
- the single step-index optical fibers for the THz scanning-probe near-field optical microscopy [26, 27];
- the optical fiber bundles for the superresolution THz imaging (Figs. 1 (h, i)) [28–30].

Most recently, the THz endoscope based on the hollow-core ARROW waveguide was developed by our group [31]. For this, the polytetrafluoroethylene (PTFE)-coated EFG-grown sapphire tube was used, as a key element, as shown in Fig. 2 (a). This system made it possible, for the first time, to quantify the THz optical properties of hard-to-access objects, such as biological tissues and internal organs. Our endoscope was attached to the in-house reflection-mode backward wave oscillator (BWO) spectrometer. The latter relies on the in-house continuous-wave BWO (the output frequency ranges from $\nu = 0.550$ to 0.715 THz, while the spectral linewidth is as narrow as $\sim 10^{-5}\nu$) [32, 33] and the in-house Golay cell (the THz-beam intensity detector) [34]. The outer end of the endoscope was closed by a $d = 1$-mm-thick c-cut (i.e. the optical axis is collinear to the sapphire c-axis) sapphire window, that serves both as a sample holder and a Fabry-Perot sensor of refractive index of an analyte.

In Figs. 2 (b–d), we show examples of the sapphire window reflectivity measured through the endoscope, when it is placed in contact with different test media, with a priori known THz refractive indices: air, liquid water, and propylene glycol (PG). Changes in the parameters of the Farby-Perot minimum in the reflectivity spectra are evident. Their analysis makes it possible to quantify the THz complex refractive index of an analyte [31]. For this, let us define the complex refractive index of sapphire

$$\tilde{n}_{Al_2O_3} = n_{Al_2O_3} - in''_{Al_2O_3} = n_{Al_2O_3} - i\frac{c_0}{4\pi\nu}\alpha_{Al_2O_3}, \qquad (1)$$

$n_{Al_2O_3}$ and $\alpha_{Al_2O_3}$ are the real refractive index and power absorption coefficient (both – for the ordinary ray) [35], $c_0 = 3 \times 10^8$ m/s is the speed of light in free space), guided mode (Fig. 1(b))

$$\tilde{n}_{eff} = n_{eff} - in''_{eff} = n_{eff} - i\frac{c_0}{4\pi\nu}\alpha_{eff} \cong 1, \qquad (2)$$

and analyte

$$\tilde{n} = n - in'' = n - i\frac{c_0}{4\pi\nu}\alpha. \qquad (3)$$

Then, the magnitude and position of the local Fabry-Perot minimum in the reflectivity curves (Figs. 2 (b–d)) take the forms [36]:

$$R_{min} = \left|\frac{\tilde{r}_{eff-Al_2O_3} - \tilde{r}_{Al_2O_3-analyte}}{1 - \tilde{r}_{eff-Al_2O_3}\tilde{r}_{Al_2O_3-analyte}}\right|^2, \qquad (4)$$

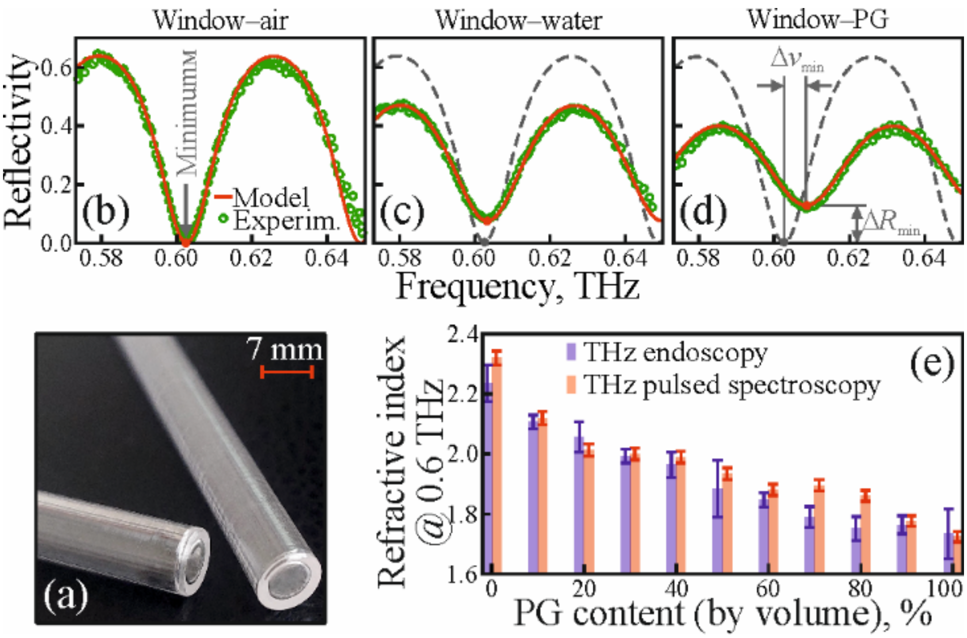

Fig. 2 THz endoscopy of hard-to-access test objects using the ARROW THz waveguide made of the EFG-grown sapphire tube coated by PTFE. (a) A photo of the THz endoscopes, with the output ends closed by monolithic (as-grown) d = 1-mm-thick sapphire window. (b–d) Fabry-Perot resonances (minima) observed in the reflectivity of the sapphire window with a free space, liquid water and PG, respectively, placed at its shadow side. (e) Endoscopic determination of the refractive index (at 0.6 THz) of the liquid analytes (namely, the PG aqueous solutions of the different volume fractions) as compared to the reference transmission-mode measurements by the THz pulsed spectrometer. Courtesy of K.I. Zaytsev.

$$\nu_{min} = \frac{c_0}{4dn_{Al_2O_3}}\left(\frac{\varphi}{\pi} + (2m+1)\right), \tag{5}$$

where $m = 0, \pm1, \pm2, \ldots$ is an integer, $\tilde{r}_{eff-Al_2O_3}$ and $\tilde{r}_{Al_2O_3-sample}$ are the Fresnel amplitude reflection coefficients (at the normal incidence) for the "waveguide core–sapphire" and "sapphire–analyte" interfaces defined as:

$$\tilde{r}_{eff-Al_2O_3} = \frac{\tilde{n}_{eff}-\tilde{n}_{Al_2O_3}}{\tilde{n}_{eff}+\tilde{n}_{AAl_2O_3}}, \tag{6}$$

$$\tilde{r}_{Al_2O_3-analyte} = \frac{\tilde{n}_{AAl_2O_3}-\tilde{n}}{\tilde{n}_{Al_2O_3}+\tilde{n}}, \tag{7}$$

φ is the phase shift at the "window–analyte" interface:

$$\varphi = arctan\left[\frac{2n_{Al_2O_3}n''}{n^2_{Al_2O_3}-n^2-n''^2}\right]. \tag{8}$$

Using the developed THz endoscope and the inferred equations, in Fig. 2 (e), we characterize the refractive indices of the PG aqueous solutions with different volume fractions. One observed good agreement between our THz endoscopic measurements and those performed by the in-house reflection-mode THz pulsed spectrometer [37–39]. This highlights capability of our THz endoscope to measure the THz dielectric response of hard-to-access objects at the distances of about ~10 cm, and even larger.

The developed THz endoscope and the related data processing routine pave the way for THz technology application in different demanding branches of science and technology, which require the THz-wave delivery to a hard-to-access object, including the THz medical diagnosis of internal tissues and organs. Moreover, the advanced chemical inertness and thermal strength of the endoscope materials (i.e., the sapphire and PTFE), make it possible to apply thus developed system for sensing in harsh environments. This feature additionally broadens the range of the THz endoscopy applications.

Nevertheless, to objectively uncover the strengths and weaknesses of the developed THz endoscopy hardware and software, additional studies of some real-world objects (such as healthy and pathologically-altered tissues, chemical and pharmaceutical analytes, materials, etc.) are in order. Reduction of the outer diameter of such a THz endoscope down to the realistic values of ~3–4 mm is also preferable for its applications in minimally-invasive medical procedures. We postpone all these studies and upgrades to our future research work.

3 Conclusion

In this paper, we focused on recent attempts to mitigate the problem of THz endoscopy of hard-to-access tissues and internal organs. The two existing principles of THz endoscopy were considered:

- The first uses the fiber-coupled THz PCAs for the THz generation and detection in close proximity to an object, while quartz optical fibers are used to deliver the laser pump and probe beams to these PCAs.
- The second relies on the THz optical fibers / waveguides to deliver THz waves to an object and

then to detect the reflected and back-propagated THz signal.

The most recent developments in the area of THz fiber optics are discussed. They pave the way to solve the challenging problem of THz endoscopy. Among them: the THz fibers, fiber bundles, waveguides, and endoscopes developed by our group relying on the EFG-grown sapphire shaped crystals.

Disclosures

All authors declare that there is no conflict of interest in this paper.

Acknowledgements

This work is supported by the Russian Science Foundation, Project # 22–79–10099.

References

1. H. Guerboukha, K. Nallappan, and M. Skorobogatiy, "Toward real-time terahertz imaging," Advances in Optics and Photonics 10(4), 843–938 (2018).
2. M. Koch, D. M. Mittleman, J. Ornik, and E. Castro-Camus, "Terahertz time-domain spectroscopy," Nature Reviews Methods Primers 3(1), 48 (2023).
3. X. Li, J. Li, Y. Li, A. Ozcan, and M. Jarrahi, "High-throughput terahertz imaging: progress and challenges," Light: Science & Applications 12(1), 233 (2023).
4. X. Guo, K. Bertling, B. C. Donose, M. Brünig, A. Cernescu, A. A. Govyadinov, and A. D. Rakić, "Terahertz nanoscopy: Advances, challenges, and the road ahead," Applied Physics Reviews 11(2), 021306 (2024).
5. J.-Y. Zhang, J.-J. Ren, L.-J. Li, J. Gu, and D.-D. Zhang, "THz imaging technique for nondestructive analysis of debonding defects in ceramic matrix composites based on multiple echoes and feature fusion," Optics Express 28(14), 19901–19915 (2020).
6. I. N. Dolganova, K. I. Zaytsev, S. O. Yurchenko, V. E. Karasik, and V. V. Tuchin, "The role of scattering in quasi-ordered structures for terahertz imaging: local order can increase an image quality," IEEE Transactions on Terahertz Science & Technology 8(4), 403–409 (2018).
7. K. I. Zaytsev, I. N. Dolganova, N. V. Chernomyrdin, G. M. Katyba, A. A. Gavdush, O. P. Cherkasova, G. A. Komandin, M. A. Shchedrina, A. N. Khodan, D. S. Ponomarev, I. V. Reshetov, V. E. Karasik, M. Skorobogatiy, V. N. Kurlov, and V. V. Tuchin, "The progress and perspectives of terahertz technology for diagnosis of neoplasms: a review," Journal of Optics 22(1), 013001 (2019).
8. G. R. Musina, P. V. Nikitin, N. V. Chernomyrdin, I. N. Dolganova, A. A. Gavdush, G. A. Komandin, D. S. Ponomarev, A. A. Potapov, I. V. Reshetov, V. V. Tuchin, and K. I. Zaytsev, "Prospects of terahertz technology in diagnosis of human brain tumors – A review," Journal of Biomedical Photonics & Engineering 6(2), 020201 (2020).
9. N. V. Chernomyrdin, G. R. Musina, P. V. Nikitin, I. N. Dolganova, A. S. Kucheryavenko, A. I. Alekseeva, Y. Wang, D. Xu, Q. Shi, V. V. Tuchin, and K. I. Zaytsev, "Terahertz technology in intraoperative neurodiagnostics: A review," Opto-Electronic Advances 6(22), 220071 (2023).
10. G. G. Hernandez-Cardoso, L. F. Amador-Medina, G. Gutierrez-Torres, E. S. Reyes-Reyes, C. A. Benavides Martínez, C. Cardona Espinoza, J. Arce Cruz, I. Salas-Gutierrez, B. O. Murillo-Ortíz, and E. Castro-Camus, "Terahertz imaging demonstrates its diagnostic potential and reveals a relationship between cutaneous dehydration and neuropathy for diabetic foot syndrome patients," Scientific Reports 12(1), 3110 (2022).
11. O. P. Cherkasova, D. S. Serdyukov, E. F. Nemova, A. S. Ratushnyak, A. S. Kucheryavenko, I. N. Dolganova, G. Xu, M. Skorobogatiy, I. V. Reshetov, P. S. Timashev, I. E. Spektor, K. I. Zaytsev, and V. V. Tuchin, "Cellular effects of terahertz waves," Journal of Biomedical Optics 26(9), 090902 (2021).
12. G. M. Katyba, N. V. Chernomyrdin, I. N. Dolganova, A. S. Kucheryavenko, Q. Shi, P.V. Aleksandrova, D. S. Ponomarev, S. V. Garnov, I. V. Reshetov, V. V. Tuchin, V. N. Kurlov, M. Skorobogatiy, and K. I. Zaytsev, "Terahertz endoscopy of hard-to-access objects in the context of neoplasms diagnosis – A review," Light: Advanced Manufacturing 6(3), 504–521 (2025).
13. Md. S. Islam, C. M. B. Cordeiro, M. A. R. Franco, J. Sultana, A. L. S. Cruz, and D. Abbott, "Terahertz optical fibers," Optics Express 28(11),16089–16117 (2020).
14. G. M. Katyba, K. I. Zaytsev, I. N. Dolganova, N. V. Chernomyrdin, V. E. Ulitko, S. N. Rossolenko, I. A. Shikunova, and V. N. Kurlov, "Sapphire waveguides and fibers for terahertz applications," Progress in Crystal Growth and Characterization of Materials 67(3), 100523 (2021).
15. M. R. Grootendorst, A. J. Fitzgerald, S. G. Brouwer De Koning, A. Santaolalla, A. Portieri, M. Van Hemelrijck, M. R. Young, J. Owen, M. Cariati, M. Pepper, V. P. Wallace, S. E. Pinder, and A. Purushotham, "Use of a handheld terahertz pulsed imaging device to differentiate benign and malignant breast tissue," Biomedical Optics Express 8(6), 2932–2945 (2017).
16. Y. Chen, S. Huang, and E. Pickwell-MacPherson, "Frequency-wavelet domain deconvolution for terahertz reflection imaging and spectroscopy," Optics Express 18(2), 1177–1190 (2010).
17. B. Chen, K. Zhou, J. Shao, X. Zhao, B. Xu, J. Zhu, B. Xue, Z. Tan, J. Cao, H. Li, and C. Wu, "A low-loss hollow-core waveguide bundle for terahertz imaging under a cryogenic environment," ACS Photonics 11(8), 3068–3078 (2024).

18. G. Xu, K. Nallappan, Y. Cao, and M. Skorobogatiy, "Infinity additive manufacturing of continuous microstructured fiber links for THz communications," Scientific Reports 12(1), 4551 (2022).
19. M. Nazarov, A. Shilov, Z. Margushev, K. Bzheumikhov, I. Ozheredov, A. Angeluts, A. Sotsky, and A. Shkurinov, "A flexible terahertz waveguide for delivery and filtering of quantum-cascade laser radiation," Applied Physics Letters 113(13), 131107 (2018).
20. T. Ma, H. Guerboukha, M. Girard, A. D. Squires, R. A. Lewis, and M. Skorobogatiy, "3D printed hollow-core terahertz optical waveguides with hyperuniform disordered dielectric reflectors," Advanced Optical Materials 4(12), 2085–2094 (2016).
21. Y. Cao, K. Nallappan, G. Xu, and M. Skorobogatiy, "Add drop multiplexers for terahertz communications using two-wire waveguide-based plasmonic circuits," Nature Communications 13, 4090 (2022).
22. K. I. Zaytsev, G. M. Katyba, V. N. Kurlov, I. A. Shikunova, V. E. Karasik, and S. O. Yurchenko, "Terahertz photonic crystal waveguides based on sapphire shaped crystals," IEEE Transactions on Terahertz Science & Technology 6(4), 576–582 (2016).
23. G. M. Katyba, K. I. Zaytsev, N. V. Chernomyrdin, I. A. Shikunova, G. A. Komandin, V. B. Anzin, S. P. Lebedev, I. E. Spektor, V. E. Karasik, S. O. Yurchenko, I. V. Reshetov, V. N. Kurlov, and M. Skorobogatiy, "Sapphire photonic crystal waveguides for terahertz sensing in aggressive environments," Advanced Optical Materials 6(22), 1800573 (2018).
24. G. M. Katyba, P. A. Chizhov, V. N. Kurlov, I. N. Dolganova, S. V. Garnov, K. I. Zaytsev, and V. V. Bukin, "THz generation by two-color laser air plasma coupled to antiresonance hollow-core sapphire waveguides: THz-wave delivery and angular distribution management," Optics Express 30(3), 4215–4230 (2022).
25. A. S. Kucheryavenko, V. A. Zhelnov, D. G. Melikyants, N. V. Chernomyrdin, S. P. Lebedev, V. V. Bukin, S. V. Garnov, V. N. Kurlov, K. I. Zaytsev, and G. M. Katyba, "Super-resolution THz endoscope based on a hollow-core sapphire waveguide and a solid immersion lens," Optics Express 31(8), 13366–13373 (2023).
26. I. V. Minin, O. V. Minin, G. M. Katyba, N. V. Chernomyrdin, V. N. Kurlov, K. I. Zaytsev, L. Yue, Z. Wang, and D. N. Christodoulides, "Experimental observation of a photonic hook," Applied Physics Letters 114(3), 031105 (2019).
27. G. M. Katyba, D. G. Melikyants, N. V. Chernomyrdin, V. N. Kurlov, and K. I. Zaytsev, "Terahertz transmission-mode scanning-probe near-field optical microscopy based on a flexible step-index sapphire fiber," Optical Engineering 60(8), 082010 (2021).
28. K. I. Zaytsev, G. M. Katyba, N. V. Chernomyrdin, I. N. Dolganova, A. S. Kucheryavenko, A. N. Rossolenko, V. V. Tuchin, V. N. Kurlov, and M. Skorobogatiy, "Overcoming the abbe diffraction limit using a bundle of metal-coated high-refractive-index sapphire optical fibers," Advanced Optical Materials 8(18), 2000307 (2020).
29. G. M. Katyba, M. Skorobogatiy, D. G. Melikyants, N. V. Chernomyrdin, A. N. Perov, E. V. Yakovlev, I. N. Dolganova, I. E. Spektor, V. V. Tuchin, V. N. Kurlov, and K. I. Zaytsev, "Superresolution imaging using a tapered bundle of high-refractive-index optical fibers," Physical Review Applied 18(3), 034069 (2022).
30. G. M. Katyba, A. V. Radivon, D. V. Lavrukhin, D. S. Ponomarev, I. N. Dolganova, A.-E. P. Protopopova, S. V. Garnov, V. N. Kurlov, M. Skorobogatiy, and K. I. Zaytsev, "Modulation-transfer-function analysis for optical fiber bundle–based superresolution imaging systems," Physical Review Applied 25(1), 014041 (2026).
31. G. M. Katyba, S. P. Lebedev, A. S. Kucheryavenko, I. N. Dolganova, N. V. Chernomyrdin, M. G. Burdanova, I. E. Spektor, M. Skorobogatiy, V. N. Kurlov, and K. I. Zaytsev, "Terahertz refractometry of hard-to-access objects using the sapphire endoscope suitable for harsh environments," Applied Physics Letters 124(24), 243703 (2024).
32. G. A. Komandin, S. V. Chuchupal, S. P. Lebedev, Y. G. Goncharov, A. F. Korolev, O. E. Porodinkov, I. E. Spektor, and A. A. Volkov, "BWO generators for terahertz dielectric measurements," IEEE Transactions on Terahertz Science & Technology 3(4), 440–444 (2013).
33. B. Gorshunov, A. Volkov, I. Spektor, A. Prokhorov, A. Mukhin, M. Dressel, S. Uchida, and A. Loidl, "Terahertz BWO-spectrosopy," International Journal of Infrared and Millimeter Waves 26(9), 1217–1240 (2005).
34. H. A. Zahl, M. J. E. Golay, "Pneumatic heat detector," Review of Scientific Instruments 17(11), 511–515 (1946).
35. A. A. Gavdush, I. E. Spektor, K. B. Dolganov, V. N. Kurlov, I. N. Dolganova, and G. A. Komandin, "Temperature evolution of the optical parameters of sapphire in the THz-IR range," Applied Optics 64(15), 4453–4460 (2025).
36. M. Born, E. Wolf, Principles of Optics, 7th ed., Cambridge University Press, Cambridge, UK (1999). ISBN 9781139644181.
37. G. R. Musina, I. N. Dolganova, N. V. Chernomyrdin, A. A. Gavdush, V. E. Ulitko, O. P. Cherkasova, D. K. Tuchina, P. V. Nikitin, A. I. Alekseeva, N. V. Bal, G. A. Komandin, V. N. Kurlov, V. V. Tuchin, and K. I. Zaytsev, "Optimal hyperosmotic agents for tissue immersion optical clearing in terahertz biophotonics," Journal of Biophotonics 13(12), e202000297 (2020).
38. D. S. Ponomarev, A. E. Yachmenev, D. V. Lavrukhin, R. A. Khabibullin, N. V. Chernomyrdin, I. E. Spektor, V. N. Kurlov, V. V. Kveder, and K. I. Zaytsev, "Optical-to-terahertz switches: state of the art and new opportunities for multispectral imaging," Physics-Uspekhi 67, 3–21 (2024).
39. TPS-PCA800. Terahertz pulse spectrometer, Avesta (accessed 08 April 2026). [https://avesta.ru/product/tps-pca800-teragertsovyj-impulsnyj-spektrome].

Development of Technology for Analysing X-Ray Images of Bone Tissue for Computer Diagnosis of Osteoporosis

Daria V. Nekrasova[1*], **Nataly Yu. Ilyasova**[1,2], **Nikita S. Demin**[1,2], **and Sergey S. Pervushkin**[3]
[1] Samara National Research University, 34 Moskovskoye Shosse, Samara 443086, Russian Federation
[2] IPSI, NRC “Kurchatov Institute”, 151 Molodogvardeyskaya str., Samara 443001, Russian Federation
[3] FSBEI HE “SamSMU” of the Ministry of Health of the Russian Federation, 89 Chapaevskaya str.,
Samara 443099, Russian Federation
*e-mail: dashanek007@gmail.com

Abstract. The interpretation of lumbar spine radiographs, the most accessible diagnostic modality for osteoporosis, is often subjective and hampered by limited accuracy. To address this, we developed a neural network-based algorithm for computer-aided diagnosis. This study provides a comparative analysis of key neural network architectures for image segmentation and classification. The proposed system, with a classification accuracy of 87.42%, offers a valuable adjunct for radiologists, mitigating diagnostic risks and enhancing the overall efficacy of osteoporosis screening.

Keywords: osteoporosis; radiography; machine learning; resnet; deeplab.

Paper #9383 received 20 Oct 2025; revised manuscript received 19 Jan 2026; accepted for publication 20 Jan 2026; published online 7 May 2026. doi: 10.18287/JBPE26.12.020303.

1 Introduction

In contemporary clinical practice, the diagnosis of osteoporosis remains a significant challenge, given the disease’s widespread prevalence, particularly among the elderly [1]. The gold standard for detecting changes in bone mineral density is dual-energy X-ray absorptiometry (DXA), which enables a quantitative assessment of bone health. However, this technique requires specialized and costly equipment, limiting its availability in many healthcare settings, especially within primary care.

Consequently, radiography persists as the most widely available and accessible imaging modality for visualizing bone structures. Although it does not provide a direct quantitative measure of mineral density, radiographs contain numerous visual indicators that allow an experienced clinician to infer the presence of osteoporosis. These indicators include alterations in the shape and architecture of vertebral bodies, as well as a disruption of the trabecular pattern [2].

Radiographic analysis can reveal signs of vertebral body deformity, such as wedging or biconcavity, suggestive of compression fractures. According to study [3], 77% of osteoporotic patients exhibit signs of vertebral remodeling resulting from multiple, often subclinical fractures. This evidence establishes radiographic evaluation as not only feasible but also a clinically valuable tool in diagnosing the disease.

Recent years have witnessed substantial research efforts directed toward the automation of spinal morphometric analysis. For instance, a study [4] introduced a method for assessing the degree of wedge deformity utilizing a convolutional neural network (CNN). The developed model achieved a high degree of accuracy, with an average measurement error of 0.9 mm. However, it is crucial to recognize that vertebral body deformation represents a consequence of osteoporosis rather than its underlying etiology. Furthermore, the visual detection of alterations in vertebral shape is a comparatively simpler task than the quantitative assessment of bone density.

The classic radiological indicator of osteoporosis is a 20–30% reduction in bone mass [5]. Nevertheless, visual identification of such a loss on a radiograph is exceptionally challenging. This limitation is particularly significant in the early stages of the disease, when structural degradation of the trabeculae is not yet pronounced.

A contemporary approach to this problem involves the automated analysis of radiographs to evaluate bone density and identify disruptions in the trabecular architecture. This methodology has the potential to significantly enhance diagnostic accuracy and reproducibility while mitigating the impact of subjective interpretation.

Figure 1 presents radiographic comparisons of healthy and osteoporotic bone tissue, illustrating the distinct visual differences in their respective trabecular structures.

This paper was presented at the XI International Conference "Information Technology and Nanotechnology" (ITNT-2025), Samarkand, Uzbekistan, October 7 – 9, 2025.

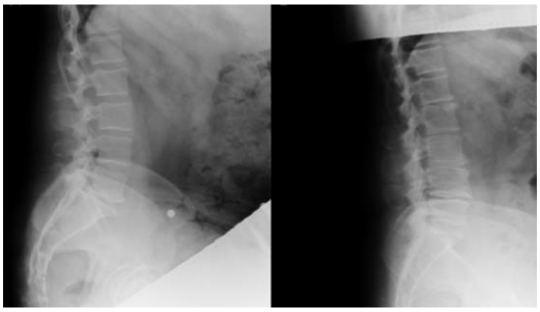
(a) (b)

Fig. 1 Lumbar radiographs (a) without disease, (b) with disease.

The study [6] presents a diagnostic technology for osteoporosis based on the analysis of femoral neck radiographs, a site particularly susceptible to osteoporotic fractures. The authors addressed the extraction and statistical processing of textural features. A classification model constructed upon the selected features achieved an accuracy of 84%, thereby substantiating the potential of textural analysis for diagnostic applications. Nevertheless, the proposed methodology exhibits inherent limitations: its efficacy demonstrates a critical dependence on image brightness and requires subjective selection of the region of interest, which constrains its broader applicability.

The present study aims to develop a comprehensive system, grounded in machine learning methods, capable of automatically segmenting radiographic images, selecting regions of interest, and performing binary classification (osteoporosis/normal), thereby minimizing human factor intervention.

2 Materials and Methods

2.1 Data Description and Preprocessing

The study utilized radiographic images of the lumbar spine as the primary data source. This anatomical region was selected for its optimal clarity and high diagnostic value in the context of osteoporosis. In contrast to the thoracic spine, where the superimposition of rib structures frequently obscures the vertebral bodies, the lumbar region affords a less obstructed view. The anatomical superimposition present in thoracic radiographs introduces significant visual noise, which complicates automated analysis and accurate computational estimation of bone density. Consequently, a focus on the lumbar spine enables more reliable feature extraction and model training.

A dataset of 252 anonymized lumbar spine radiographs, acquired with a Siemens X-ray apparatus, was procured from Samara State Medical University. The images were stored in the Digital Imaging and Communications in Medicine (DICOM) format, ensuring high fidelity and the preservation of essential metadata required for subsequent analysis.

Prior to the experiment, all data were manually annotated by a qualified radiology technician and categorized into two cohorts: 149 images from patients with a confirmed diagnosis of osteoporosis, and 103 images from patients exhibiting no evidence of the pathology.

During the preparation of the training set, each vertebra was systematically categorized into one of two classes: vertebrae obscured by superimposition of adjacent bony structures (e.g., the iliac bone or sacrum), and fully visible vertebrae devoid of such anatomical overlap. This classification served to enhance the quality of the training data and minimize potential errors during model training.

Figure 2 provides an example of an annotated lumbar spine image with delineated regions of interest.

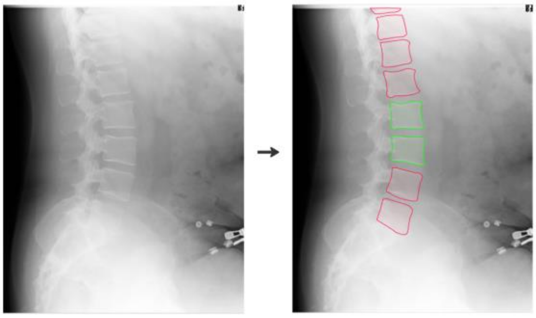

Fig. 2 Labeled image for model training.

For the construction and evaluation of machine learning models, the original dataset was partitioned into a training set and a validation set. The training set, comprising 157 images, was utilized to train the neural network in the recognition of pathological features. The validation set, consisting of 40 images, was designated for assessing the model's generalizability and mitigating overfitting.

Prior to being input into the segmentation model, the radiographic images underwent a preprocessing pipeline consisting of resizing and normalization. The original DICOM images, which exhibit heterogeneous dimensions, were standardized to a uniform size of 1024×1024 pixels. This standardization was achieved via interpolation to preserve maximal informational integrity.

Subsequently, the images were normalized to a consistent numerical scale. To compensate for variations in illumination and contrast, a second normalization step was applied using predetermined mean and standard deviation values derived from the ImageNet dataset. This alignment is particularly crucial due to the limited volume of annotated medical images available for this study, as it enables effective utilization of transfer learning. All models were initialized with weights pre-trained on ImageNet, a standard practice that provides robust feature extractors and significantly enhances training stability on small datasets. This approach mitigates the risk of overfitting and improves generalization capability, thereby compensating for the constrained dataset size while maintaining model reliability.

2.2 Review of Segmentation Model Architectures

This section compares three segmentation architectures employed in this study: U-Net, U-Net++, and DeepLabV3+. These models were selected based on their proven efficacy in medical image segmentation, particularly for X-ray analysis [7–9].

U-Net establishes a foundational encoder-decoder framework for biomedical image segmentation. The encoder extracts hierarchical features through convolutional and downsampling operations, while the decoder reconstructs spatial dimensions to generate segmentation masks [10]. Its distinctive skip connections concatenate high-resolution encoder features with upsampled decoder outputs, enabling precise feature localization and enhanced accuracy for fine anatomical structures. U-Net++ constitutes an architectural refinement of the standard U-Net, engineered to improve performance through a more complex and densely connected topology. It incorporates a series of nested, dense skip pathways between the encoder and decoder, creating an ensemble of U-Net-like architectures of varying depths. This design enhances feature propagation, mitigates the vanishing gradient problem, and enables more effective learning on complex datasets. The result is a model capable of producing more precise and detailed segmentation masks.

DeepLabV3+ constitutes a sophisticated segmentation architecture founded on deep convolutional neural networks with an advanced encoder-decoder structure [11]. A principal feature of this model is the implementation of atrous (dilated) convolutions, which enables the expansion of the receptive field without a proportional increase in computational parameters. This facilitates the integration of multi-scale contextual information, thereby enhancing segmentation precision while maintaining computational efficiency. Furthermore, this approach confers robustness to variations in object scale within the input imagery.

Model performance was quantified using the Dice coefficient, a similarity metric for segmentation tasks. The coefficient is defined by the following Eq.:

$$DC = \frac{2|A \cap B|}{|A|+|B|}, \qquad (1)$$

where A is the segmented region of the image, and B is the actual area.

To optimize the model, the Focal Loss function was employed as the primary loss metric. Although originally formulated for object detection, this function is effectively adapted to segmentation by addressing class imbalance. Focal Loss modifies the standard cross-entropy loss such that the model’s attention is redirected towards hard-to-classify pixels, while diminishing the contribution of easily classified examples during training. This mechanism enhances the model’s capacity for accurate identification of underrepresented classes. The loss function is defined as follows:

$$FL(p_t) = -(1-p_t)^{\gamma}\, log(p_t), \qquad (2)$$

where p_t is the probability of belonging to the correct class, γ is a parameter that allows focus tuning [8].

2.3 Review of Classification Model Architectures

To address the classification objective, an evaluation of five prominent convolutional neural network architectures was conducted: ResNet-18, ResNet-34, ResNet-50, EfficientNet-B0, and EfficientNet-B1. This selection was predicated on their well-documented efficacy in image analysis tasks, prevalence in the scientific literature, and systematically varying architectural depth, thereby enabling an assessment of the relationship between model complexity and classification performance [12, 13].

The ResNet architecture family (Residual Networks) is distinguished by its use of residual connections. These skip connections mitigate the problem of gradient degradation, thereby facilitating the stable training of substantially deeper networks. Among the selected variants, ResNet-18 and ResNet-34 represent computationally efficient models with 18 and 34 layers, respectively. In contrast, ResNet-50 employs a more complex structure utilizing bottleneck blocks, which increases computational cost while offering a potential gain in representational capacity and accuracy [14].

The EfficientNet models (B0 and B1) represent a subsequent architectural paradigm based on a compound scaling method that uniformly optimizes network depth, width, and input resolution. This principled approach to scaling yields architectures that achieve an optimal trade-off between accuracy and computational efficiency, rendering them particularly suitable for scenarios demanding a balance between performance and resource constraints [15].

Model performance was quantified using a comprehensive set of evaluation metrics to facilitate a multi-faceted analysis. These included Accuracy, Recall (Sensitivity), Precision, the F_1-score (the harmonic mean of precision and recall), and the Cross-Entropy Loss function. The collective use of these metrics provides a robust assessment of classification quality from complementary perspectives. The metrics were calculated as follows:

$$Accuracy = \frac{TP+TN}{TP+TN+FP+FN}, \qquad (3)$$

$$Precision = \frac{TP}{TP+FP}, \qquad (4)$$

$$Recall = \frac{TP}{TP+FP}, \qquad (5)$$

$$F_1 = 2\frac{Precision \times Recall}{Precision+Recall}, \qquad (6)$$

$$CE(p,y) = -\sum_{i=1}^{C} y_i \cdot log(p_i), \qquad (7)$$

where *TP* are true positives, *TN* are true negatives, *FP* are false positives, *FN* are false negatives, *C* is the number of classes, y_i is the true label (one-hot), p_i – predicted probability of class membership.

3 Results and Discussion

3.1 Quantitative Evaluation of Segmentation Models

This section provides a detailed analysis of the efficacy of three modern architectures for semantic segmentation: the foundational U-Net, its enhanced variant U-Net++, and the advanced DeepLabV3+ model. The models were evaluated on a single dataset under identical training conditions to ensure a valid comparative analysis. The evaluation focused on two principal criteria: segmentation accuracy, quantified by the Dice coefficient, and training stability, assessed through the dynamics of the loss function.

The experimental results, summarized in Table 1, reveal notable differences between the architectures. DeepLabV3+ achieved the highest Dice coefficient of 0.8439, exceeding the baseline U-Net by 2% and U-Net++ by 3.5%. While this absolute difference may appear modest, the improvement is significant in the context of medical segmentation, where precise boundary delineation is critical. It should be noted that the higher Focal Loss value observed for DeepLabV3+ (0.0466 versus 0.0324 for U-Net) is attributable to its greater architectural complexity. This does not, however, preclude its application, as the primary objective remains the maximization of the Dice coefficient.

Table 1 Segmentation model training results.

Metric	**Architecture**		
	U-Net	**U-Net++**	**DeepLabV3+**
Dice	0.8272	0.8089	0.8439
Focal loss	0.0324	0.0423	0.0466

The training dynamics, illustrated in Figs. 3–5, further distinguish the models. U-Net demonstrates stable growth of the Dice metric for the first 15 epochs, followed by a plateau, indicating a favorable balance between learning rate and final accuracy. U-Net++ is characterized by rapid convergence, attaining its peak accuracy by epoch 7; however, a subsequent slight regression in metrics suggests an onset of overfitting. In contrast, DeepLabV3+ requires a substantially longer training period (62 epochs) but exhibits a consistent, monotonic improvement in performance without indications of overfitting, a characteristic of complex architectures with extensive parameter spaces.

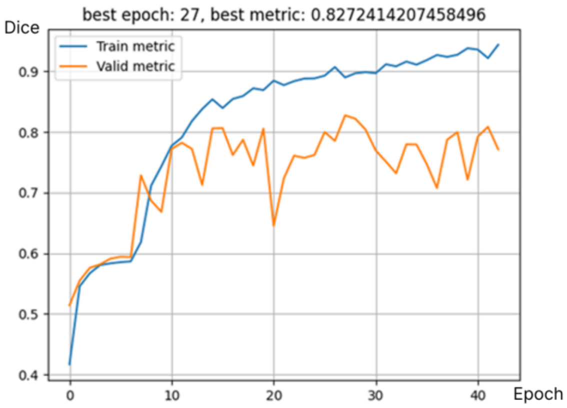

Fig. 3 Training and validation metrics across epochs for U-Net model.

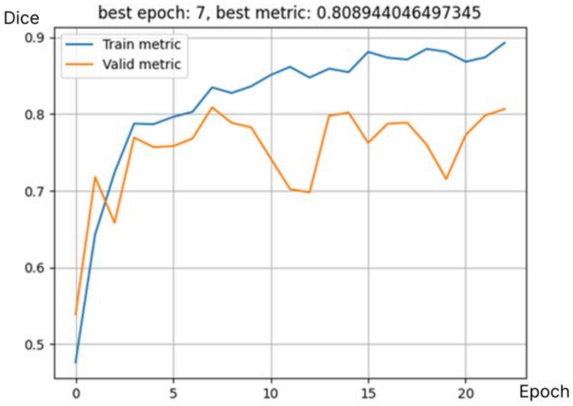

Fig. 4 Training and validation metrics across epochs for U-Net++ model.

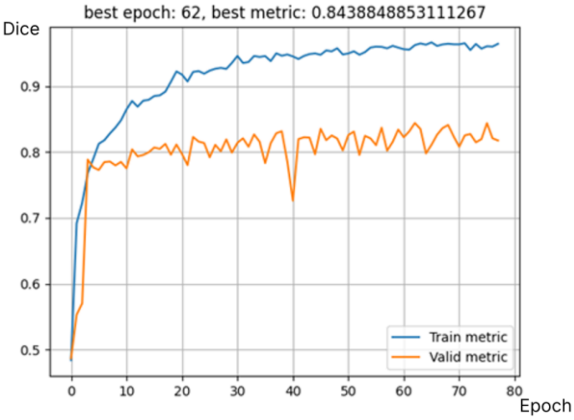

Fig. 5 Training and validation metrics across epochs for DeepLabV3+ model.

The outputs of each model are juxtaposed in Fig. 6. The DeepLabV3+ exemplar demonstrates superior performance in delineating object boundaries, particularly in complex regions characterized by heterogeneous texture. This architecture exhibits enhanced capability in segmenting fine anatomical details and generates fewer spurious artifacts compared to its counterparts. A critical advantage is its consistent maintenance of topological integrity in challenging anatomical domains, where U-Net and U-Net++ occasionally produce topological errors.

The selection of DeepLabV3+ as the final model is justified by a confluence of factors. Its statistically significant superiority on the primary accuracy metric is coupled with robust training dynamics and a demonstrated capacity for resolving complex segmentation challenges. Although the model demands greater computational resources for training, this expenditure is offset by the substantial improvement in final output quality. Furthermore, the architecture presents significant potential for future performance gains through hyperparameter optimization, the use of pre-trained encoders, and the application of advanced data augmentation techniques. Within the context of medical image analysis, where segmentation precision is paramount, these collective advantages establish DeepLabV3+ as the optimal choice.

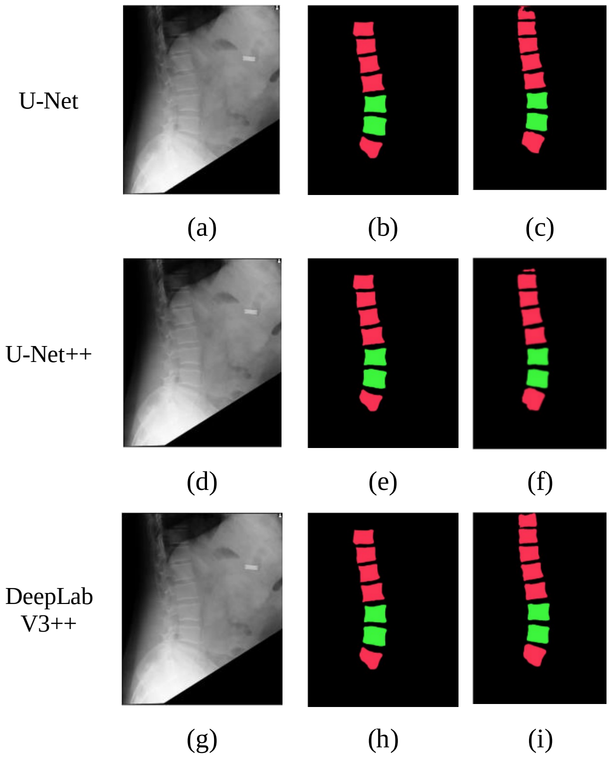

Fig. 6 Experimental outputs of the segmentation models. (a, d, g) Images; (b, e, h) Ground Truth Masks; (c, f, i) Predicted masks.

3.2 Quantitative Evaluation of Classification Models

This study conducts a comparative analysis of deep learning architectures for classifying vertebral pathology. The proposed methodology processes individual vertebrae as separate images with subsequent aggregation of results, preserving diagnostically critical features while maintaining clinical applicability. The training dataset comprised exclusively non-overlapping vertebrae, retaining minimal background tissue to provide essential anatomical context without introducing substantial noise.

Training dynamics, illustrated in Figs. 7–11, reveal substantial performance disparities among architectures. ResNet-34 emerged as the most promising model, attaining the highest quantitative evaluation score (0.8857 at epoch 65) while demonstrating consistent improvement throughout training. Conversely, the deeper ResNet-50 architecture, despite achieving a comparable performance peak (0.8786 at epoch 46), exhibited substantial overfitting, as indicated by significantly elevated cross-entropy values.

The EfficientNet architectures produced divergent outcomes. While EfficientNet-B0 achieved competitive recall rates, its precision marginally trailed ResNet-34, potentially increasing false positive instances in clinical deployment. EfficientNet-B1 demonstrated the least effectiveness among all evaluated models, suggesting limited suitability for this specific diagnostic application.

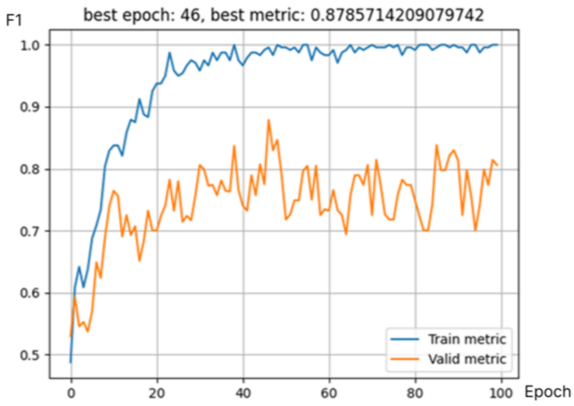

Fig. 7 Training and validation metrics across epochs for ResNet-18 model.

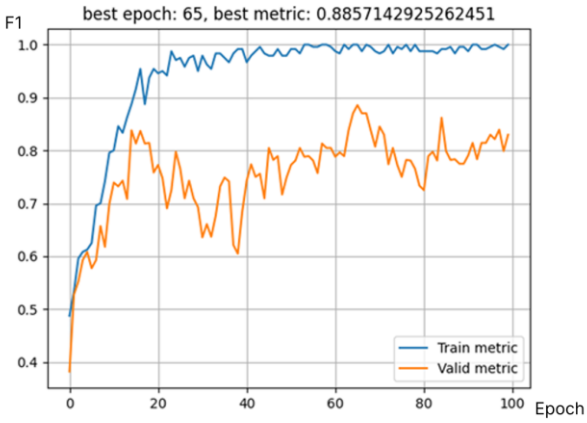

Fig. 8 Training and validation metrics across epochs for ResNet-34 model.

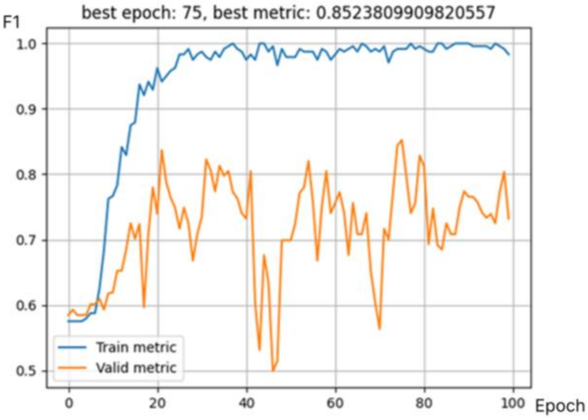

Fig. 9 Training and validation metrics across epochs for ResNet-50 model.

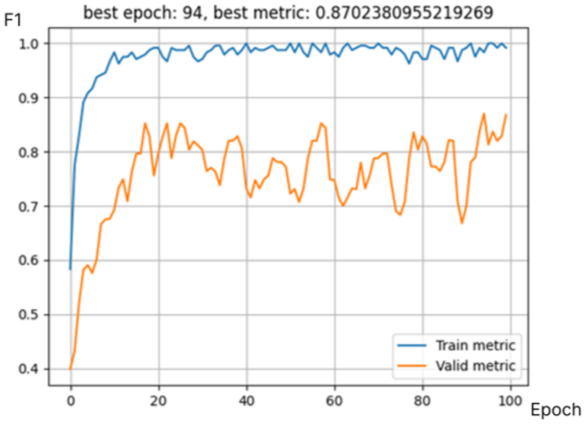

Fig. 10 Training and validation metrics across epochs for EfficientNetB0 model.

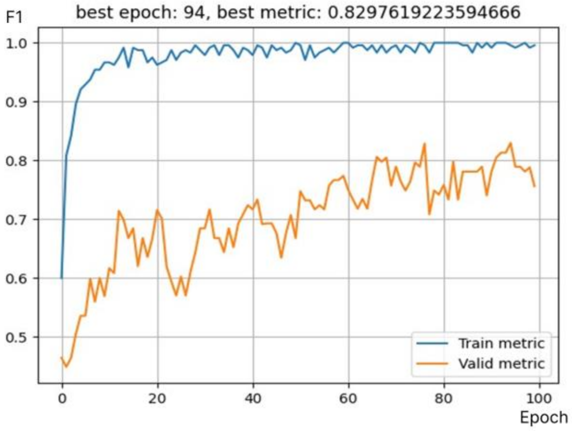

Fig. 11 Training and validation metrics across epochs for EfficientNetB1 model.

Comprehensive metric analysis presented in Table 2 confirms ResNet-34's superior performance across all evaluation criteria. This model achieves an optimal balance between precision and recall while maintaining minimal prediction uncertainty – a crucial consideration in medical diagnostics. The consistently elevated recall values observed across all models reflect an essential clinical principle: the preference for cautious diagnosis over missed pathology.

Table 2 Classification model training results.

Metric	Architecture				
	RN-18	**RN-34**	**RN-50**	**ENB0**	**ENB1**
F_1	0.8523	0.8857	0.8524	0.8702	0.8298
Cross-entropy	0.3611	0.3568	0.6736	0.8515	0.8096
Recall	0.8273	0.8742	0.8273	0.8811	0.8450
Precision	0.8237	0.8742	0.8237	0.8745	0.8387
Accuracy	0.8273	0.8742	0.8273	0.8811	0.8450

3.3 Complete System Execution Results

The final system architecture was derived from a comprehensive comparative analysis, integrating the highest-performing models identified in our evaluation. Figure 12 illustrates a representative output of the fully integrated system.

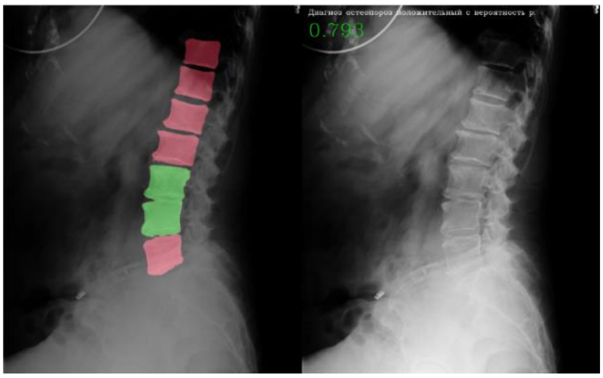

Fig. 12 Output of the resulting system.

3.4 Model Optimization Strategy

The developed neural network for osteoporosis diagnosis from spinal X-rays exhibits a critical limitation: low interpretability. This opacity in decision-making hinders clinical trust and complicates implementation. To address this, we introduce a complementary image processing approach designed to enhance both model transparency and accuracy.

The pipeline utilizes isolated vertebral images, with background removed by the segmentation model, to focus analysis exclusively on bone architecture. Preliminary processing involves contrast enhancement using either adaptive CLAHE or linear stretching to accentuate structural details.

A crucial preprocessing step is precise vertebral orientation. The minimum bounding rectangle is calculated to determine angular deviation from the vertical axis. The vertebral center of mass is subsequently identified through image moments to ensure positional accuracy.

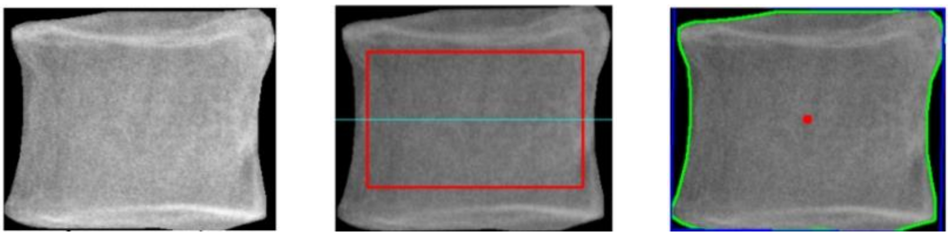

(a) (b) (c)

Fig. 13 Example of preprocessing. (a) After preprocessing, (b) cropping, (c) 0.8° angle.

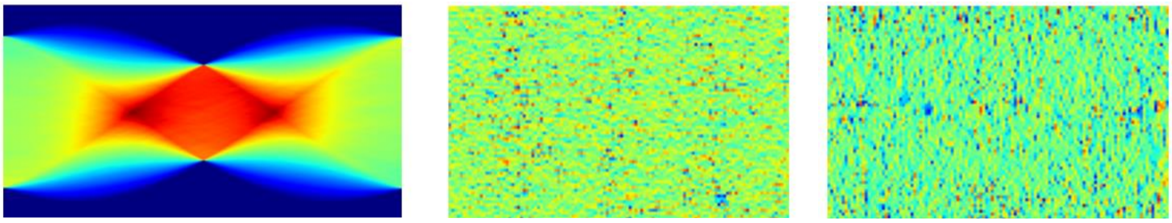

(a) (b) (c)

Fig. 14 Radon and Wavelet transform visualization. (a) Sinogram, (b) Wavelet (cH1 – Horizontal Details), (c) Wavelet (cV1 – Vertical Details).

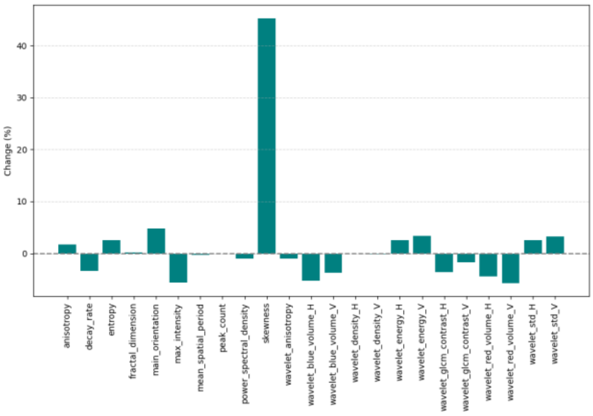

Fig. 15 Percentage difference between healthy and affected vertebrae.

Following alignment, cropping is performed based on anatomical landmarks. The vertical axis of symmetry is established through the center of mass. The width is determined by vertebral boundaries at the center mass level with a 5% margin to exclude edge artifacts. The height is set at 60% of the total image height, centered vertically on the mass coordinate. This method ensures inclusion of the most diagnostically relevant central structures while eliminating peripheral noise. The processed result is demonstrated in Fig. 13.

To extract the most informative features, we implemented two complementary mathematical methods: Radon transform and wavelet analysis. The Radon transform characterizes spatial density distribution patterns within bone tissue, while wavelet analysis facilitates multi-scale texture examination. The implemented code calculates 18 distinct metrics, including principal orientation, anisotropy coefficient, entropy, fractal dimension, and other parameters that quantitatively describe bone tissue status. These metrics constitute a set of transparent and interpretable features for the neural network model, enabling clinicians to identify precisely which structural characteristics of the vertebra contributed to the diagnostic outcome. An example of the applied transformations is presented in Fig. 14.

This methodology was applied to 241 vertebral images. Figure 15 presents a comparative analysis via a bar chart, illustrating the percentage difference in extracted feature values between the two diagnostic classes, thereby highlighting the most discriminative parameters.

4 Conclusion

The system developed in this study enables automated osteoporosis diagnosis through the analysis of lumbar spine radiographs. The implementation of the DeepLabV3+ architecture, which achieved a Dice coefficient of 0.8439 for segmentation, coupled with the ResNet-34 model, attaining a classification accuracy of 87.42%, substantiates the system's high efficacy. This integrated approach mitigates radiologist workload and reduces diagnostic subjectivity, offering particular utility in clinical settings with constrained access to advanced modalities such as densitometry.

A principal limitation of the system, however, is the limited interpretability of its results for clinical practitioners. The deployed deep learning models operate as functional "black boxes", obscuring the specific features that drive diagnostic decisions. This opacity may impede trust and hinder seamless integration into routine clinical workflows.

Future work will focus on enhancing the system's transparency by integrating advanced image processing techniques, including wavelet analysis and the Radon transform. These methods are anticipated to elucidate the structural features of vertebrae that underpin the model's decisions, thereby fostering clinical trust and adoption. Furthermore, we plan to extend the system's analytical capabilities by incorporating additional quantifiable biomarkers of bone tissue integrity. These developments are directed toward augmenting the system's diagnostic robustness and versatility, with the ultimate objective of improving patient care outcomes.

Ethical approval for this study was ensured through the informed voluntary consent obtained from all patients, in accordance with the Order of the Ministry of Health of the Russian Federation (No. 1051n, November 12, 2021).

Acknowledgments

This work was carried out within the state assignment of NRC "Kurchatov Institute".

Disclosures

All authors declare that there is no conflict of interest in this paper.

References

1. J. A. Kanis, C. Cooper, R. Rizzoli, and J. Y. Reginster, "European guidance for the diagnosis and management of osteoporosis in postmenopausal women," Osteoporosis International 30(1), 3–44 (2019).
2. G. Guglielmi (Ed.), Osteoporosis and Bone Densitometry Measurements, Springer Berlin, Heidelberg (2013). ISBN: 978-3-642-27884-6 (eBook).
3. E. M. Eidlyna, G. V. Diachkova, and K. A. Diachkov, "Modern radiation diagnosing the spine pathological fractures thro ugh osteoporosis," Genij Ortopedii 2, 38–43 (2012). [in Russian]
4. A. V. Petraikin, Zh. E. Belaya, A. N. Kiseleva, Z. R. Artyukova, M. G. Belyaev, V. A. Kondratenko, M. E. Pisov, A. V. Solovev, A. K. Smorchkova, L. R. Abuladze, I. N. Kieva, V. A. Fedanov, L. R. Iassin, D. S. Semenov, N. D. Kudryavtsev, S. P. Shchelykalina, V. V. Zinchenko, E. S. Akhmad, K. A. Sergunova, V. A. Gombolevsky, L. A. Nisovstova, A. V. Vladzymyrskyy, and S. P. Morozov, "Artificial intelligence technology for recognition of vertebral compression fractures using a morphometric analysis model based on convolutional neural networks," Problems of Endocrinology 66(5), 48–60 (2020). [in Russian]
5. Zh. A. Klimova, A. A. Zaft, and V. B. Zaft, "Modern laboratory diagnosis of osteoporosis," International Journal of Endocrinology 7.63, 75–84 (2014).
6. A. Gaidel, S. Pervushkin, "Research of the textural features for the bony tissue diseases diagnostics using the roentgenograms," Computer Optics 37(1), 113–119 (2013).
7. I. A. Belozerov, V.A. Sudakov, "Investigation of machine learning models for medical image segmentation," Keldysh Institute Preprints 37, 1–15 (2022).
8. Z. Zhou, M. M. R. Siddiquee, N. Tajbakhsh, and J. Liang, "UNet++: a nested U-Net architecture for medical image segmentation," Deep Learning in Medical Image Analysis and Multimodal Learning for Clinical Decision Support 11045, 3–11 (2018).
9. I. A. Lozhkin, M. E. Dunaev, K. S. Zaytsev, and A. A. Garmash, "Augmentation of image datasets for training neural networks in semantic segmentation tasks," International Journal of Open Information Technologies 11(1), 109–117 (2023).
10. O. Ronneberger, P. Fischer, and T. Brox, "U-Net: convolutional networks for biomedical image segmentation," Medical Image Computing and Computer-Assisted Intervention 9351, 234–241 (2015).
11. L. C. Chen, Y. Zhu, G. Papandreou, F. Schroff, and H. Adam, "Encoder-decoder with atrous separable convolution for semantic image segmentation," European Conference on Computer Vision 11211, 801–818 (2018).
12. G. Amiya, K. Ramaraj, P.R. Murugan, V. Govindaraj, M. Vasudevan, and A. Thiyagarajan, "A review on automated algorithms used for osteoporosis diagnosis," Lecture Notes in Networks and Systems. Inventive Systems and Control 436, 247–262 (2022).
13. K. He, X. Zhang, S. Ren, and J. Sun, "Deep residual learning for image recognition," IEEE Conference on Computer Vision and Pattern Recognition, 770–778 (2016).
14. D. Sarwinda, R. H. Paradisa, A. Bustamam, and P. Anggia, "Deep learning in image classification using residual network (resnet) variants for detection of colorectal cancer," Procedia Computer Science 179, 423–431 (2021).
15. M. Tan, Q. V. Le, "EfficientNet: rethinking model scaling for convolutional neural networks," International Conference on Machine Learning 97, 6105–6114 (2019).

Machine Learning Classification of Augmented Raman Serum Spectra for Chronic Heart Failure Detection

Yulia A. Khristoforova*, Ekaterina O. Salnikova, and Irina A. Matveeva
Samara National Research University, 34 Moskovskoe shosse, Samara 443080, Russian Federation

*e-mail: khristoforova.yua@ssau.ru

Abstract. In this work, we propose a promising non-invasive approach based on the Raman spectroscopy of human serum for chronic heart failure (CHF) diagnosis. Due to the limited sample size, which limits the performance of machine learning classifiers, this study explores data augmentation techniques to improve the classification of low- and high-grade CHF spectra using k-nearest neighbor (kNN) and partial least squares discriminant analysis (PLS-DA) algorithms. Raman spectra of 151 patients with CHF of the different stages were acquired at 532 nm excitation from serum samples collected at Samara City Clinical Hospital. Two augmentation approaches were systematically evaluated: (1) combined approach based on the linear spectral transformations (wavenumber shifting ±1–2 cm^{-1}, intensity stretching 0.9-1.1) and (2) Wasserstein Generative Adversarial Network (WGAN)-based synthetic spectrum generation, expanding training datasets 10-fold while preserving physiochemical realism. Augmentation based on linear spectral transformations yielded algorithm-specific results: kNN showed no significant receiver operating characteristic area under curve (ROC AUC) improvement (0.67 ± 0.11 original vs. 0.67–0.69 augmented), while PLS-DA achieved statistically significant gains (0.71 ± 0.11 vs. 0.80–0.81; $z = 2.3–2.6$, $p < 0.05$). WGAN augmentation proved superior across both methods, with k-NN reaching 0.74 ± 0.08 and PLS-DA achieving 0.83 ± 0.09. These findings establish WGAN as an optimal augmentation strategy for Raman-based CHF classification, achieving clinically relevant performance (ROC AUC > 0.80) from limited cohorts while enabling biomarker identification for cardiovascular diagnostics.

Keywords: Raman spectroscopy; chronic heart failure; data augmentation; kNN; PLS-DA; binary classification; WGAN.

Paper #9555 received 18 Mar 2026; revised manuscript received 20 Apr 2026; accepted for publication 21 Apr 2026; published online 7 May 2026. doi: 10.18287/JBPE26.12.020304.

1 Introduction

Cardiovascular diseases (CVDs) are the leading cause of death globally, claiming 17.9 million lives each year [1]. Chronic heart failure (CHF) affects over 64 million people worldwide and is a key component of the CVD burden, which is projected to increase by 90% from 2025 to 2050 due to population aging [1]. In Russia, the prevalence of CHF in European regions is about 7-10% but these cases are often underdiagnosed due to their subtle symptoms [2]. The number of severe CHF cases (HIIB, HIII) has grown more sharply, comprising about 38% of all CHF cases and contributes to higher hospitalization and mortality rates.

Early and accurate diagnosis of CHF is crucial, as it allows for timely intervention to improve patient outcomes and reduce hospitalizations. Current diagnostic methods for CHF, such as NT-proBNP/BNP biomarker assays, echocardiography, and clinical scoring systems (e.g., HFA-PEFF) [3], face significant limitations, including reducing accuracy for comorbidities, a lack of standardization across tests, and reliance on specialized equipment, which limits accessibility primary care. The diagnostic value of brain natriuretic peptide (BNP)/ N-terminal part of its prohormone (NT-proBNP) is valuable [3, 4], but it is limited by various confounding factors, such as levels rising in conditions other than CHF, such as chronic kidney disease, atrial fibrillation, pericardial disease, pulmonary embolism, and aging [3, 4]. Obesity can also suppress their levels, making individualized interpretation necessary in the presence of comorbidities. These limitations are particularly significant for early detection of diseases in patients who may have asymptomatic or mild symptoms [3, 5]. NT-proBNP levels in these patients may remain normal or only slightly elevated, leading to missed diagnoses and delayed intervention. Therefore, the development of new promising diagnostic techniques is essential to overcome these challenges.

Non-invasive techniques such as Raman spectroscopy are becoming increasingly important for detecting chemical changes in the biofluids of patients with different diseases [6–9]. These techniques offer the potential for label-free analysis of bioliquids and tissue, which is not possible with current diagnostic methods that rely on invasive biomarkers. This highlights the need for more advanced spectral techniques, especially in resource-limited settings.

Raman spectroscopy is an optical, non-destructive analytical method based on inelastic scattering of photons by molecular bond vibrations and rotations. It produces a unique “chemical fingerprint” spectrum where each peak corresponds to specific vibrational or rotational modes of molecules within the analyte, enabling detailed characterization of complex biological samples like tissues [7] or fluids [8, 10, 11].

In biological samples, the Raman spectrum provides a composite contribution from biochemical components, including proteins, lipids, nucleic acids, and metabolites [12]. These components can be used to identify alterations in molecular composition associated with the progression of the disease [6]. Integration with machine learning algorithms [8, 11, 13] can help extract hidden spectral similarities and differences between different groups, for example between diseased and healthy groups or between different stages of diseases. This can be done by identifying subtle peak shifts and intensity variations that may be overlooked by traditional analysis methods.

Developing new diagnostic approaches requires statistically reliable data in large volumes. However, collecting real biomedical spectral data is time-consuming and resource-intensive, often taking years to acquire samples and perform spectral measurements under controlled conditions. As a result, many studies rely on small sample sizes, typically dozens [14, 15] rather than thousands. Small sample sizes can lead to overfitting, poor generalization, and inaccurate metric estimates, especially for high-dimensional spectral data [16]. In other cases, researchers acquire numerous spectra from a single sample [14], limiting generalizability to diverse patient populations.

Another approach is applying augmentation methods [17–20] to real data for generating synthetic data, which simulates variability in spectral profiles while preserving biochemical features, thereby enhancing model robustness without extended collection efforts. Common transformations for spectral data augmentation include frequency shifting, intensity stretching, noise injection, and generative models [17–19]. Data augmentation can help avoid overfitting on a limited number of real-world samples, allowing training on larger datasets that can produce more stable and reliable models [17–20]. For example, Zhao et al. [18] demonstrated skin cancer detection using Raman spectroscopy, where data augmentation strategies – including random noise addition, spectral shifting, linear combinations, and 1D-GAN-generated spectra – increased training data from 512 to 14608 spectra. The classification performance of PLS-DA, PC-LDA, and SVM was essentially independent of the number of 1D-GAN synthesized spectra, whereas 1D-CNN improved until reaching a plateau at around $n = 10000$ and LR showed no meaningful benefit even at the maximum augmentation size (n=30000). It should be noted, analysis of the extended dataset not only can elevate performance across convolutional neural network (CNN) and conventional machine learning algorithms (PLS-DA, SVM) by 2–4% but also enhanced robustness on noisy or shifted test spectra. Therefore, the results achieved in studies on clinical Raman applications emphasize the critical role of augmentation in stabilizing machine learning models.

In this study, we aim to investigate the impact of data augmentation methods on the performance of machine learning models trained on Raman spectroscopy data. We apply these models to serum spectra from patients with CHF, specifically to distinguish between initial clinical phase (HIIA) and advanced phases (HIIB, HIII) of the disease in accordance with Strazhesko-Vasilenko classification. The use of augmentation techniques is necessary due to the limited size of our spectral dataset, which is a common challenge in pilot biomedical studies that involve Raman spectroscopy of biofluids.

2 Materials and Methods

2.1 Experimental Data

Study protocols were approved by the Ethics Committee of Samara State Medical University (protocol #268, September 11, 2023). All involved subjects agreed to participate in this study by informed consent. Human serum were taken from 151 patients with initial clinical phase (HIIA) and advanced phases (HIIB, HIII) of CHF at the Cardiology Department of Samara City Clinical Hospital No. 1 (N.I. Pirogov). CHF diagnoses were confirmed via NT-proBNP testing results. Blood serum sampling was performed at the early stage of hospitalization, before treatment in the surgical department had been initiated. Detailed information on medications, comorbidities, and diet was not systematically recorded or balanced between groups.

Therefore, we acknowledge that differences in these confounding factors may influence the observed spectral patterns and should be considered a limitation of our work.

The serum samples were collected from patients in the morning, after they had fasted. Each sample was placed in a labelled, sterile tube. The tubes were immediately frozen at −16 °C and then transferred to the laboratory for Raman analysis in the freezer. Immediately before the analysis, the samples were defrosted at room temperature. A sample of serum in a volume of 10 μl was placed on aluminum foil and allowed to air dry at room temperature until it was completely dry. The total set of experimental data includes 151 spectra, consisting of 69 spectra of patients with initial CHF stages and 82 with advanced stages.

2.2 Spectroscopic Measurements

Raman measurements were performed using an EnSpectr R532 ADF U300 spectrometer equipped with a 532 nm excitation laser and a 50× LMPlan objective. Spectra were recorded in the 89−3892 cm^{-1} range with a spectral resolution of 1.5 cm^{-1}. The diameter of the laser spot in focus was 5 microns. Human blood serum was analyzed using a laser power of 27 mW. Before recording the spectral characteristics of the blood serum sample, a preliminary recording of the ambient background signal was performed. After that, the background component was automatically subtracted from the registered serum spectrum using the built-in software algorithm. The Raman spectra were registered with 2 s exposure time and 10 accumulations to improve the signal-to-noise ratio. Each of the resulting spectra is a discrete set of 3502 parameters.

2.3 Augmentation Procedure

In this work, we used several approaches for augmentation of Raman spectra: (1) combined augmentation approach, incorporating wavenumber axis shifting and intensity axis stretching, and (2) synthetic spectrum generation via Wasserstein generative adversarial networks (WGAN) method [22].

A combined approach was used to generate two augmented sets of Raman spectra. For the first set, the original data was shifted by ±1 cm^{-1} and stretched by 0.9 arbitrary units (a.u.) in intensity. For the second set, the data was shifted by ±2 cm^{-1} and stretched by 1.1 a.u. in intensity.

The use of WGAN makes obtaining Raman data much more complicated than the combined approach based on simple linear transformations. WGAN generates synthetic Raman spectra using a minimax framework with (Wasserstein–1) distance. This augmentation was performed separately on the low and high stages CHF class subsets to preserve class-specific discriminative features. The generator takes random noise and label and produces artificial spectra from random noise, while the discriminator estimates the distance between real and synthetic spectral distributions. If the discriminator is able to successfully distinguish between synthetic and real spectra, it will signal the generator to adjust its parameters in order to improve the realism of the generated spectra and minimize the loss function. This process of iterative refinement will continue until the synthetic spectra are indistinguishable from the real spectra, at which point, the discriminator will no longer be able to differentiate between the two [22]. Gradient penalty enforces the 1–Lipschitz constraint, ensuring training stability and realistic spectral peak morphology preservation. This approach effectively augments limited Raman datasets while maintaining biochemical feature integrity for downstream classification tasks.

The WGAN was implemented with a fully connected critic-generator structure applied separately to each class. For the first class (69 spectra) and the second class (82 spectra), both of length 744, the generator takes a 690-dimensional latent vector sampled from a standard normal distribution and maps it through two dense layers (512 and 1024 units) with ReLU activation, a dropout layer (rate 0.2), and a final dense layer (744 units) with tanh activation to produce synthetic spectra in the range [−1,1]. The critic processes a spectrum of length 744 through three dense layers (1024, 512, 256 units) with ReLU activation, a dropout layer (rate 0.2), and a final scalar output. The model was trained with RMSprop (learning rate 0.001), updating the critic 5 times per generator step, after z-score normalization of each spectrum.

2.4 Analyzing and Preprocessing

The spectral range between 800 and 1800 cm^{-1} was selected for further augmentation and analysis. This corresponds to a set of 744 discrete parameters, representing the Raman intensity at specific wavenumbers. The experimental dataset was randomly divided into training and test sets: 80% of the spectra were allocated to the training set, while the remaining 20% formed the test set. The test set was held out from all augmentation procedures and was not used at any stage of synthetic data generation. Augmentation using three approaches was applied exclusively to the training set, which initially comprised 120 spectra and was expanded to 1320 spectra. In this way, two independent models were constructed: one trained on the original real spectra only, and the second trained on the original spectra together with the augmented spectra. Both models were subsequently evaluated on the same held-out test set consisting exclusively of real spectra. This design allowed for a direct comparison of model performance under identical testing conditions and ensured that the test results reflected the effect of augmentation on generalization to unseen real data rather than any influence from synthetic samples.

Afterward, Raman spectra of both extended training and test sets were preprocessed by smoothing using the Savitzky-Golay filter (15 window was selected as the standard choice for spectroscopic applications, with a polynomial order of $p = 3$ to balance peak intensity preservation against residual noise) and normalization to standard normal variation.

To classify Raman spectra of low and high CHF classes, *k*NN and PLS-DA binary model were built.

The *k*NN algorithm classifies Raman spectra by computing Euclidean distances in spectral feature space and assigning the class label of the majority among the *k* closest training spectra. In our model, optimal k=6 neighbors were determined through minimization of root mean square error (RMSE), balancing bias-variance trade-off while preserving spectral discrimination between serum samples of CHF patients with different stages patients with different stages.

PLS-DA constructs latent variables (LV) through partial least squares regression between spectral predictors and class indicators, maximizing covariance to achieve optimal class separation.

Additionally, to assess the validity of the WGAN-generated spectra, PLS-DA models were constructed and evaluated on three separate datasets: (1) the original real spectra ($n = 120$), (2) the synthetically generated spectra alone ($n = 1200$), and (3) the combined dataset of real and synthetic spectra ($n = 1320$). The PLS-DA model trained on the original real spectra served as a reference to characterize the inherent discriminative ability of the experimental data. The model built on the generated spectra alone was used to evaluate whether the synthetic data preserved the same spectral patterns and class structure as the real data. Finally, the PLS-DA model fitted on the merged dataset (real and synthetic spectra) allowed us to investigate how the addition of augmented samples affected classification performance, stability, and latent-space structure.

ROC-AUC served as the primary metric for evaluating classification performance improvement, with its standard deviation assessing model stability. Comparative analysis was conducted between *k*NN and PLS-DA classification results obtained from both original and augmented datasets, employing the *z*-statistic for significance testing. The γ correlation coefficient between ROC curves of the compared datasets was calculated [23]. Following *z*-statistic computation, the null hypothesis H_0 (no significant stability improvement) was either accepted or rejected. A significance level of $\alpha = 0.05$ was adopted, corresponding to a critical value $z_{crit} = 1.96$; thus, H_0 was rejected when $|z| \geq 1.96$ and accepted when $|z| < 1.96$.

3 Results and Discussion

Figure 1 shows the 532 nm stimulated serum Raman spectra of patients with low and high CHF stages and differenced spectrum. Biological samples, particularly human serum, are known to contain carotenoids that produce characteristic resonance Raman signals under 532 nm laser excitation. These carotenoids generate prominent Raman bands at 1150 cm^{-1} (ν(C-C)) and 1515 cm^{-1} (ν(C=C)) [24]. Additionally, both spectral profiles exhibit a distinct peak at 1004 cm^{-1}, attributable to carotenoid C-CH$_3$ rocking vibrations, which may overlap with the phenylalanine ring mode. Other prominent peaks also are observed at 1445 cm^{-1} (CH$_2$/CH$_3$ scissoring & bending in proteins and lipids) and 1665 cm^{-1} (Amide I (C=O stretching) in proteins). The differenced spectrum has prominent features at 1004, 1150, 1515 cm^{-1} that corresponds to the typical Raman bands in serum. Blood sampling at the early stage of hospitalization, before treatment reduces the likelihood that the spectra were influenced by in-hospital therapy. Nevertheless, information on medications taken prior to admission was not available, and the potential effects of comorbidities, diet, and other confounders.

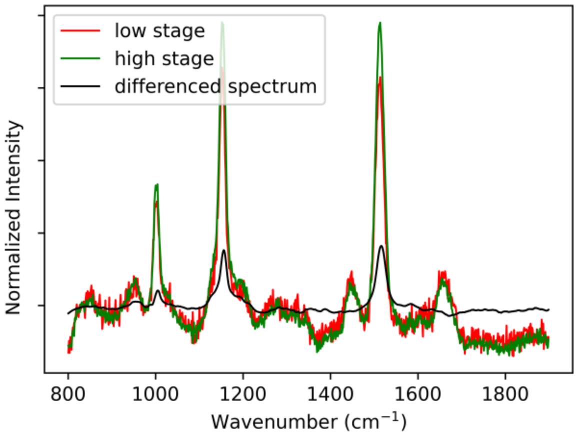

Fig. 1 Serum Raman spectra of patients with low and high CHF stages.

The original dataset was extended 10-fold, resulting in three sets of 1320 spectra including original and augmented spectra. Two sets were generated using a combined approach with different coefficients for linear transformations, and one set was generated using WGAN. Figure 2 presents original and augmented Raman spectra.

Fig. 2(a) shows an example of spectrum transformation through wavenumber shifting and stretching. Wavenumber axis shifting (±1–2 cm^{-1}) simulates instrumental variations inherent to Raman spectroscopy, including laser wavelength drift, spectrometer calibration inaccuracies, and sample positioning effects. These perturbations represent realistic experimental uncertainty encountered across multiple measurements and instruments. The intensity axis stretching ($S_y = 0.9–1.1$) takes into account physiological and measurement variability, especially biological factors. This includes fluctuations in serum analyte concentrations, variations in protein binding, and differences in carotenoid content between patients. Such transformations preserve intrinsic spectral shape and peak position relationships while introducing statistically plausible perturbations observed in real-world serum Raman datasets.

*k*NN classification showed that augmentation using combined approach through linear spectral transformations (wavenumber shifting and intensity stretching) did not produce statistically significant improvements in ROC AUC compared to the original dataset. This lack of significant improvement persisted across both augmented datasets created with different linear transformation coefficients. The ROC AUC values for CHF stage classification using *k*NN were 0.67 ± 0.11 (original dataset), 0.69 ± 0.10 (augmented set with ±1 cm^{-1} shift and 0.9 stretch), and 0.67 ± 0.09 (augmented set with ±2 cm^{-1} shift and 1.1 stretch). Nevertheless, model performance was stable across datasets that differed by an order of magnitude in size (10-fold expansion), without any observed degradation in classification ability.

In contrast to *k*NN results, PLS-DA classification demonstrated statistically significant ROC AUC improvement following spectral augmentation using linear transformations, according to *z*-value analysis. Specifically, the original dataset yielded an AUC of 0.71 ± 0.11, while the two augmented datasets produced AUC values of 0.80 ± 0.10 and 0.81 ± 0.09, respectively.

We can assume the observed difference between *k*NN and PLS-DA can be explained by their intrinsic working principles. *k*NN is a distance-based classifier that relies on local neighborhood structure in the raw feature space; linear spectral transformations (wavenumber shifts and intensity stretches) produce smooth, controlled perturbations that preserve the global topology and neighbor relationships, so the model shows only minor changes in ROC-AUC without statistically significant improvement.

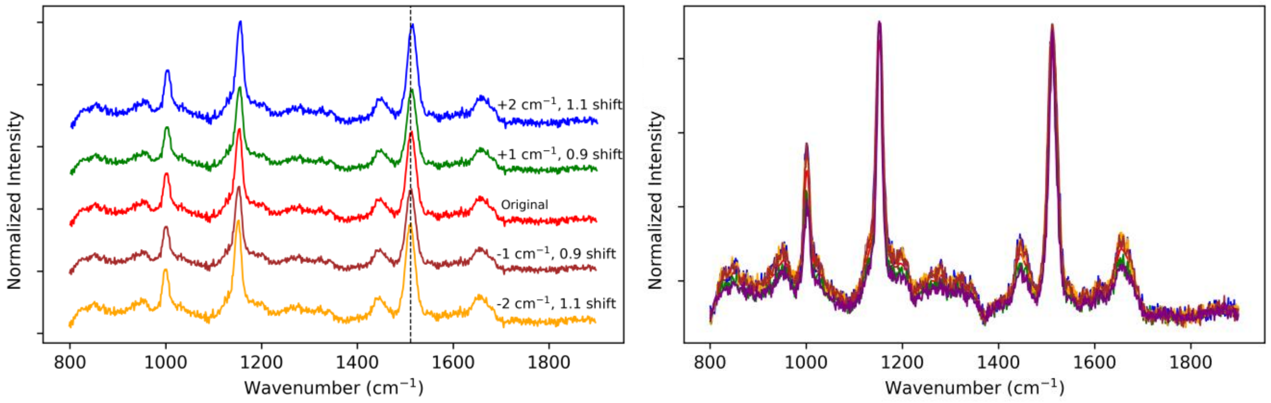

(a) (b)

Fig. 2 Original and augmented serum Raman spectra using different approaches: (a) combined method based on linear transformations, (b) WGAN synthezied spectra.

Table 1 Comparison of the performance of classification models on the initial and augmented datasets (SD – standart deviation).

Classification method	**Analyzed data**	**ROC AUC ± SD**	***z*-value**	**Improving**
*k*NN	Original set	0.67 ± 0.11	–	–
	Combined approach (±1cm^{-1} shift, 0.9 stretch)	0.69 ± 0.10	<1.96	No
	Combined approach (±2cm^{-1} shift, 1.1 stretch)	0.67 ± 0.09	<1.96	No
	WGAN	0.74 ± 0.08	2.38	Yes
PLS-DA	Original set	0.71 ± 0.11	–	–
	Combined approach (±1cm^{-1} shift, 0.9 stretch)	0.80 ± 0.10	2.30	Yes
	Combined approach (±2cm^{-1} shift, 1.1 stretch)	0.81 ± 0.09	2.56	Yes
	WGAN	0.83 ± 0.09	2.95	Yes

In contrast, PLS-DA is a covariance-based latent-variable method that explicitly seeks directions of maximum covariance between spectra and class labels; the enlarged, augmented training set provides richer sampling of the spectral manifold, enabling more robust latent-variable estimation and clearer class separation, which leads to a statistically significant gain in ROC-AUC.

Fig. 2(b) shows an example of serum Raman spectra generated using WGAN. Application of WGAN-generated synthetic spectra further enhanced classification performance across both algorithms: kNN and PLS-DA. For kNN, the augmented WGAN dataset yielded ROC AUC = 0.74 ± 0.08, representing a significant improvement over the initial 0.67 ± 0.11. This statistically significant enhancement ($z \approx 2.38$, $p < 0.05$) demonstrates WGAN's capacity to generate realistic spectral perturbations beyond simple linear transformations.

The performance of PLS-DA has been further improved, achieving an AUC of 0.83 ± 0.09 on the WGAN-expanded dataset. This represents a 17% relative improvement over the baseline (0.71 ± 0.11) and a 4% absolute gain over augmentation based on linear transformations. A *z*-test comparison has confirmed the high statistical significance of the difference between the results of PLS-DA with and without WGAN augmentation ($z \approx 2.6$, $p < 0.01$).

To evaluate the representativeness of the WGAN-generated spectra, PLS-DA models were built and assessed on three different datasets: (1) the original real spectra only, (2) the synthetic spectra generated by the WGAN, and (3) the combined dataset of real and synthetic spectra. The PLS-DA model trained on the original real spectra achieved an accuracy of 0.71 ± 0.11, reflecting the baseline discriminative capability of the measured experimental data. The model fitted on the synthetic spectra alone reached 0.85 ± 0.08, indicating that the generated spectra preserved sufficient class-separating information and spectral patterns to support a stable classification, even in the absence of real data. Finally, the PLS-DA model trained on the merged dataset (real and synthetic spectra) yielded an accuracy of 0.83 ± 0.09, which is slightly higher than that of the real-only model while maintaining a comparable level of variability. These results suggest that the WGAN-generated spectra are consistent with the real data in terms of class structure and underlying spectral features.

WGAN augmentation proved effective due to its ability to synthesize physiochemically plausible Raman spectra that preserve peak morphology, baseline characteristics, and signal-to-noise relationships characteristic of real serum measurements. Reduced standard deviation across both techniques indicates improved model stability and resistance to overfitting, with dataset expansion directly contributing to variance reduction (standard deviation (SD) decreased from 0.11 to 0.08–0.09). This improved performance is crucial for clinical translation, where patient cohorts display significant biological diversity, as larger training sets better capture the full range of physiological and experimental variations inherent in real-world Raman serum measurements.

These findings support the use of WGAN as an optimal augmentation strategy for Raman spectroscopic classification of CHF. This approach allows us to minimize the link between the limited number of experimental datasets available and the statistical power needed for reliable diagnosis, while preserving accuracy, which is crucial for discovering important spectral trends.

Additionally, it is interesting to observe the different levels of differentiation among the *k*NN and PLS-DA methods. The comparison between *k*NN and PLS-DA reveals that these algorithms have different sensitivities to the size of the dataset. PLS-DA shows a pronounced dependence on the dataset size, achieving better generalization on the 10-fold expanded dataset. This enhanced performance is likely due to PLS-DA's ability to exploit increased spectral variance from linear transformations, which simulates biological sample variability observed in real-world serum measurements. These transformations effectively capture physiological fluctuations and experimental inconsistencies, providing a more representative training distribution for PLS-DA. Covariance-based methods, such as PLS-DA, require robust latent variable construction, and this augmentation provides them with a more representative distribution for training, leading to better performance.

Results from the augmented datasets (10-fold expansion to $n = 1200$ training spectra) demonstrate reduced SD in ROC AUC compared to the original dataset ($n = 120$), indicating lower variance and enhanced model stability across both *k*NN and PLS-DA classifiers. For *k*NN, SD decreased from 0.11 (original) to 0.08 (WGAN-augmented), a 27% variance reduction; PLS-DA showed similar improvement from 0.11 to 0.09 (17% relative gain). This narrower spread reflects more consistent performance across cross-validation folds, minimizing overfitting risks inherent to small biomedical cohorts.

Notably, neither *k*NN nor PLS-DA exhibited performance degradation post-augmentation, maintaining or improving ROC-AUC despite 10-fold dataset expansion. Nevertheless, this stability may however stem from the limited variability introduced by the employed augmentation methods (linear transformations and WGAN), which simulate controlled spectral perturbations rather than the full spectrum of real-world biological heterogeneity. Actual serum samples often display unpredictable physiological variations – such as patient-specific protein profiles, medication effects, comorbidities (e.g., renal dysfunction, diabetes), diurnal hormone fluctuations, and dietary influences on carotenoid/lipid content – that exceed the controlled perturbations generated by current augmentation methods (linear transformations, WGAN).

Summary, results from the current cohort provisionally confirm the feasibility of using Raman spectroscopy to differentiate CHF stages, establishing proof-of-concept for future clinical validation. Raman's molecular sensitivity enables detection of systemic metabolic shifts during CHF noninvasively. Advanced CHF stages (HIIB–III) were accompanied by significant elevation of N-terminal pro-B-type natriuretic peptide (NT-proBNP) and reduced glomerular filtration rate, confirming disease severity. However, these biochemical differences may reflect both direct CHF effects and comorbid conditions more prevalent in severe cases – for instance, type 2 diabetes mellitus occurred in 21% of early-stage (HIIA) vs. 53% of advanced-stage (HIIB–III) patients. Raman spectroscopy captures these composite metabolic shifts noninvasively, demonstrating feasibility for CHF staging. In accordance with our spectral data progressive CHF stages can characterize by reduced carotenoid content (1004, 1150, 1515 cm^{-1}) that can reflect antioxidant depletion and increased protein/lipid ratios (1445, 1665 cm^{-1}) indicating inflammation, validated by PLS-DA (ROC AUC = 0.83). Also, augmentation results of this work yielded positive outcomes, confirming classification performance's dependence on effective sample size, validating augmentation as a viable strategy when real sample accrual is constrained. Ideally, model robustness requires continuous expansion with authentic biological specimens to capture full clinical heterogeneity. However, given persistent resource limitations in pilot biomedical spectroscopy studies, continued augmentation research remains essential – exploring advanced techniques like variational autoencoders (VAE), diffusion models, and physics-informed GANs. Future validation should include a variety of classification tasks, such as multi-diagnosis cohorts (for example, CHF with comorbidities) and sub-class analyses (HIIA subtypes). Additionally, it is important to cross-validate the model against independent serum collections in order to ensure its generalization against complex physiological variability found in real-world clinical settings.

4 Conclusions

This study focuses early CHF detection in high-risk patients by differentiating early-stage (HIIA) from progressive stages (HIIB–III) using serum Raman analysis to identify initial biochemical changes, positioning it as a promising screening tool. We evaluated data augmentation strategies for enhancing Raman spectroscopic classification of CHF using limited human serum samples. Linear spectral transformations (wavenumber shifting and intensity stretching) demonstrated algorithm-specific efficacy, providing statistically significant ROC AUC improvements for PLS-DA (0.71 → 0.80–0.81, $p < 0.05$) but not *k*NN, highlighting fundamental differences in distance-based versus covariance-based classification sensitivities.

WGAN-based augmentation emerged as the optimal methodology, achieving higher performance across both algorithms: *k*NN improved from 0.67 ± 0.11 to 0.74 ± 0.08 (27% variance reduction), while PLS-DA reached 0.83 ± 0.09 (17% relative gain). The consistent standard error reduction not only underscores enhanced model stability critical for heterogeneous clinical cohorts but also demonstrates that increased case numbers through synthetic data expansion directly contribute to lower variance, enabling more reliable performance as patient cohort sizes grow.

Key findings demonstrate that WGAN effectively simulates physiochemically realistic spectral variance – encompassing biological heterogeneity, carotenoid content fluctuations, and instrumental effects – beyond the capabilities of linear methods. PLS-DA exhibited pronounced dataset size dependence, leveraging expanded feature spaces for optimal latent variable construction. These results establish WGAN augmentation as a good tool for Raman-based diagnostics, particularly for CHF, enabling higher CHF staging (ROC AUC > 0.80) from small patient cohorts.

Future work can explore an expanded class of augmentation methods, including variational autoencoders (VAE), diffusion models, and physics-informed GAN architectures, to further enhance spectral realism. Systematic investigation of classifier performance dependencies on varying dataset sizes ($n = 50–5000$), augmentation ratios, and sample heterogeneity will optimize augmentation protocols for clinical deployment. Hybrid augmentation strategies combining WGAN with machine learning classification approach and clinical metadata (NT-proBNP levels, ejection fraction) may yield personalized diagnostic models with enhanced prognostic capability.

Funding

This research was funded by Russian Science Foundation, grant number 25-75-00146; https://rscf.ru/project/25-75-00146/.

Disclosures

The authors declare that they have no conflicts of interest or competing financial interests related to this work.

References

1. Cardiovascular diseases (CVDs), WHO, 31 July 2025 (accessed 2 March 2026) [https://www.who.int/news-room/fact-sheets/detail/ cardiovascular-diseases-(cvds)].
2. A. S. Galyavich, S. V. Nedogoda, G. P. Arutyunov, Yu. N. Belenkov, "About the classification of heart failure," Russian Journal of Cardiology 28(9), 5584 (2023). [in Russian]
3. B. Bozkurt, A. J. S. Coats, H. Tsutsui, et al., "Universal definition and classification of heart failure: a report of the Heart Failure Society of America, Heart Failure Association of the European Society of Cardiology, Japanese Heart

Failure Society and Writing Committee of the Universal Definition of Heart Failure: Endorsed by the Canadian Heart Failure Society, Heart Failure Association of India, Cardiac Society of Australia and New Zealand, and Chinese Heart Failure Association," European Journal of Heart Failure 23(3), 352–380 (2021).

4. S. A. Hill, R. A. Booth, P. L. Santaguida, A. Don-Wauchope, J. A. Brown, M. Oremus, U. Ali, A. Bustamam, N. Sohel, R. McKelvie, C. Balion, and P. Raina, "Use of BNP and NT-proBNP for the diagnosis of heart failure in the emergency department: a systematic review of the evidence," Heart Failure Reviews 19(4), 421–438 (2014).
5. T. A. McDonagh, M. Metra, M. Adamo, et al., "2023 Focused Update of the 2021 ESC Guidelines for the diagnosis and treatment of acute and chronic heart failure: Developed by the task force for the diagnosis and treatment of acute and chronic heart failure of the European Society of Cardiology (ESC) With the special contribution of the Heart Failure Association (HFA) of the ESC," European Heart Journal 44(37), 3627–3639 (2023).
6. Y. Khristoforova, L. Bratchenko, and I. Bratchenko, "Raman-Based Techniques in Medical Applications for Diagnostic Tasks: A Review," International Journal of Molecular Sciences 24(21), 15605 (2023).
7. L. A. Bratchenko, Y. A. Khristoforova, Y. G. Loginova, A. A. Moryatov, V. P. Zakharov, O. I. Kaganov, and I. A. Bratchenko, "Raman *in Vivo* Analysis of Melanoma Invasion Level," Journal of Biomedical Photonics & Engineering 11(3), 030303 (2025).
8. L. A. Bratchenko, Y. A. Khristoforova, I. A. Pimenova, E. N. Tupikova, M. A. Skuratova, G. A. Dvoynikov-Sechnoy, S. Wang, P. A. Lebedev, and I. A. Bratchenko, "SERS-based technique for accessible and rapid diagnosis of multiple myeloma in blood serum analysis," Light: Advanced Manufacturing, 6(2), 284–294 (2025).
9. H. Yilmaz, A. Ramoji, A. Winterfeld, H. Salehi, A. Ozkul, and J. Popp, "Applications of Raman Spectroscopy in Pandemic Virology: A Comprehensive Review," ACS Photonics 13(6), 1568–1590 (2026).
10. D. W. Shipp, F. Sinjab, and I. Notingher, "Raman spectroscopy: techniques and applications in the life sciences," Advances in Optics and Photonics 9(2), 315–428 (2017).
11. L. A. Bratchenko, Y. A. Khristoforova, I. A. Pimenova, M. S. Snegerev, V. I. Kupaev, P. A. Lebedev, Y. V. Kistenev, and I. A. Bratchenko, "Comparative Study Into the Effect of Detector Noises and Sensitivity on the Serum SERS Analysis: Example of Non-Communicable Diseases Discrimination," Journal of Biophotonics 18(4), e202400475 (2025).
12. J. De Gelder, K. De Gussem, P. Vandenabeele, and L. Moens, "Reference database of Raman spectra of biological molecules," Journal of Raman Spectroscopy 38(9), 1133–1147 (2007).
13. N. M. Ralbovsky, I. K. Lednev, "Towards development of a novel universal medical diagnostic method: Raman spectroscopy and machine learning," Chemical Society Reviews 49(20), 7428–7453 (2020).
14. S. Jiang, X. Sha, S. Qu, Z. Jiang, Y. Shen, Q. Wang, M. Kang, and G. Fang, "Label-Free SERS spectroscopy of Serum: Early screening and therapeutic evaluation for ovarian tumor patients," Microchemical Journal 215, 114180 (2025).
15. S. Ahmad, M. I. Majeed, H. Nawaz, M. R. Javed, N. Rashid, M. Abubakar, F. Batool, S. Bashir, M. Kashif, S. Ali, M. Tahira, S. Tabbasum, and I. Amin, "Characterization and prediction of viral loads of Hepatitis B serum samples by using surface-enhanced Raman spectroscopy (SERS)," Photodiagnosis and Photodynamic Therapy 35, 102386 (2021).
16. C. Beleites, U. Neugebauer, T. Bocklitz, C. Krafft, and J. Popp, "Sample size planning for classification models," Analytica Chimica Acta 760, 25–33 (2013).
17. X. Zhang, H. Li, X. Tian, C. Chen, Y. Su, M. Li, J. Lv, C. Chen, and X. Lv, "Application of spectral small-sample data combined with a method of spectral data augmentation fusion (SDA-Fusion) in cancer diagnosis," Chemometrics and Intelligent Laboratory Systems 231, 104681 (2022).
18. J. Zhao, H. Lui, S. Kalia, T. K. Lee, and H. Zeng, "Improving skin cancer detection by Raman spectroscopy using convolutional neural networks and data augmentation," Frontiers in Oncology 14, 1320220 (2024).
19. M. Wu, S. Wang, S. Pan, A. C. Terentis, J. Strasswimmer, and X. Zhu, "Deep learning data augmentation for Raman spectroscopy cancer tissue classification," Scientific Reports 11(1), 23842 (2021).
20. S. Laitrakun, S. Deepaisarn, S. Gulyanon, C. Srisumarnk, N. Chiewnawintawat, A. Angkoonsawaengsuk, and N. Jaikaew, "Toward Practical Augmentation of Raman Spectra for Deep Learning Classification of Contamination in HDD," Journal of Information and Communication Convergence Engineering 21(3), 208–215 (2023).
21. D. Ma, L. Shang, J. Tang, Y. Bao, J. Fu, and J. Yin, "Classifying breast cancer tissue by Raman spectroscopy with one-dimensional convolutional neural network," Spectrochimica Acta Part A: Molecular and Biomolecular Spectroscopy 256, 119732 (2021).
22. M. Patil, M. M. Patil, and S. Agrawal, "WGAN for Data Augmentation," in GANs for Data Augmentation in Healthcare, A. Solanki, M. Naved (Eds.), Springer International Publishing, 223–241 (2023).
23. J. A. Hanley, B. J. McNeil, "A method of comparing the areas under receiver operating characteristic curves derived from the same cases," Radiology 148(3), 839–843 (1983).
24. J. Udensi, J. Loughman, E. Loskutova, and H. J. Byrne, "Raman Spectroscopy of Carotenoid Compounds for Clinical Applications - A Review," Molecules 27(24), 9017 (2022).

Variational and Numerical Analysis of Contour-Based Segmentation Methods in Cephalometry

Yulia Zh. Pchelkina
Samara National Research University, 34 Moskovskoe shosse, Samara 443086, Russian Federation
*e-mail: pchelkina.yuj@ssau.ru

Abstract. A method for the automatic extraction of the soft-tissue facial profile contour is proposed, along with the detection of key cephalometric landmarks based on extremum analysis of a parameterized contour function and subsequent determination of the profile type and its harmony. A variational and numerical analysis of the influence of weighting coefficients in the energy functional on segmentation accuracy and diagnostic indicators is conducted, allowing the parameter selection to be justified and ensuring robust automatic annotation comparable to manual cephalometric analysis.

Keywords: variational methods; contour segmentation; image segmentation; model parameter analysis; orthodontics, cephalometry.

Paper #9561 received 26 Mar 2026; revised manuscript received 30 Apr 2026; accepted for publication 30 Apr 2026; published online 17 Jun 2026. doi: 10.18287/JBPE26.12.020309.

1 Introduction

Digital processing of biomedical images is one of the key directions in modern medical engineering, providing objectivity in diagnostics and reducing dependence on the subjective factor. One of the clinically significant applied tasks in this field is the automated cephalometric analysis of soft-tissue facial profile photographs, used in orthodontics and orthognathic surgery. During such analysis, the orthodontist evaluates both anatomical and aesthetic characteristics of the patient's face, including face shape, soft-tissue proportions, and possible dentofacial anomalies. These data are recorded in the descriptive section of the photo protocol and serve as an important basis for diagnosis, treatment planning, and subsequent outcome evaluation [1].

Currently, the identification of key cephalometric landmarks on photographs, measurement of angles and linear dimensions, and computation of derived anthropometric characteristics are typically performed manually. This approach is time-consuming, places high demands on specialist qualification, and is subject to subjectivity, which may lead to measurement variability between different clinicians and between repeated measurements of the same case.

Automation of biomedical facial image analysis allows measurements to be standardized, examination time to be reduced, and human error to be minimized – which is especially important when processing large clinical datasets and preparing training samples for intelligent diagnostic systems. The task of facial contour extraction and cephalometric landmark localization is addressed using computer vision and digital image processing methods – from simple threshold-based approaches to complex variational and machine-learning models. The choice of algorithm is determined by accuracy requirements: in cephalometric tasks, correct extraction of the soft-tissue boundary and precise landmark positioning are critical, since even small errors can affect profile type classification and facial harmony assessment. Therefore, the active contour variational method is chosen in this work as the primary tool for soft-tissue profile extraction, enabling iterative deformation of an initial contour until it coincides with the actual object boundary, thus ensuring the required accuracy and robustness of biomedical segmentation.

2 Anthropometric Analysis of the Facial Profile

Anthropometric analysis of the facial profile is based on a geometric description of the relative positions of key cephalometric landmarks located on the soft-tissue facial contour. Within the classical approach, profile type assessment is performed by measuring the angle between two lines passing through predefined reference points. These lines model the general contour of the frontonasal and nasal-chin segments of the profile and allow quantitative characterization of the degree of convexity or concavity of the facial profile relative to a conventional neutral (straight) configuration.

Standard cephalometric landmarks are used as reference points. The Gl point (glabella) is defined as the most anteriorly projecting point of the forehead in the sagittal plane and serves as an orientation point for the upper facial segment. The Sn point (subnasale) is located at the junction of the nasal septum skin and the upper lip, reflecting the transition from the nasal to the labial segment. The Pg point (pogonion) corresponds to the maximum anterior projection of the soft-tissue chin and characterizes the distal facial segment. Together, these points form the minimally sufficient set for a primary angular assessment of facial profile shape.

The angle between the lines drawn through these points is interpreted in terms of three main profile types in anthropometric analysis. The profile is considered straight if the measured angle is close to 180°, indicating a balanced position of the frontal, nasal, and chin segments without pronounced prognathia or retrognathia. If the angle is less than 170°, the profile is classified as convex; this configuration is typically associated with relative protrusion of the midface or chin retrognathia. When the angle exceeds 170°, the profile is assessed as concave, which generally reflects relative anterior displacement of the chin or a flatter midface position [2].

Additionally, the Ricketts aesthetic line is widely used in aesthetic profile analysis. It is defined as the line connecting the tip of the nose and the most prominent point of the chin. The position of the lips relative to this line serves as a qualitative and quantitative criterion of soft-tissue profile harmony (Fig.1).

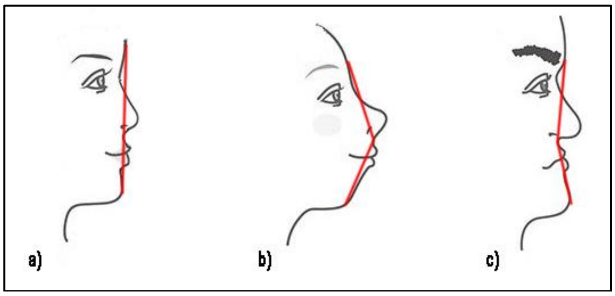

Fig. 1 Facial profile types: a) straight profile, b) convex profile, c) concave profile.

The profile is considered harmoniously developed when the aesthetic line does not intersect the lip contour and the lips either touch it or are positioned within the acceptable posterior deviation (the upper lip is 2–3 mm posterior to this line, the lower lip is 1–2 mm posterior). This state is interpreted as a sign of balanced facial proportions and compliance with accepted aesthetic norms. A disharmonious profile is almost always associated with dentofacial anomalies and carries not only aesthetic but also functional problems requiring various orthodontic interventions depending on the profile type [3].

3 Contour Extraction Method

For contour extraction in an image, the segmentation task is formulated as variational minimization of the energy functional of a curve defined on the image plane. Let $I(x, y)$ – be the scalar intensity field of the source image, and let the closed contour C be given in parametric form:

$$C(s) = \big(x(s), y(s)\big),\ s \in [0, 1].$$

The contour behavior is then described through the total energy, which depends both on its own geometry and on the image properties in the neighborhood of the contour points.

In the discrete formulation used in this work, the initial contour is represented as an ordered set of vertices $\{v_i\}_{i=1}^{n}$, where $v_i = (x_i, y_i)$ and n is the number of vertices. The contour iteratively changes its shape until it approximates the object geometry to a specified accuracy [4–6]. For each vertex v_i a scalar energy is introduced:

$$E_i(v_i) = a \cdot E_{int}(v_i) + b \cdot E_{ext}(v_i),$$

where $E_{int}(v_i)$ is the contribution of the internal (geometric) energy depending on the contour shape and smoothness in the neighborhood of v_i; $E_{ext}(v_i)$ is the contribution of the external energy determined by the image structure $I(x, y)$ in the neighborhood of v_i; a and $b > 0$ are weighting coefficients regulating the balance between regularization and boundary attraction.

To obtain the object contour, the total energy is minimized:

$$\textstyle\sum_{i=1}^{n} E_i(v_i).$$

Minimization is performed iteratively: at each step, each contour vertex v_i moves to the position corresponding to a reduction of local energy E_i Deformation continues until changes in energy and/or vertex positions fall below a specified threshold, which is interpreted as reaching an approximate local minimum of the functional.

The energy functions in this model are defined in discrete form and interpreted as matrices (or window filters) defined in the neighborhood of each contour point. The central element of such a matrix corresponds to the value of the chosen energy function computed directly at the contour point. The remaining elements contain values of the same energy function for a set of points belonging to a local neighborhood of that point in the image. Thus, each energy function is described not only at a single point but in a neighborhood of v_i, allowing the local image structure to be taken into account when evaluating energy and updating the contour.

The internal energy affects the shape and smoothness of the contour and is designed to constrain contour shape, preventing jaggedness and unnatural oscillations. It models the elastic-rigid properties of the curve. In discrete notation, the internal energy is represented as a combination of two components:

$$a \cdot E_{int}(v_i) = \mathrm{c} \cdot E_{con}(v_i) + d \cdot E_{bal}(v_i),$$

where $E_{con}(v_i)$ is the smoothing energy (configurational energy controlling distances and relative positions of neighboring vertices), $E_{bal}(v_i)$ is the so-called balloon (bursting) energy responsible for displacing the contour outward or inward relative to the object; $c,\ d > 0$ are the corresponding weighting coefficients.

Elements of the smoothing energy matrix for a closed contour are computed as:

$$e_{jk}(v_i) = \frac{n}{\sum_{i=1}^{n}|v_{i+1}-v_i|^2} \cdot \left| p_{jk}(v_i - \frac{v_{i-1}+v_{i+1}}{2cos\,(\frac{2\pi}{n})}) \right|^2,$$

where $p_{jk}(v_i)$ are the neighborhood points of v_i in the image (discrete mask around the vertex), n is the number of contour vertices. This formula implements a discrete approximation of the second derivative (curvature) of the curve accounting for its cyclic (closed) structure: the expression

$$(v_{i-1} + v_{i+1})/2\,cos\left(\frac{2\pi}{n}\right)$$

defines the "expected" vertex position for uniformly distributed points on a circle, and the magnitude of the difference with the actual position $p_{jk}(v_i)$ measures the degree of local deviation from a smooth configuration.

The normalization factor $n/\sum_{i=1}^{n}|v_{i+1} - v_i|^2$ makes the smoothing energy invariant to the overall scale of the contour: dividing by the total squared arc length ensures that E_{con} does not grow simply because the contour is large, allowing the weighting coefficient c to be interpreted independently of image resolution.

The factor $1/(2cos(2\pi/n))$ arises from the expected position of a vertex on a regular n-gon inscribed in a circle: for equally spaced points, the midpoint of the neighbors $(v_{i-1} + v_{i+1})/2$ lies at distance $r\ cos(2\pi/n)$ from the centre, where r is the polygon radius. This term serves as a discrete normalisation ensuring that the smoothing energy vanishes for a uniformly sampled circle.

The balloon energy $E_{bal}(v_i)$ deforms the contour in one direction, is introduced to control the radial displacement of the contour relative to the object, and can be written as:

$$e_{jk}(v_i) = n_i\left(v_i - p_{jk}(v_i)\right),$$

where $n_i$is the vector defining the preferred deformation direction (e.g., the normal to the contour at v_i), and $p_{jk}(v_i)$ are the neighborhood points relative to which the displacement is assessed. Thus, the internal energy defines a nonlocal regularizing term ensuring contour robustness to noise and small artifacts.

The external energy is responsible for attracting the contour to object boundaries detected by brightness and gradient characteristics of the image. In the model used, it takes the form:

$$a \cdot E_{ext}(v_i) = g \cdot E_{mag}(v_i) + h \cdot E_{grad}(v_i),$$

where $E_{mag}(v_i)$ reflects the contribution of absolute brightness values, and $E_{grad}(v_i)$ is the contribution of the brightness gradient magnitude; $g,\ h > 0$ are weighting coefficients regulating the role of each factor.

Elements of the image energy matrix $E_{mag}(v_i)$ are defined directly by brightness:

$$e_{jk}(v_i) = I\left(p_{jk}(v_i)\right),$$

meaning the darker (or, depending on the convention chosen, the brighter) the region, the lower (or higher) its energy contribution.

Elements of the gradient energy matrix $E_{grad}(v_i)$ are defined as:

$$e_{jk}(v_i) = -\left|\overline{\nabla I}\left(p_{jk}(v_i)\right)\right|,$$

where $\overline{\nabla I}$ is the discrete brightness gradient at point $p_{jk}(v_i)$, representing a two-dimensional vector of partial derivatives in the vertical and horizontal directions. The negative sign ensures contour attraction to regions with high gradient magnitude (boundaries), since such points yield minimum energy.

Together, the parameters a, b, c, d, g, h define the weighting coefficients in the generalized energy functional and allow fine-tuning the trade-off between contour smoothness and accuracy of fit to the object boundary. With correct selection of these coefficients, the resulting contour approximates the desired facial boundary with the required degree of accuracy and robustness to noise and illumination variations [7].

Total energy minimization is performed using the greedy algorithm. At each iteration, the algorithm sequentially processes all n contour vertices. For each vertex v_i, a discrete neighborhood $N(v_i)$ is formed – a discrete mask of size $(2s + 1) \times (2s + 1)$ pixels, where parameter s defines the search radius. Within this neighborhood, values of all energy functional components are computed, and the vertex is moved to the point with the minimum total local energy. If the neighborhood center is already the minimum (the vertex did not move), a "fixed point" is recorded, which is used in the stopping criterion. The procedure repeats until the stopping criterion is met: iterations cease if the fraction of fixed vertices in one iteration exceeds threshold θ_{stop}, or the change in total energy $|E^t\ -\ E^{\{t-1\}}|$ becomes less than a specified ε, or the maximum number of iterations T_{max} is reached. The greedy algorithm has computational complexity $O(nm)$, which is more than an order of magnitude faster than the dynamic programming approach with complexity $O(nm^3)$.

4 Contour Extraction for Facial Profile Detection

In most applications of the described contour method, the initial contour is set manually by the user. To automate this step, pre-trained face detection models are used: a

Haar cascade classifier or the Dlib model [8, 9]. The center of the detected facial region serves as the center of the initial circular contour.

An important role in active contour methods is played not only by initial contour placement and image preprocessing, but also by parameter selection. The parameters a, b, c, d, g, h should be chosen to balance the contributions of internal and external energies: the contour must be sufficiently smooth while also being close to the real object boundary. In practice, it is necessary to determine the relative weights of different terms in the energy functional and find ratios at which the minimum of this functional yields the desired contour [10].

From a mathematical analysis perspective, the following key selection principles should be considered:

1 Energy normalization. It is advisable to first estimate the magnitudes of the energy functions on test images by computing the mean or median value of each energy across contour points and multiple images: $\bar{E}_{con}, \bar{E}_{bal}, \bar{E}_{mag}, \bar{E}_{grad}$.

Weights are then chosen so that the contribution of each term to the total energy is of comparable order:

$$c \sim \frac{1}{\bar{E}_{con}}, d \sim \frac{1}{\bar{E}_{bal}}, g \sim \frac{1}{\bar{E}_{mag}}, h \sim \frac{1}{\bar{E}_{grad}}.$$

The entire set is then scaled by the common pair a, b according to the desired contour “stiffness”.

2 Coefficient ratios. For contour evolution via gradient descent, what matters is not the absolute magnitude of the functional but the relative contribution of terms to its derivative. Therefore, it is preferable to tune the ratios of coefficients rather than their absolute values

The ratio $a\!:\!b$ shows how much stronger the internal energy is relative to the external energy. If $a \geq b$, the contour will be very smooth but will weakly respond to image details, increasing the risk of under-segmentation (the initial contour may not reach the real boundary). If $a \leq b$, the contour will aggressively track any gradients and contrasts, potentially leading to noise and false boundaries.

The ratio $c\!:\!d$ is the ratio of contour smoothness to balloon expansion capability. A large value of c will cause the contour to tend toward a more uniform shape and contract quickly, potentially losing fine profile details. An excessively large value of d may cause the contour to compress too aggressively.

The ratio $g\!:\!h$ governs sensitivity to brightness versus sensitivity to boundaries (gradient). Coefficient g orients the contour toward regions of specific brightness (e.g., darker soft tissues against background). Coefficient h orients the contour toward lines with maximum gradient magnitude (i.e., boundaries), which is critical for well-defined contours, especially in medical images with clear tissue transitions. In facial profile cephalometry, the soft-tissue boundary is typically well described by the gradient (skin-background contrast), so in practice it is advisable to choose $h > g$, placing the main emphasis on E_{grad} and using the brightness term as an additional stabilizing component

5 Contour Analysis Algorithm for Cephalometric Tasks

Once the closed soft-tissue facial profile contour is obtained, the task reduces to finding extremal points – local maxima and minima corresponding to key cephalometric landmarks (nose tip, lips, chin, forehead, nasion, etc.). Computationally, this is a problem of analyzing a single-variable function defined on a closed curve. The following algorithm is proposed:

1. Transformation to polar coordinates.
2. Contour unrolling.
3. Finding extrema of the profile function.
4. Inverse transformation to Cartesian coordinates.
5. Correspondence of extrema to anatomical points.
6. Vector-angular analysis for profile type classification.
7. Assessment of profile harmony.

Let the closed contour after segmentation be parametrically defined as a set of points $A_k = (x_k, y_k)$, $k = 1, 2, \dots, N$, arranged clockwise or counterclockwise. A reference center $O = (0, 0)$ is chosen. In this work, the center of the initial contour or the centroid of the detected profile is conveniently used as the center. Each contour point A_k is converted to polar coordinates:

$$\varphi_k = arctg\left(\frac{y_k}{x_k}\right); \;\; \rho_k = \sqrt{x_k^2 + y_k^2}.$$

Here φ_k is the angle between the x-axis and the radius vector connecting point A_k with center O, and ρ_k is the distance from the center to the point. In the context of this article $arctg\,(y_k/x_k)$ returns values in $(-\pi/2, \pi/2)$; the correct quadrant is determined by the signs of x_k and y_k according to the standard convention: φ_k is adjusted by $(+\pi)$ if $x_k < 0$ and $y_k \geq 0$, by $(-\pi)$ if $x_k < 0$ and $y_k < 0$, and is undefined for $x_k = 0$. Points with $x_k = 0$ are handled as special cases with $\varphi_k = \pi/2$ if $y_k > 0$ and $\varphi_k = -\pi/2$ if $y_k < 0$.

Thus, the original two-dimensional contour C is represented as a one-dimensional periodic function $\rho(\varphi) \approx \rho_k$ on a discrete set of angles $\{\varphi_k\}_{k=1}^{N}$. This unrolling converts the closed profile into a radius-versus-angle function defined on the interval $(-\pi, \pi]$ or $[0, 2\pi)$ with periodic boundary conditions.

The search for extrema of the profile function is performed to identify key cephalometric landmarks. Local maxima of $\rho(\varphi)$ correspond to the most prominent profile regions (nose tip, chin, forehead, lip vertices). Local minima correspond to the most recessed regions (subnasale area, nasion, etc.).

Computationally, finding local extrema of the discrete sequence $\{\rho_k\}$ is based on the following criterion: point with index k is a local maximum of order m if $\rho_k > \rho_{k-j}$ and $\rho_k > \rho_{k+j}$ for all $j = 1, 2, \dots, m$. A local minimum is defined analogously.

The parameter m defines the neighborhood size within which locality of the extremum is verified. Increasing m filters out small noise oscillations and retains only major, anatomically significant extrema.

Arrays of maxima and minima of the contour function are then formed and sorted by angle φ in the traversal direction, with the starting point chosen as the extremum located to the right of and below the center of the initial contour – this fixes the baseline reference point on the profile.

For subsequent cephalometric analysis, all extremal points are converted back to the Cartesian coordinate system. For each extremum point $(\varphi_1,\ \rho_1)$, the coordinates are computed as:

$$x_2 = \rho_1 \cos(\varphi_1) + x_c,\ \ y_2 = \rho_1 \sin(\varphi_1) + y_c,$$

where (x_c, y_c) are the coordinates of the initial contour center, accounting for any coordinate system shift relative to the source image. Each extremal point thus receives coordinates in the source image system.

The extrema are ordered so that the first element of the maxima array $A_1(x_1, y_1)$, located to the right of and below the center, corresponds to the nose tip. Continuing counterclockwise, the next three maxima $A_2(x_2, y_2)$, $A_3(x_3, y_3)$, $A_4(x_4, y_4)$ correspond to the upper lip, lower lip, and the most prominent point of the chin, respectively. The last maximum $A_5(x_5, y_5)$ corresponds to the most prominent point of the forehead. The first minimum $A_6(x_6, y_6)$ and the last minimum $A_7(x_7, y_7)$ correspond to the subnasale point and the nasion, respectively.

Thus, through strict ordering of the extrema and their positions relative to the center and to each other, an unambiguous correspondence is established between the mathematically detected extremal points and the clinically significant cephalometric landmarks (Fig. 2a).

Based on the identified points, line segments are formed from which the angles characterizing the profile type are calculated.

The angle characterizing the profile type is computed from vectors formed by the point pairs (A_4, A_6) and (A_5, A_6):

$$u = (m_1, n_1) = (x_6 - x_4, y_6 - y_4),$$

$$v = (m_2, n_2) = (x_6 - x_5, y_6 - y_5),$$

$$\varphi = arccos\left(\frac{m_1 m_2 + n_1 n_2}{\sqrt{m_1^2 + n_1^2} \cdot \sqrt{m_2^2 + n_2^2}}\right).$$

The resulting angle φ is assessed against threshold values defining the acceptable variation range for a straight profile, accounting for anatomical variability and measurement errors (Fig. 2b):

- $170^o \leq \varphi \leq 190^o$ – straight profile;
- $\varphi < 170^o$– convex profile;
- $\varphi > 190^o$– concave profile.

The Ricketts aesthetic line is defined as the line passing through points $A_1(x_1, y_1)$ and $A_4(x_4, y_4)$, corresponding to the nose tip and the most prominent point of the chin. The equation of this line can be written as:

$$\frac{x - x_1}{x_4 - x_1} = \frac{y - y_1}{y_4 - y_1},$$

or in general form: $ax + by + c = 0$. For the lip points $A_2(x_2, y_2)$ and $A_3(x_3, y_3)$, the signs and magnitudes of algebraic distances to this line are computed. If both points are on the same side of the line and do not lie on it or cross it (e.g., they are posterior by no more than a specified threshold), the profile is considered harmoniously developed; otherwise, the profile is considered disharmonious (Fig. 2c).

6 Experimental Results

The dataset consists exclusively of profile-view photographs; automated processing of frontal (en-face) images does not present significant methodological challenges and is not the focus of this study. Standard side-profile photographs taken under controlled lighting conditions against a uniform, neutral background were selected for processing. The images were taken from a publicly available face image dataset. The 120 images are evenly distributed across three profile types: 40 images per class (straight, convex, concave). Prior to annotation, all images underwent a standardized pre-processing pipeline: cropping to the facial bounding box detected by a Haar cascade classifier; conversion to grayscale; rescaling to a uniform resolution; noise removal using morphological operations (erosion, dilation, opening, closing, and logical filters); contrast enhancement; blurring via the Inverse Gaussian Gradient. After pre-processing, all images were annotated in two independent ways: automatically using the proposed algorithm, and manually by a medical specialist serving as ground truth. In both cases, three annotation tasks were performed: localization of seven key cephalometric landmarks; multi-class profile type classification (straight/convex/concave); binary harmony assessment.

Automatic annotation accuracy was evaluated using three metrics:

1 Localization accuracy of seven key cephalometric points. The mean displacement σ of automatically detected points (x_j, y_j) from reference points (x_i, y_i) was used as the metric:

$$\sigma = \frac{1}{7\,N}\sum_{i,j=1}^{7}\sqrt{\left(x_j - x_i\right)^2 + \left(y_j - y_i\right)^2}.$$

2 Multi-class profile type classification accuracy. The fraction of incorrect decisions when assigning the profile to one of three classes (straight, convex, concave) was evaluated. The indicator P_{type} was used as the misclassification probability.

3 Binary profile harmony assessment accuracy P_{harm} was evaluated analogously as the fraction of incorrect answers when determining profile harmony.

Experiments were conducted with different sets of weighting coefficients governing the contributions of contour smoothing energy, balloon energy, and gradient energy. For each set, σ, P_{type}, and P_{harm} were computed (Table 1).

To assess the statistical robustness of results, 95% confidence intervals for classification indicators were constructed for each set of weighting coefficients. Since P_{type} and P_{harm} represent sample proportions at $N = 120$, the Wilson score interval was applied for interval estimation (preferred over the normal approximation for small samples and extreme proportion values):

$$CI_{95\%}(\hat{p}) = \frac{\hat{p}+\frac{z^2}{2N}\pm z\sqrt{\frac{\hat{p}(1-\hat{p})}{N}+\frac{z^2}{4N^2}}}{1+\frac{z^2}{N}}, \qquad z = 1.96.$$

The anomalous result in row 2 ($P_{harm} = 0.97$ despite $P_{type} = 0.11$) is explained by the increased smoothing coefficient $E_{con} = 0.02$: the higher contour stiffness preserves major extrema (nose tip, chin, forehead) used for profile type assessment, but suppresses the smaller lip-vertex extrema (A_2, A_3) critical for Ricketts line computation, leading to systematic failure of harmony assessment.

A statistically significant negative result is $P_{harm} = 0.97$ with confidence interval [0.922; 0.989]. For this parameter set, profile harmony is incorrectly determined in almost all cases, since the confidence interval lies entirely in the region of high errors.

Values $P_{type} = 0.02$ и $P_{harm} = 0.03$ were obtained with optimal coefficient selection. In this case, the upper bound of the confidence intervals for both indicators does not exceed 0.08, which is clinically interpreted as acceptable accuracy for automated primary annotation tasks.

At relatively high coefficient values, the internal and external energies form a contour that may be insufficiently stable: localization accuracy σ for key cephalometric landmarks remains relatively high, while misclassification probabilities for profile type and harmony vary strongly depending on the balance between smoothing and gradient.

Table 1 Experimental results for different sets of weighting coefficients.

Values of the coefficients corresponding to the energy functions			**Localization accuracy**	**Probability of automatic misclassification / confidence interval**	
E_{con}	E_{bal}	E_{grad}	σ	P_{type} **[95% CI]**	P_{harm} **[95% CI]**
0.01	0.01	0.01	29.76	0.64 [0.551; 0.720]	0.12 [0.073; 0.190]
0.02	0.01	0.01	25.27	0.11 [0.066; 0.179]	0.97 [0.922; 0.989]
0.05	0.01	0.01	37.41	0.08 [0.044; 0.143]	0.86 [0.787; 0.911]
0.01	0.01	0.05	26.83	0.48 [0.393; 0.569]	0.09 [0.051; 0.155]
0.001	0.001	0.005	74.35	0.98 [0.936; 0.994]	0.23 [0.164; 0.313]
0.001	0.001	0.001	3.66	0.02 [0.006; 0.064]	0.03 [0.011; 0.078]

(a) (b) (c)

Fig. 2 Results of automatic processing of a profile photograph: (a) extracted soft-tissue contour (blue) with detected extrema – maxima (cyan dots) and minima (yellow dots); initial circular contour shown in red dashed line; (b) profile type assessment – lines through landmarks Gl, Sn, Pg (blue dots) with the computed angle φ; (c) Ricketts aesthetic line through the nose tip and pogonion with lip position (blue dots).

However, at optimal energy parameters, the error in detecting key landmarks becomes sufficiently small, the discrepancy between automatic and manual classification of profile type and harmony is minimal and clinically negligible. This means the method can be used for automated primary annotation of large datasets, preparation of training samples for neural network models, and as an auxiliary tool in clinical decision support systems in orthodontics (Fig. 2).

For reference, landmark localization errors reported for CNN-based methods on similar cephalometric tasks range from 1.5 to 6 px [11, 12], which is comparable to the $\sigma = 3.66$ px achieved by the proposed training-free variational approach.

7 Conclusion

The results obtained confirm the applicability of the proposed variational active contour method to the task of automated biomedical image processing of the soft-tissue facial profile. With optimal selection of the energy functional weighting coefficients, the algorithm achieves a mean displacement of key cephalometric landmarks $\sigma = 3.66$ px and misclassification probabilities for profile type and harmony not exceeding 0.03 – which is clinically interpreted as acceptable accuracy for primary automatic annotation systems.

From a clinical application perspective, the proposed method can be used to accelerate medical documentation, reduce the workload of the orthodontist during screening examinations, and for standardized preparation of annotated training datasets for the development of neural network models for cephalometric feature recognition. The ability to operate without prior training on annotated data distinguishes the proposed variational approach from dominant deep learning methods and makes it suitable for clinical institutions with limited archival data.

Future development of the method is promising in the direction of adaptive parameter tuning of active contours for image type and quality, integration with three-dimensional craniofacial models, and closer combination with deep learning methods – including within hybrid architectures combining variational segmentation and neural network classification of biomedical images.

The proposed method does not rely on dataset-specific training and operates on standard profile photographs with uniform background; its applicability to images with cluttered backgrounds or non-standard lighting may require adjustment of the gradient energy weight h.

Results obtained in similar biomedical segmentation tasks using CNN and hybrid DL models, as well as experience in localizing anatomical landmarks in craniofacial images, confirm the potential of integrating the variational approach with modern deep learning methods [11–13].

Disclosures

The authors declare no conflicts of interest in this paper.

References

1. I. V. Tokarevich, N. V. Korkhova, I. V. Moskaleva, L. V. Kipkaeva, T. V. Terekhova, D. V. Khandogiy, Yu.Ya. Naumovich, and S. S. Denisov, General Orthodontics, BSMU, Minsk (2015). ISBN: 978-985-567-355-3.[in Russian]
2. P. Farha, S. A. Arqub, and M. S. Ghoussoub, "Correlation between cephalometric values and soft tissue profile in class I and class II adult patients based on vertical patterns," Turkish Journal of Orthodontics 37(1), 36-43 (2024).
3. S. Pandey, S. Kapoor, S. Agarwal, and I. Shukla, "Evaluation of lip position in esthetically pleasing profiles using different reference lines: a photographic study," Journal of Indian Orthodontic Society 55(3), 261-269 (2021).
4. Y. Chen, P. Ge, G. Wang, G. Weng, and H. Chen, "An overview of intelligent image segmentation using active contour models," Intelligence & Robotics 3(1), 23–55 (2023).
5. F. Pierre, M. Amendola, C. Bigeard, T. Ruel, and P.-F. Villard, "Segmentation with Active Contours," Image Processing On Line 11, 120–141 (2021).
6. Z. Wang, N. Li, Q. Zhang, J. Wei, L. Zhang, and Y. Wang, "Directionally weakened diffusion for image segmentation using active contours," Frontiers in Applied Mathematics and Statistics 9, 1275588 (2023).
7. A. A. Memon, S. Soomro, M. T. Shahid, A. Munir, A. Niaz, and K. N. Choi, "Segmentation of Intensity-Corrupted Medical Images Using Adaptive Weight-Based Hybrid Active Contours," Computational and Mathematical Methods in Medicine 2020, 317415 (2020).
8. P. Viola, M. J. Jones, "Robust Real-Time Face Detection," International Journal of Computer Vision 57(2), 137–154 (2004).
9. V. Kazemi, J. Sullivan, "One millisecond face alignment with an ensemble of regression trees," in Proceedings of the IEEE conference on computer vision and pattern recognition, 1867-1874 (2014).
10. A. Joshi, M. S. Khan, A. Niaz, F. Akram, H. C. Song, and K. N. Choi, "Active contour model with adaptive weighted function for robust image segmentation under biased conditions," Expert Systems with Applications 175, 114811 (2021).
11. A. H. Jalalzadeh, M. H. Kamangar, "A Hybrid Super-Resolution Method for Medical Images Using Transfer Learning," Journal of Biomedical Photonics & Engineering 11(4), 040304 (2025).

12. B. A. R., V. K. R. S., and K. S. S., "The Implications of Varying Batch-Size in the Classification of Patch-Based Lung Nodules Using Convolutional Neural Network Architecture on Computed Tomography Images," Journal of Biomedical Photonics & Engineering 10(1), 010305 (2024).
13. I. Shchechkin, S. Rodimova, A. Mozherov, V. Elagin, N. Bobrov, V. Shcheslavsky, V. Zagainov, E. Zagaynova, and D. Kuznetsova, "Neural Networks for Medical Data Processing: Segmentation of Fluorescence Lifetime Imaging Microscopy," Journal of Biomedical Photonics & Engineering 11(3), 030304 (2025).

The Effect of Riboflavin and Blue Laser Irradiation on B16-F10 Melanoma Cell Death

Aigul K. Gilmutdinova*, Elena V. Iurova, Evgeniya V. Pogodina, Anna V. Khokhlova, Dmitry E. Sugak, and Yury V. Saenko
Federal State Budgetary Educational Institution of Higher Education “Ulyanovsk State University”,
42 L. Tolstoy str., Ulyanovsk 432017, Russian Federation

*e-mail: gilmutdinovaajjgul@gmail.com

Abstract. Riboflavin, a natural photosensitizer, is of significant interest for the development of low-toxicity photodynamic therapy (PDT) protocols. This study is focused on the evaluation of the cytotoxic effect and ionic imbalances in B16-F10 melanoma cells induced by riboflavin when irradiating with blue laser light (450 nm wavelength). The dynamics of cell death and changes in intracellular sodium, potassium, and calcium ion concentrations were analyzed with the use of fluorescence microscopy. At a riboflavin concentration of 50 μM under laser irradiation, the signal corresponding to early apoptotic features in B16-F10 cells increased by 2.2 times compared to the control group. The maximum increase associated with late apoptosis and necrosis was observed 6 h after exposure and exceeded the values of the control group by 1.61 times, whereas under combined treatment this effect was detected as early as 1 h after exposure (1.32 times relative to the control group). Analysis of ion homeostasis revealed that riboflavin treatment, particularly in combination with laser irradiation, led to an increase in intracellular Ca^{2+} levels (up to 1.9-fold relative to the control at 6 h after exposure). This was accompanied by an increase in Na^+ levels and a decrease in K^+ levels, with minimal K^+ values observed at 6 h after exposure (approximately 0.6 of the control level). Overall, the results demonstrate the photosensitizing activity of riboflavin and support its further investigation in photodynamic approaches for melanoma. The observed effects provide a basis for further investigation of riboflavin-mediated PDT in combination with other anticancer agents to enhance therapeutic efficacy.

Keywords: photodynamic therapy; riboflavin; B16-F10 melanoma; blue laser light; apoptosis; ion homeostasis.

Paper #9451 received 11 Dec 2025; revised manuscript received 03 Apr 2026; accepted for publication 01 May 2026; published online 30 Jun 2026. doi: 10.18287/JBPE26.12.020312.

1 Introduction

Modern treatment methods of malignant tumors, including surgery, chemotherapy, and radiotherapy, are often associated with pronounced side effects and the development of drug resistance. In recent years, more attention has been paid to minimally invasive and targeted approaches aimed at selectively destroying tumor cells with minimal damage to surrounding tissues [1, 2]. In this context, photodynamic therapy is considered as an alternative approach that minimizes systemic exposure and increases selectivity for tumor cells [3].

Photodynamic therapy (PDT) continues to attract attention as a safe and locally targeted antitumor therapy method that combines the use of a photosensitizer, light of a specific wavelength, and oxygen to generate reactive oxygen species (ROS). The efficacy of PDT is largely determined by the properties of the photosensitizer: its ability to accumulate in tumor cells selectively, photostability, and minimal toxicity to normal tissues.

Among natural photosensitizers, riboflavin (vitamin B_2) and its derivatives stand out due to their high biocompatibility and endogeneity. Riboflavin is a precursor of the coenzymes flavin mononucleotide (FMN) and flavin adenine dinucleotide (FAD), which are involved in mitochondrial redox processes, reducing the risk of long-term toxicity [4]. FMN often functions as a cofactor in membrane-bound flavoproteins (i.e., it is embedded in a protein complex), and such complexes are localized near membranes and enzymatic electron transfer centers [5]. The localization of flavin cofactors near membrane proteins creates a “spot” formation of ROS near the lipid layer, which increases the probability of damage to membrane components during photosensitization [6]. Under the influence of blue light, flavins effectively generate ROS, including singlet oxygen and superoxide, causing damage to cellular structures and inducing a phototoxic effect [7].

Cutaneous melanoma, one of the most aggressive forms of tumors, exhibits high metastatic activity and resistance to systemic therapies which makes localized therapies particularly important [8]. Riboflavin-based photodynamic therapy (PDT) for melanoma seems to be a promising treatment method: low systemic toxicity, selective tumor targeting, and potential for combination with other therapeutic approaches provide the basis for treatment optimization [9].

Despite progress in studying the photodynamic properties of riboflavin, the effect of photosensitizer concentration on the efficacy of PDT for melanoma remains understudied. There is also limited data on how photodynamic action of riboflavin influences intracellular ion homeostasis – the concentrations of Ca^{2+}, K^+, and Na^+, which play a key role in regulating apoptosis and necrosis. Understanding these relationships will not only help to clarify the mechanisms of phototoxicity but also optimize PDT parameters to increase its selectivity and therapeutic potential. Therefore, this study aims to evaluate the relationship between the photodynamic efficacy of riboflavin and its concentration and analyze the associated changes in ionic balance in melanoma cells. Unlike most studies focused primarily on the general phototoxicity of riboflavin, the present work provides a time-resolved analysis of the relationship between apoptosis- and PI-associated signals and changes in Na^+-, K^+-, and Ca^{2+}-associated fluorescence in B16-F10 melanoma cells following photoactivation of riboflavin with blue light. In addition, intracellular ROS generation was assessed to further support the photodynamic mechanism of action.

2 Methods and Materials

B16-F10 murine melanoma cell culture was used in the experiments. Cells were obtained from the American Type Culture Collection (ATCC).

The experimental scheme is illustrated in Fig. 1.

Murine melanoma B16-F10 cells were cultured in a Sanyo MCO-18AIC incubator (Helicon, Japan) at 37 °C in a humidified atmosphere containing 5% CO_2. Cells were maintained in RPMI-1640 medium (PanEco, Russia) supplemented with 10% fetal bovine serum (Biosera, France) and 80 mg/L gentamicin (PanEco, Russia). One day prior to the experiment, cells were seeded into 8-well chamber slides (SPL Lifesciences, South Korea) at a density of 5×10^4 cells per well.

2.1 Experimental Design

The following experimental groups were established:

- Control – cells without riboflavin and without laser irradiation;
- IR – cells exposed to laser irradiation only;
- RBF – cells treated with riboflavin only;
- IR + RBF – cells treated with riboflavin followed by laser irradiation.

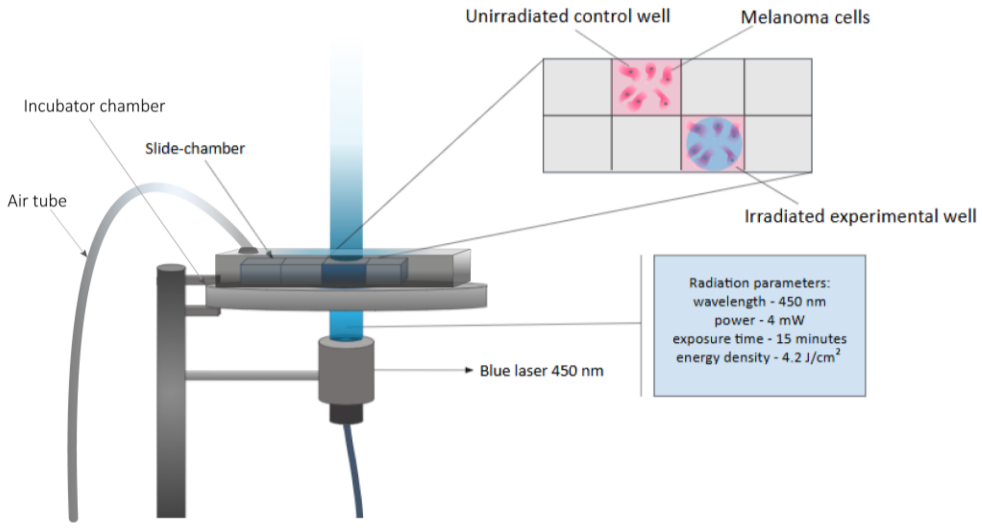

Fig. 1 Experimental scheme.

2.2 Laser Irradiation

Irradiation was carried out in a UNO H501-T benchtop incubator (Okolab, Italy) under standard culture conditions. Cells were irradiated using a 450 nm laser diode (MDL-111-450, Changchun New Industries Optoelectronics Tech, China) with an output power of 4 mW. The irradiation time was 15 min, corresponding to an energy density of 4.2 J/cm^2 over an exposed area of 0.857 cm^2.

The energy density (E, J/cm^2) was calculated as:

$$E = (P \times t) / S,$$

where P is the output power (W), t is the irradiation time (s), and S is the exposed area (cm^2).

2.3 Fluorescence Microscopy and Image Analysis

Fluorescence images were acquired using a Nikon Ti-S (Nikon Corporation, Tokyo, Japan) inverted microscope. Image analysis was performed using ImageJ software (NIH, USA).

Quantitative analysis was based on the corrected total cell fluorescence (CTCF) parameter.

For each experimental group, three fields of view were analyzed per experiment. For each field, paired images were acquired: a brightfield image to define cell boundaries and the corresponding fluorescence image.

Brightfield and fluorescence images were overlaid to ensure accurate alignment of cell contours with fluorescence signals. Cell boundaries were manually delineated as regions of interest (ROI) based on visible cell contours. A total of 50 cells were analyzed per field of view, resulting in 150 analyzed cells per group.

For each ROI, the following parameters were measured: area and integrated density.

Background fluorescence was determined individually for each field of view by selecting five regions devoid of cells and calculating the mean background intensity.

CTCF was calculated using the following Eq.:

$$CTCF = ID - (A \times B),$$

where $CTCF$ is the corrected total cell fluorescence; ID is the integrated density; A is the area of the selected region of interest (ROI); and B is the mean background fluorescence of the corresponding microscopic field. Fluorescence values were normalized to the control group and expressed in relative units.

2.4 Selection of Riboflavin Concentration

A preliminary experiment was performed to determine the working concentration of the photosensitizer. Riboflavin in the form of flavin mononucleotide (Pharmstandard -UfaVITA, Russia) was applied at concentrations of 10, 50, and 100 μM. After 24 h of culture, the medium was replaced with fresh medium containing riboflavin, and cells were incubated for 90 min in the dark. Subsequently, cells were washed with phosphate-buffered saline (PBS, pH 7.4). These measurements correspond to a preliminary concentration-dependent experiment (3 h time point).

Cell death was assessed 3 h after treatment using Yo-PRO-1 and propidium iodide (PI) at a final concentration of 1 μM each.

2.5 Dynamics of Cell Death

Cell death was evaluated using the fluorescent dyes Yo-PRO-1 and propidium iodide (PI) at a final concentration of 1 μM each. Measurements were performed at 1, 6, and 18 h after irradiation. Cells positive for Yo-PRO-1 staining were classified as early apoptotic cells, whereas PI-positive cells were considered to have compromised plasma membrane integrity, corresponding to late apoptosis or necrosis.

2.6 Assessment of Intracellular ROS Levels

Intracellular reactive oxygen species (ROS) levels were evaluated using the fluorescent probe 2′,7′-dichlorodihydrofluorescein diacetate (DCFH-DA). Cells were incubated with DCFH-DA at a final concentration of 10 μM for 30 min at 37 °C in the dark. After incubation, cells were washed with phosphate-buffered saline (PBS, pH 7.4) to remove excess probe.

Fluorescence measurements were performed immediately after photodynamic treatment and 3 h later.

Fluorescence images were acquired using a Nikon Ti-S (Nikon Corporation, Tokyo, Japan) inverted microscope under identical acquisition settings for all experimental groups. Quantitative analysis was performed using ImageJ software (NIH, USA) based on the CTCF parameter, as described below.

2.7 MTT Assay

After irradiation, the medium was removed and replaced with an equal volume of fresh pre-warmed culture medium. Cells were incubated for 3 h in a humidified CO_2 incubator at 37 °C. After this incubation period, the medium was removed and replaced with 100 μL of fresh warm medium containing 10 μL of MTT solution (5 mg/mL; PanEco, Russia). Cells were additionally incubated for 3 h at 37 °C in a CO_2 incubator.

After incubation, 100 μL of solubilization solution was added to each well to dissolve intracellular formazan crystals. The solubilization solution consisted of 99.4 mL dimethyl sulfoxide (Helicon, Russian Federation), 0.6 mL glacial acetic acid (Ecos-1, Russia), and 10 g sodium dodecyl sulfate (PanEco, Russian Federation). The contents of the wells were then aspirated and transferred to a 96-well plate. Absorbance was measured using a Multiskan FC plate reader (Thermo Scientific, USA) at 620 nm. Cell viability in each well was calculated relative to the absorbance value of the control group, followed by graphical presentation of the data.

2.8 LDH Assay

After irradiation, the medium was removed and replaced with an equal volume of fresh pre-warmed culture medium. Cells were incubated for 3 h in a humidified CO_2 incubator at 37 °C. After incubation, the culture medium from each well was collected into precooled microcentrifuge tubes and centrifuged for 10 min at 1500 × g. The supernatant was transferred into fresh precooled tubes.

After medium removal, 500 μL of cold PBS was added to each well, collected into microcentrifuge tubes, and centrifuged for 5 min at 1500 rpm. The supernatant was discarded. Then, 100 μL of lysis buffer (Cloud-Clone Corp., China) was added to each well, and the plate was additionally incubated for 30 min at room temperature. The lysates were collected into tubes containing the cell pellet and centrifuged for 30 min at 1500 × g. Then, 90 μL of the resulting supernatant was diluted in 360 μL of cold PBS.

LDH concentration was measured using an ERBA XL-100 biochemical analyzer (Erba Lachema, Czech Republic) with a Lactate Dehydrogenase-P kit (Erba Lachema, Czech Republic). The data were calculated as the concentration of LDH released into the medium relative to the LDH concentration in the corresponding cell lysate.

2.9 Intracellular Ion Levels

Intracellular ion levels were evaluated using the fluorescent dyes Rhod-2 AM, ION NatriumGreen 2 AM, and ION PotassiumGreen 2 AM at a final concentration of 1 μM each. Measurements were performed at 1, 6, and 18 h after irradiation. Fluorescence intensity of ion-sensitive dyes was interpreted as a relative indicator of changes in intracellular Ca^{2+}, Na^{+}, and K^{+} levels rather than a direct quantitative measurement of absolute ion concentrations.

2.10 Statistical Analysis

All experiments were performed in at least three independent replicates. Statistical analysis was carried out using Microsoft Excel. Differences between groups were evaluated using the Mann–Whitney *U*-test. Results were considered statistically significant at $p \leq 0.05$.

3 Results

3.1 Selection of Riboflavin Concentration

Incubation of B16-F10 murine melanoma cells with the photosensitizer riboflavin showed a direct relationship between riboflavin concentration and the level of apoptosis (Fig. 2(a)).

As follows from Fig. 2(a), there is a noticeable The data presented in Fig. 2(b) show that B16-F10 cells treated with riboflavin at concentrations of 10, 50, and 100 μM and exposed to laser irradiation exhibited an increased level of apoptotic cells, with the maximum observed at a concentration of 50 μM (2.2-fold higher than in the control group).

Figure 3 presents the results of the study examining the effects of riboflavin and laser irradiation on necrotic cell death in B16-F10 melanoma cells.

A comparative analysis showed that the level of necrosis in cells treated with riboflavin at a concentration of 10 μM and exposed to laser irradiation was significantly lower than in the corresponding non-irradiated group. The CTCF values for incubation with riboflavin at concentrations of 50 and 100 μM in the study groups did not differ significantly.

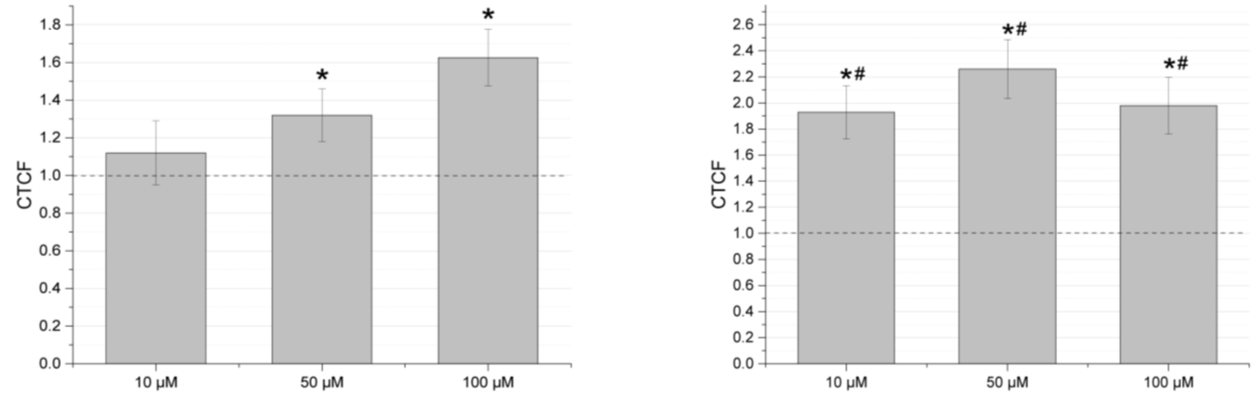

(a) (b)

Fig. 2 (a) Effect of riboflavin concentration on apoptosis in B16-F10 melanoma cells. (b) Effect of riboflavin concentration combined with laser irradiation (450 nm, 4.2 J/cm²) on apoptosis in B16-F10 melanoma cells 3 h after exposure. Fluorescence intensity is presented as corrected total cell fluorescence (CTCF) normalized to the control group. * $p < 0.05$ vs control; # $p < 0.05$ vs irradiated group.

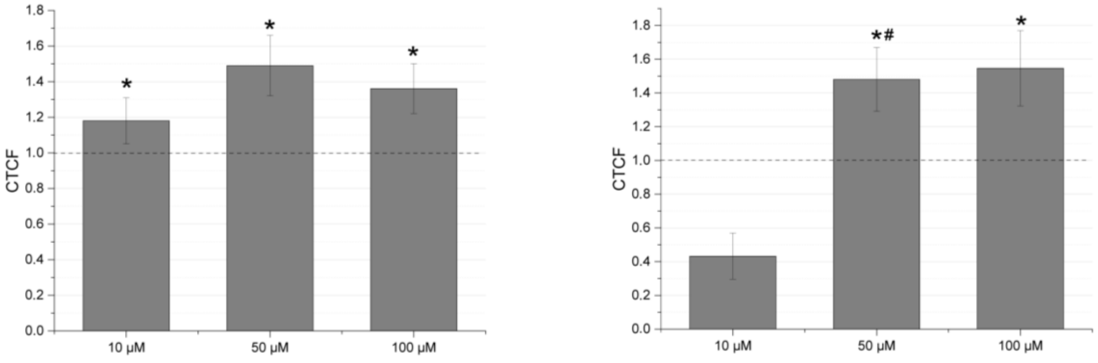

(a)   (b)

Fig. 3 (a) Effect of riboflavin concentration on necrosis in B16-F10 melanoma cells. (b) Effect of riboflavin concentration combined with laser irradiation (450 nm, 4.2 J/cm²) on necrosis in B16-F10 melanoma cells 3 h after exposure. Fluorescence intensity is presented as corrected total cell fluorescence (CTCF) normalized to the control group. * $p < 0.05$ vs control; # $p < 0.05$ vs irradiated group.

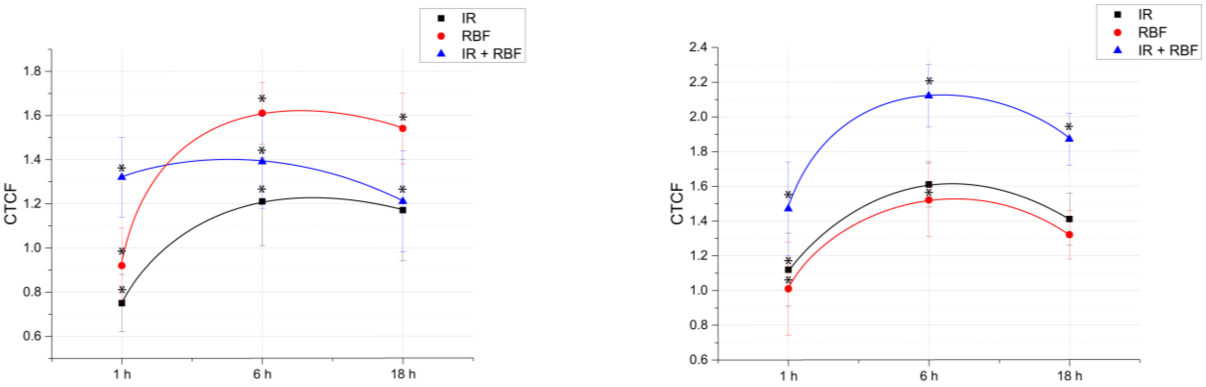

(a)   (b)

Fig. 4 Dynamics of cell death in B16-F10 melanoma cells at 1, 6, and 18 h after treatment. (a) Apoptosis. (b) Necrosis. Fluorescence intensity is presented as corrected total cell fluorescence (CTCF) normalized to the control group. IR – laser irradiation (450 nm, 4.2 J/cm²); RBF – riboflavin (50 µM); IR+RBF – combined treatment with riboflavin and laser irradiation. * $p < 0.05$ compared with the control group.

3.2 Dynamics of Cell Death

Figure 4 shows the dynamics of cell death in B16-F10 melanoma cells.

In all experimental groups, an increase in cell death was observed 6 h after treatment, followed by a decrease by 18 h.

Analysis of apoptotic cell death in melanoma cells showed that the highest levels were observed in the combined treatment group, reaching a maximum of 2.12-fold at 6 h after treatment. In the single-treatment groups, CTCF values varied only slightly throughout the observation period.

Analysis of necrotic cell death showed that the highest level was observed in the riboflavin group, reaching the value of 1.61 higher relative to the control group at 6 h. Laser irradiation alone did not result in significant changes. In contrast, combined treatment induced earlier necrotic cell death: at 1 h after treatment, CTCF levels were 1.32 times higher than in the control group, while remaining lower in the other experimental groups.

These results indicate that the combined treatment with riboflavin and laser irradiation enhances cell death and accelerates the onset of necrotic processes.

3.3 Intracellular ROS Generation

As shown in Fig. 5, the results showed that immediately after exposure, the level of reactive oxygen species in the laser irradiation group was 1.46 relative to the control, while in the riboflavin group it was 1.20. The combined exposure to laser irradiation and riboflavin led to the most pronounced increase in reactive oxygen species levels, reaching 1.84 relative to the control.

At 3 h after exposure, an increase in reactive oxygen species levels was also observed under combined exposure, reaching 1.39 relative to the control. The combined exposure to laser irradiation and riboflavin was observed to enhance the generation of reactive oxygen species, which is consistent with a photodynamic mechanism of action.

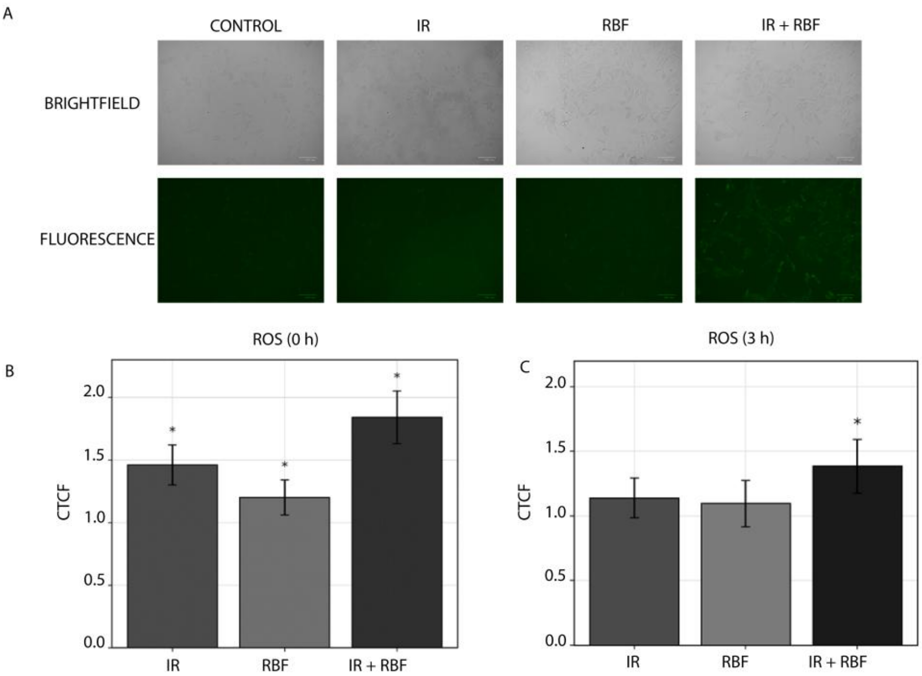

Fig. 5 Intracellular reactive oxygen species (ROS) levels in B16-F10 melanoma cells after photodynamic treatment. (A) Representative brightfield and fluorescence images of B16-F10 melanoma cells. The upper row shows brightfield images, and the lower row shows fluorescence corresponding to intracellular ROS detected using the DCFH-DA probe. Images were obtained immediately after treatment. (B) Intracellular ROS levels immediately after treatment. (C) Intracellular ROS levels 3 h after treatment. Fluorescence intensity is presented as corrected total cell fluorescence (CTCF) normalized to the control group. Data are presented as mean ± SD. Experimental groups: Control – untreated cells; IR – laser irradiation (450 nm, 4.2 J/cm²); RBF – riboflavin (50 µM); IR+RBF — combined treatment with riboflavin and laser irradiation. * $p < 0.05$ compared with the control group.

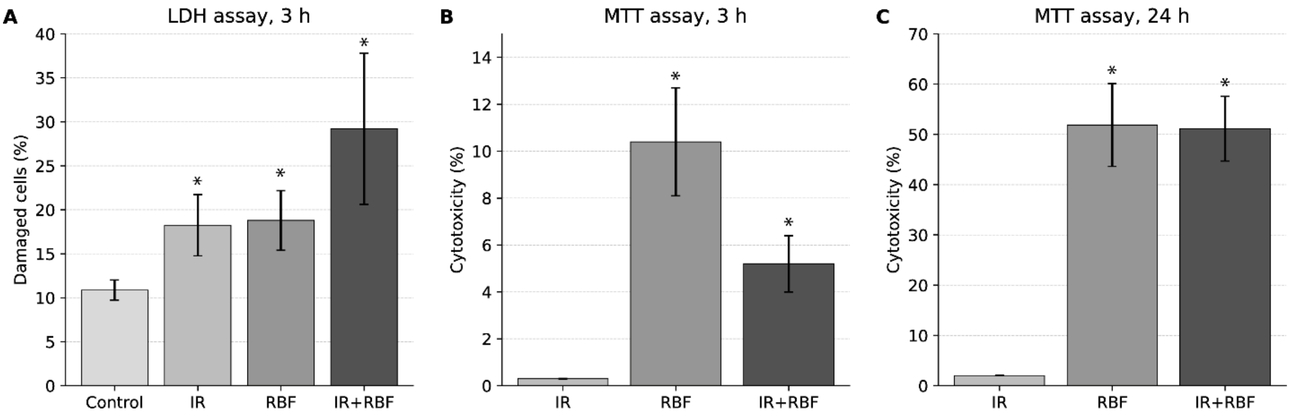

Fig. 6 Assessment of membrane damage and metabolic activity in B16-F10 melanoma cells after photodynamic treatment. (A) LDH assay, 3 h, (B) MTT assay, 3 h, (C) MTT assay, 24 h. The LDH assay reflects membrane integrity, whereas the MTT assay evaluates cellular metabolic activity. Data are presented as mean ± SD. IR – laser irradiation (450 nm, 4.2 J/cm²); RBF – riboflavin (50 µM); IR+RBF – combined treatment with riboflavin and laser irradiation. * $p < 0.05$ compared with the control group.

3.4 Membrane Damage and Metabolic Activity

The effects of photodynamic treatment on membrane integrity and metabolic activity of B16-F10 melanoma cells were assessed using LDH and MTT assays (Fig. 6).

At 3 h after treatment, the LDH assay demonstrated an increased proportion of damaged cells in all experimental groups compared with the control group. The highest level of membrane damage was observed in the group with combined exposure to laser irradiation and riboflavin (29.21%), while the laser irradiation group and the riboflavin group showed comparable values (18.25% and 18.79%, respectively) relative to the control group (10.87%).

According to the MTT assay, decrease in metabolic activity at 3 h remained low in all groups, reaching 0.3% in the laser irradiation group, 10.4% in the riboflavin group, and 5.2% in the group with combined exposure.

At 24 h, a pronounced decrease in metabolic activity was observed in the riboflavin group (51.87%) and in the group with combined exposure (51.15%), whereas the laser irradiation group showed only minimal changes (2.01%).

3.5 Changes in Intracellular Sodium Levels

Figure 7 shows the dynamics of changes in intracellular sodium levels in B16-F10 melanoma cells. High sodium levels were observed in the experimental groups 6 h after exposure (up to ~2.6 times in the RBF group and ~2.0 times in the IR+RBF group relative to the control group). However, the values in the group exposed only to riboflavin were significantly higher than in both the combined treatment group and the laser irradiation group. After 18 h, a decrease in sodium levels was observed in all study groups, approaching ~1.1–1.3-times relative to the control group.

3.6 Changes in Intracellular Calcium Levels

Changes in intracellular calcium levels are presented in Fig. 8. Figure 8 shows changes in intracellular calcium levels in the B16-F10 cell culture at 1, 6, and 18 h after exposure. Exposure to the photosensitizer, both alone and in combination with laser irradiation, results in a marked increase in calcium levels, reaching ~1.6 times higher at 1 h and peaking at ~1.9–2.0 at 6 h relative to the control group. Calcium levels then remain elevated but begin to decline by 18 h (~1.4–1.6-fold). In the group exposed only to laser irradiation, minimal changes in calcium levels were observed at all-time intervals studied (~0.8–0.9 times relative to the control group).

3.7 Changes in Intracellular Potassium Levels

As shown in Fig. 9, a significant decrease in potassium levels was observed 6 h after exposure in all study groups (to ~0.7–0.8 times higher relative to the control group). In the groups exposed to laser irradiation or riboflavin, a further decrease in potassium levels was observed after 18 h (to ~0.6–1.1-fold). In contrast, in the group that received the combined treatment, potassium levels increased by 18 h (~1.2–1.3-fold) and remained the highest among all study groups.

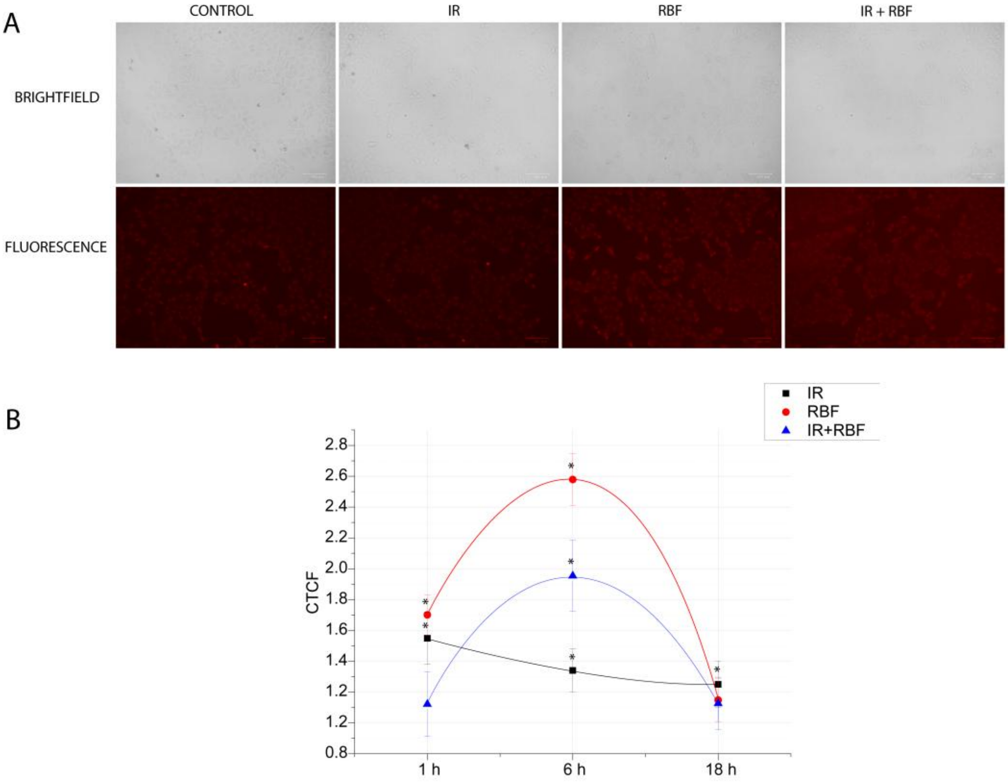

Fig. 7 Intracellular sodium dynamics in B16-F10 melanoma cells after photodynamic treatment. (A) Representative brightfield and fluorescence images of B16-F10 cells in the Control, IR, RBF, and IR+RBF groups. The upper row shows brightfield images, and the lower row shows fluorescence corresponding to intracellular sodium levels. Images were obtained 1 h after treatment. (B) Time-dependent changes in intracellular sodium levels at 1, 6, and 18 h after treatment. Fluorescence intensity is presented as corrected total cell fluorescence (CTCF) normalized to the control group. Data are presented as mean ± SD. IR – laser irradiation (450 nm, 4.2 J/cm^2); RBF – riboflavin (50 μM); IR+RBF – combined treatment with riboflavin and laser irradiation. * $p < 0.05$ compared with the control group.

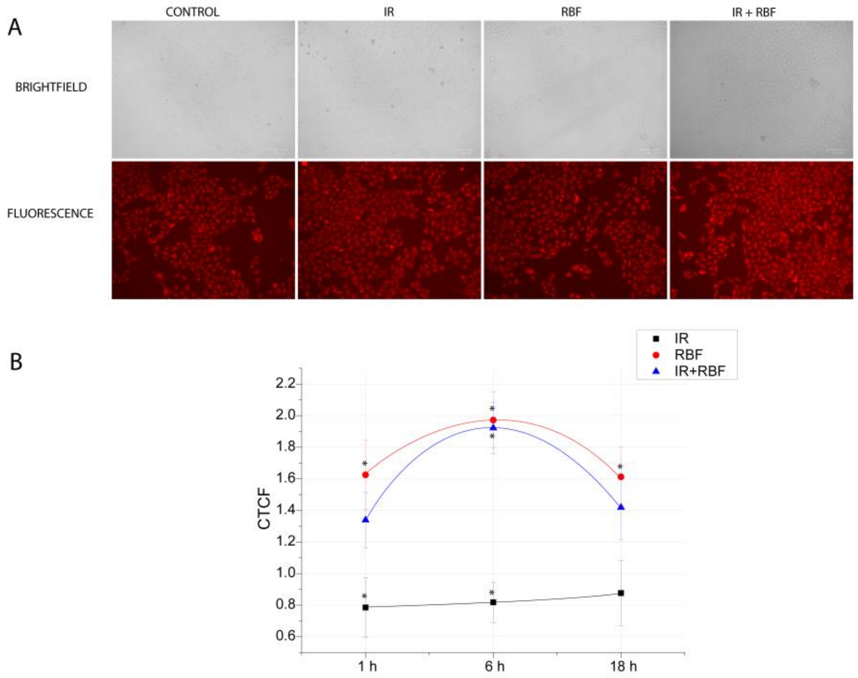

Fig. 8 Intracellular calcium dynamics in B16-F10 melanoma cells after photodynamic treatment. (A) Representative brightfield and fluorescence images of B16-F10 cells in the Control, IR, RBF, and IR+RBF groups. The upper row shows brightfield images, and the lower row shows fluorescence corresponding to intracellular calcium levels. Images were obtained 1 h after treatment. (B) Time-dependent changes in intracellular calcium levels at 1, 6, and 18 h after treatment. Fluorescence intensity is presented as corrected total cell fluorescence (CTCF) normalized to the control group. Data are presented as mean ± SD. IR – laser irradiation (450 nm, 4.2 J/cm^2); RBF – riboflavin (50 µM); IR+RBF – combined treatment with riboflavin and laser irradiation. * $p < 0.05$ compared with the control group.

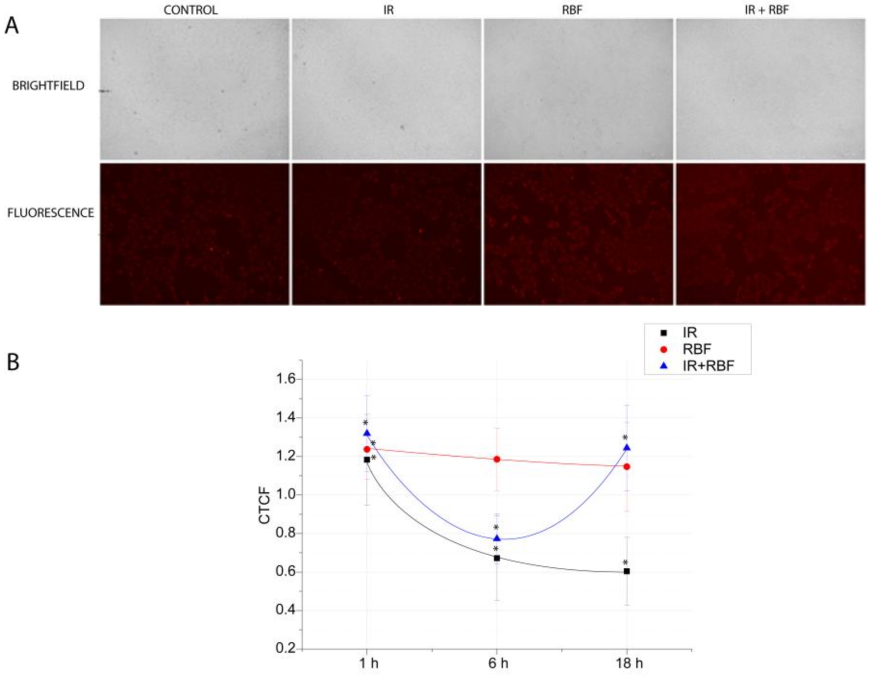

Fig. 9 Intracellular potassium dynamics in B16-F10 melanoma cells after photodynamic treatment. (A) Representative brightfield and fluorescence images of B16-F10 cells in the Control, IR, RBF, and IR+RBF groups. The upper row shows brightfield images, and the lower row shows fluorescence corresponding to intracellular potassium levels. Images were obtained 1 h after treatment. (B) Time-dependent changes in intracellular potassium levels at 1, 6, and 18 h after treatment. Fluorescence intensity is presented as corrected total cell fluorescence (CTCF) normalized to the control group. Data are presented as mean ± SD. IR – laser irradiation (450 nm, 4.2 J/cm^2); RBF – riboflavin (50 µM); IR+RBF – combined treatment with riboflavin and laser irradiation. *$p < 0.05$ compared with the control group.

4 Discussion

In this study, using the B16-F10 cell line model, we demonstrated the significant cytotoxic activity of riboflavin in combination with blue laser irradiation ($\lambda = 450$ nm, $E = 4.2$ J/cm²) and identified key features associated with changes in ion homeostasis and the temporal dynamics of apoptosis/necrosis.

In the vast majority of studies, free riboflavin (and related water-soluble flavins FMN, FAD, and derivatives) exhibit little or no cytotoxicity in the dark at typical concentrations used for photo-dynamics – most cell death occurs upon photo-activation [10, 11]. Our results demonstrate that riboflavin induces apoptosis and necrosis in B16-F10 cells in the absence of laser photo-activation, indicating its dark toxicity starting at a concentration of 10 µM. These data are inconsistent with the results previously published by Insińska-Rak et al., who found no cytotoxicity at concentrations up to 50 µM [12], as well as with data by Akasov et al., who reported the safety of riboflavin up to 100 µM [13], and other studies [14]. This may be associated with the participation of riboflavin in metabolic processes and the ability to oxidize and reduce partially the effect on intracellular structures.

The effectiveness of a photosensitizer in PDT directly depends on its concentration. At moderate doses, ROS generation occurs at levels sufficient to trigger caspase-dependent apoptosis, but insufficient to cause uncontrolled damage to cell membranes and organelles. At high concentrations, excessive ROS generation is observed, leading to photo-destruction, decreased selectivity, and a switch to a necrotic cell death pathway [15]. In our experiments, photo-activation with blue laser radiation significantly enhanced apoptotic processes, with the maximum effect achieved at 50 µM riboflavin, after which a decrease in apoptosis and necrosis became predominant at 100 µM. These data are consistent with the results on the effect of flavin mononucleotide in melanoma cell lines, where IC_{50} were in the range of ~10–30 µM under 450 nm irradiation [13], and the peak of necrosis was noted at 100 µM. Thus, a concentration of 50 µM can be considered optimal, since at this concentration apoptosis dominates over necrosis, which is preferable from a therapeutic point of view [16].

The temporal dynamics of cell death (at 50 µM riboflavin) reveals additional details. The peak of cell death for all groups is observed approximately 6 h after treatment, especially apoptosis with combined exposure, which correlates with the mechanisms of photodynamic therapy, in which ROS generation and organelle damage trigger caspase-dependent pathways within the first few hours after irradiation [17]. The early phase of necrosis observed in our data indicates rapid oxidative damage to membranes, which leads to a necrotic outcome even before apoptosis. A higher proportion of necrotic cells in the group treated with riboflavin without irradiation indicates the predominance of disordered forms of cell death, most likely associated with redox stress and direct membrane damage. With photodynamic exposure, a redistribution towards apoptosis is observed, which is consistent with a caspase-dependent mechanism and singlet oxygen generation. One can assume that photo-activation of riboflavin not only enhances its cytotoxicity but also shifts the cellular response from a necrotic to an apoptotic state. The decrease in the apoptotic fraction by 18 h probably reflects either the further transformation of apoptosis into late necrosis or the removal of apoptotic bodies from the culture and the inability to detect them with a fluorescent dye [18].

Our data show that melanoma cells treated with riboflavin, laser irradiation, and their combination undergo significant changes in ion concentration, suggesting profound ion dysregulation as part of the cellular response. This dysregulation includes Na^+ influx, K^+ efflux or reorganization, and Ca^{2+} overload or reduction, depending on the type of treatment and time point. The observed maximum change in the concentration of most ions at ~6 h after treatment is consistent with the temporal concept of the photodynamic response: the initial phase (1 h) is characterized by early disruption of membrane barrier function; by 6 h, ROS-mediated damage to organelles and channels accumulates and apoptotic mechanisms are triggered; and by 18 h, either compensatory mechanisms are activated or cell death occurs.

A significant increase in intracellular Na^+ is observed with both non-irradiated and irradiated riboflavin treatment, particularly pronounced by 6 h. This effect may be caused by ROS-mediated membrane damage and decreased Na^+/K^+ ATPase activity, which increases Na^+ permeability, disrupts ionic balance, and promotes cell stress and death. This mechanism is supported by experimental data, where an increase in Na^+ inside tumor cells led to their death [19].

One hour after treatment with riboflavin and the combined exposure, a moderate increase in intracellular K^+ is observed, reflecting the early adaptive activity of K^+ channels and an attempt to maintain homeostasis. At the point of 6 h, coinciding with the peak of apoptosis and necrosis, a sharp decrease in K^+ and a simultaneous increase in Na^+ are observed. A drop in K^+ facilitates the activation of caspases and the implementation of apoptosis, and an increase in Na^+ reflects a disruption in membrane permeability and a compensatory response to osmotic imbalance, which may also indicate partial necrotic cell damage [20, 21].

With riboflavin, and especially with combined exposure, a significant increase in intracellular Ca^{2+} (up to 1.9 by 6 h) was also observed. ROS-mediated damage to the endoplasmic reticulum and mitochondria can cause the release of Ca^{2+} from internal stores or enhance its entry from the outside through channels, consistent with the dynamics of K^+ and Na^+. This is confirmed by reviews on melanoma, where calcium signaling plays a key role in apoptosis and the vulnerability of melanoma cells, as well as in the control of the stress response and drug sensitivity [22]. With exposure of laser alone, Ca^{2+} decreased (up to 0.8 times), which may indicate the activation of compensatory mechanisms, such as increased extrusion of Ca^{2+} or limitation of release from stores. Modern approaches to photodynamic therapy for melanoma confirm a direct link between ROS generation, Ca^{2+} changes and cell death [23, 24].

By 18 h of combined exposure, K^+ levels are restored above baseline values, and Na^+ levels stabilize, indicating the survival of some cells and restoration of ionic balance. In general, the dynamics of Na^+, K^+, and Ca^{2+} may reflect the following sequence: early adaptation → apoptotic/necrotic phase with a decrease in K^+ and an increase in Na^+, and an increase in Ca^{2+} → recovery of some cells and restoration of ionic homeostasis.

The obtained results on intracellular ROS levels, as well as MTT and LDH assays, further support the proposed mechanisms of photodynamic action. The pronounced increase in ROS generation observed immediately after combined treatment confirms the key role of oxidative stress in initiating cell death. The LDH assay demonstrated early membrane damage at 3 h, particularly in the combined treatment group, indicating disruption of membrane integrity under photodynamic conditions. At the same time, the MTT assay showed a delayed decrease in metabolic activity, with a marked increase in cytotoxicity at 24 h, especially in the riboflavin and combined treatment groups. This suggests that metabolic impairment develops progressively following the initial oxidative and membrane damage. Together, these findings indicate that photodynamic exposure induces a cascade of events including ROS generation, membrane disruption, and subsequent loss of cellular metabolic activity.

5 Conclusion

This study demonstrates that riboflavin exhibits photosensitizing activity in B16-F10 melanoma cells and enhances cytotoxic effects upon blue laser irradiation. In addition, measurable cytotoxicity was observed in the absence of irradiation, which should be interpreted with caution and may depend on specific experimental conditions.

The combined use of riboflavin and laser irradiation was associated with increased ROS generation and disruption of ion homeostasis, including alterations in Na^+, K^+, and Ca^{2+} levels, which is consistent with enhanced cell death.

These findings suggest that riboflavin-mediated photodynamic treatment may contribute to cytotoxic effects in melanoma cells and provide a basis for further investigation of its potential application in combination with other therapeutic strategies.

Acknowledgments

This work was done under the financial support of the Ministry of Science and Higher Education of the Russian Federation (Project No. FEUF-2025-0001 (125041105147-5)).

Disclosures

All authors declare that there is no conflict of interest in this paper.

References

1. R. Kaur, A. Bhardwaj, and S. Gupta, “Cancer treatment therapies: traditional to modern approaches to combat cancers,” Molecular Biology Reports 50(11), 9663–9676 (2023).
2. D. T. Michaeli, J. C. Michaeli, and T. Michaeli, “Advances in cancer therapy: clinical benefit of new cancer drugs,” Aging 15(12), 5232–5234 (2023).
3. Y. Allamyradov, J. Ben Yosef, B. Annamuradov, M. Ateyeh, C. Street, H. Whipple, and A. O. Er, “Photodynamic therapy review: past, present, future, opportunities and challenges,” Photochem 4(4), 434–461 (2024).
4. M. Insińska-Rak, M. Sikorski, and A. Wolnicka-Glubisz, “Riboflavin and its derivates as potential photosensitizers in the photodynamic treatment of skin cancers,” Cells 12(18), 2304 (2023).
5. P. Carpentier, F. Pierrel, N. Duraffourg, B. Guigliarelli, M. Hajj Chehade, L. Flandrin, C. Basset, C. Caux, S. Torelli, and V. Nivière, “Studies of the membrane-bound flavocytochrome MsrQ flavin mononucleotide (FMN)-binding site reveal an unexpected ubiquinone cofactor,” The FEBS Journal 292(20), 5491–5505 (2025).
6. A. Okamoto, S. Kalathil, X. Deng, K. Hashimoto, R. Nakamura, and K. H. Nealson, “Cell-secreted flavins bound to membrane cytochromes dictate electron transfer reactions to surfaces with diverse charge and pH,” Scientific Reports 4(1), 5628 (2014).
7. M. Insińska-Rak, M. Sikorski, “Riboflavin interactions with oxygen-a survey from the photochemical perspective,” Chemistry – A European Journal 20(47), 15280–15291 (2014).
8. M. Hsieh, S.-K. Hsu, T.-Y. Liu, C.-Y. Wu, and C.-C. Chiu, “Melanoma biology and treatment: a review of novel regulated cell death-based approaches,” Cancer Cell International 24(1), 63 (2024).
9. G. Gunaydin, M. E. Gedik, and S. Ayan, “Photodynamic therapy—current limitations and novel approaches,” Frontiers in Chemistry 9, 691697 (2021).
10. M.-Y. Yang, C.-J. Chang, and L.-Y. Chen, “Blue light induced reactive oxygen species from flavin mononucleotide and flavin adenine dinucleotide on lethality of HeLa cells,” Journal of Photochemistry and Photobiology B: Biology 173, 325–332 (2017).
11. A. V. Juarez, L. D. V. Sosa, A. L. De Paul, A. P. Costa, M. Farina, R. B. Leal, A. I. Torres, and P. Pons, “Riboflavin acetate induces apoptosis in squamous carcinoma cells after photodynamic therapy,” Journal of Photochemistry and Photobiology B: Biology 153, 445–454 (2015).

12. A. Wolnicka-Glubisz, A. Pawlak, M. Insinska-Rak, and A. Zadlo, "Analysis of photoreactivity and phototoxicity of riboflavin's analogue 3MeTARF," Journal of Photochemistry and Photobiology B: Biology 205, 111820 (2020).
13. R. A. Akasov, N. V. Sholina, D. A. Khochenkov, A. V. Alova, P. V. Gorelkin, A. S. Erofeev, A. N. Generalova, and E. V. Khaydukov, "Photodynamic therapy of melanoma by blue-light photoactivation of flavin mononucleotide," Scientific Reports 9(1), 9679 (2019).
14. S. Kacar, C. Hacioglu, and F. Kar, "Irradiated riboflavin over nonradiated one: Potent antimigratory, antiproliferative and cytotoxic effects on glioblastoma cells," Journal of Cellular and Molecular Medicine 28(8), e18288 (2024).
15. D. L. Sai, J. Lee, D. L. Nguyen, and Y.-P. Kim, "Tailoring photosensitive ROS for advanced photodynamic therapy," Experimental & Molecular Medicine 53(4), 495–504 (2021).
16. D. Machado, S. M. Shishido, K. C. S. Queiroz, D. N. Oliveira, A. L. C. Faria, R. R. Catharino, C. A. Spek, and C. V. Ferreira, "Irradiated riboflavin diminishes the aggressiveness of melanoma *in vitro* and *in vivo*," PLoS ONE 8(1), e54269 (2013).
17. P. Agostinis, K. Berg, K. A. Cengel, T. H. Foster, A. W. Girotti, S. O. Gollnick, S. M. Hahn, M. R. Hamblin, A. Juzeniene, D. Kessel, M. Korbelik, J. Moan, P. Mroz, D. Nowis, J. Piette, B. C. Wilson, and J. Golab, "Photodynamic therapy of cancer: An update," CA: A Cancer Journal for Clinicians 61(4), 250–281 (2011).
18. C. Saenz, M. Ethirajan, E. C. Tracy, M.-J. Bowman, J. Cacaccio, T. Ohulchanskyy, H. Baumann, and R. K. Pandey, "Charged groups on pyropheophorbide-based photosensitizers dictate uptake by tumor cells and photodynamic therapy efficacy," Journal of Photochemistry and Photobiology B: Biology 227, 112375 (2022).
19. N. Clemente, S. Baroni, S. Fiorilla, F. Tasso, S. Reano, C. Borsotti, M. R. Ruggiero, E. Alchera, M. Corrazzari, G. Walker, A. Follenzi, S. G. Crich, and R. Carini, "Boosting intracellular sodium selectively kills hepatocarcinoma cells and induces hepatocellular carcinoma tumor shrinkage in mice," Communications Biology 6, 574 (2023).
20. F. Lang, E. K. Hoffmann, "Role of ion transport in control of apoptotic cell death," Comprehensive Physiology 2(3), 2037–2061 (2012).
21. C. D. Bortner, J. A. Cidlowski, "Cell shrinkage and monovalent cation fluxes: Role in apoptosis," Archives of Biochemistry and Biophysics 462(2), 176–188 (2007).
22. H. Zhang, Z. Chen, A. Zhang, A. A. Gupte, and D. J. Hamilton, "The role of calcium signaling in melanoma," International Journal of Molecular Sciences 23(3), 1010 (2022).
23. W.-H. Chan, "Photodynamic treatment induces an apoptotic pathway involving calcium, nitric oxide, p53, p21-activated kinase 2, and c-Jun N-terminal kinase and inactivates survival signal in human umbilical vein endothelial cells," International Journal of Molecular Sciences 12(2), 1041–1059 (2011).
24. N. Sobhani, A. A. Samadani, "Implications of photodynamic cancer therapy: an overview of PDT mechanisms basically and practically," Journal of the Egyptian National Cancer Institute 33(1), 34 (2021).

Detritylation by Self-Contained Photoacid Generators on the Base of Substituted Benzo[b]thiophene-2-Carboxanilides under UV-Laser and Lamp Irradiation

Natalia V. Izmailova*, Lubov G. Samsonova, and Ruslan M. Gadirov
Tomsk State University of Control Systems and Radioelectronics, 40 Lenina av., Tomsk 634050, Russian Federation
*e-mail: nataliagoleinova@mail.ru

Abstract. New self-contained acid photogenerators based on substituted benzo[b]thiophene-2-carboxanilides were studied under irradiation with the 3rd harmonic of an Nd-YAG laser (355 nm) and an excimer XeCl lamp (308 nm) in toluene and methylene chloride solutions. The quantum yield of phototransformations of compounds during lamp and laser photolysis was estimated for both solvents. A model experiment was carried out using photogenerated acids to remove the dimethoxytrityl group from 5′-O-(4,4′-dimethoxytrityl)-2-deoxythymidine-3′-O-[O-(2-cyanoethyl)-N,N′-diisopropylphosphoramidite].

Keywords: acid photogenerators; 6π-electrocyclization; benzo[b]thiophene-2-carboxanilides; laser photolysis; detritylation.

Paper #9518 received 16 Feb 2026; revised manuscript received 26 Mar 2026; accepted for publication 31 Mar 2026; published online 28 May 2026. doi: 10.18287/JBPE26.12.020305.

1 Introduction

Many technological processes such as polymerization initiation, deprotection during oligonucleotide synthesis, production of polymer coatings, resins, adhesives, inks and others require the participation of acid at a certain stage. Photogenerated acids have been used for these purposes for decades. Compounds – Photoacid generators (PAGs) – undergo photochemical transformations when exposed to light, one of the products of which is acid. PAGs are divided into two broad classes: ionic and nonionic. Among the ionic PAGs, the most popular are the onium salts of diaryliodonium and triarylsulfonium, which contain strong acid anions as counterions. These complexes have been known for over a century and can vary significantly in stability and solubility [1]. They are widely used in photoinitiation of cationic polymerization of epoxy monomers and other cationically polymerizable monomers such as vinyl esters, as well as in the manufacture of photoresists, photocurable coatings, printing inks, and adhesives. However, the narrow spectral range for excitation and the limited range of organic solvents, especially non-polar ones, limit their application in other areas.

Non-ionic PAGs have also been known for decades. Nonionic PAGs are mostly esters, and the most popular among them are iminosulfonates, imidosulfonates and benzylsulfonates. When irradiated with light, they generate carboxylic, sulfonic, phosphoric, and hydrohalic acids. A review of both types of PAG can be found in Refs. [1–3].

To form a Brønsted acid, both ionic and nonionic PAGs extract a proton from a proton-donating environment. When working with aprotic solvents, such PAGs are ineffective.

In the last decade, scientists have turned their interest to so-called “self-contained” compounds that generate both acid ions when irradiated. Such compounds are characterized by 6π-electrocyclization initiated by light. The mechanism of photoacid formation is shown in Fig. 1. One of the first works on photogeneration of acid through photo-electrocyclic ring closure was carried out on benzothiophene carboxanilides [4] Compounds of the terarylene series are also promising [5–8]. In our previous work [9], we investigated a number of new compounds from the class of benzothiophene carboxanilides with various substituents in the benzothiophene moiety with the formation of hydrochloric, methanesulfonic, and toluenesulfonic acids in toluene solutions. 4,6-Bis[5-(9-ethyl-9H-carbazol-3-yl)thiophen-2-yl]pyrimidine (IND) was used as an acid indicator, which readily forms a protonated form, giving the solution a crimson color. The compounds were irradiated with the 3rd harmonic of an Nd-YAG laser with a wavelength of 355 nm.

This paper was presented at the XXIII All-Russian Samara Youth Competition and Conference on Optics, Laser Physics and Plasma Physics, Samara, Russian Federation, November 11 – 15, 2025.

In the present work, we expanded the set of PAGs and investigated them for deprotection of the dimethoxytrityl (DMT) group from 5′-O-(4,4′-dimethoxytrityl)-2′-deoxythymidine-3′-O-[O-(2-cyanoethyl)-N,N′-diisopropylphosphoramidite] (DMT-dT) which is commonly used in the phosphoramidite approach for oligonucleotide synthesis [10]. Two sources were used for irradiation: the 3rd harmonic of an Nd-YAG laser (355 nm) and an excimer XeCl lamp (308 nm). It should be noted that the excitation at 355 nm occurs in the red wing of the main absorption band far from the maximum, where the extinction coefficient is at best ~1000 $dm^3mol^{-1}cm^{-1}$, while the emission at 308 nm is close to the maximum of the absorption bands.

2 Experimental Part

The studied compounds were synthesized at the I. Ya. Postovsky Institute of Organic Synthesis, Ural Branch of the Russian Academy of Sciences and described in Ref. [9].

The structures of the molecules are shown in Fig. 1. Solutions of the compounds with a volume of 2 ml were irradiated in a standard quartz cuvette with a $Nd^{3+:}$YAG laser (type LQ529B, Solar Laser Systems, Republic of Belarus) with characteristics – 355 nm, 33 mJ/pulse, 0.17 J/cm^2, σ_{imp}=10 ns or an excimer XeCl lamp – 308 nm, type BD P (barrier discharge, portable). The excilamp has a cylindrical shape and is enclosed in a metal housing with an output UV window of 60 cm^2. The excilamp is developed at the Institute of High Current Electronics SB RAS [11–13]. The distance from the excilamp to the irradiated solution was 13 cm. The intensity of the incident radiation on the cuvette was 3 mW/cm^2. To record the absorption spectra, an AvaLight-DH light source and an AvaSpec 2048-2 spectrometer (Avantes V.B., Netherlands) were used, located perpendicular to the radiation source.

To confirm acid formation during photolysis, the pyrimidine derivative 4,6-Bis[5-(9-ethyl-9H-carbazol-3-yl)thiophen-2-yl]pyrimidine (further in the text IND) was used. The absorption bands of its neutral (420 nm) and protonated (530 nm) forms are spectrally well separated and do not overlap with the absorption of the photolysis products of the starting compounds.

Detritylation was performed in dichloromethane (DCM) solutions at PAGs concentrations of 10^{-3} mol/L and DMT-dT– 5×10^{-5} mol/L.

The quantum yield of the compound phototransformation in DCM is determined in the same way as in Ref. [9] using the following Eq.:

$$\gamma = \frac{N_{ph}}{N_{abs}}, \qquad (1)$$

where Nph is the number of molecules that have undergone phototransformation while $Nabs$ is the number of absorbed photons. Nph was determined by the decrease in the intensity of the main absorption band at the initial stage of photolysis when the absorption of photoproducts in this region is negligible:

$$N_{ph} = \frac{(D_0 - D)\times C_0 NV}{D_0 \times 10^3}, \qquad (2)$$

where D_0 and D are the optical density of the solution before and after irradiation, C_0 is the initial concentration of the compounds (in our case, $C_0=10^{-4}$ mol L^{-1}), N is the Avogadro constant, V is the irradiated volume (2 ml). Since the excitation in both cases was carried out by monochromatic radiation, the energy absorbed by the volume of the solution (in J) can be converted easily into the number of photons, taking into account the transmittance of the solution at the excitation wavelength (T) and the photon energy $E_{355}=5.6\times10^{-19}$ J, $E_{308}=6.44\times10^{-19}$ J.

$$N_{abs}^{308} = \frac{W\cdot t\cdot S\cdot(1-T_{308})}{h\nu_{308}} \quad \text{or} \quad N_{abs}^{355} = \frac{E_{imp}\cdot n\cdot(1-T_{355})}{h\nu_{355}}, \qquad (3)$$

where W – the lamp power density ($W\cdot cm^{-2}$), t – time of irradiation (s), S – the irradiated solution area (cm^2), E_{imp} – impulse energy (J), n– the number of laser pulses and T – transmission at excitation wavelength.

3 Results and Discussion

As mentioned above, self-contained acid photogenerators are interesting in that they generate both acid counterions when irradiated. The mechanism of light-induced 6π--electrocyclization is shown in Fig. 1.

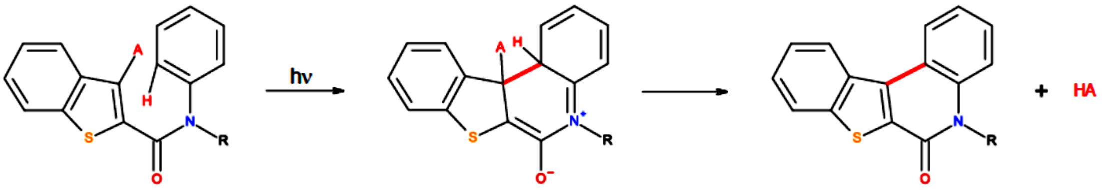

Fig. 1 The mechanism of photogeneration of acid by 6π electrocyclization.

Table 1 Spectral characteristics of the studied compounds in methylene chloride.

Compound	λ_{abs}, **nm**	ε_{max}, **dm^{3}mol^{-1}cm^{-1}**	ε_{308}, **dm^{3}mol^{-1}cm^{-1}**	ε_{355}, **dm^{3}mol^{-1}cm^{-1}**
PAG1	299 244	12740 20100	11770	830
PAG2	302 244	13900 19420	13310	950
PAG3	303 246	15650 21700	15250	1130
PAG4	290 238	11820 16950	7700	130
PAG5	291 240	10990 17630	7840	90

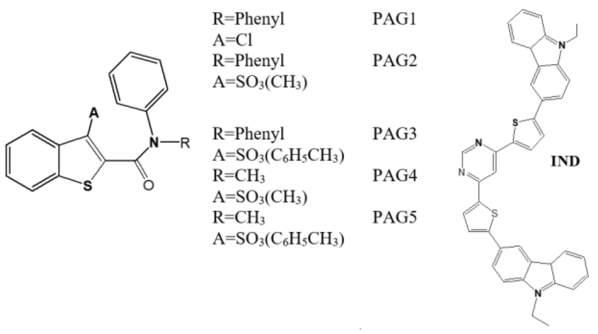

Fig. 2 Structure of the studied PAGs and indicator.

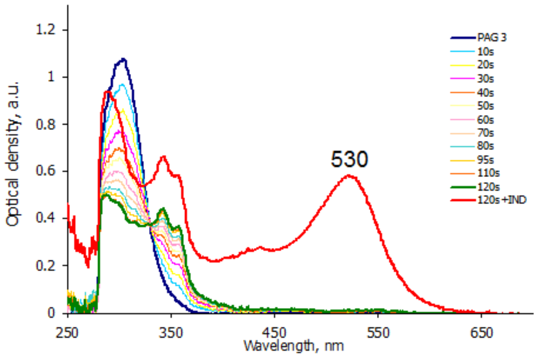

Fig. 3 Phototransformation of PAG3 in toluene (C=10^{-4} mol L^{-1}) upon irradiation with a XeCl-lamp. The indicator is added after irradiation for 120 s.

Figure 2 shows the structures of the studied compounds. PAGs (1–3) differ from each other only in their acidic substituents, which form hydrochloric, methylsulfonic, and toluenesulfonic acids upon photolysis. In PAGs (3–4), one phenyl ring on the right moiety is replaced by a methyl group, resulting in a slight (~10 nm) blue shift of the absorption band, but a noticeable decrease in extinction at the laser excitation wavelength (Table 1).

Figure 3 shows the dynamics of changes in the absorption spectrum for PAG3 in toluene when irradiated with a XeCl lamp. Since the fundamental structure of the molecules is similar, the photolysis pattern is similar for all PAGs, for both excitation sources. The spectrum contains isosbestic point, which indicates that two compounds are recorded: the original and the photoproduct. The formation of acid during photolysis is confirmed by an indicator added to the irradiated solution, which forms a protonated form (~530 nm). The protolytic properties of the indicator molecule were investigated in our previous work [9].

Using Eq. (1), the quantum yield of phototransformation of compounds was estimated upon irradiation with a XeCl lamp and Nd:YAG laser in solutions of toluene and DCM (Table 2). When irradiated with a laser, the quantum yield values are of the same order of magnitude – 10^{-2} in both solvents, with some difference depending on the substituent. When they irradiated with a lamp, the quantum yield values for toluene and DCM differ significantly. In toluene it is almost ten times higher than DCM. It should be noted that in DCM the decay quantum yield for both excitation sources is of the same order (~10^{-2}). Since photolysis for all cases of excitation and solvents occurs with the formation of isobestic points in the absorption spectra, it can be assumed that the obtained values of the quantum yield are also the same for the formation of acid, since non-proton-donating solvents were used.

Figure 4 shows the intensity of the protonated form of the indicator (PF-IND) at λ=530 nm added to irradiated compounds with a XeCl lamp for 150 s in toluene and DCM. The intensity of PF-IND may depend on the quantum yield of photoacid formation, its activity in different solvents and its molecular nature. In our case, hydrochloric, methylsulfonic and toluenesulfonic acids are form. Based on the quantum yield, the PF-IND intensity in irradiated toluene should be much higher (since the quantum yield is significantly higher) than we observe in DCM in Fig. 4. The comparable PF-IND intensities in both solvents for all PAGs (except PAG1) are most likely due to the different activities of the formed acids in toluene and DCM. It is significantly higher in DCM, as can be seen from the figure. Interestingly, the indicator does not detect hydrochloric acid in toluene. Either its activity in toluene is so low, or the chlorine anion formed during photolysis chemically reacts with toluene.

Table 2 Quantum yield of the compound phototransformation upon irradiation with a XeCl lamp and the 3rd harmonic of a Nd:YAG laser in toluene and dichloromethane solutions.

PAGs	**λ_{ex} = 355 nm**		**λ_{ex} = 308 nm**	
	Toluene	**DCM**	**Toluene**	**DCM**
PAG1	0.024	0.025	0.15	0.042
PAG2	0.06	0.018	0.30	0.021
PAG3	0.072	0.03	0.36	0.038
PAG4	–	–	0.11	0.022
PAG5	–	–	0.11	0.022

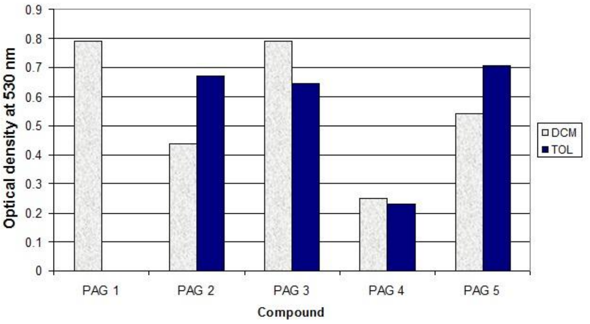

Fig. 4 Optical density of the IND protonated form when the PAGs ($C = 10^{-4}$ mol L^{-1}) were irradiated with XeCl-lamp for 150 s in toluene (TOL) and dichloromethane (DCM).

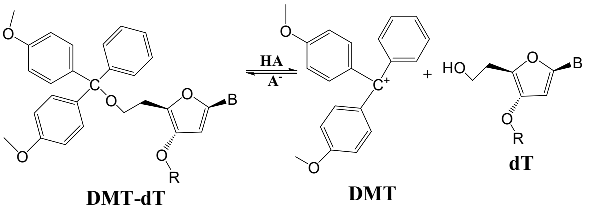

Fig. 5 Reaction of DMT cation formation in an acidic environment.

Deprotection, removal of the dimethoxytrityl group, during the synthesis of oligonucleotides is typically carried out with dichloro- or trichloroacetic acid of a certain concentration according to Fig. 5. The resulting cation (DMT) imparts a yellow-orange color to the solution and is easily detected by its strong absorption in the 506–511 nm region. Various PAGs have already been used in Refs. [10, 14–17] to remove the DMT group from both nucleoside monomers and synthesized nucleic acid chains during oligonucleotide synthesis [15–17]. In this study, detritylation was performed by irradiating PAGs ($C = 10^{-3}$ mol L^{-1}) with the addition of DMT-dT at a concentration of 5×10^{-5} mol L^{-1} in a dichloromethane solution. Both excitation sources were used.

Figure 6 shows the photolysis of PAG3 in DMC mixed with DMT-dT under irradiation with a XeCl excilamp (308 nm). For other PAGs, as well as with laser irradiation, the spectral changes are similar. Based on the DMT absorption intensity at 506 nm, it can be concluded that detritylation by photogenerated acids is efficient.

Figure 7 shows the dependence of the absorption of the DMT cation on the irradiation time for both light sources. When comparing PAGs (1–3), which differ only in that they generate different acids, at the beginning of irradiation, hydrochloric and toluenesulfonic acids begin to work simultaneously (curves 1, 3), while methanesulfonic acid lags behind (curve 2). With longer irradiation, the process of detritylation in a medium with hydrochloric acid is noticeably inhibited (curves 1, Fig. 7(a, b)), whereas with methanesulfonic and toluenesulfonic acids it continues. It should be noted that this behavior of PAGs is typical both when irradiated by a lamp and a laser.

PAGs (4, 5), in which one phenyl ring on the right moiety of the molecules is replaced by a methyl group, resulting in a slight blue shift of the bands but a dramatic decrease in extinction at 355 nm, are not suitable for laser excitation. When irradiated with a lamp, their efficiency is only slightly weaker than PAGs (1–3) (curves 4, 5, Fig. 7(a)). In general, the detritylation process is more efficient with toluene sulfonic acid.

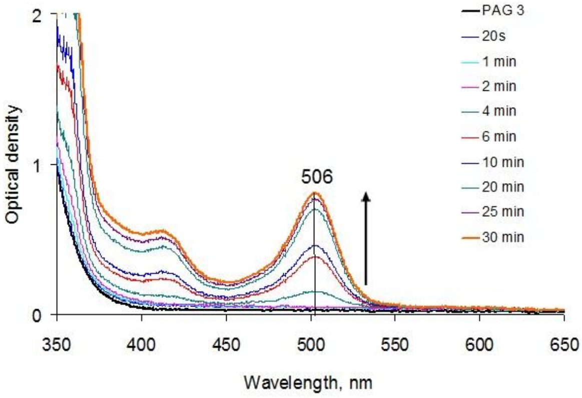

Fig. 6 Photochemical accumulation of DMT- cation at 506 nm during irradiation of a mixture PAG3 ($C = 10^{-3}$ mol L^{-1}) and DMT-dT ($C = 5\times10^{-5}$mol L^{-1}) in DCM under excitation 308 nm.

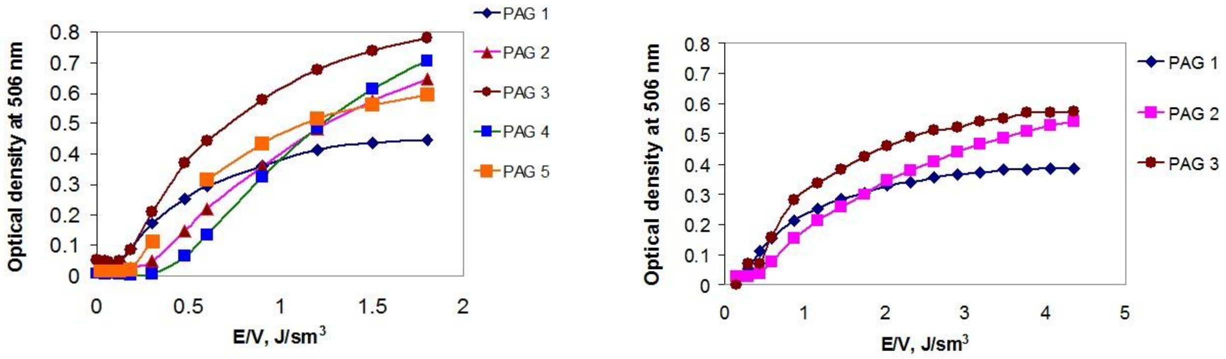

(a) (b)

Fig. 7 Formation of DMT-cations in DCM during irradiation of PAGs with (a) a XeCl-lamp and (b) Nd:YAG-laser (b). Concentration of PAGs are 10^{-3} mol L^{-1}, DMT-dT – 5×10^{-5} mol L^{-1}. E/V is the energy (dose) of the absorbed radiation in the volume of the solution, taking into account the transmission.

4 Conclusion

Thus, all the studied compounds form acids, both when irradiated with a XeCl lamp (308 nm) and with the 3rd harmonic of an Nd:YAG laser (355 nm) in both toluene and dichloromethane. An indicator was used to confirm acid formation. The formation of the acid in an aprotic solvent confirms the mechanism of 6π--photo-electrocyclization.

Photogenerated acids were tested for the removal of the dimethoxytrityl group from 5′-O-(4,4′-dimethoxytrityl)-2′-deoxythymidine-3′-O-[O-(2-cyanoethyl)-N,N′-diisopropylphosphoramidite under both lamp and laser irradiation. It has been shown that the fastest and most complete effect is achieved with toluenesulfonic acid.

Disclosures

The authors declare no conflicts of interest in this paper.

Acknowledgment

This work was performed within the framework of the State Assignment of the Ministry of Science and Higher Education of the Russian Federation (Project No. FEWM-2024-0001).

References

1. M. Shirai, M. Tsunooka, “Photoacid and Photobase Generators: Chemistry and Applications to Polymeric Materials,” Progress in Polymer Science 21(1), 1–45 (1996).
2. N. A. Kuznetsova, G. V. Malkov, and B. G. Gribov, “Photoacid Generators. Application and Current State of Development,” Russian Chemical Reviews 89(2), 173–190 (2020). [in Russian]
3. C. J. Martin, G. Rapenne, T. Nakashima, and T. Kawai, “Recent Progress in Development of Photoacid Generators,” Journal of Photochemistry and Photobiology C: Photochemistry Reviews 34, 41–51 (2018).
4. M. Sarker, T. Shahrin, and M. G. Steinmetz, “Photochemical Eliminations Involving Zwitterionic Intermediates Generated via Electrocyclic Ring Closure of Benzothiophene Carboxanilides,” Organic Letters 13(5), 872–875 (2011).
5. T. Nakashima, K. Tsuchie, R. Kanazawa, R. Li, S. Iijima, O. Galangau, H. Nakagawa, K. Mutoh, Y. Kobayashi, J. Abe, and T. Kawai, “Self-Contained Photoacid Generator Triggered by Photocyclization of Triangle Terarylene Backbone,” Journal of the American Chemical Society 137, 7023–7026 (2015).
6. O. Galangau, S. Delbaere, N. Ratel-Ramond, G. Rapenne, R. Li, J. P. D. Cruz Calupitan, T. Nakashima, and T. Kawai, “Dual Photochemical Bond Cleavage for a Diarylethene-Based Phototrigger Containing both Methanolic and Acetic Sources,” The Journal of Organic Chemistry 81, 11282–11290 (2016).
7. R. Li, T. Nakashima, and T. Kawai, “A Self-Contained Photoacid Generator for Super Acid Based on Photochromic Terarylene,” Chemical Communications 53, 4339–4341 (2017).
8. A. V. Migulin, C. V. Milyutin, and A. N. Komogortsev, “Novel Photoacid Generators Derived From Allomaltol Containing Terarylenes With 2-Aminooxazole Fragment,” Journal of Heterocyclic Chemistry 63(4), 579–589 (2026).
9. L. G. Samsonova, N. V. Izmailova, R. M. Gadirov, R. A. Irgashev, N. A. Kazin, Yu. A. Kvashnin, A. S. Steparuk, G. L. Rusinov, and E. V. Verbitskiy, “Photoacid Generation from Substituted Benzo[b]thiophene-2-Carboxanilides,” Mendeleev Communications 36(1), 50–52 (2026).
10. P. J. Serafinowski, P. B. Garland, “Novel photoacid generators for photodirected oligonucleotide synthesis,” Journal of the American Chemical Society 125, 962 (2003).

11. V. F. Tarasenko, E. B. Chernov, and M. V. Erofeev, "UV and VUV excilamps excited by glow, barrier and capacitive discharges," Applied Physics A 69, 327–329 (1999).
12. A. M. Boychenko, M. I. Lomayev, A. N. Panchenko, E. A. Sosnin, and V. F. Tarasenko, Ultraviolet and Vacuum-Ultraviolet Excilamps: Physics, Technology and Applications, STT, Tomsk (2011). ISBN: 978-5-93629-433-4 [in Russian]
13. E. A. Sosnin, V. A. Panarin, V. S. Skakun, V. F. Tarasenko, S. M. Avdeev, and D. S. Pechenitsyn, Radiation source, RU Patent 200241, published on 14.10.2020.
14. P. J. Serafinowski, P. B. Garland, "Substituted 2-nitrobenzyltrichloroacetate esters for photodirected oligonucleotide detritylation in solid films," Organic & Biomolecular Chemistry 6, 3284 (2008).
15. X. Gao, E. LeProust, H. Zhang, O. Srivannavit, E. Gulari, P. Yu, C. Nishiguchi, Q. Xiang, and X. Zhou, "A flexible light-directed DNA chip synthesis gated by deprotection using solution photogenerated acids," Nucleic Acids Research 29(22), 4744 (2001).
16. V. V. Shelkovnikov, V. A. Loskutov, E. V. Vasil'ev, N. V. Shekleina, V. A. Ryabinin, and A. N. Sinyakov, "New Acid Photogenerators Based on Thioxanthen 9 one Sulfonium Derivatives for Detritylation in the Oligonucleotide Synthesis," Russian Chemical Bulletin 60, 561–569 (2011).
17. A. N. Sinyakov, E. V. Kostina, D. E. Zaytsev, N. V. Chukanov, G. N. Kamaev, V. P. Bessmeltsev, V. V. Shelkovnikov, and E. V. Vasil'ev, "New photoacids in microarray synthesis of oligonucleotides," Journal of Saudi Chemical Society 27, 101709 (2023).

Linear Dichroism and Birefringence in Polarization-Modulation Pump-Probe Spectroscopy

Denis A. Volkov[*1], **Maxim V. Belashov**[1,2], **Maxim E. Sasin**[1], **and Oleg S. Vasyutinskii**[1]
[1] Ioffe Institute, Russian Academy of Sciences, 26 Polytekhnicheskaya str., St. Petersburg 194021, Russian Federation
[2] ITMO University, 9 Lomonosova str., St. Petersburg 191002, Russian Federation
*e-mail: volkovda@mail.ioffe.ru

Abstract. We present the refinement of the Polarization-Modulation Pump-Probe method developed recently in our group (PCCP V. 22, 18155 (2020)) for separation and quantitative determination of linear dichroism and birefringence of the probe laser beam in biologically relevant molecules. The method was used in the study of ultrafast relaxation dynamics in the excited states of NADH in aqueous solution. The probe beam birefringence contained contributions both from resonance pump beam absorption in NADH and from nonlinear coherent effect that was attributed to the stimulated Raman scattering in water, the latter manifested as a very intense and narrow peak at sub-picosecond delay times between pump and probe pulses. The probe beam dichroism contained the contribution from the resonance pump beam absorption in NADH and practically no contribution from nonlinear coherent effects. In this case the experimental signal was approximately twice smaller than that of the birefringence case. Therefore, it was suggested that the birefringence detection allows to achieve higher sensitivity for determination of the relatively long relaxation times than the linear dichroism detection.

Keywords: polarization-modulation pump-probe; linear dichroism; birefringence; NADH; Stimulated Raman Scattering.

Paper #9496 received 26 Jan 2026; accepted for publication 28 Apr 2026; published online 28 May 2026. doi: 10.18287/JBPE26.12.020306.

1 Introduction

Ultrafast pump-probe polarization spectroscopy has emerged as a powerful tool for investigation of photoinduced processes, biomedical imaging, and material science including molecular reorientation, energy transfer, and anisotropic relaxation dynamics [1–13]. Excitation of polyatomic molecules in fluid solution with polarized light can lead to transient birefringence (BR) and linear dichroism (LD) resulting in the change of polarization of the probe beam passed through a molecular sample. In both cases the experimentally measured value is usually recorded as a difference between the intensities of two orthogonal transient probe beam polarization components.

If the pump and probe laser pulses do not overlap in time the physical quantities that underlie the recorded experimental signals are the real and imaginary parts of the linear susceptibility $\chi^{(1)}$ [1, 3, 4, 11, 13]. In the field of ultrafast dynamics in transparent fluids that is widely used nowadays this phenomenon is usually named optical Kerr effect (OKE) [2, 5, 9]. If the pump and probe laser pulses overlap in time the physical quantities that underlie the recorded experimental signals are often the real and imaginary parts of the nonlinear third- order susceptibility tensor $\chi^{(3)}$ measured within the Raman-induced Kerr effect (RIKE) [6, 7, 14]. According to our recent theoretical analysis [15, 16] both effects can be described by the same light polarization dependencies and treated in a uniform way.

The advantage of the pump-probe polarization spectroscopy is its ability to provide polarization-sensitive images reflecting molecular reorientation and anisotropic relaxation processes at high spatial and sub-picosecond temporal resolution. On the other hand, a disadvantage of all pump-probe schemes is that they require the measurement of a weak differential transmission signal sitting on top of the large and

This paper was presented at the International Russian-Chinese Workshop on Light for Life Sciences, St. Petersburg, Russian Federation, October 17 – 20, 2025.

fluctuating background given by the probe light beam. Another important source of experimental errors in the pump-probe method is the heating of a molecular sample by the pulsed laser beams that form an oscillating thermal lens that disperses the probe beam. A common way of extraction of the differential polarization signals is modulation of the pump light beam intensity with following lock-in detection at the modulation frequency [1–8]. This technique allows to decrease significantly the excess fluctuations of the probe laser beam intensity in the frequency band below the modulation frequency. However, the modulation of the pump beam intensity causes a thermal lens in the molecular sample that oscillates at the modulation frequency and gives contribution to the signal noise.

An additional effective approach for intrinsic rejection of excess laser noise is the balanced detection scheme [7]. Within this approach the orthogonal polarization components of the probe beam are separated by a polarization prism and then recorded simultaneously by two identical photodetectors and subtracted from each other by a differential integrator. However, the authors of Ref. [7] still used the pump beam intensity modulation and therefore their results were not free from the thermal lens effect.

We have recently suggested a new method that we call Polarization-Modulation Pump-Probe (POMO-PP). The main idea of our method is high-frequency modulation of the pulse train polarization in the pump beam with following balanced detection scheme of the transmitted probe beam polarization components, and recording of the differential signal at the modulation frequency using lock-in detector. The modulation of the pump beam polarization allows to keep constant the pump laser intensity in the molecular sample and thus avoid the oscillating thermal lens effect that allows for effective suppression of both laser beam noise and thermal lens effect [10, 11]. The polarization modulation was used before [9], however without the balance detection scheme, and the pump beam intensity modulation was still utilized. The combination of experimental techniques used in our method dramatically increased sensitivity and allowed to use laser pulses from a femtosecond oscillator with energies lower than a nJ for effective detection of LD in the excited state of nicotinamide-adenine-dinucleotide (NADH) molecules diluted at low concentration in various solutions [11].

In this work we further developed the POMO-PP method suggested in our papers [10, 11]. The key improvement of the method lies in the ability to independently isolate and quantify the LD and BR signals induced in the molecular sample by polarized pump pulses. The verification of the method was performed through the analysis of polarized beam propagation by means of the Müller matrix formalism [17]. The method allows to combine the detailed study of ultrafast photophysical processes and energy transfer in molecular excited states with unprecedented sensitivity of the approach developed before [11].

2 Experiment

2.1 Experimental Method

The main features of the method are as follows. A linearly polarized pump femtosecond laser pulse interacts with initially isotropic molecular sample and produces the anisotropic distribution of excited molecular axes. This anisotropy is detected by a collinearly propagated probe laser beam polarized at 45° to the direction of the pump beam polarization. The femtosecond probe pulse is delayed by the time τ with respect to the pump one. Passing through the anisotropic sample the probe beam undergoes linear dichroism and birefringence that result in the rotation of its polarization plane and in the appearance of ellipticity. The change of the polarization state of the probe pulse is detected by sequentially installed quarter wave plate and a Glan prism.

As is well known, the experimental signal recorded within such experimental schemes is usually noisy suffering mainly from the fluctuations of the probe laser beam intensity and the thermal lens effect [18, 19]. For significant reduction of the influence of both these effects the polarization of the pump beam was modulated at the frequency of 100 kHz resulting in the periodic linear polarization change from horizontal (X) to vertical (Y) positions. Also, the detection of the probe beam polarization changes was made through a balanced detection scheme that consisted of two identical photodiodes and a home-made differential integrator. The resulting differential signal, modulated at 100 kHz, was demodulated using a lock-in amplifier with a bandwidth of 3 Hz. Separation of the linear dichroism and birefringence effects was realized by changing the direction of the quarter-wave plate axis that was set at $\theta = 0$ and $\theta = \pi/4$ for detection of the probe beam linear dichroism and birefringence, respectively. The developed method allows to separate the effects of linear dichroism and birefringence of the probe beam with unprecedented detection sensitivity.

Justification of the method was carried out by calculating the change of the probe beam polarization using Müller matrix formalism [17]. The expression for the difference of the probe light orthogonal polarization component intensities $\Delta I = I_x - I_y$ after passing through the quarter wave plate and the Glan prism as a function of the quarter wave axis direction angle θ can be presented in the form:

$$\begin{aligned}\Delta I = I_{pr}(S_1 \cos^2[2\theta] - \\ - S_2 \cos[2\theta] \sin[2\theta] - S_3 \sin[2\theta]),\end{aligned} \tag{1}$$

where S_1, S_2, S_3 are the Stokes parameters that define the light polarization before the quarter wave plate, θ is the angle of fast axis of quarter-wave plate relative to the vertical direction y, and I_{pr} is the probe beam intensity.

The Stokes parameters are defined as following Eq. (2) [20]

$$\begin{aligned} I_{pr} &= I_x + I_y, \\ S_1 &= \frac{I_x - I_y}{I_{pr}}, \\ S_2 &= \frac{I_{x\prime} - I_{y\prime}}{I_{pr}}, \\ S_3 &= \frac{I_{RC} - I_{LC}}{I_{pr}}, \end{aligned} \tag{2}$$

where I_x and I_y are intensities of the orthogonal polarization components along x and y axes, $I_{x'}$ and $I_{y'}$ are the intensities of the orthogonal polarization components along the axes x' and y' that are rotated by the angle of 45°, and I_{RC} and I_{LC} are the intensities of right- and left-handed circular polarization components.

As can be seen in Eq. (1) if the angle θ is equal to 0 then only the Stokes parameter S_1 contributes to the detected signal, while if this angle is equal to $\pi/4$, then only the Stokes parameter S_3 contributes. These angles also satisfy the balanced detection scheme used in our experiment that yields a zero output signal when the pump beam is turned off. Therefore, at the angles $\theta = 0$ and $\theta = \pi/4$ the noise of the probe beam intensity fluctuations in the recorded signals is effectively reduced. Moreover, the modulation of the pump beam polarization at 100 kHz combined with the balance detection scheme and the following lock-in detection result in an additional significant reduction of noise from the probe laser intensity fluctuations and the thermal lens effect. As a result, as shown in this paper (see also Refs. [10, 11]) the anisotropic relaxation processes in the excited states of polyatomic molecules can be recorded by relatively low-energy (nJ) femtosecond pulses from a femtosecond oscillator without an amplifier.

3 Experimental Setup

A simplified scheme of the experimental setup is shown in Fig. 1.

A femtosecond oscillator MaiTai HP (Spectra Physics, USA) was used as a light source. A laser pulse duration was about 180 fs with a bandwidth of 8 nm and the repetition rate of 80 MHz. The laser fundamental output at 736 nm was split into two beams, one of them was directed on to the second harmonic generator (SHG) (Inspire Blue, Spectra Physics, Spain) to produce the pump beam at 368 nm. The pump beam passed through a photoelastic modulator (PEM) (PEM-100, Hinds Instruments, USA) operating at the frequency of 50 kHz. The modulation of the pump beam polarization resulted in the periodic linear polarization change from horizontal (*X*) to vertical (*Y*) at the frequency of 100 kHz. The modulated pump beam was focused on a 1 mm cuvette with solution, forming a spot of approximately 43 μm. After passing through the cuvette, the pump beam was reflected by a dichroic mirror (DM2) on a silicon photodetector (D) that controlled the beam intensity.

The second beam at the fundamental wavelength of 736 nm was directed to a motorized delay line and used as a probe beam. The probe beam passed through a delay line, was reflected from a dichroic mirror (DM1), and propagated toward the cuvette collinearly with the pump beam. The probe beam polarization plane was set at 45° to the vertical polarization plane (y) of the pump beam. It was focused into the spot of about 50 μm in the cuvette.

After the cuvette the probe beam passed through DM2, an absorption filter, and then was directed to the analyzer consisted of a quarter-wave plate ($\lambda/4$) and a Glan prism (GP). Two orthogonal polarization components of the probe beam were separated by the Glan prism and then recorded by a balanced detection scheme. The scheme consisted of two identical silicon photodiodes (*Dx*, *Dy*) (DET10A/M, ThorLabs, USA) and a home-made differential integrator (DI) with a passband of 0–4 MHz. The resulting differential signal, modulated at 100 kHz, was demodulated using a lock-in amplifier (SR844 RF, Stanford Instruments, USA) with a bandwidth of 3 Hz and subsequently recorded for computer analysis. The laser pulses energies in front of the cuvette were controlled by attenuators and set to 470 and 170 pJ for pump and probe beams, respectively.

The direction of the quarter-wave plate $\lambda/4$ axis was set at $\theta = 0$ and $\theta = \pi/4$ for detection of the probe beam linear dichroism and birefringence, respectively.

In experiments we used freshly prepared water solutions of β-Nicotinamide Adenine Dinucleotide (NADH, disodium salt, Sigma-Aldrich). The β-NADH salt was dissolved in distilled water to a concentration of 0.4 mM. This resulted in an absorption of about 14% of pump beam. This absorbance level was chosen to ensure sufficient signal while preventing effects associated with absorption heterogeneity across the 1 mm cuvette path length.

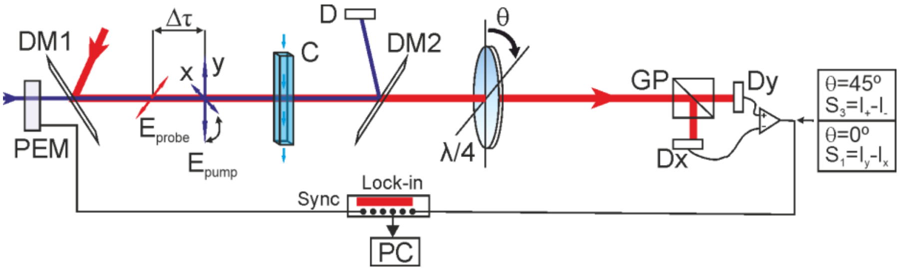

Fig. 1 Scheme of the birefringence and linear dichroism measurements; $\Delta\tau$ is a delay time between the pump and probe pulses; PEM is a photoelastic modulator; DM1, DM2 are dichroic mirrors; GP is a Glan prism; D, D_x, D_y are detectors; *C* is a cuvette with solution; θ is an angle of quarter-wave plate fast axis relative to the vertical axis *y*.

4 Results and Discussion

The BR and LD signals of the probe laser beam recorded in NADH in aqueous solution are shown in Figs. 2 and 3, respectively, as a function of the delay time τ between the pump and probe pulses.

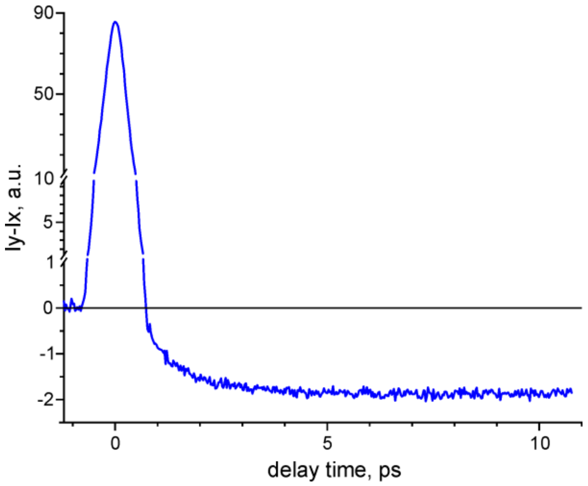

Fig. 2 BR signal of 0.4 mM NADH up to 11 ps at 45°.

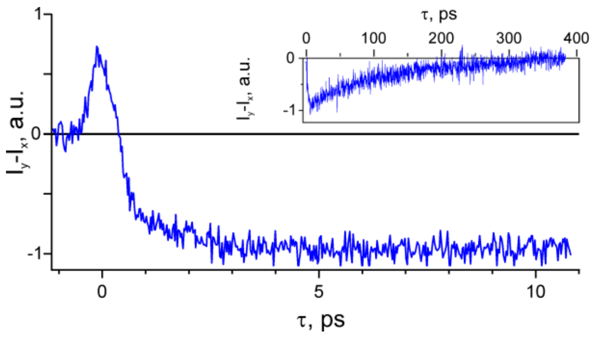

Fig. 3 Linear dichroism signal of 0.4 mM NADH up to 11 ps at 0°. The inset shows the long signal up to 400 ps.

As can be seen in Fig. 2 the BR signal consists of a very intense and narrow (a few tenths of a ps) peak in the vicinity of zero delay time τ, followed by a much smaller signal of opposite sign that is significantly broader and extends to the delay times up to hundreds of ps. The first intensive peak relates to the temporal overlap of the pump and probe laser pulses. We suggest that this peak was due to the third-order nonlinear Stimulated Raman Scattering (SRS) [7] of the probe beam in water. This signal was observed in our experiments even in pure water without any NADH dissolved. According to our recent theoretical publication [15] the SRS BR effect can be observed only when the pump and probe light frequencies are essentially non-resonant with respect to the excited molecular states that perfectly fits the experimental condition in Fig. 2.

The second, much less intense but significantly broader signal in Fig. 2 can be associated with the linear pump-probe BR effect in NADH. In this case, the pump beam resonantly excited the molecule from the ground state S_g to the first excited electronic state S_1 and the probe beam frequency was out of resonance between the vibrational states v_1 of the first excited electronic state S_1 and the vibrational states v_2 of the second excited electronic state S_2. This signal was not observed in pure aqueous solution and appeared only in the presence of NADH. According to our analysis [15] this signal is characterized by the relatively short vibration relaxation time τ_v and longer rotational diffusion time τ_{rot}.

As can be seen in Fig. 3 the LD signal contains a relatively small signal observed at the delay times τ from a few and up to hundreds of ps. This signal is presented in a smaller scale and longer delay times in the inset. We believe that the wide negative signal in Fig. 3 can be associated with the pump-probe LD effect in NADH. According to the theory [15] and the experimental observation shown in the inset in Fig. 3 this signal has an extremum due to competition of the relatively fast vibration relaxation with the time τ_v and much slower rotational diffusion with the time τ_{rot}.

As can be seen in Fig. 3 the recorded LD signal contains only a relatively small narrow peak in the vicinity of zero delay time τ. We believe that a residual small peak at short delay times in Fig. 3 was due to insufficiently fine alignment of the experimental scheme. The absence of the third-order nonlinear Stimulated Raman Scattering (SRS) signal in Fig. 3 is in perfect agreement with our theoretical prediction [16] that the LD is an essentially resonant effect that could not be observed in pure water in the conditions of our experiments.

Therefore, the experimental data in Figs. 2 and 3 manifest that the POMO-PP method allows for almost complete separation of the contributions from the BR and LD effect that combines with possibility to use relatively small laser pulse energies of a tenths of nJ to obtain high signal-to-noise ratio. As can be seen in Figs. 2 and 3 the method also allows for effective separation of linear pump-probe signals from the third-order nonlinear SRS signals.

5 Conclusion

In this work we developed the POMO-PP method suggested in our previous study for separation of the LD and BR signals and their quantitative determination from experiment. The method was used to acquire LD and BR signals of NADH excited states in aqueous solution. In the case of BR detection both the 3rd order SRS in water and the 1st order pump-probe in NADH were observed. The SRS signal was presented as a very sharp and intensive peak at the delay times of a few tens of ps and the BR pump-probe signal in NADH was presented by a much smaller but wider curve with an extremum. In case of LD detection, the SRS peak in water was practically absent and only the pump-probe signal in NADH was observed. The BR signal in NADH was approximately twice as large than the corresponding LD signal without increasing the pump and probe intensities, thus achieving higher sensitivity for determination of the rotational diffusion times longer than the duration of the SRS peak.

The LD signal was found to be more suitable for the study of the fast vibrational relaxation processes.

Disclosures

The authors declare no conflicts of interest in this paper.

References

1. D. Waldeck, A. J. Cross, D. B. McDonald, and G. R. Fleming, "Picosecond pulse induced transient molecular birefringence and dichroism," The Journal of Chemical Physics 74(6), 3381–3387 (1981).
2. D. Mcmorrow, W. Lotshaw, and G. Kenney-Wallace, "Femtosecond Optical Kerr Studies on the Origin of the Nonlinear Responses in Simple Liquids," IEEE Journal of Quantum Electronics 24(2), 443–454 (1988).
3. J. Chesnoy, A. Mokhtari, "Resonant impulsive-stimulated Raman scattering on malachite green," Physical Review A 38, 3566 (1988).
4. D. M. Jonas, M. J. Lang, Y. Nagasawa, T. Joo, and G. R. Fleming, "Pump-Probe Polarization Anisotropy Study of Femtosecond Energy Transfer within the Photosynthetic Reaction Center of *Rhodobacter sphaeroides R26*," The Journal of Physical Chemistry 100(30), 12660–12673 (1996).
5. Q. Zhong, J. T. Fourkas, "Optical Kerr Effect Spectroscopy of Simple Liquids," The Journal of Physical Chemistry B 112(49), 15529–15539 (2008).
6. C. W. Freudiger, M. B. J. Roeffaers, X. Zhang, B. G. Saar, W. Min, and X. S. Xie, "Optical Heterodyne-Detected Raman-Induced Kerr Effect (OHD-RIKE) Microscopy," The Journal of Physical Chemistry B 115(18), 5574–5581 (2011).
7. E. Molotokaite, V. Kumar, C. Manzoni, D. Polli, G. Cerullo, and M. Marangoni, "Raman-induced Kerr effect microscopy with balanced detection," Journal of Raman Spectroscopy 44(10), 1385–1392 (2013).
8. A. Taschin, P. Bartolini, R. Eramo, R. Righini, and R. Torre, "Optical Kerr effect of liquid and supercooled water: The experimental and data analysis perspective," The Journal of Chemical Physics 141(8), 084507 (2014).
9. M. Tros, S. Woutersen, "Polarization-modulation setup for ultrafast infrared anisotropy experiments to study liquid dynamics," Optics Letters 40(11), 2607 (2015).
10. I. A. Gorbunova, M. E. Sasin, and O. S. Vasyutinskii, "Observation of Anisotropic Relaxation in Biological Molecules with Subpicosecond Temporal Resolution," Technical Physics Letters 46(2), 158–160 (2020).
11. I. A. Gorbunova, M. E. Sasin, Y. M. Beltukov, A. A. Semenov, and O. S. Vasyutinskii, "Anisotropic relaxation in NADH excited states studied by polarization-modulation pump–probe transient spectroscopy," Physical Chemistry Chemical Physics 22(32), 18155–18168 (2020).
12. A. Taschin, P. Bartolini, S. Fanetti, A. Lapini, M. Citroni, R. Righini, R. Bini, and R. Torre, "Pressure Effects on Water Dynamics by Time-Resolved Optical Kerr Effect," The Journal of Physical Chemistry Letters 11(8), 3063–3068 (2020).
13. J. Jiang, D. Grass, Y. Zhou, W. S. Warren, and M. C. Fischer, "Beyond intensity modulation: new approaches to pump-probe microscopy," Optics Letters 46(6), 1474 (2021).
14. M. D. Levenvon, S. S. Kano, Introduction to Nonlinear Laser Spectroscopy, Academic Press, San Diego, CA (1988). ISBN O-12-444722-8.
15. B. V. Semak, O. S. Vasyutinskii, "Linear Dichroism and Birefringence of Probe Radiation in Pump-Probe Spectroscopy of Polyatomic Molecules," Optics and Spectroscopy 129(9), 1007–1017 (2021).
16. B. V. Semak, Y. M. Beltukov, and O. S. Vasyutinskii, "Probe Beam Dichroism and Birefringence in Stimulated Raman Scattering in Polyatomic Molecules," ChemPhysChem 24(22), e202300405 (2023).
17. P. S. Theocaris, E. E. Gdoutos, Matrix theory of photoelasticity, Springer Series in Optical Sciences, Springer (2013). ISBN: 978-3-540-35789-6 (eBook).
18. A. Marcano, C. Loper, and N. Melikechi, "Pump–probe mode-mismatched thermal-lens Z scan," Journal of the Optical Society of America B19(1), 119 (2002).
19. A. L. Glazov, A. D. Il'ina, A. A. Sukharev, and O. S. Vasyutinskii, "Study of the relaxation rate of photoexcited indole molecules by the interferometric pump-and-probe method at picosecond resolution," Technical Physics Letters 43(9), 846–848 (2017).
20. R. M. A. Azzam, "Stokes-vector and Mueller-matrix polarimetry [Invited]," Journal of the Optical Society of America A 33(7), 1396–1408 (2016).

SLM-Based System for Localized Targeted Irradiation of Cells and Noninvasive Monitoring of Cell Death

Andrey V. Belashov[1], Anna A. Zhikhoreva[1*], Maxim V. Belashov[1,2], Anna V. Salova[3], Tatiana N. Belyaeva[3], Ilia K. Litvinov[3], Elena S. Kornilova[3], and Irina V. Semenova[1]
[1] Ioffe Institute, Russian Academy of Sciences, 26 Polytekhnicheskaya str., St. Petersburg 194021, Russian Federation
[2] ITMO University, 49 Kronverkskiy pr., St. Petersburg 197101, Russian Federation
[3] Institute of Cytology, Russian Academy of Sciences, 4 Tikhoretsky pr., St. Petersburg 194064, Russian Federation
*e-mail: anna_zhikhoreva@mail.ru

Abstract. The paper presents the development and validation of an experimental technique enabling localized targeted photodynamic treatment at subcellular level and further noninvasive monitoring of variations in cell morphology using low-coherence holographic microscopy realized in the configuration of spatial light interference microscopy (SLIM). The key element of the setup is spatial light modulator (LCOS SLM) which enabled both the targeted irradiation and continuous quantitative monitoring of cell response. To confirm the reconstruction accuracy of phase images of microscopic objects, a test sample comprising a set of polystyrene microspheres was analyzed. Targeted photodynamic treatment was tested by localized irradiation of HeLa cells photosensitized with Radachlorin. Irradiation of cells triggered their death by apoptosis and necrosis. SLIM-assisted monitoring of cells provided quantitative data on the dynamics of changes in their morphological parameters caused by treatment.

Keywords: spatial light interference microscopy (SLIM); spatial light modulator (LCOS SLM); localized irradiation; targeted photodynamic treatment; photosensitizer; Radachlorin; apoptosis; necrosis.

Paper #9486 received 23 Jan 2026; revised manuscript received 15 Apr 2026; accepted for publication 20 Apr 2026; published online 9 June 2026. doi: 10.18287/JBPE26.12.020307.

1 Introduction

Spatial light modulators (SLMs) enabling arbitrary changes of the amplitude and phase distributions in the light field with a response time of several milliseconds [1] have found wide application in various fields of modern physics [2]. The applications include data transmission [3], information encoding and decoding [4], monitoring of microscopic objects [5], improvement of microscopic techniques [6], etc. An important area of application of these devices is development of optical methods related to phase imaging [7, 8], generation of optical beams with specific properties [9], or creation of augmented reality (AR) displays [10]. Utilization of Liquid Crystal on Silicon Spatial Light Modulators (LCOS SLM) for recording phase images of various biological objects has been repeatedly demonstrated, see e.g. [11–13]. The ability of these devices to precisely control the phase distribution of the wavefront allows generating arbitrary intensity distributions on the sample, which was applied for creation of optical tweezers [14], focusing laser radiation through scattering tissues [15, 16], and local action on different areas of a sample in optogenetics [17].

Photodynamic therapy (PDT) is a promising cancer treatment modality, which enables intracellular generation of reactive oxygen species (ROS) upon light irradiation of photosensitizer (PS) molecules. As known, the PDT efficacy and initiation of specific cell death pathways depend on intracellular distribution and localization of PS molecules [18, 19]. The subcellular organelle-targeted treatment strategies providing an impact directed precisely onto specific organelles receive growing research interest as a promising cancer treatment modality, however specific details of cell death processes still remain poorly understood [20]. Several PSs have been developed that selectively accumulate in specific organelles, including plasma membrane, nuclei, mitochondria, lysosomes,

This paper was presented at the International Russian-Chinese Workshop on Light for Life Sciences,
St. Petersburg, Russian Federation, October 17 – 20, 2025.

endoplasmic reticulum and Golgi apparatus (see Ref. [21] and references therein). Further localized irradiation of the photosensitized organelles causes localized generation of ROS and allows for investigation of cellular response to damage of these compartments, which can help understand their functioning, assess intercellular signaling associated with cell death and cell resistance to treatment and oxidative stress [22]. Less selective targeted irradiation of individual photosensitized cells or groups of cells in a sample with different irradiation durations can be used to analyze cell resistance to different treatment doses [23].

The response of cells to photodynamic treatment of specific organelles requires long-term noninvasive monitoring of the samples. The techniques of quantitative phase imaging (QPI), being label-free and utilizing low-power radiation, are best suited for assessing quantitative data on variations of morphological and optical parameters of cells in dynamics [23–25]. One of the promising QPI techniques is spatial light interference microscopy (SLIM) [13], which can be realized on common biological microscopes and allows for combination with fluorescence-based measurements in a single multimodal system [7].

In this paper, we present the developed experimental approach enabling localized targeted irradiation at subcellular level and further noninvasive monitoring of variations in cell morphology using SLIM. The technical realization of the approach was based on utilization of a spatial light modulator, which allowed for both the targeted irradiation and continuous quantitative monitoring of cell response. The approach was validated on localized photodynamic treatment of HeLa cells photosensitized with Radachlorin PS.

2 Methods and Materials

2.1 Spatial Light Interference Microscopy

The low-coherence quantitative phase imaging in the SLIM configuration was implemented on an inverted fluorescence microscope Nikon Ti-2A using the LCOS SLM PLUTO-2.1 NIR-133 (Holoeye) by creating an external channel of phase-contrast imaging. The phase shift of the reference wave, not scattered in the course of its propagation through the object, was formed on the SLM located in the plane conjugate to the image plane, as shown in Fig. 1(a). A ring-shaped phase pattern, mimicking the annular aperture of sample illumination, was formed on the SLM and phase shifts were sequentially introduced into the reference wave in the range of 0–3π/2 with the π/2 step, as illustrated in the inset in Fig. 1(a). This enabled observation of phase-contrast images of cytological samples without utilization of special phase-contrast microobjectives. In experiments, we used a 40× microobjective with numerical aperture of 1.15 and working distance of 0.6 mm.

For radiation source in the SLIM setup we used the standard LED light source of the Nikon microscope, the working range of 510–560 nm was selected by a bandpass filter BP535/50 (Chroma). The reference wave reflected from the phase-shifting ring on the SLM interfered with the object wave, scattered by the sample and passed by the phase-shifting ring, on the sensor matrix of the digital camera ToupCam UHCCD05000KPA (Touptek, China). The phase distribution of the object wave was then reconstructed from the four recorded phase-shifted holograms using a phase-step algorithm [26], modified for proper account of a partial contribution of light scattered by the sample into the reference wave (annular aperture) [27, 28]. Propagation of a fraction of light scattered by the sample through the ring aperture of the reference wave may lead to formation of halo-shaped image artifacts, which should then be eliminated using a filtering procedure [29, 30]. A more detailed description of the data processing algorithms used for data retrieval in the SLIM technique can be found in Ref. [13].

Despite the artifacts associated with the incomplete separation of the reference and object waves, utilization of low-coherence radiation for hologram recording enables elimination of coherent noise [31, 32], which is a source of a reduced image quality in traditional off-axis digital holographic microscopy based on the Mach-Zehnder interferometer and utilizing laser as a radiation source (Fig. 1(b)). The lack of coherent noise in SLIM allows increasing the spatial resolution and phase-shift measurement accuracy on the obtained images. Besides that, implementation of this approach on a standard inverted microscope enables combination of this technique with other methods, fluorescence analysis in particular [7].

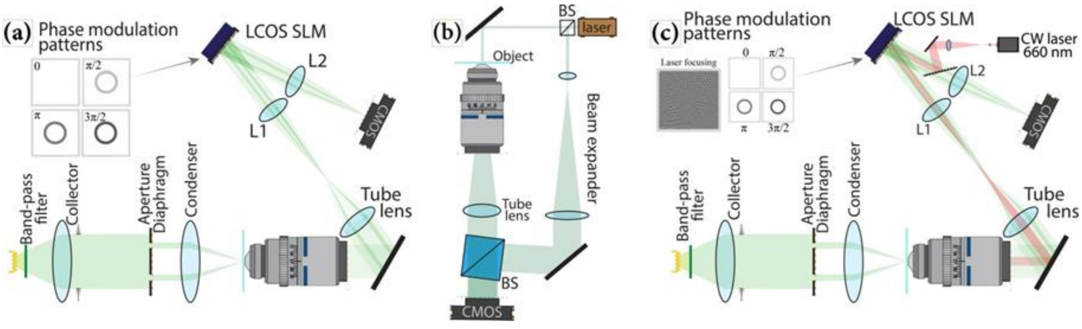

Fig. 1 Schematics of the experimental setups: (a) spatial light interference microscopy, (b) off-axis digital holographic microscopy, (c) spatial light interference microscopy with localized irradiation of a sample.

2.2 Localized Photodynamic Treatment of Individual Cells

As known, along with implementation of the external phase contrast with controlled phase distribution LCOS SLMs can also be used to generate laser beams with specific properties [33, 34], or to shape arbitrary intensity distributions in a desired plane by generating a specific phase pattern and then diffracting the resulting wavefront [35, 36]. The quite short response time of the SLMs (10.5 ms for PLUTO-2.1) enables a multipurpose utilization of this device in the course of a single experiment. In our realization the modulator was used for both localized targeted laser irradiation of individual photosensitized cells and subsequent monitoring of changes in their morphology in the SLIM channel. The experimental schematic is illustrated in Fig. 1(c).

Experiments were performed on samples of live cells of the established line HeLa (human cervix epidermoid carcinoma). Cell samples were obtained from the shared research facility "Vertebrate Cell Culture Collection" of the Institute of Cytology RAS. Cells were grown in monolayers in Petri dishes at 37 °C in 5% CO_2 atmosphere for 48 h in the Dulbecco modified Eagle medium (DMEM) (GIBCO, USA) supplemented with 10% fetal bovine serum (FBS) (GIBCO, USA) and 1% penicillin-streptomycin. After that Radachlorin photosensitizer (RadaPharma) was added to the culture medium at the concentration of 20 µg/ml, and cells were incubated in this solution for 24 h. Our previous work [37] has shown that 24-h incubation with Radachlorin provides efficient uptake of PS molecules by cells and their accumulation mostly in cellular lysosomes. After that, the cells were washed in PBS and fresh culture medium was added to the sample. For photodynamic treatment several cells in the sample were exposed to laser radiation at 660 nm, at the maximum of Q absorption band of the PS. Irradiation caused excitation of PS molecules in cells and induced generation of reactive oxygen species, triggering cell death.

It is worth noting that accumulated photosensitizer caused enhanced photosensitivity of cells in the wavelength range corresponding to the absorption spectrum of the PS, therefore the wavelength range of light used for monitoring the cytological sample in the SLIM setup should be outside the absorption band of the PS. Radachlorin absorption in the ranges of 300–450 nm and 590–690 nm limits utilization of blue and red light for cells' monitoring. The working spectral range of our setup of 510–530 nm allowed for noninvasive monitoring of cells for extended periods of time.

3 Results

3.1 Validation of the SLIM Performance

The operability of the experimental setup and performance of algorithms developed for processing of four on-axis interference patterns and retrieval of the resulting phase distributions have been validated using a test microscopic object comprising polystyrene beads, 2 µm in diameter ($n = 1.593$) placed in glycerol ($n = 1.477$) (Fig. 2). Differential interference contrast (DIC) images of beads are shown in Fig. 2(a).

The known parameters of the beads and surrounding medium allowed us to simulate phase distributions introduced by these microspheres into the transmitted wavefront and to compare them with the experimentally obtained phase distributions. Note that according to the manufacturer, the bead diameter could deviate from 2 µm in 10–15%. To conduct the validation experiment the microsphere concentration was chosen to minimize aggregation and prevent formation of multi-layer structures, which would complicate numerical processing of the resulting phase-shift patterns. Phase images of the beads were recorded in the SLIM channel (Fig. 2(b)).

For additional verification of the results obtained we also recorded off-axis digital holograms of the same test object by means of the traditional coherent holographic microscopy, which allowed us to eliminate the first-order diffraction and to reconstruct the corresponding spatial distributions of phase shift using Fourier transform (Fig. 2(c)). Comparison of the simulated phase distributions with those obtained experimentally using low-coherence SLIM and off-axis digital holography with coherent laser radiation (Fig. 2(d)) demonstrated that low-coherence phase imaging provides reliable data on phase shift distributions of phase objects.

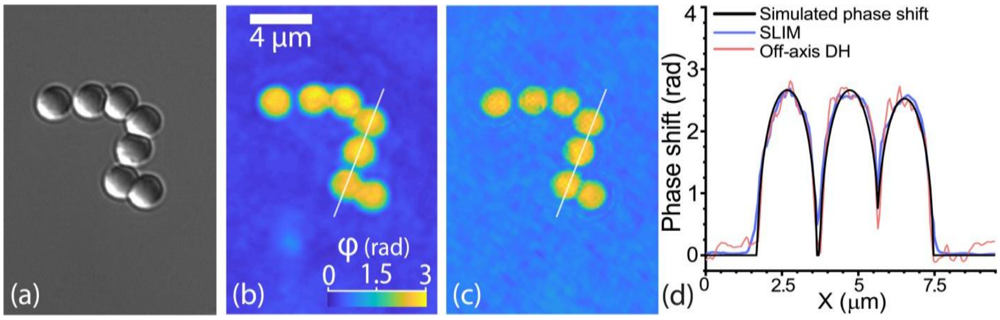

Fig. 2 Images of beads obtained by: (a) DIC, (b) SLIM, (c) off-axis holographic microscopy with the coherent light source. (d) Comparison of the simulated phase distribution with those obtained from images in panels (b) and (c) for the three beads marked by the white line.

The measurement error in SLIM did not exceed 0.05 radians. This error was due to a combination of various factors, such as defects in the bead shape, the accuracy of phase pattern formation on the SLM, halo-related data processing artifacts, noise on the photodetector during image acquisition, potential microscopic movement of the object during image acquisition, etc. The halo filtering was performed using the algorithm described in Ref. [29].

3.2 Analysis of the Response of Individual Cells to Localized Photodynamic Treatment

To generate the desired arbitrary pattern of localized laser irradiation of cells, we first recorded an image of a group of cells using wide-field microscopy. The local areas chosen to be subjected to laser irradiation were marked on this image (Fig. 3(a)). According to our previous work [37], Radachlorin accumulates mainly in lysosomes; in HeLa cells these organelles are clustered in the perinuclear area. Therefore, radiation was focused onto the presumed locations of lysosome clusters. These locations were selected by visual observation of maximal intensity of Radachlorin fluorescence in the perinuclear areas using the microscope camera. The areas subjected to irradiation at 660 nm are indicated in Fig. 3(a) by yellow arrows.Then the phase pattern was calculated, so that diffraction of laser radiation would lead to formation of the required intensity distribution on the sample [38, 39]. Subsequent observation of the combined image of the cells and the formed pattern of localized laser irradiation allowed us to adjust the generated pattern and make corrections to spot locations or sizes, if necessary. Note that the minimal diameter of the irradiation spot in our setup was about 0.7 μm, which allows for selective targeted irradiation of larger cellular compartments, such as nucleus, Golgi apparatus, lysosomal clusters and endoplasmic reticulum. The technique also allows regulating the relative intensity of laser irradiation in different areas of the field of view; however, in this study the initial laser radiation power was distributed uniformly among all irradiated locations in cells (≈ 2.6 μW at each spot).

Irradiation of the chosen areas in photosensitized cells for 5 min led to excitation of photosensitizer molecules and intracellular generation of reactive oxygen species, which initiated cell death. After irradiation of cells, the SLM was reconfigured for operation in the SLIM setup and a set of digital holograms of the field of view was recorded aimed for monitoring the cell response to treatment. Examples of the phase images of the group of cells shown in Fig. 3(a) obtained in the course of their post-treatment monitoring are demonstrated in Fig. 3(c). As can be seen in Fig. 3(c), localized photodynamic treatment of three of six HeLa cells in the group (cells 4, 5, 6), caused variations, characteristic of death processes.

Significant changes in morphology of the cells 5 and 6 (initial formation of small bubbles and subsequent membrane damage and efflux of the intracellular medium manifested by formation of large bubbles) are clearly visible on the phase images in Fig. 3(c). Such changes are characteristic of cell necrosis. At the same time, the cell 4 shows a different scenario of changes (initial formation of small bubbles and, after some time, an increase in the phase shift), characteristic for cell apoptosis. Phase images of non-irradiated cells (cells 1, 2, 3) clearly demonstrate the absence of any changes in cell morphology, validating their survival.

We have previously shown that the value of phase shift, averaged over the entire cell, is a robust quantitative parameter, characterizing death-specific variations in cellular morphology [24]:

$$\varphi_{av} = \frac{1}{S_{cell}} \int_{S_{cell}} \Delta\varphi(x,y)dxdy, \tag{1}$$

where $Q = 2.26 \cdot 10^6$ J/kg – specific heat of water where $\Delta\varphi(x, y)$ is the phase shift introduced by a cell to the transmitted wave front in a certain point (x, y) and S_{cell} is the cell projected area.

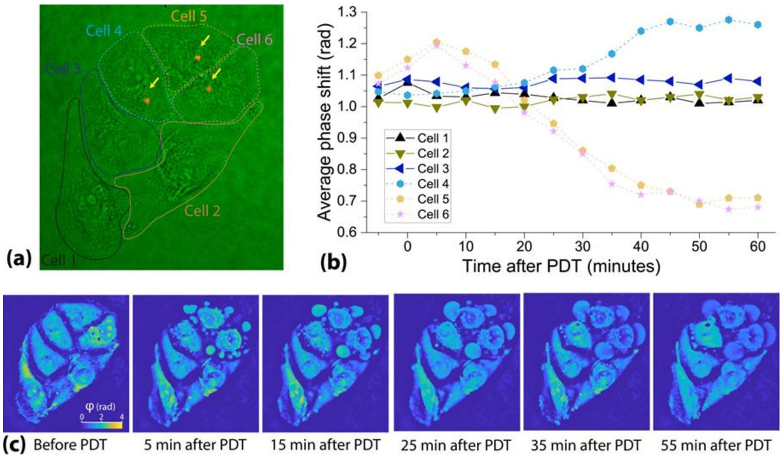

Fig. 3 (a) Bright-field microscopic image of 6 HeLa cells, yellow arrows indicate the areas of localized irradiation. (b) Average phase shift in 6 HeLa cells before and after localized irradiation of the three cells (cells 4, 5, 6). (c) Phase images of the same HeLa cells before and after PDT.

The dynamics of average phase shift after photodynamic treatment was shown in Ref. [24] to clearly correlate with the type of cell death. Utilization of the commonly used fluorescent live-dead test assays, Acridine Orange and Ethidium Bromide (AO/EB) and Annexin V/Propidium Iodide, allowed us to validate that an exponential decrease of the average phase shift was characteristic of cell necrosis, while its increase was due to cell dehydration and rounding in the course of apoptosis. The absence of average phase shift variations at low irradiation doses corresponded to cell survival, which was also confirmed by the fluorescence test assays. These results provided a basis for drawing conclusions on death pathways of cells from the dynamics of average phase shift in individual cells observed in this study. Note that this method is noninvasive and does not require utilization of additional exogenous fluorescent dyes. Mention that spatial distribution of the parameter $\Delta\varphi(x, y)$ can also be used further for calculation of several important morphological and physiological parameters of cells [40], for analysis of cell states [23, 41] and rates of their death [42].

Figure 3(b) shows the dynamics of average phase shift in all the six cells shown in Fig. 3(a). As can be seen from the graphs, the dynamics of φav in non-irradiated cells clearly demonstrate the absence of statistically significant variations of this parameter, while that in the cell 4 is characteristic for apoptosis and those in cells 5 and 6 – for secondary necrosis (see Ref. [24] for the detailed explanation).

It is worth noting that, despite the same irradiation doses applied to the three cells, one of them (cell 4) underwent apoptosis, while two others (cells 5 and 6) died by necrosis. This may be due to both a lower amount of photosensitizer in the irradiated area of cell 4 and to the higher resistance of this cell to photodynamic treatment, which could be due to such factors as, e.g., different phase of the cell cycle or lower amount of oxygen in the area subjected to treatment. The heterogeneity in cell response to photodynamic treatment at the same dose and within the single sample was also demonstrated in our recent paper [41]. It was shown that at each irradiation dose in the sample there were cells in all the three states: live, apoptotic and necrotic. However, depending upon the dose one of the states prevailed.

4 Summary and Conclusions

Therefore, we implemented and tested the experimental setup based on the inverted fluorescence microscope and LCOS SLM for localized photodynamic treatment and noninvasive monitoring of living cells. Validation of the performance of SLIM channel on the model object providing the phase shift similar to that of living cells in a culture medium demonstrated that this low-coherence QPI method enables reconstruction of high-quality phase images of microscopic objects. The spatial light modulator used to generate interference patterns with a specified phase shift was shown to be applicable also for localized irradiation of cells. Its operationability was demonstrated on targeted photodynamic treatment of HeLa cells photo- sensitized with Radachlorin. The small size of the irradiation spot enables selective targeted irradiation of individual cellular compartments, such as nucleus, Golgi apparatus, lysosomal clusters and endoplasmic reticulum. The appropriate selection of the spectral range for QPI allows for long-term noninvasive monitoring of photosensitized cells without significant changes in their morphological or physiological parameters. We have shown that utilization of the LCOS SLM allows implementation of a full range of experimental methods for studying the mechanisms of photodynamic treatment of individual cells. Although studies of cell response to external stimuli are typically conducted on a large population of cells to obtain statistically significant results, the sub-cellular targeted localized treatment and further noninvasive monitoring of individual cells may be quite promising for more deep analysis of subtle intracellular processes in response to specific treatment modalities.

Declaration of Competing Interests

The authors declare that they have no known competing financial interests or personal relationships that could have appeared to influence the work reported in this paper.

Data Availability

Data will be made available on request.

References

1. M. Pivnenko, K. Li, and D. Chu, "Sub-millisecond switching of multi-level liquid crystal on silicon spatial light modulators for increased information bandwidth," Optics Express 29(16), 24614–24628 (2021).
2. Y. Yang, A. Forbes, and L. Cao, "A review of liquid crystal spatial light modulators: devices and applications," Opto-Electronic Science 2(8), 230026 (2023).
3. M. Wang, L. Zong, L. Mao, A. Marquez, Y. Ye, H. Zhao, and F. Vaquero Caballero, "LCoS SLM study and its application in wavelength selective switch," Photonics 4(2), 22 (2017).
4. T. Z. Minikhanov, E. Y. Zlokazov, P. A. Cheremkhin, R. S. Starikov, and N. N. Evtikhiev, "Computer-generated holography methods for data page reconstruction using phase-only medium," Applied Sciences 13(7), 4479 (2023).
5. Y. Lin, H.-C. Chen, H.-Y. Tu, C.-Y. Liu, and C.-J. Cheng, "Optically driven full-angle sample rotation for tomographic imaging in digital holographic microscopy," Optics Letters 42(7), 1321 (2017).

6. C. Garbellotto, J. M. Taylor, "Multi-purpose SLM-light-sheet microscope," Biomedical Optics Express 9(11), 5419 (2018).
7. A. A. Zhikhoreva, A. V. Belashov, A. V. Salova, I. K. Litvinov, T. N. Belyaeva, E. S. Kornilova, I. V. Semenova, and O. S. Vasyutinskii, "QPI- and FLIM-assisted multimodal analysis of the dynamics of morphological and physiological parameters of cells," Light: Advanced Manufacturing 6(4), 843–855 (2026).
8. J. Chatterjee, K. Bhattacharya, "High resolution microscopic imaging using a phase SLM," Journal of Optics 54(2), 286–291 (2025).
9. A. Keskin, G. Kaya, N. Kaya, J. Strohaber, A. A. Kolomenskii, and H. A. Schuessler, "Dynamic control of airy beams using real-time phase-amplitude encoding on a spatial light modulator," Optics 5(4), 581–594 (2024).
10. K. Fan-Chiang, S. Huang, C. Shen, H. Wang, Y. Li, H. Tsai, and Y. Huang, "Analog LCOS SLM devices for AR display applications," Journal of the Society for Information Display 28(7), 581–590 (2020).
11. C. Fan, H. Zhao, Z. Zhao, J. Li, Y. Du, X. Yang, and L. Zhang, "Single-shot quantitative phase imaging with phase modulation of a liquid crystal spatial light modulator (LC-SLM) under white light illumination," Optics Letters 47(20), 5264 (2022).
12. I. Shevkunov, V. Katkovnik, N. V. Petrov, and K. Egiazarian, "Super-resolution microscopy for biological specimens: lensless phase retrieval in noisy conditions," Biomedical Optics Express 9(11), 5511 (2018).
13. Z. Wang, L. Millet, M. Mir, H. Ding, S. Unarunotai, J. Rogers, M. U. Gillette, and G. Popescu, "Spatial light interference microscopy (SLIM)," Optics Express 19(2), 1016 (2011).
14. I. A. Favre-Bulle, A. B. Stilgoe, E. K. Scott, and H. Rubinsztein-Dunlop, "Optical trapping *in vivo*: theory, practice, and applications," Nanophotonics 8(6), 1023–1040 (2018).
15. I. Galaktionov, A. Nikitin, J. Sheldakova, V. Toporovsky, and A. Kudryashov, "Focusing of a laser beam passed through a moderately scattering medium using phase-only spatial light modulator," Photonics 9(5), 296 (2022).
16. S. Mukherjee, A. Vijayakumar, and J. Rosen, "Spatial light modulator aided noninvasive imaging through scattering layers," Scientific Reports 9(1), 17670 (2019).
17. Z. Zhang, L. E. Russell, A. M. Packer, O. M. Gauld, and M. Häusser, "Closed-loop all-optical interrogation of neural circuits *in vivo*," Nature Methods 15(12), 1037–1040 (2018).
18. F. M. Engelmann, I. Mayer, D. S. Gabrielli, H. E. Toma, A. J. Kowaltowski, K. Araki, and M. S. Baptista, "Interaction of cationic meso-porphyrins with liposomes, mitochondria and erythrocytes," Journal of Bioenergetics and Biomembranes 39(2), 175–185 (2007).
19. B. W. Pogue, B. Ortel, N. Chen, R. W. Redmond, and T. Hasan, "A photobiological and photophysical-based study of photo- toxicity of two chlorins," Cancer Research 61(2), 717–724 (2001).
20. J. Yang, A. Griffin, Z. Qiang, and J. Ren, "Organelle-targeted therapies: a comprehensive review on system design for enabling precision oncology," Signal Transduction and Targeted Therapy 7(1), 379 (2022).
21. X. Du, S. Huang, Z. Lin, G. Chen, Y. Jiang, and H. Zhang, "Organelle-targeted small molecular photosensitizers for enhanced photodynamic therapy: a minireview for recent advances and potential applications," Chemical Communications 61(40), 7236–7252 (2025).
22. M. J. Iqbal, A. Kabeer, Z. Abbas, H. A. Siddiqui, D. Calina, J. Sharifi-Rad, and W. C. Cho, "Interplay of oxidative stress, cellular communication and signaling pathways in cancer," Cell Communication and Signalling 22(1), 7 (2024).
23. A. V. Belashov, A. A. Zhikhoreva, A. V. Salova, T. N. Belyaeva, I. K. Litvinov, E. S. Kornilova, and I. V. Semenova, "SLIM-assisted automatic cartography of cell death types and rates resulting from localized photodynamic treatment," Journal of the Optical Society of America A 41(11), C72 (2024).
24. A. V. Belashov, A. A. Zhikhoreva, T. N. Belyaeva, N. N. Nikolsky, I. V. Semenova, E. S. Kornilova, and O. S. Vasyutinskii, "Quantitative assessment of changes in cellular morphology at photodynamic treatment in vitro by means of digital holographic microscopy," Biomedical Optics Express 10(10), 4975 (2019).
25. A. V. Belashov, A. A. Zhikhoreva, V. G. Bespalov, V. I. Novik, N. T. Zhilinskaya, I. V. Semenova, and O. S. Vasyutinskii, "Refractive index distributions in dehydrated cells of human oral cavity epithelium," Journal of the Optical Society of America B 34(12), 2538 (2017).
26. I. Shevkunov, N. V. Petrov, "Phase retardation analysis in a rotated plane-parallel plate for phase-shifting digital holography," Journal of Imaging 8(4), 87 (2022).
27. Z. Wang, G. Popescu, "Quantitative phase imaging with broadband fields," Applied Physics Letters 96(5), 051117 (2010).
28. G. Popescu, L. P. Deflores, J. C. Vaughan, K. Badizadegan, H. Iwai, R. R. Dasari, and M. S. Feld, "Fourier phase microscopy for investigation of biological structures and dynamics," Optics Letters 29(21), 2503–2505 (2004).
29. Y. Pan, S. Guo, Z. J. Smith, and K. Chu, "Simultaneous 3D deconvolution and halo removal for spatial light interference microscopy through a two-edge apodized Wiener filter," Journal of the Optical Society of America A 39(2), 287–296 (2022).
30. T. H. Nguyen, M. Kandel, H. M. Shakir, C. Best-Popescu, J. Arikkath, M. N. Do, and G. Popescu, "Halo-free phase contrast microscopy," Scientific Reports 7(1), 44034 (2017).

31. A. A. Kerov, A. V. Kozlov, P. A. Cheremkhin, A. V. Shifrina, R. S. Starikov, E. Y. Zlokazov, E. K. Petrova, V. A. Nebavskiy, and N. N. Evtikhiev, "Speckle noise reduction in digital holography by 3D adaptive filtering," Sensors 25(17), 5402 (2025).
32. P. A. Cheremkhin, N. N. Evtikhiev, A. V. Kozlov, V. V. Krasnov, V. G. Rodin, and R. S. Starikov, "An optical-digital method of noise suppression in digital holography," Journal of Optics 24(11), 115702 (2022).
33. R. Bowman, N. Muller, X. Zambrana-Puyalto, O. Jedrkiewicz, P. Di Trapani, and M. J. Padgett, "Efficient generation of Bessel beam arrays by means of an SLM," The European Physical Journal Special Topics 199(1), 159–166 (2011).
34. C. Rosales-Guzmán, N. Bhebhe, and A. Forbes, "Simultaneous generation of multiple vector beams on a single SLM," Optics express 25(21), 25697 (2017).
35. V. Nikolenko, D. S. Peterka, R. Araya, A. Woodruff, and R. Yuste, "Spatial light modulator microscopy," Cold Spring Harbor Protocols 2013(12), pdb.top079517 (2013).
36. X. Li, Y. Zhou, Y. Cai, Y. Zhang, S. Yan, M. Li, R. Li, and B. Yao, "Generation of hybrid optical trap array by holographic optical tweezers," Frontiers in Physics 9, 591747 (2021).
37. A. V. Belashov, A. A. Zhikhoreva, A. V. Salova, T. N. Belyaeva, I. K. Litvinov, E. S. Kornilova, I. V. Semenova, and O. S. Vasyutinskii, "Analysis of Radachlorin localization in living cells by fluorescence lifetime imaging microscopy," Journal of Photochemistry and Photobiology B: Biology 243, 112699 (2023).
38. Y. Wu, J. Wang, C. Chen, C.-J. Liu, F.-M. Jin, and N. Chen, "Adaptive weighted Gerchberg-Saxton algorithm for generation of phase-only hologram with artifacts suppression," Optics Express 29(2), 1412–1427 (2021).
39. D. Kim, A. Keesling, A. Omran, H. Levine, H. Bernien, M. Greiner, M. D. Lukin, and D. R. Englund, "Large-scale uniform optical focus array generation with a phase spatial light modulator," Optics Letters 44(12), 3178 (2019).
40. P. Girshovitz, N. T. Shaked, "Generalized cell morphological parameters based on interferometric phase microscopy and their application to cell life cycle characterization," Biomedical Optics Express 3(8), 1757 (2012).
41. A. V. Belashov, A. A. Zhikhoreva, T. N. Belyaeva, A. V. Salova, E. S. Kornilova, I. V. Semenova, and O. S. Vasyutinskii, "Machine learning assisted classification of cell lines and cell states on quantitative phase images," Cells 10(10), 2587 (2021).
42. A. A. Zhikhoreva, A. V. Belashov, A. B. Danilova, N. A. Avdonkina, I. A. Baldueva, M. L. Gelfond, T. L. Nekhaeva, I. V. Semenova, and O. S. Vasyutinskii, "Significant difference in response of malignant tumor cells of individual patients to photodynamic treatment as revealed by digital holographic microscopy," Journal of Photochemistry and Photobiology B: Biology 221, 112235 (2021).

Alternating Magnetic Field Effect on Oxygen Transport Function of Red Blood Cells *in Vitro*

Olga V. Slatinskaia[1], Alexander V. Priezzhev[1*], Lizaveta V. Uzlova[2], Victor V. Zinchuk[2], and Andrei E. Lugovtsov[1]
[1] Faculty of Physics, M.V. Lomonosov Moscow State University, GSP-1, Leninskie gory, Moscow 119911, Russian Federation
[2] Grodno State Medical University, 80 Gorkogo str., Grodno 230009, Republic of Belarus
*e-mail: avp2@mail.ru

Abstract. The study presents data on the influence of alternating magnetic field (AMF) on blood *in vitro*, manifested by a decrease in hemoglobin's affinity for oxygen and an increase in nitrate/nitrite content. The effect of short-term exposure (30 min) to AMF with the strength of 300 mT and frequency of 20 Hz (corresponding to the radiation from static magnetic field sources) on the oxygen transport function (OTF) of erythrocytes and conformation of Fe-containing hemoporphyrin and globin of hemoglobin was demonstrated using Raman spectroscopy. Alteration in the content of hemoglobin in the T and R-forms was revealed, indicating a different affinity of hemoglobin for ligands and associated with changes in the polarity of the globin amino acids. It was also demonstrated that exposure of erythrocytes to AMF for 360 s modifies their gasotransmitter-forming function. These changes can significantly influence the alteration of blood OTF and change the blood flow in meeting tissue oxygen demands. The obtained results indicate the point to the involvement of the gasotransmitter-forming function in modifying blood OTF and, consequently, in altering the adequacy of blood flow in meeting tissue oxygen demands.

Keywords: oxygen transport function; magnetic field; erythrocyte; Raman spectroscopy.

Paper #9544 received 1 Mar 2026; revised manuscript received 24 May 2026; accepted for publication 26 May 2026; published online 15 Jun 2026. doi: 10.18287/JBPE26.12.020308.

1 Introduction

The adaptive capabilities of erythrocytes are limited by cytoplasmic mechanisms, in which hemoglobin (Hb) plays a key role. It serves as a temporary transport depot for oxygen and possesses a number of properties that ensure both the intensive formation of oxygenated hemoglobin and the timely release of O_2. The state of the cytoplasm system of regulating Hb's affinity for oxygen significantly influences the mobility of changes in blood. At the same time, this autonomous system, operating on a feedback principle, is capable of maintaining the adaptive properties of blood independently of circulatory conditions. In the real conditions of the organism during hypoxia, the action of various modulators causes changes in Hb's affinity for oxygen. This is particularly important for ensuring adequate oxygen flow to tissues and can be used to eliminate oxygen deficiency [1].

Impaired tissue oxygenation underlined the pathogenesis of a wide range of diseases, from cardiovascular and chronic lung diseases to critical conditions accompanied by multiple organ dysfunction syndrome. One of the factors reducing treatment effectiveness is tissue hypoxia. It is known that the oxygen transport function of blood is determined by the interaction of erythrocytes with other cells, plasma components, and vascular cells [2]. The main component of red blood cells that transports oxygen is the tetrameric protein hemoglobin (Hb), which contains Fe^{2+}-protoporphyrin IX (heme). Heme is known to exist in two conformational states [3, 4]: when Hb binds oxygen, a conformational change occurs, increasing Hb's affinity for molecular oxygen. This model of cooperative O_2 binding is based on two Hb states:

This paper was presented at the International Russian-Chinese Workshop on Light for Life Sciences, St. Petersburg, Russian Federation, October 17 – 20, 2025.

– R-state (“flat” heme conformation) with high affinity for oxygen-oxyhemoglobin (oHb);

– T-state (“domed” (non-planar) conformation) with low affinity for oxygen-deoxyhemoglobin (dHb).

Depending on the number of O_2 molecules bound by Hb subunits, local concentrations of H^+ ions, CO_2, etc., it is possible to observe the R-state of heme not bound to O_2 and the T-state conformation of heme bound to O_2. The transition between T and R states is a trigger that initiates a series of structural cooperative changes of globin during the dissociation (or binding) of O_2 [5]. In this case, oHb is characterized by higher packing density globule structure than dHb [6]. For non-invasive assessment of the oxygen transport function (OTF) and conformation of Hb molecules in the cytoplasm of erythrocytes, Raman spectroscopy is widely used [6–9].

One of the promising methods for influencing the erythrocytes OTF is low-intensity magnetic field (MF) exposure, which demonstrates a pronounced anti-hypoxic effect: improved tissue oxygenation and reduced Hb affinity for oxygen (facilitating O_2 release in the microcirculatory bed). The sensitivity of erythrocytes to a magnetic field (100–600 mT) has been previously demonstrated: the binding of oxygen to Hb affects its magnetic susceptibility, reduces blood viscosity, leads to an increase in osmotic fragility, a decrease in the elasticity of the plasma membrane and a change in blood flow velocity [10–13].

Furthermore, prolonged or high-intensity magnetic field exposure can affect the tertiary structure of the protein, which in turn influences Hb’s affinity for ligands [14]. However, the operation of molecular-cellular mechanisms following magnetic field exposure is still not fully understood. Studies [15, 16] discuss the hypothesis of mediated regulation through the gasotransmitter systems of erythrocytes (nitric oxide NO and hydrogen sulfide H_2S). These systems can alter the hemoglobin conformation through the formation of nitroso- and sulfo-derivatives, thereby changing its affinity for oxygen.

The goal of this work is aimed at studying the influence of short-term exposure of erythrocytes to alternating magnetic field (AMF) (30 min, 300 mT, 20 Hz) on cytoplasmic Hb. As a control for changes in heme conformation, purified Hb isolated from erythrocytes (isolated Hb) was used.

2 Materials and Methods

2.1. Experiments with Rat Blood

2.1.1 Isolation Erythrocytes from Rat Blood

Blood samples were collected on white male-rats weighing 250–300 g. Animal manipulations were performed under conditions of adequate analgesia in accordance with the recommendations and decision of the Committee on Biomedical Ethics of Grodno State Medical University. For 7–10 days prior to each stage of the study, the animals were acclimatized to vivarium conditions. The studies were conducted in the first half of the day.

Erythrocytes were obtained by separating the whole blood samples into plasma and leukocyte- and platelet-depleted mass of erythrocytes (at 1500 g), followed by triple washing of the erythrocytes with the isotonic 0.9% NaCl solution.

2.1.2 Effect of Alternating Magnetic Field (AMF)

The “UniSPOK” with the IAMV-4 inductor (LLC “MagnoMed”, Belarus) was used as the AMF source. With the pulsed current with a frequency 60–200 Hz, modulated at 10 Hz, the magnetic induction was 150 mT.

In the first series of experiments, AMF exposure was applied to the erythrocyte suspensions (in isotonic 0.9% NaCl solution or blood plasma) for 360 s. In the second series of experiments, 1 ml of whole blood was exposed to AMF with different durations (120 and 360 s). As a control, the erythrocytes with added isotonic 0.9% NaCl solution or plasma depleted of leukocytes and platelets were used. The number of replicates was 9.

2.1.3 Oxygen Transport Function (OTF) of Blood

OTF indicators were determined at 37 °C using the micro-gas analyzer “Synthesis-15” (Instrumentation Laboratory, USA) based on the measurement of p50 parameter (pO_2 at 50% blood oxygen saturation) by the spectrophotometric method at actual values of temperature, pH, and pCO_2 ($p50_{real}$). Parameter $p50_{stand}$ was calculated using the J. W. Severinghaus formulas [17]. Based on the $p50_{real}$ and Hill equation, the position of the oxyhemoglobin dissociation curve was calculated. NO production was assessed by the concentration of nitrate/nitrites (NO_3^-/N O_2^-) using the Griess reagent [18] on a PV1251C spectrophotometer (Solar, Belarus) at the wavelength of 540 nm.

2.2 Experiments with Human Blood

2.2.1 Isolation Erythrocytes from Human Blood

Blood from healthy donors was collected from the cubital vein into vacuum tubes (Vacuette, Russia) with heparin (20–50 U/mL blood) as an anticoagulant and stored at 4°C for 3 h after collection. The erythrocyte fraction was sedimented by centrifuging the blood at 1500 g for 5 min at 4°C (Laborfuge 400R, Thermo Scientific, USA). The resulting supernatant was removed, and the pellet was washed in Allen’s solution (145 mM NaCl, 5 mM KCl, 4 mM Na_2HPO_4, 1 mM NaH_2PO_4, 1 mM $MgSO_4$, 5 mM glucose, 1 mM $CaCl_2$ (Sigma, USA), pH 7.4). The washing procedure was repeated three times. Washed erythrocytes were suspended in Allen’s solution (Ht = 40%), stored at 4 °C and used in the experiment within 3 h after isolation.

Experiments with human blood were conducted in accordance with the principles of biomedical ethics as formulated in the Declaration of Helsinki of 1964 and its subsequent amendments and were approved by the local bioethics committee of the Lomonosov Moscow State University.

2.2.2 Isolation of Hb from the Erythrocytes

Phosphate buffer (pH 7.4) was added to the erythrocytes in a 1:10 ratio. The suspension was thoroughly mixed and centrifuged at 6000 g for 10 min at +4 °C. The supernatant was separated and stored at +4 °C. The sample was used within 3 h after isolation.

2.2.3 Exposure to an Alternating Magnetic Field (AMF)

A magnetic device (Department of Biophysics, Lomonosov Moscow State University, Russia) was used to generate the AMF: magnetic induction 300 mT, rotation frequency ~20 Hz). When studying the effect of AMF on Hb, the magnetic device was positioned above the capillary at a distance of ≈ 1.5 cm. The exposure time was 30 min. Changes in the conformation of the heme and globin were recorded after 1 min. During Raman signal acquisition, the magnetic device was turned off. All experiments were performed at room temperature.

2.2.4 Raman Spectroscopy (RS)

The signal from cytoplasmic Hb was recorded by the NTEGRA-SPECTRA confocal microscope-spectrometer (NT-MDT, Russia) in the range of 1000–3000 cm^{-1}, grid: 600 lines per mm with a measurement step of 0.8 cm^{-1}. CCD detector with Peltier cooling to –50°C was used (objective 5× with an aperture of 0.15 (Olympus, Japan)). Line excitation was 532 nm (2 mW per 10–12 μm laser spot size to record resonance Raman scattering of Hb in individual erythrocytes), the recording time for one spectrum was 10 s. Measurements were performed at room temperature (22–25 °C). To record the Raman spectra, the sample (Hb or erythrocytes) was placed in a hematocrit capillary (Agat-Med, Russia) with a cross-sectional diameter of 1 mm. The spectrum processing included baseline subtraction and smoothing with Origin2021 (Origin-Lab Corp., United States).

To analyze conformational changes of the heme and globin in Hb the following ratios of characteristic Raman bands were used [6, 19–21]:

I_{1375}/I_{1127} – contribution of lateral –CH_3 groups of pyrrole half-rings in hemoporphyrin. It changes along with the changes in globin conformations in the immediate vicinity of the heme. It characterizes the manifestation of symmetrical and asymmetrical vibrations of pyrrole half-rings (a decrease indicates an increase in heme mobility and the proportion of oxyhemoglobin);

I_{1375}/I_{1172} – contribution of the asymmetrical and symmetrical vibrations of pyrrole rings in hemoporphyrin (depends on the action of the protein environment of globin and on changes in heme pyrroles);

I_{1580}/I_{1550} – contribution of the vibrations of methine bridges between pyrroles in hemoporphyrin emerging in macrocycle deformations (an increase indicates a rise of the Hb affinity to ligands);

$I_{1375}/I_{(1355+1375)}$ – increase indicates an increase in the relative amount of oxygenated Hb complexes;

I_{1618}/I_{1580} – contribution of the stretching vibrations (C_1C_2) of vinyl groups relative to C_aC_mH, methine bridge vibrations. An increase indicates an increase in the relative amount of Hb complexes with NO (the Hb–NO(I) complex);

I_{2850}/I_{2880} – contribution of the symmetrical vibrations of methylene groups in –CH amino acids of globin (an increase characterizes a rise of the packing density of amino acids);

I_{2880}/I_{2930} – contribution of asymmetric vibrations of C-H stretch vibrations from free amino acid side-chain CH_2 groups of amino acids (an increase characterizes a rise in the orderliness and packing density of amino acids).

Due to the fact that rat blood has less stable parameters during long-term measurements, the work was carried out on human blood using the Raman method [22].

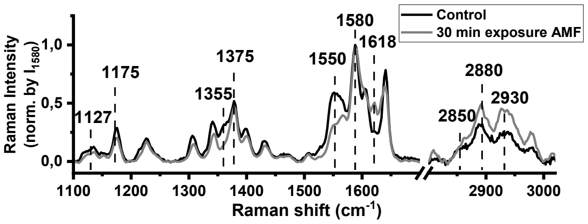

Fig. 1 Raman spectrum of erythrocyte's hemoglobin before (control) and after 30 min of AMF exposure. The spectra are normalized to the maximum intensity of the peak at 1580 cm^{-1}.

2.3 Statistical Analysis

The *t*-test was used to assess the statistical significance of the results. The results were considered significantly different at $p < 0.05$. The number of measurements was 3.

3 Results and Discussion

3.1 Changes in the Oxygen-Transport Function of Erythrocytes after Exposure to AMF

It is hypothesized that blood cellular elements may significantly influence the changes in the OTF during *in vitro* AMF exposure. Therefore, to assess the influence of AMF on the OTF of rat erythrocytes,

Table 1 Effect of the oxygen affinity of Hb (M ± m) following AMF exposure to rat erythrocytes *in vitro* (* – $p < 0.05$ relative to the control (without exposure to AMF)).

Parameters	**Exposure AMF**			
	Addition of 0.9% NaCl isotonic solution		**Addition of plasma**	
	Control	**Erythrocytes**	**Control**	**Erythrocytes**
$p50_{real}$, mm Hg	42.8 ± 2.9	50.7 ± 1.7*	41.1 ± 1.4	46.2 ± 0.8*
$p50_{stand}$, mm Hg	35.1 ± 2.04	39.8 ± 1.01*	38.2 ± 1.16	38.9 ± 1.52*

AMF – alternating magnetic field.

Table 2 Changes in nitrate/nitrite content after AMF exposure in rat blood *in vitro* (M ± m) (* – $p < 0.05$ relative to control (without exposure to AMF)).

Parameters	**Control**	**AMF exposure time**	
		120 s	**360 s**
nitrate/nitrites, μmol	7.32 ± 0.34	8.61 ± 0.41*	9.26 ± 0.4*

AMF – alternating magnetic field.

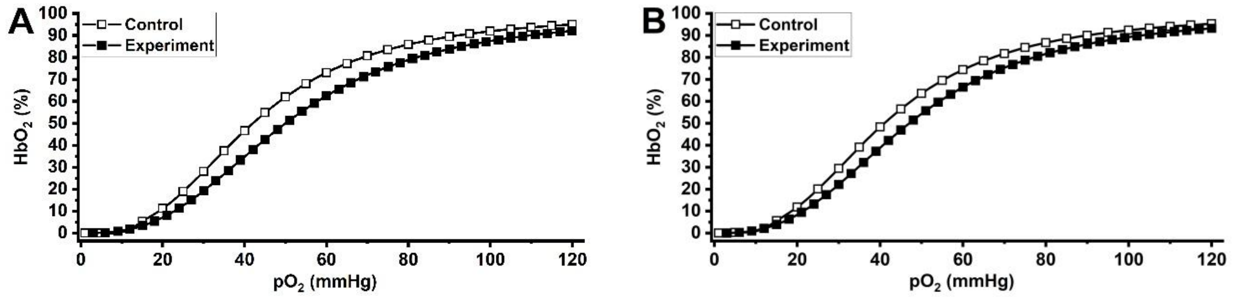

Fig. 2 The effect of AMF exposure on the position of the oxyhemoglobin dissociation curve in (A) erythrocytes with the addition of isotonic 0.9% NaCl solution and in (B) erythrocytes with the addition of plasma.

mixtures of erythrocytes with an isotonic 0.9% NaCl solution and erythrocytes with plasma depleted of leukocytes and platelets were prepared (Table 1, Fig. 2). After exposing *in vitro* the erythrocyte samples to AMF for 120 s, we found that the value of the $p50_{real}$ parameter increased more markedly in the erythrocytes mixture with the addition of the isotonic 0.9% NaCl solution-by 33.18% ($p < 0.05$)-compared to the erythrocytes mixture with added plasma (where the increase in $p50_{real}$ was 12.41% ($p < 0.05$)). This indicates a rightward shift of the oxyhemoglobin dissociation curve under the influence of AMF. The $p50_{stand}$ value also increased in the erythrocytes with the isotonic 0.9% NaCl solution by 13.39% ($p < 0.05$).

The production of the gasotransmitter NO was assessed by the content of nitrate/nitrites in blood plasma (Table 2). At the 120-s mark, this indicator increased by 17.62% ($p < 0.01$), and a further increase in exposure time was accompanied by a rise in NO concentration by 26.5% relative to the control ($p < 0.01$) at 360 s of exposure.

Thus, we have demonstrated that the AMF exposure for 360 s causes a modification of the gasotransmitter producing function. These changes may significantly influence the alteration of the blood's OTF and, consequently, the adequate provision of tissue oxygen demands by blood flow [16]. The obtained results indicate the lack of contribution from blood cellular elements leukocytes and platelets to the change in OTF and the involvement of the gasotransmitter-producing function in modifying the blood's OTF.

3.2 Changes in Hb Conformation after Exposure to AMF

Changes in the conformation of the heme and the packing density of the globin amino acids in isolated and cytoplasmic Hb under the exposure of AMF were assessed in human erythrocytes with measurements taken every minute for 30 min. To analyze the conformational changes, the following ratios of characteristic Raman bands for Hb molecule after AMF exposure and without AMF exposure were analyzed (Fig. 3). We have demonstrated that the dynamics of changes in the ratios of Raman spectrum band intensities in the absence of AMF exposure do not show statistically significant changes relative to the onset of changes. Conformational changes in isolated erythrocytes may be caused by gradual oxygenation of the erythrocytes and the thermal effect of the laser (~0.03 J in 10 s). At the same time, erythrocytes during their vital activity (NO synthesis, decrease in ATP, glucose) can extract oxygen from the buffer, which also affects the conformation of the heme. However, the dynamics of changes in the absence and with AMF exposure differ. The observed conformational changes during the measurement of isolated Hb are likely caused by reversible photodissociation of the Fe-O bond [23]. Therefore, it can be concluded that the observed changes with AMF exposure are caused by the magnetic field, not the thermal effect of the laser.

Notably, the groups of isolated Hb and cytoplasmic Hb (Hb_b) without and with AMF exposure, showed different patterns relative to the start of the experiment. Thus, changes in the conformation of Hb are caused by the action of AMF.

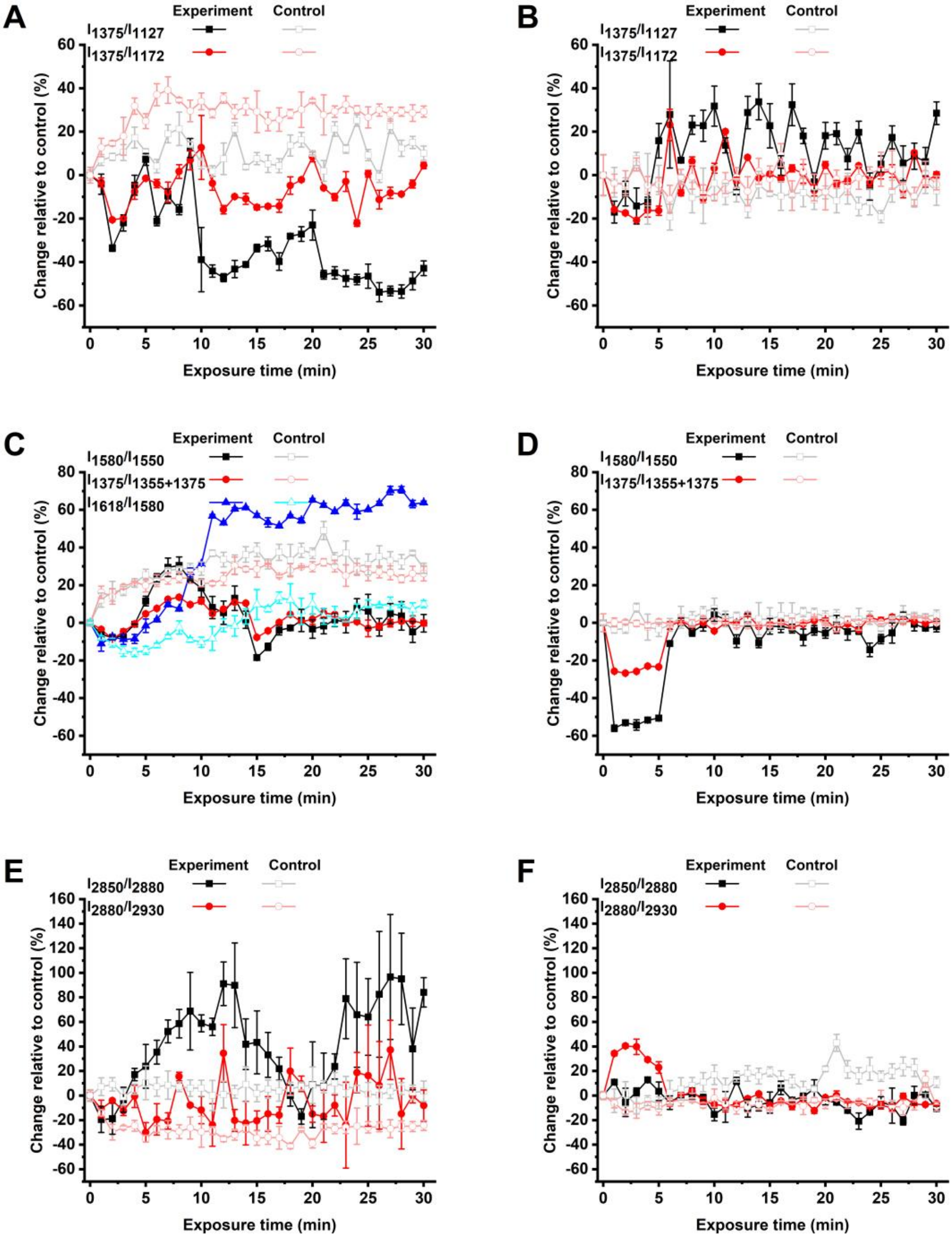

Fig. 3 Changes in the intensity ratio of the Raman peaks for (A, C, E) Hb in the erythrocyte cytoplasm (Hb_b) and for (B, D, F) isolated Hb in phosphate buffer (*in vitro*). (A–D) panels demonstrate changes in heme conformation, (E–F) panels demonstrate changes in conformation of globin. The data are expressed as a change relative to the baseline (0 min). Open circles demonstrate the ratio values for the control group (without AMF exposure). The data are normalized to the beginning of the measurements without the influence of AMF.

We have established that the effects of AMF on the conformation and packing density of isolated Hb and cytoplasmic Hb are manifested differently. This may be due to both the oligomerization of Hb molecules inside the erythrocyte and the biochemical processes within the cell in response to AMF exposure. Specifically, changes in the conformation of isolated Hb were most pronounced in the first 5 min of PMF exposure (Fig. 3, (B, D, F)): an increase in globin packing density is accompanied by a decrease in the proportion of oxyhemoglobin in the sample, indicating a decrease in the affinity of Hb for oxygen. Probably, AMF affects the mobility of heme (an increase in the I_{1375}/I_{1127} ratio), which leads to an increase in the proportion of oHb in the sample to the initial values (without the influence of AMF) from the 5th min of measurements.

For the cytoplasmic Hb, the most pronounced changes in heme conformation are observed during the first 12 min of exposure to an AMF (Fig. 3 (A, C, E)): the proportion of Hb with a planar heme conformation increases, ligand affinity rises (increase in I_{1580}/I_{1550}, $I_{1375}/I_{(1355+1375)}$), and the packing density of globin increases (I_{2880}/I_{2930}, I_{2850}/I_{2880}), indicating an increase in the fraction of oHb in the sample. Considering that the changes in Hb conformation are accompanied by an increase in the number of Hb complexes with NO (a 60% increase in I_{1618}/I_{1580}, $p < 0.05$), the AMF appears to influence the activation of the NO synthase enzyme inside erythrocytes. Subsequently, when the content of Hb-NO complexes reaches a steady-state level, a decrease in ligand affinity and an increase in the proportion of Hb with a dome-shaped heme conformation by 10–12% relative to the control were detected. Thus, changes in the cytoplasm (ordering of Hb molecules, alteration of their conformation, and possible redistribution within the erythrocyte cytoplasm [19–21]) lead to changes in the content of total nitrates/nitrites and their complexes in the erythrocyte cytoplasm.

Increasing the AMF exposure time to 15–30 min, changes in the valence vibrations of the pyrrole rings (decrease in I_{1375}/I_{1172}) and an increase in the packing density of globin (I_{2880}/I_{2930}) were revealed. The observed changes in globin packing density may indicate an alteration in the membrane surface charge and the binding of Hb molecules to band 3 protein (AE1) [24].

The experiment demonstrated that the exposure to AMF for 30 min is accompanied by a non-monotonic change in heme conformation and globin packing density. Depending on the exposure duration, the OTF of erythrocytes is influenced by the activity of NO synthase, which leads to increased binding of NO by Hb molecules in erythrocytes upon AMF exposure. Another contributing factor is the conformational changes of the heme. We hypothesize that with AMF exposure times exceeding 15 min, the decrease in hemoglobin’s oxygen affinity may be due to a changes in the spin state of Fe [25, 26].

4 Conclusions

In this study, we demonstrated that exposure to AMF for 30 min significantly affects not only the OTF of erythrocytes and isolated Hb but also the mobility of the globin. Exposure to AMF is accompanied by an increase in NO_3^-/NO_2^- levels and a decrease in hemoglobin's affinity for oxygen, suggesting that AMF-induced changes in OTF are primarily mediated by the gasotransmitter nitric oxide.

Exposure to AMF for 30 min leads to an increased proportion of Hb with the T- state heme and enhanced affinity for ligands (oxygen and NO) (I_{1375}/I_{1127}, I_{1580}/I_{1550}), decrease in the proportion of oHb in the sample (changes in the ratio of Raman scattering band intensities $I_{1375}/I_{(1355+1375)}$. AMF has a significant effect on increasing the packing density of CH-groups of globin amino acids of intracellular Hb (I_{2850}/I_{2930}, I_{2880}/I_{2930}), which may affect the efficiency of OTF. Moreover, the effects of AMF are more pronounced in Hb of erythrocytes than in isolated Hb and do not depend on the presence of other blood cellular elements (leukocytes, platelets).

Conflicts of Interest

The authors declare that they have no conflicts of interest or competing financial interests related to this work.

References

1. V. V. Zinchuk, N. V. Hlutkina, “Hemoglobin affinity to oxygen during coronavirus infection: New faces of a known problem,” Journal of Evolutionary Biochemistry and Physiology 59(6), 2242–2257 (2023).
2. A.V. Muravyov, I. A. Tikhomirova, S. V. Bulaeva, V. A. Vdovin, and A. A. Muravyov, “The study of the role of individual blood characteristics in its fluidity alteration and transport efficiency,” Russian Journal of Biomechanics 16(3), 32–41 (2012). [in Russian]
3. J. L. Hoard, “Stereochemistry of Hemes and Other Metalloporphyrins: The remarkably varied stereochemistry of the iron porphyrins is utilized in the hemoprotein function,” Science 174(4016), 1295–1302 (1971).
4. Y. Sugita, M. Nagai, and Y. Yoneyama, “Circular dichroism of hemoglobin in relation to the structure surrounding the heme,” Journal of Biological Chemistry 246(2), 383–388 (1971).
5. J. Monod, J. Wyman, and J.-P. Changeux, “On the nature of allosteric transitions: A plausible model,” Journal of Molecular Biology 12(1), 88–118 (1965).

6. S. C. Goheen, L. J. Lis, O. Kucuk, M. P. Westerman, and J. W. Kauffman, "Study of intact and modified erythrocyte membranes with laser Raman spectroscopy," Journal of Raman Spectroscopy 24(9), 599–602 (1993).
7. B. R. Wood, B. Tait, and D. McNaughton, "Micro-Raman characterisation of the R to T state transition of haemoglobin within a single living erythrocyte," Biochimica et Biophysica Acta (BBA) - Molecular Cell Research 1539(1–2), 58–70 (2001).
8. B. R. Wood, D. McNaughton, "Micro-Raman characterization of high- and low-spin heme moieties within single living erythrocytes," Biopolymers 67(4–5), 259–262 (2002).
9. E. S. Allakhverdiev, E. A. Rezukhina, O. V. Slatinskaya, O. V. Rodnenkov, G. V. Maksimov, and T. V. Martynyuk, "Possibility of evaluation of oxygen transport function in PAH patients on effective selexipag-based therapy," Eurasian Heart Journal (3), 44–52 (2023). [in Russian]
10. A. N. Shalygin, S. B. Norina, and E. I. Kondorsky, "Behaviour of erythrocytes in high gradient magnetic field," Journal of Magnetism and Magnetic Materials 31–34, 555–556 (1983).
11. R. Tao, K. Huang, "Reducing blood viscosity with magnetic fields," Physical Review E 84(1), 011905 (2011).
12. T. E. Shalaby, M. M. Shawki, "Biophysical and biochemical changes in the characteristics of rat blood exposed to combined alternating and static magnetic fields," Romanian Journal of Biophysics 16(3), 169–180 (2006).
13. S. Sharma, U. Singh, and V. K. Katiyar, "Magnetic field effect on flow parameters of blood along with magnetic particles in a cylindrical tube," Journal of Magnetism and Magnetic Materials 377, 395–401 (2015).
14. E. Calabro, S. Magazu, "Unfolding-induced in hemoglobin by exposure to electromagnetic fields: A FTIR spectroscopy study," Oriental Journal of Chemistry 30(1), 31–35 (2014).
15. V. V. Zinchuk, V. O. Lepeev, and I. E. Hulyai, "Participation of Gas Transmitters in the Modification of Blood Oxygen Transport Function under the Effect of a Magnetic Field," I.M. Sechenov Russian Physiological Journal 102(10), 1176–1184 (2016).
16. V. V. Zinchuk, V. O. Lepeev, "The in vitro Effect of a Magnetic Field on the Oxygen-Transport Function and the Gaseous Transmitter System in Blood," Biophysics 63(3), 436–440 (2018).
17. J. W. Severinghaus, "Blood gas calculator," Journal of Applied Physiology 21(3), 1108–1116 (1966).
18. I. Guevara, J. Iwanejko, A. Dembińska-Kieć, J. Pankiewicz, A. Wanat, P. Anna, I. Gołąbek, S. Bartuś, M. Malczewska-Malec, and A. Szczudlik, "Determination of nitrite/nitrate in human biological material by the simple Griess reaction," Clinica Chimica Acta 274(2), 177–188 (1998).
19. N. A. Brazhe, S. Abdali, A. R. Brazhe, O. G. Luneva, N. Y. Bryzgalova, E. Y. Parshina, O. V. Sosnovtseva, and G. V. Maksimov, "New insight into erythrocyte through *in vivo* surface-enhanced Raman spectroscopy," Biophysical Journal 97(12), 3206–3214 (2009).
20. B. R. Wood, L. Hammer, and D. McNaughton, "Resonance Raman spectroscopy provides evidence of heme ordering within the functional erythrocyte," Vibrational Spectroscopy 38(1–2), 71–78 (2005).
21. K. R. Ward, I. T. Filho, R. W. Barbee, L. Torres, M. H. Tiba, P. S. Reynolds, R. N. Pittman, R. R. Ivatury, and J. Terner, "Resonance Raman spectroscopy: A new technology for tissue oxygenation monitoring," Critical Care Medicine 34(3), 792–799 (2006).
22. C. Layssol-Lamour, T. Lavabre, J. Braun, C. Trumel, and N. Bourgès-Abella, "The effects of storage at 4°C and 20°C on the hemograms of C57BL/6 mice and Wistar rats using the IDEXX ProCyte Dx and blood smear evaluations", Veterinary Clinical Pathology 48(4), 652–667 (2019).
23. G. A. Zalesskaya, E. G. Sambor, and A. V. Kuchinskii, "Effect of intravenous laser irradiation on the molecular structure of blood and blood components," Journal of Applied Spectroscopy 73(1), 115–122 (2006).
24. O. V. Kosmachevskaya, E. I. Nasybullina, V. N. Blindar, and A. F. Topunov, "Binding of erythrocyte hemoglobin to the membrane to realize signal-regulatory function," Applied Biochemistry and Microbiology 55(2), 83–98 (2019).
25. M. Meuwly, M. Karplus, "The functional role of the hemoglobin-water interface," Molecular Aspects of Medicine 84, 101042 (2022).
26. S. Mayda, Z. Kandemir, N. Bulut, and S. Maekawa, "Magnetic mechanism for the biological functioning of hemoglobin," Scientific Reports 10(1), 8569 (2020).

New Opportunities for Non-Invasive Assessment of Blood Microcirculation Parameters in Patients with Cardiac Pathology

Yury Gurfinkel, Simon Matskeplishvili, Petr Ermolinskiy[*], Larisa Dyachuk, Andrei Lugovtsov, Andrei Yamaev, and Alexander Priezzhev
M.V. Lomonosov Moscow State University, 1 Leninskie Gory, Moscow 119991, Russian Federation
*e-mail: ermolinskiy.pb15@physics.msu.ru

Abstract. Cardiovascular diseases such as hypertension (AH), coronary artery disease (CHD), and atrial fibrillation (AF) require precise diagnostic methods to assess the condition of the microvascular bed, which plays an important role in the etiology and progression of these socially significant diseases. In this article, we discuss new possibilities for assessing microcirculation parameters in healthy individuals and patients suffering from hypertension, CHD or AF using non-invasive digital optical capillaroscopy. Thanks to the new image processing program based on the principles of machine learning, it became possible not only to monitor the movement of blood in microvessels, but also to quantitatively assess the range of parameters important for the clinician and, above all, the speed of capillary blood flow, the number and size of erythrocyte aggregates. The results of our study showed a significant decrease in capillary blood flow velocity and an increase in erythrocyte aggregation in patients with hypertension, coronary artery disease, and AF compared to healthy people. These results suggest that the technique could potentially be used in future, dedicated studies to evaluate the effects of antiplatelet and anticoagulant therapies widely used in modern cardiology, assess optimal dosage, and identify early signs of increased bleeding in pericapillary tissues.

Keywords: microcirculation; erythrocyte aggregation; digital capillaroscopy; arterial hypertension; coronary heart disease; atrial fibrillation; capillary blood flow velocity.

Paper #9510 received 9 Feb 2026; revised manuscript received 15 Apr 2026; accepted for publication 16 Apr 2026; published online 23 Jun 2026. doi: 10.18287/JBPE26.12.020310.

1 Introduction

Microrheological parameters reflect the fluidity of blood within capillaries and small vessels. These properties are largely determined by the characteristics of blood cells (such as their size and deformability) as well as by the interactions between formed elements, including erythrocyte and platelet aggregation, and the dynamic interplay between blood cells and the vascular endothelium.

The study of blood microcirculation is one of the most important topics in the assessment of pathophysiological processes occurring in the human body in cardiovascular diseases (CVD). Its relevance is due to the continuing spread of this pathology in the world. According to the World Health Organization, one of the most common cardiovascular pathologies is arterial hypertension (AH). Worldwide, it affects 1.28 billion adults aged 30–79 years [1]. The prevalence of hypertension among adults aged 30–79 years is 34% in men and 32% in women [2].

AH is caused by a persistent increase in blood pressure, the cause of which is dysregulation of vascular tone and at the same time is one of the main pathological links that have a negative impact on the microcirculatory vascular bed, disrupting its functioning [3]. Since these changes are systemic in nature, they eventually lead to

This paper was presented at the International Russian-Chinese Workshop on Light for Life Sciences, St. Petersburg, Russian Federation, October 17 – 20, 2025.

functional and organic damage to the most important organs: the heart, kidneys, and the central nervous system AH [4].

The study of the anatomical and physiological features of precapillary arterioles in arterial hypertension unequivocally indicates an increase in the thickness of their muscular wall with a simultaneous narrowing of their lumen. This process is called remodeling and as shown in several studies, can manifest itself in patients with arterial hypertension even in the earliest stages [5].

Pathological changes in the microcirculation system may be associated not only with a decrease in the diameter of the blood-supplying microvessels, but also with rheological disorders of blood flow associated with intravascular aggregation of erythrocytes and local blood coagulation in microvessels [4].

Various physiological factors are involved in functional and structural changes in microcirculation in hypertension. Pathological processes such as activation of the renin-angiotensin-aldosterone system, increased growth of smooth muscle cells, remodeling of the extracellular matrix, increased deposition of collagen and fibronectin accompany the development of this disease [5, 6].

Most of the circulating cells in our blood interact with each other. Under physiological conditions, the processes of aggregation and disaggregation of erythrocytes are constantly in a state of relative equilibrium [7]. However, the mechanisms for maintaining the balance of erythrocyte aggregation become insufficient with age [8]. This is especially pronounced in patients suffering from coronary heart disease (CHD). This disease is also socially significant, often complicating the cause of hypertension and being one of the main causes of mortality, as well as temporary and permanent disability of the population in the developed countries of the world. Recent research has increasingly emphasized rheological and microcirculatory dysfunction in these diseases. Our preliminary studies have shown an increase in erythrocyte aggregation in patients with CHD [6]. Under pathological conditions, erythrocytes can form persistent aggregates, which can further interact with each other at a weak shear, forming larger and stronger aggregates.

Atrial fibrillation (AF) is a supraventricular arrhythmia with uncoordinated activation of the atria, leading to the loss of effective atrial contractility – a pathology associated with heart rhythm disorders, chaotic contraction of certain groups of atrial muscle fibers with a frequency of up to 300–500 per min. In AF, ordered cardiac activity is replaced by irregular contractions of the ventricles, which affects the rhythmic work of the entire circulatory system. A particular risk in AF is the high likelihood of a blood clot forming in the appendage of the left atrium, which can enter the brain with the blood flow and cause a stroke. This complication is the cause of 15–20% of all stroke cases [9]. Strokes occurring in patients with AF tend to be more severe, resulting in higher mortality rates [10]. Since AF primarily affects older adults (prevalence: 10–20% in people aged ≥ 85 years compared to 0.4–1.0% in people aged 55–60 years), the overall prevalence of AF is projected to more than double by 2050 due to increased life expectancy [11]. All this makes the study of this type of pathology and the need to control the state of aggregation processes against the background of anticoagulant therapy extremely relevant.

The main objective of the work was a noninvasive study of the parameters of blood microcirculation in the capillaries of the nail bed and, above all, the quantitative characteristics of erythrocyte aggregates circulating in the microvascular bed in patients with hypertension, coronary artery disease, and AF.

2 Materials and Methods

2.1 Patients

A total of 171 people were examined; of these, 19 were healthy volunteers of the control group. The remaining 152 people included in the study were patients of the cardiology department of the Medical Research and Education Center of Lomonosov Moscow State University. They were divided into 3 groups: 56 patients with AH, 46 patients with CHD, and 50 patients with AF (see Table 1). In the group with AH, there were 27 men and 29 women. In the CHD group, men prevailed – 34, and 12 women. In the group of patients with AF there were 24 men and 26 women. The control group consisted of 9 men and 10 women.

Table 1 Characteristics of the groups of patients suffering from arterial hypertension (AH), coronary artery disease (CHD), atrial fibrillation (AF), and the control group (Control).

Parameter	**Control**	**AH**	**CHD**	**AF**
Individuals	19	56	46	50
Males	9	27	34	24
Females	10	29	12	26
Mean age ± SD (years)	28 ± 12	60 ± 16	69 ± 10	72 ± 10

Patients with AF in the study took oral anticoagulants (mainly apixaban and rivaroxaban) according to the protocol adopted by the cardiology department. Patients with CHD received antiplatelet therapy, mainly Plavix (Clopidogrel).

The exclusion criteria were as follows: patients over 85 years of age, patients with oncological pathology, chronic liver and kidney diseases, type 2 diabetes mellitus, heart valve pathology, connective tissue, or central nervous system diseases.

2.2 Digital Optical Capillaroscopy

One of the methods for the intravital study of the microrheological properties of blood is digital capillaroscopy, a method of optical non-invasive microscopy that allows you to directly visualize the surface microvessels of the skin and the surrounding tissue *in vivo* [12].

Image processing software allows for non-invasive quantification of static and dynamic microcirculation parameters [13]. Capillaroscopy can be used to quantify important factors such as the degree of swelling of the perivascular tissue, the size of the capillary diameters, the measurement of the velocity of capillary blood flow, and the visualization of blood aggregates within the capillaries. Progress in the approach to the study of blood microcirculation is based on the use of software that allows not only to visually assess the presence of erythrocyte aggregates in the capillary bed, but also to quantify them. This is an important point, since it allows for personalized dosage of antiplatelet and oral anticoagulants, which have become widespread in clinical practice in recent years.

To visualize the capillaries of the human nail bed, a digital capillaroscope “Capillaroscan-1” (AET, Russia) was used, equipped with a high-speed CCD camera (1/3-inch monochrome IT CCD sensor with progressive scanning, resolution 640 × 480 pixels) and up to 200 frames per second, TM-6740GE (JAI, Japan)). The nail bed was illuminated using an LED lighting system. Two magnification options were used: 125× and 400×. 125-fold magnification was used to obtain panoramic images of the capillary bed. At the same time, 400-fold magnification made it possible to obtain more detailed images of the blood circulating in the capillaries, the presence or absence of erythrocyte aggregates, the static parameters of individual capillaries, their length and the size of the perivascular zone, and the capillary blood velocity (CBV).

The study was conducted after a 15- to 20-min rest in a sitting position between 10 and 12 a.m. in a temperature-controlled room ranging from 22 to 23.5 °C. The fingers of the left hand, on which the studies were usually conducted, were at the level of the heart. All participants were asked to refrain from smoking and caffeinated beverages the day before the survey.

Skin temperature was measured in the area of the dorsal middle phalanx of the tested finger of the left hand by precision medical thermometry; the mean skin temperature was 33.2 ± 1.7 °C with no significant differences in the study groups.

To determine the CBV after recording a video fragment, the program stabilizes the dynamic images of the capillaries and then processes the images in a given area of interest in an autonomous mode (Fig. 1). Traces of specific spots differ in the level of light intensity. The software detects different inclusions in the flow of moving capillary blood, marks them, and then recognizes them in the next frame. In this way, the average velocity along the axis of the capillary over 5-sec time intervals (500 frames) is determined. The CBV is evaluated in at least 6 capillaries and the results are averaged. We evaluated the CBVs only in the first-line capillaries, where the capillaries are in the same layer. Thus, the obtained CBV values are not affected by the movement of blood in the vessels lying above and below the capillary under study. A detailed procedure for measuring the CBV is described in our previous article [14].

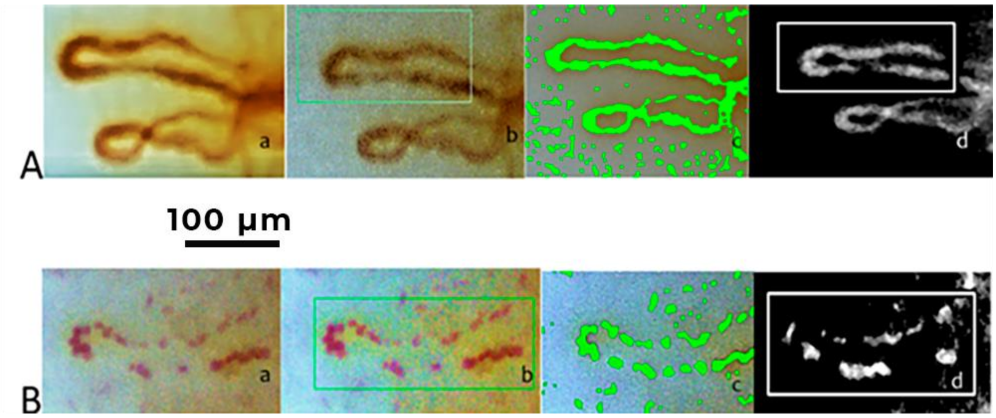

Fig. 1 Stages of software processing of capillary images on the nail bed. (A) Imaging of capillaries without erythrocyte aggregates, (a) before processing; (b) identification of the area of processing; (c) binarization (recognition of capillaries by a program); (d) processing of the selected image. (B) Imaging of capillaries with aggregates of erythrocytes, (a) before processing; (b) designation of a treatment area; (c) binarization (recognition of capillaries by a program); (d) processing of the selected image. Magnification 400×.

To analyze the obtained video recordings of blood flow in the capillary nail bed, an advanced computer program based on complex image analysis was used. The analysis algorithm included three stages: (1) stabilization of the video stream and suppression of noise in the image; (2) cumulative construction of the shape of the capillary and determination of its sections (arterial, transitional and venous sections); 3) straightening of the capillary image into a linear form, which makes it possible to calculate both the number of aggregates and their velocities. Only video recordings obtained with a magnification of 400× were processed with the help of the program. Each video had a duration of approximately 5 s, and 6–10 videos were recorded for each person, giving a total of 10–12 capillary images. In cases of stasis or pathology, the number of recorded video recordings, and, consequently, capillaries, increased. The following parameters characterizing the aggregation of erythrocytes were calculated: the number of blood aggregates per min, the size of blood aggregates (μm^2), and the CBV (μm/s).

2.3 Statistical Analysis

The data was processed, and the graphs were built using a program created by the authors in the Python programming language. In the "research results" Section, the figures show box plots, in which the lower and upper boundaries of the rectangle correspond to the first quartile (Q1) and the third quartile (Q3) with the median inside this rectangle. The whiskers in the drawings indicate standard deviations, the average values (white diamonds) are in the middle. Statistical significance between the experimental groups was determined using the Brunner-Müntzel test [15]. Two samples representing the experimental groups were considered statistically significantly different if the p-value was less than 0.05 (* $p < 0.05$; ** $p < 0.01$; *** $p < 0.001$; **** $p < 0.0001$). The data in the tables are presented as averages ± standard deviations.

3 Research Results

The results obtained are presented in Table 1. These data show that the appearance of aggregates in most cases is accompanied by a slowdown in the velocity of capillary blood flow.

These results are also visualized and displayed in Fig. 2–4. A significant difference was found between healthy people (control group) and patients (CHD, AH, and AF groups) in terms of indicators associated with the presence of erythrocyte aggregates in the bloodstream (Figs. 2–3). In the control group, there are practically no aggregates of erythrocytes, for example, the number of blood aggregates per minute is less than 1 (Table 2). Statistically significant differences are observed between the CHD and AF groups in the number of blood aggregates per minute ($p = 0.0007$) (Fig. 2) and in the velocity of capillary blood flow ($p = 0.035$) (Fig. 4). Statistically significant differences are also observed between the AH and AF groups in the number of blood aggregates per min ($p = 0.03$) (Fig. 2) and the size of blood aggregates ($p = 0.04$) (Fig. 4).

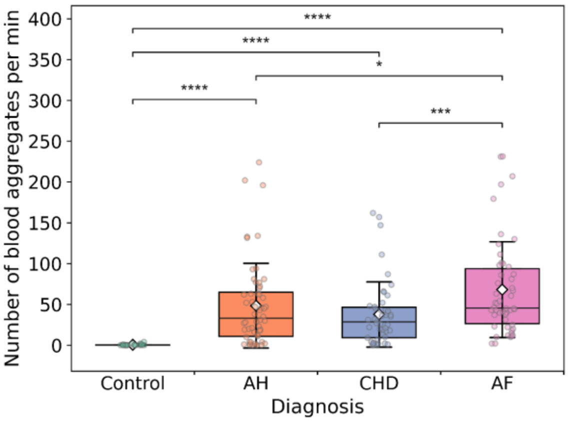

Fig. 2 Number of blood aggregates per minute for 4 groups: Control, AH, CHD and AF. Each point in the figure corresponds to the average for a single donor or patient. The lower and upper boundaries of the rectangle correspond to the first (Q1) and third quartile (Q3) with a median in the form of a horizontal line inside. Errors in the graph are standard deviations. The white rhombus in the center of the rectangle is the average value. * p <0.05; *** $p < 0.001$; **** $p < 0.0001$.

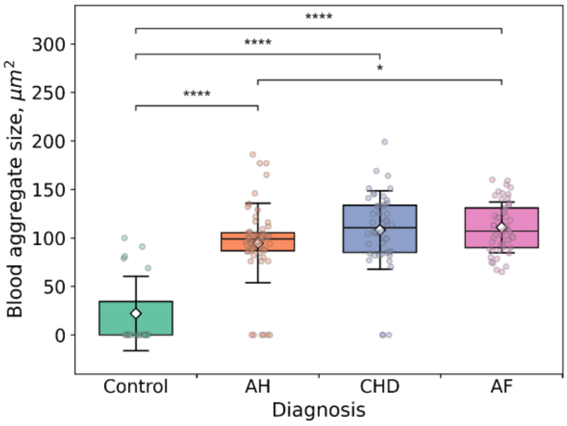

Fig. 3 The average size of the aggregates for the 4 groups: Control, AH, CHD, and AF. Each point in the figure corresponds to the average value for a single donor or patient. The lower and upper boundaries of the rectangle correspond to the first (Q1) and third quartile (Q3) with a median in the form of a horizontal line inside. Errors in the graph are standard deviations. The white rhombus in the center of the rectangle is the average value. * p <0.05; **** $p < 0.0001$.

Table 2 Microcirculation parameters in 4 patient groups: Control group, AH, CHD and AF. Average values and standard deviations of the data are presented.

Parameter	Group (number of individuals)			
	Control (*N* = 19)	**AH (*N* = 56)**	**CHD (*N* = 46)**	**AF (*N* = 50)**
Number of blood aggregates per min	0.5 ± 1	48 ± 52	38 ± 40	68 ± 59
Blood aggregate size, μm^2	22 ± 38	95 ± 41	108 ± 40	111 ± 26
Capillary blood velocity, μm/s	1501 ± 378	1220 ± 588	1398 ± 737	1098 ± 626

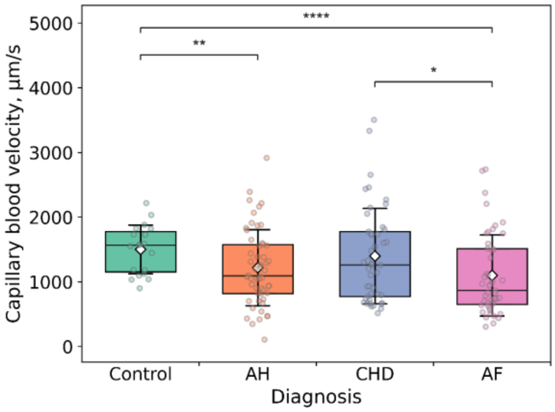

Fig. 4 Capillary blood flow velocity for 4 groups: Control, AH, CHD and AF. Each point in the figure corresponds to the average value for one donor or patient. The lower and upper boundaries of the rectangle correspond to the first (Q1) and third quartile (Q3) with a median in the form of a horizontal line inside. Errors in the graph are standard deviations. The white rhombus in the center of the rectangle is the average value. * p <0.05; ** p <0.01; **** p < 0.0001.

4 Discussion

The data obtained during the study show that the appearance of aggregates in most cases is accompanied by a slowdown in the velocity of capillary blood flow. The reason for this is probably that in hypertension there is an increase in vasoconstriction and/or weakening of vasodilation, as a reaction of precapillary smooth muscle cells, associated with the activation of the sympathoadrenal system. At the same time, the ratio of the wall thickness of the precapillary vessels, mainly arterioles relative to the lumen of the vessel, increases, which leads to a decrease in tissue perfusion, which is especially important for vital organs – the heart, brain, kidneys [4].

As shown in Table 2, the capillary blood flow rate in patients with hypertension was reduced – 1220 ± 588 μm/s, while in the control group of patients without cardiac pathology this indicator was 1501 ± 378 μm/s. In hypertension, the number of aggregates circulating in the capillary network significantly exceeded the same indicator in the group in the group of healthy volunteers, although significantly less than in patients with CHD and AF. It should be noted that 12 out of 56 patients in this group took aspirin.

However, patients with AF are most at risk of impaired rheological properties of the blood. In this group, the lowest capillary blood flow velocity was found – 1098 ± 626 μm/s, the largest number of aggregates per minute – 68 ± 59, as well as the highest size of aggregates compared to patients in the other group, even though almost all patients with AF were taking oral anticoagulants (rivaroxaban, apixaban, dabigatran). Higher doses of anticoagulants could improve the situation but could also increase the risk of bleeding. We consider it expedient to conduct studies on a larger number of patients with this pathology.

Detection of early signs of microcirculation disorders makes it possible to implement a novel approach to the diagnosis and treatment of hypertension patients and, as a result, reduce the risk of complications [16, 17]. In patients with CHD, the average blood flow velocity was 1398 ± 737 μm/s, which is significantly lower than in healthy controls (1501 ± 378) and higher than in AF patients (1098 ± 626) (see Table 2). For the CHD group, the number of aggregates per minute was 38 ± 40, which was the lowest in the presented groups of patients. This is apparently because almost all patients with CHD were taking antiplatelet drugs (aspirin, clopidogrel), and some (three people) were taking a combination of both drugs.

The study showed that erythrocyte aggregates may not necessarily appear in all the capillaries observed. This is clearly seen in Fig. 5A. The arrows indicate aggregates in the bed of two capillaries, while in the other capillaries no aggregates are found. The cause of this phenomenon is not fully understood. This may be due to the unstable activity of the smooth muscle sphincters of the overlying arterioles, caused by a chaotic heart rhythm.

Thus, a non-invasive study of blood microcirculation using capillaroscopy of the nail bed can serve not only scientific purposes but also find wide application in clinical practice for the optimal dosage of antiplatelet agents and anticoagulants. Early detection of the presence of microhemorrhages (Fig. 5B) can allow the doctor to more accurately monitor other possible signs of bleeding and, if necessary, reduce the dose of the anticoagulant in a timely manner, and if there is a high risk of bleeding, cancel it.

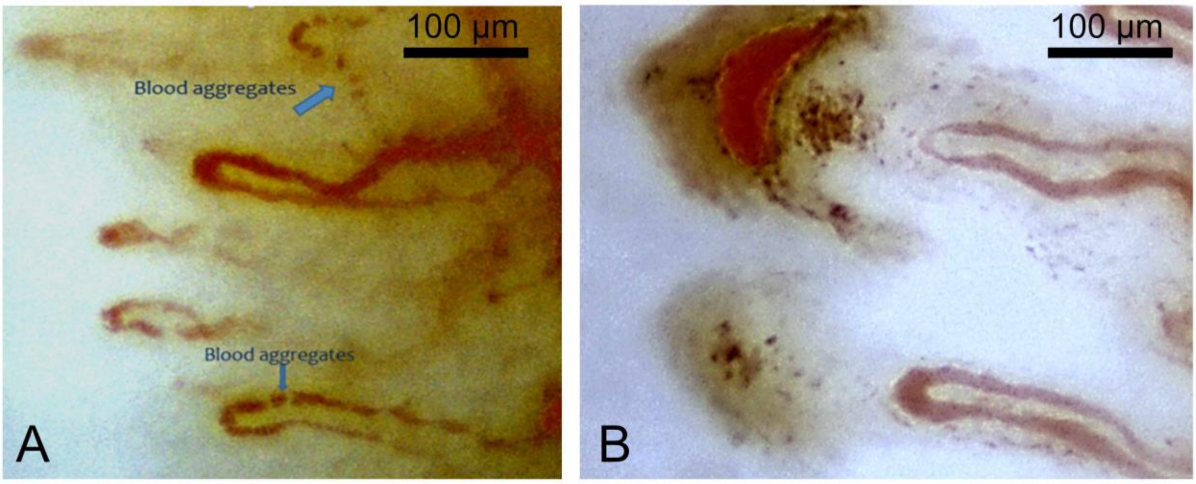

Fig. 5 (A) Nail bed capillaries. The arrows indicate the erythrocyte aggregates in two capillaries. Magnification 400×. (B) Nail bed capillaries with microhemorrhages around them in a patient with AF taking rivaroxaban. Magnification 400×.

This study has some limitations. One of them is the relatively small size of the control group, due to strict volunteer selection criteria. Another limitation is the lack of differentiation of healthy volunteers by age, while age may affect microcirculation indices to a certain extent. In general, it should be noted that capillaroscopy allows one to examine mainly the nail bed capillaries and surrounding tissues. At the same time, this method is non-invasive and does not cause any inconvenience to the patient. Capillaroscopy has already entered medical practice and is widely used in rheumatology [18], for the diagnosis of connective tissue diseases [19–21]. Apparently, the non-invasive method of optical digital capillaroscopy will eventually find application in cardiac pathology.

5 Conclusions

New approaches to the detection and quantification of circulating aggregates in the capillary channel using digital capillaroscopy could pave the way for novel diagnostic and therapeutic strategies in cardiac pathology. In a clinical context, this might help mitigate the risk of complications related to oral anticoagulant and antiplatelet therapy. An important aspect is the relative simplicity and non-invasiveness of the method of digital optical capillaroscopy, which allows it to be used repeatedly to assess the capillary bed and tissues adjacent to the capillaries in dynamics.

Compliance with Ethical Standards

The Ethics Committee of the Medical Research and Education Center of Lomonosov Moscow State University (No11/22 of 05.12.2022) approved the study design. Patients and healthy volunteers participating in the study were informed of the purpose of the study and gave written informed consent in accordance with the Declaration of Helsinki.

Sources of Funding

The study was supported by a grant from the Russian Science Foundation No 25-15-00172.

Conflict of Interest

The authors declare that there is no financial or commercial conflict of interest.

Contribution of the Authors

The idea of the work and the design of the experiment (Y.I.G., A.V.P., L.I.D.), data collection (Y.I.G.), data processing (E.N.S., A.A.R.), writing a video image processing program (A.A.Y.), writing and editing a manuscript (Y.I.G., P.B.E., A.V.P., A.E.L.).

References

1. G. Mancia, R. Kreutz, M. Brunström, et al., “2023 ESH Guidelines for the management of arterial hypertension The Task Force for the management of arterial hypertension of the European Society of Hypertension,” Journal of Hypertension 41, 1874–2071 (2023).
2. B. Zhou, R. M. Carrillo-Larco, G. Danaei, et al., “Worldwide trends in hypertension prevalence and progress in treatment and control from 1990 to 2019: a pooled analysis of 1201 population-representative studies with 104 million participants,” The Lancet 398, 957–980 (2021).
3. D. Rizzoni, C. Agabiti-Rosei, and C. De Ciuceis, “State of the Art Review: Vascular Remodeling in Hypertension,” American Journal of Hypertension 36(1), 1–13 (2023).

4. D. Rizzoni, C. Agabiti-Rosei, G. E. M. Boari, M. L. Muiesan, and C. De Ciuceis, "Microcirculation in Hypertension: A Therapeutic Target to Prevent Cardiovascular Disease?," Journal of Clinical Medicine 12(15), 4892 (2023).
5. E. Agabiti-Rosei, D. Rizzoni, "Microvascular structure as a prognostically relevant endpoint," Journal of Hypertension 35(5), 914–921 (2017).
6. A. Maslianitsyna, P. Ermolinskiy, A. Lugovtsov, A. Pigurenko, M. Sasonko, Y. Gurfinkel, and A. Priezzhev, "Multimodal Diagnostics of Microrheologic Alterations in Blood of Coronary Heart Disease and Diabetic Patients," Diagnostics 11(1), 76 (2021).
7. O. K. Baskurt, A. Temiz, and H. J. Meiselman, "Red blood cell aggregation in experimental sepsis," Journal of Laboratory and Clinical Medicine 130, 183–190 (1997).
8. G. Barshtein, "Biochemical and Biophysical Properties of Red Blood Cells in Disease," Biomolecules 12(7), 923 (2022).
9. P. A. Wolf, R. D. Abbott, and W. B. Kannel, "Atrial fibrillation as an independent risk factor for stroke: the Framingham Study.," Stroke 22(8), 983–988 (1991).
10. M. Lamassa, A. Di Carlo, G. Pracucci, A. M. Basile, G. Trefoloni, P. Vanni, S. Spolveri, M. C. Baruffi, G. Landini, A. Ghetti, C. D. A. Wolfe, and D. Inzitari, "Characteristics, Outcome, and Care of Stroke Associated With Atrial Fibrillation in Europe: Data From a Multicenter Multinational Hospital–Based Registry (The European Community Stroke Project)," Stroke 32(2), 392–398 (2001).
11. A. S. Go, E. M. Hylek, K. A. Phillips, Y. Chang, L. E. Henault, J. V. Selby, and D. E. Singer, "Prevalence of Diagnosed Atrial Fibrillation in Adults," JAMA 285, 2370 (2001).
12. B. Fagrell, M. Intaglietta, "Microcirculation: its significance in clinical and molecular medicine," Journal of Internal Medicine 241, 349–362 (1997).
13. Yu. I. Gurfinkel, M. L. Sasonko, M. I. Kuznetzov, and A. V. Priezzhev, "Importance of image processing in digital optical capillaroscopy for early diagnostics of arterial hypertension," in 2015 International Conference on BioPhotonics (BioPhotonics) IEEE (2015).
14. A. E. Lugovtsov, Y. I. Gurfinkel, P. B. Ermolinskiy, A. I. Maslyanitsina, L. I. Dyachuk, and A. V. Priezzhev, "Optical assessment of alterations of microrheologic and microcirculation parameters in cardiovascular diseases," Biomedical Optics Express10, 3974–4 (2019).
15. E. Brunner, A. C. Bathke, and F. Konietschke, Rank and Pseudo-Rank Procedures for Independent Observations in Factorial Designs, Springer International Publishing, Cham (2018). ISBN 978-3-030-02912-8.
16. C. L. C. Junqueira, E. Ferreira, A. S. M. Junqueira, F. Z. G. A. Cyrino, P. A. Maranhão, L. G. Kraemer-Aguiar, D. A. Bottino, M. das G. C. de Souza, and E. Bouskela, "Peripheral microvascular dysfunction is also present in patients with ischemia and no obstructive coronary artery disease (INOCA)," Clinical Hemorheology and Microcirculation 79, 381–393 (2021).
17. M. Roustit, J. Cracowski, "Non-invasive Assessment of Skin Microvascular Function in Humans: An Insight Into Methods," Microcirculation 19, 47-64 (2012).
18. H. M. A. Hofstee, E. H. Serne, C. Roberts, R. Hesselstrand, A. Scheja, T. L. Moore, M. Wildt, J. B. Manning, A. Vonk Noordegraaf, A. E. Voskuyl, and A. L. Herrick, "A multicentre study on the reliability of qualitative and quantitative nail-fold videocapillaroscopy assessment," Rheumatology 51(4), 749–755 (2012).
19. F. Ingegnoli, V. Smith, A. Sulli, and M. Cutolo, "Capillaroscopy in Routine Diagnostics: Potentials and Limitations," Current Rheumatology Reviews 14, 5–11 (2018).
20. G. Maldonado, R. Guerrero, C. Paredes, and C. Ríos, "Nailfold capillaroscopy in diabetes mellitus," Microvascular Research 112, 41–46 (2017).
21. B. Ruaro, C. Pizzorni, S. Paolino, V. Smith, M. Ghio, A. Casabella, E. Alessandri, M. Patané, A. Sulli, and M. Cutolo, "Correlations between nailfold microvascular damage and skin involvement in systemic sclerosis patients," Microvascular Research 125, 103874 (2019).

Numerical Modeling and Spectral Balancing of an LED-Based Reflectance Spectrophotometer (360–760 nm)

Mikhail E. Parfyonov* **and Dmitry N. Artemyev**
Samara National Research University, 34 Moskovskoe shosse, Samara, 443086, Russian Federation
*e-mail: m.parfyonov@icloud.com

Abstract. This study presents numerical modeling and constrained spectral balancing of a compact LED-based reflectance spectrophotometer operating in the 360–760 nm range. The detected spectral response was modeled as a weighted superposition of individual LED emission spectra explicitly multiplied by the wavelength-dependent detector quantum efficiency $QE(\lambda)$. In the baseline configuration with unit weights, the detected spectrum exhibited strong modulation, characterized by a coefficient of variation CV of 41.5%, peak-to-peak deviation of 131%, and maximum-to-minimum ratio of 4.24. Spectral balancing was formulated as a constrained minimization of the normalized variance over a 0.5 nm wavelength grid using a differential evolution algorithm with bounded non-negative weights. The optimized configuration reduced CV to 8.36%, peak-to-peak deviation to 32.2%, and max/min ratio to 1.39, corresponding to an approximately 80% reduction in global spectral non-uniformity as quantified by variance-based metrics. The proposed approach provides a quantitative methodology for spectral equalization in multi-LED reflectance spectrophotometers.

Keywords: reflectance spectrophotometry; diffuse reflection; optical design; CCD detector; constrained optimization.

Paper #9513 received 15 Feb 2026; revised manuscript received 6 Apr 2026; accepted for publication 6 Apr 2026; published online 29 Jun 2026. doi: 10.18287/JBPE26.12.020311.

1 Introduction

Reflectance spectrophotometry is widely applied for quantitative characterization of materials and functional surfaces through wavelength-resolved analysis of diffusely reflected radiation [1–6]. In biomedical applications, reflectance spectrophotometry provides diagnostically relevant information on tissue condition [7] which motivates further improvement of spectrophotometric systems. In laboratory-scale instruments broadband sources such as tungsten-halogen or xenon lamps are typically employed to provide continuous spectral output. Although such sources ensure broad spectral coverage, they are associated with elevated power consumption, thermal instability, limited lifetime, reduced suitability for compact or field-deployable configurations and some sources exhibit reduced radiant output in the ultraviolet region [8]. The development of solid-state optoelectronics [9–10] has enabled alternative architectures based on discrete light-emitting diodes (LEDs), offering improved energy efficiency, spectral selectivity, and mechanical robustness [11]. In LED-based reflectance systems, broadband coverage is approximated through superposition of multiple emitters with distinct peak wavelengths. However, the aggregate spectral distribution formed by a finite set of LEDs is inherently non-uniform. Moreover, the effective signal registered by the detector is additionally modulated by its wavelength-dependent quantum efficiency. As a consequence, even if the emitted optical power appears approximately balanced at the source level, the detected spectral response may exhibit pronounced variations across the operating range. Such non-uniformity introduces systematic bias in reflectance measurements and reduces comparability between spectral regions; therefore, it is important to ensure uniform illumination, which becomes increasingly difficult as the number of light sources increases [12].

The present work addresses this limitation through numerical modeling and constrained spectral balancing of a compact LED-based reflectance spectrophotometer operating in the 360–760 nm range.

This paper was presented at the XXIII All-Russian Samara Youth Competition and Conference on Optics, Laser Physics and Plasma Physics, Samara, Russian Federation, November 11 – 15, 2025.

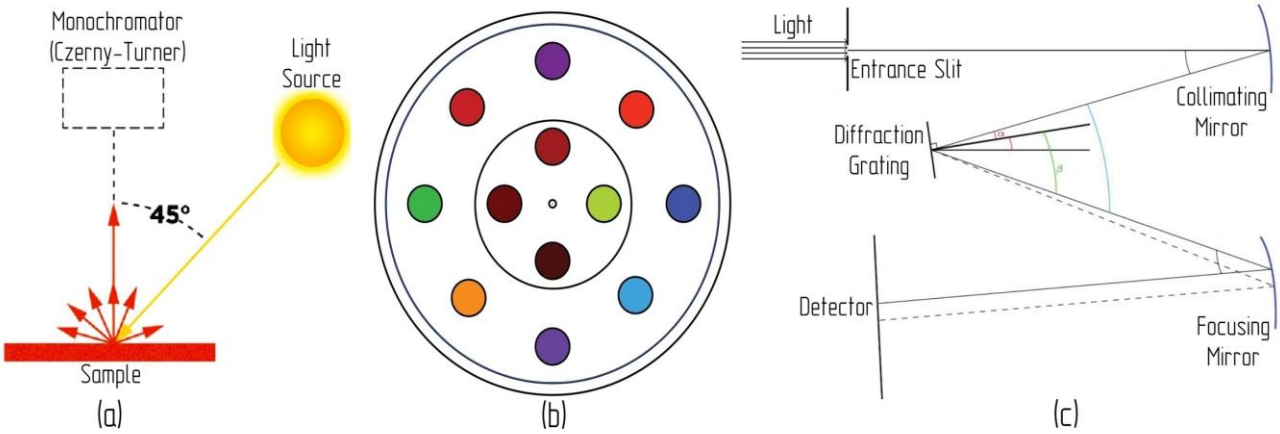

Fig. 1 Optical configuration of the proposed reflectance spectrophotometer, including (a) measurement geometry, (b) illumination system, and (c) spectral dispersion module based on a Czerny-Turner monochromator.

The proposed architecture that combines a 45/0 illumination geometry with a fiber-coupled Czerny-Turner monochromator [13] is shown in Fig. 1(a).

To realize broadband excitation within this configuration, a set of twelve commercially available LEDs with peak wavelengths distributed from the near-ultraviolet to the near-infrared domain is employed. The illumination module is conceptualized as a concentric dual-ring LED arrangement centered on the optical axis of the system and is shown in Fig. 1(b). In addition, to mitigate thermal accumulation, the highest-power LEDs can be spatially distributed across different regions of the array rather than concentrated locally. Such a placement strategy reduces localized heat density, promotes more uniform thermal dissipation, and improves overall thermal stability of the illumination module.

The spectrally resolved detection is achieved using a Czerny-Turner monochromator, schematic of which is shown in Fig. 1(c). In this configuration, incident light enters through the entrance slit and is collimated by a concave mirror. The collimated beam is then directed onto a diffraction grating, where angular dispersion occurs according to wavelength. The diffracted light is subsequently collected and focused by a second concave mirror onto the detector plane. The geometry is defined by the incidence (α) and diffraction (β) angles at the grating, as well as the respective reflection angles at the collimating and focusing mirrors, ensuring spectral separation and imaging onto the detector. The optimization of the angular parameters of the present optical configuration lies outside the scope of this study. The initial angular settings that are often used in the pre-optimization stage can be found in study [14].

The detector quantum efficiency is explicitly incorporated through the wavelength-dependent function $QE(\lambda)$ (Fig. 2), enabling estimation of the effective detected spectral response.

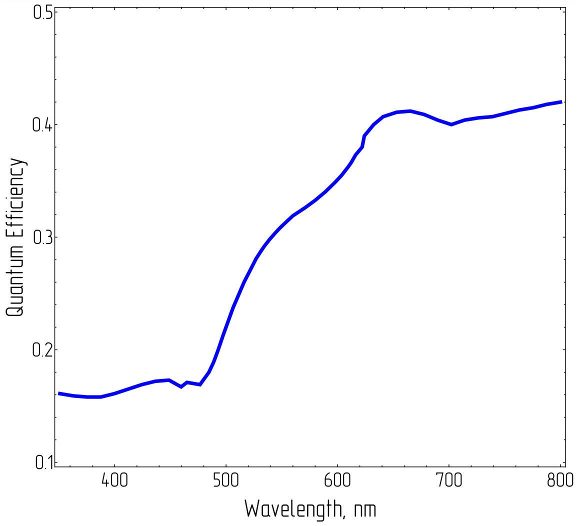

Fig. 2 Quantum Efficiency of a TCD1304DG-UV linear CCD Detector (Toshiba, Japan).

The TCD1304DG-UV linear CCD sensor was selected due to its extended ultraviolet sensitivity and monochrome architecture, which ensure reliable quantum efficiency across the full 360–760 nm spectral range considered in this study. Its high pixel count and 8 μm pixel pitch provide adequate spectral sampling for compact Czerny-Turner configurations, while the absence of a protective cover glass improves short-wavelength transmission. The device also offers straightforward electronic integration, making it suitable for a compact broadband reflectance spectrophotometer.

In the present first-order model, the overall optical throughput of the spectrometer was approximated by a wavelength-independent factor $T \sim 0.5$. This value corresponds to an estimated average transmission of approximately 0.85 per optical element over four sequential components (e.g., fiber coupling, reflective mirrors, diffraction grating efficiency), yielding $0.85^4 \approx 0.52$.

In future work, experimentally measured spectral throughput of the complete optical path will be incorporated as a wavelength-dependent function $T(\lambda)$, allowing more physically accurate modeling and refined optimization of the LED weighting coefficients.

The total detected spectral response is represented as a weighted superposition of individual LED emission spectra multiplied by the detector quantum efficiency. The baseline (pre-optimization) weights w_i^0 were initialized uniformly, with all coefficients set to unity, i.e., $w_i^0 = 1$ for all LEDs. This corresponds to an unweighted superposition and serves as a neutral reference prior to optimization. The weighting coefficients are subsequently treated as optimization variables, representing relative drive currents under physically realistic constraints (e.g., non-negativity).

A numerical minimization of the normalized variance of the detected spectrum over a discrete wavelength grid is performed to achieve maximal spectral uniformity within the specified range. The approach enables quantitative comparison between unweighted and optimized configurations using metrics such as coefficient of variation - CV, peak-to-peak deviation $P2P_{rel}$, and maximum-to-minimum ratio - $R_{max/min}$.

2 Numerical Optimization of Spectral Uniformity

2.1 Mathematical Formulation of the Detected Signal

The detected spectral response of the system was modeled as a weighted superposition of individual LED emission spectra with explicit account of detector quantum efficiency. For a set of N LEDs, the spectral signal at the detector plane was written as follows:

$$S(\lambda) = TQE(\lambda)\sum_{i=1}^{N} w_i L_i(\lambda), \tag{1}$$

where $L_i(\lambda)$ stands for the interpolated spectral power distribution of the i-th LED obtained from the manufacturer emission profiles. Since the objective was spectral uniformity, the constant T does not influence normalized metrics and was therefore retained as a scaling parameter.

All LED spectra and the quantum efficiency curve were reconstructed from tabulated data using cubic interpolation [15]. The operating spectral range was limited to 360–760 nm. For optimization purposes, the wavelength axis was discretized with a step of 0.5 nm, forming a grid $\{\lambda_j\}_{j=1}^{M}$.

The discrete detected signal was then expressed in a vector form as:

$$s_j(\boldsymbol{w}) = QE(\lambda_j)\sum_{i=1}^{N} w_i L_i(\lambda_j), \tag{2}$$

where $\boldsymbol{w} = (w_1, \dots, w_\mathrm{N})^T$ is a vector of optimization variables. Although a wavelength-dependent throughput function is not yet incorporated, it can be introduced multiplicatively into Eq. (2) once experimental transmission data become available.

2.2 Objective Function

Spectral balancing was formulated as a constrained minimization problem. The objective was to reduce the deviation of the detected spectrum from its mean value over the considered wavelength range. The mean signal level was defined as:

$$\mu(\boldsymbol{w}) = \frac{1}{M}\sum_{j=1}^{M} s_j(\boldsymbol{w}), \tag{3}$$

and normalized variance functional was introduced as:

$$J(\boldsymbol{w}) = \frac{1}{\mu(w)^2}\sum_{j=1}^{M}\left(s_j(\boldsymbol{w}) - \mu(\boldsymbol{w})\right)^2. \tag{4}$$

Minimization of $J(\boldsymbol{w})$ corresponds to minimizing the squared coefficient of variation of the detected spectrum. This formulation ensures scale invariance and directly targets spectral flatness rather than absolute signal level.

2.3 Constraints and Baseline Configuration

The initial (baseline) configuration was defined as an unweighted superposition of LED spectra, where every single weight is set to 1.

To reflect practical limitations of current control and optical power adjustment, each weighting coefficient was restricted to an interval $w_i \in \left[w_i^{(0)} - \Delta w, w_i^0 + \Delta w\right]$, with physical constraint $w_i \geq 0$. In present model $\Delta w = 1.5$. The constrained formulation prevents unrealistically large compensation of individual spectral regions and ensures physical feasibility of the solution.

2.4 Numerical Procedure

The optimization problem $\min_{w} J(\boldsymbol{w}), 0 \leq w_i \leq$ ≤ 2.5 was solved numerically using a differential evolution algorithm [16–17]. This population-based global optimization method was selected to reduce sensitivity to local minima arising from partial spectral overlap between adjacent LEDs and non-uniform detector responsivity. A maximum iteration count of 5000 was employed to ensure convergence stability. The optimized weight vector $\boldsymbol{w}^*$ was then used to reconstruct the continuous spectral response $S(\lambda)$ with a 0.5 nm sampling step for visualization and post-analysis.

2.5 Evaluation Metrics

To quantify the degree of spectral equalization achieved through constrained optimization, the baseline and optimized configurations were evaluated using multiple complementary metrics. All metrics were computed over the discrete wavelength grid $\{\lambda_j\}_{j=1}^{M}$ used in the optimization procedure.

The coefficient of variation:

$$CV = \frac{\sigma}{\mu}, \tag{5}$$

provides a normalized measure of spectral non-uniformity that is independent of absolute signal scaling. Since the objective function $J(\boldsymbol{w})$ is proportional to CV^2, reduction of CV directly reflects the effectiveness of the optimization process.

To characterize extremal deviations, the normalized peak-to-peak variation was introduced:

$$P2P_{rel} = \frac{S_{max} - S_{min}}{\mu}, \tag{6}$$

where $S_{max} = \max_j s_j$, $S_{min} = \min_j s_j$. This metric captures the full dynamic range of spectral variation relative to the mean level and is particularly sensitive to localized spectral dips or peaks.

Additionally, the maximum-to-minimum ratio:

$$R_{max/min} = \frac{S_{max}}{S_{min}}, \tag{7}$$

was evaluated as a dimensionless indicator of spectral flatness. Unlike variance-based metrics, this ratio directly reflects worst-case deviation and is therefore relevant for applications requiring bounded systematic error across the spectral range.

The simultaneous use of statistical (CV), range-based ($P2P$), and extremal (max/min ratio) measures ensures robust characterization of spectral uniformity. Agreement among these metrics confirms that the observed improvement is not confined to a limited portion of the wavelength range but represents global flattening of the detected spectral response.

3 Results

The illumination assembly comprises twelve commercially available LEDs with nominal peak wavelengths at 365, 385, 430, 480, 535, 568, 600, 635, 680, 700, 740, and 765 nm. Manufacturer-provided spectral data were used to obtain continuous spectral representations $L_i(\lambda)$ via cubic interpolation to ensure smooth reconstruction over the 360–760 nm range. The aggregate emitted spectrum was initially constructed as an unweighted superposition, corresponding to equal relative drive currents for all channels.

Direct summation of the unweighted spectra produced a strongly modulated aggregate profile, characterized by pronounced local maxima at the individual LED emission peaks and reduced intensity in inter-peak regions where spectral overlap was limited. This behavior is inherent to discrete multi-source architectures, where finite spectral bandwidths and unequal peak intensities prevent natural formation of a flat broadband distribution. When multiplied by the detector quantum efficiency $QE(\lambda)$, the modulation became further amplified. In particular, spectral regions coinciding with high detector responsivity were disproportionately emphasized, whereas regions of reduced quantum efficiency experienced additional attenuation. As a consequence, the baseline detected spectrum exhibited substantial non-uniformity across the 360–760 nm range, even though the nominal spectral coverage of the LED set was continuous.

To visualize the initial spectral behavior of the system, Fig. 3 presents the individual LED emission profiles, the detector quantum efficiency curve $QE(\lambda)$, and the resulting aggregate responses prior to optimization.

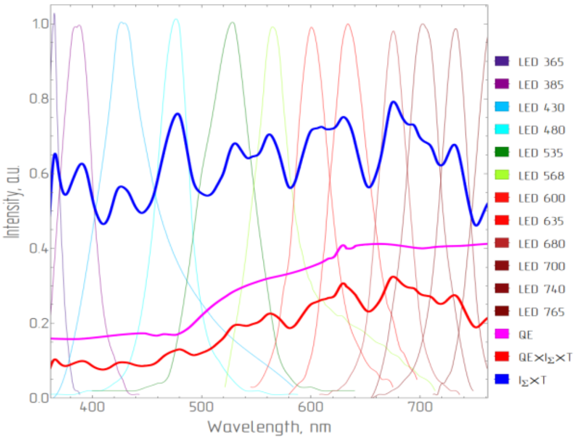

Fig. 3 Individual LED emission spectra, detector quantum efficiency, and baseline detected response prior to spectral optimization.

Fig. 3 illustrates that even after accounting for the uniform throughput factor, the aggregate spectrum remains strongly modulated.

To reduce the observed spectral modulation, a constrained numerical optimization of the LED weighting coefficients w_i was performed. The detected signal was reformulated as stated in Eq. (1), and the weighting coefficients were obtained through constrained minimization of the normalized variance functional described in Section 2. The optimization was carried out over the 360–760 nm range using bounded non-negative weights to preserve physical feasibility with respect to practical current control limitations. The optimized weight vector was determined by minimizing the objective functional within predefined bounds and was found to be $\boldsymbol{w}^* = (2.193, 2.175, 2.500, 1.584, 0.977, 0.851, 0.872, 0.700, 0.651, 0.733, 0.772, 1.146)$, corresponding to the LEDs at 365, 385, 430, 480, 535, 568, 600, 635, 680, 700, 740, and 765 nm, respectively. The resulting weighting distribution reflects the non-uniform spectral sensitivity of the system and compensates for both LED emission characteristics and detector QE variations. This redistribution leads to a more balanced aggregate spectrum prior to final evaluation.

The reconstructed detected spectrum obtained using these optimized coefficients is presented in Fig. 4. Although Fig. 4 provides a complete representation of the illumination subsystem, including the individual LED emission spectra, the large dynamic range associated with the discrete emission peaks dominates the vertical scale of the plot. As a result, the aggregate detected responses $S(\lambda)$ become visually compressed, and subtle variations between the baseline and optimized spectra are partially masked. This scaling effect reduces the interpretability of global spectral flattening and obscures the quantitative impact of the optimization procedure.

For clarity of analysis and to enable direct visual assessment of spectral uniformity, Fig. 5 therefore presents only the QE-scaled detected responses before and after optimization, without the individual LED components.

Fig. 5 demonstrates that numerical optimization of the LED weighting coefficients significantly reduces spectral modulation of the detected response. In the baseline configuration (red curve), the signal exhibits pronounced amplitude variations across the 360–760 nm range, whereas the optimized spectrum (blue curve) shows markedly improved uniformity and a substantially lower maximum-to-minimum ratio. The optimized profile remains broadband while exhibiting reduced peak dominance and attenuated trough depth, confirming effective redistribution of optical power among the LED channels.

While the graphical comparison visually indicates substantial reduction of spectral modulation after optimization, a quantitative assessment (see Section 2) is required to rigorously evaluate the degree of equalization achieved. The statistical and extremal metrics introduced above were therefore computed for both the baseline and optimized configurations over the same discrete wavelength grid used in the optimization procedure. The calculated values of the coefficient of variation CV, normalized peak-to-peak deviation $P2P_{rel}$, maximum-to-minimum ratio $R_{max/min}$ demonstrate significant improvement in spectral uniformity following constrained optimization. Variance-based measures and extremal metrics show coherent reduction, confirming that the observed flattening is not limited to isolated spectral regions but reflects global redistribution of optical power across the full operating range. Direct numerical comparison of these metrics for the baseline and optimized configurations is summarized in Table 1.

These results confirm the utility of constrained numerical spectral balancing for compact multi-LED reflectance systems and provide quantitative evidence supporting the proposed procedure.

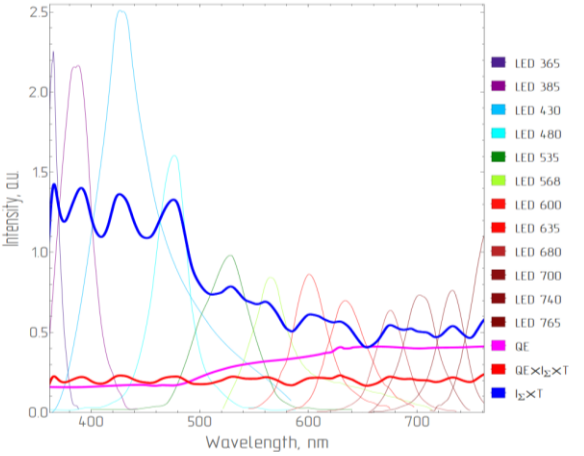

Fig. 4 Individual LED emission spectra, detector quantum efficiency, and detected response after optimization.

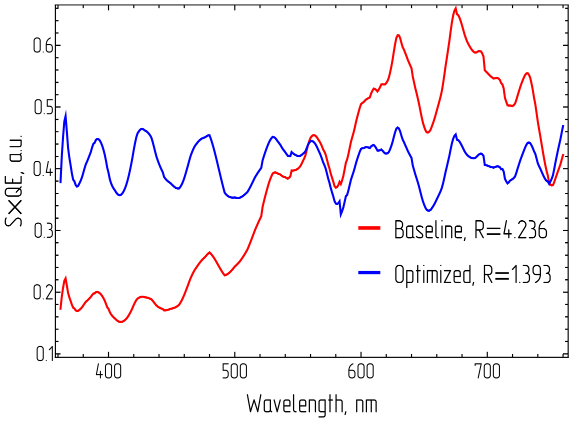

Fig. 5 S×QE, a. u. modeled detected signal with baseline (red) and optimized (blue) weights.

4 Conclusion

This study has developed and numerically validated a constrained optimization framework for spectral equalization in a compact LED-based reflectance spectrophotometer operating over the 360–760 nm range. The proposed architecture integrates discrete multi-wavelength LED illumination, a 45/0 diffuse reflectance geometry, and a fiber-coupled Czerny-Turner monochromator, with explicit incorporation of detector quantum efficiency into the forward model of the detected signal.

Table 1 Quantitative comparison of baseline and optimized spectral uniformity metrics.

Metric	**Baseline**	**Optimized**	**Relative reduction**
CV	41.46%	8.36%	79.8%
$P2P_{rel}$	131.72%	32.20%	75.6%
$R_{max/min}$	4.236	1.393	67.1%

The analysis demonstrates that broadband spectral coverage achieved through discrete emitters does not guarantee uniform detected response. The combined spectral structure of LED emission profiles and wavelength-dependent detector responsivity inherently produces systematic modulation of the measured signal.

This observation highlights a fundamental limitation of source-level balancing approaches that neglect detector characteristics. By formulating spectral equalization as a constrained minimization of normalized variance, the present work establishes a scale-invariant optimization criterion directly linked to statistical measures of spectral uniformity.

The imposed bounds on LED weighting coefficients ensure physical realizability, while the use of a global differential evolution algorithm provides robust convergence under partial spectral overlap between channels. Quantitative evaluation confirmed substantial suppression of spectral non-uniformity across the full operating range.

Beyond the specific numerical results, the principal contribution of this work lies in the explicit coupling of illumination synthesis and detector responsivity within a unified optimization framework. The methodology is not restricted to the particular LED set or detector employed and can be extended to alternative wavelength intervals, detector types, or illumination architectures.

Future developments will extend the model toward a complete radiometric description of the measurement system. Incorporation of a wavelength-dependent throughput function $T(\lambda)$, evaluation of diffuse coupling efficiency into the collection fiber, and quantification of residual specular contributions will enable physically rigorous prediction of measurement bias. In parallel, parametric optimization of the dispersive subsystem under constraints of spectral resolution, optical throughput, and mechanical compactness will facilitate integrated opto-mechanical co-design.

From a practical implementation perspective, the obtained results indicate that spectral uniformity in multi-LED reflectance systems can be achieved through control of individual LED drive currents without modification of the optical layout. This follows directly from the fact that the detected spectral response is formed as a linear superposition of emitter contributions weighted by controllable coefficients.

As a result, compact spectrophotometric devices can be calibrated post-assembly by adjusting channel weights using measured emission spectra and detector responsivity functions. In practical implementations, it is therefore advisable to (i) ensure independent current control for each LED channel, (ii) incorporate experimentally measured spectral characteristics of both emitters and detector into the optimization procedure, and (iii) account for thermal effects when assigning elevated weights to specific LEDs, since non-uniform power distribution inherently leads to localized heat accumulation and may affect spectral stability.

In comparison with conventional broadband illumination systems based on halogen or xenon lamps, the proposed approach relies on discrete, independently controllable emitters rather than a continuous source spectrum. This architectural difference enables direct redistribution of optical power across the spectral range through numerical optimization, which is not accessible in fixed-spectrum sources without additional optical filtering. At the same time, solid-state emitters are intrinsically associated with lower power consumption, reduced thermal load, and improved mechanical robustness, making them suitable for compact and field-deployable systems.

A detailed quantitative comparison with existing systems requires experimental validation and is therefore beyond the scope of the present work. Nevertheless, the presented results demonstrate that numerical spectral balancing constitutes a physically consistent and scalable approach to achieving broadband spectral uniformity in multi-LED spectrophotometric systems.

The proposed framework thus provides a systematic and extensible foundation for the development and optimization of compact, spectrally balanced, solid-state reflectance spectrophotometers suitable for laboratory and field-deployable applications.

Disclosures

All authors declare that there is no conflict of interest in this paper.

Reference

1. T. A. Germer, J. C. Zwinkels, and B. K. Tsai (Eds.), Spectrophotometry: Accurate Measurement of Optical Properties of Materials, vol. 46, Elsevier, Oxford, UK (2014). ISBN: 978-0-12-386022-4.
2. G. Kortüm, Reflectance Spectroscopy: Principles, Methods, Applications, Springer, Berlin, Heidelberg (2012). ISBN: 978-3-642-88073-5.
3. A. Springsteen, Applied Spectroscopy: A Compact Reference for Practitioners, Academic Press, 193–224 (1998). ISBN: 978-0-12-764070-9.
4. I. Badura, M. Dąbski, "Reflectance spectroscopy in geology and soil sciences: literature review," Quaestiones Geographicae 41(3), 157–167 (2022).
5. M. Witteveen, D. J. Faber, H. J. C. M. Sterenborg, T. J. M. Ruers, T. G. Van Leeuwen, and A. L. Post, "Opportunities and pitfalls in (sub)diffuse reflectance spectroscopy," Frontiers in Photonics 3, 964719 (2022).
6. E.W. Ciurczak, B. Igne, J. Workman, and D.A. Burns (Eds.), Handbook of Near-Infrared Analysis, 4th ed., CRC Press, Boca Raton (2021). ISBN: 978-1-35-126988-9.

7. M. B. Wallace, A. Wax, D. N. Roberts, and R. N. Graf, “Reflectance spectroscopy,” Gastrointestinal Endoscopy Clinics of North America 19(2), 233–242 (2009).
8. I. T. Young, Y. Garini, H. R. C. Dietrich, W. Van Oel, and G. Liqui Lung, LEDs for fluorescence microscopy, Proceedings of SPIE, 5324, 208 (2004).
9. W. Demtröder, Laser Spectroscopy, Springer, Berlin, Heidelberg (2003). ISBN: 978-3-540-73418-5
10. E. F. Schubert, Light-Emitting Diodes, 2nd ed., Cambridge University Press (2006). ISBN: 978-0-511-79054-6
11. S. Pimputkar, J. S. Speck, S. P. DenBaars, and S. Nakamura, “Prospects for LED lighting,” Nature Photonics 3, 180–182 (2009).
12. Y. Ryu, D. D. Baldocchi, J. Verfaillie, S. Ma, M. Falk, I. Ruiz-Mercado, T. Hehn, and O. Sonnentag, “Testing the performance of a novel spectral reflectance sensor, built with light emitting diodes (LEDs), to monitor ecosystem metabolism, structure and function,” Agricultural and Forest Meteorology 150(12), 1597–1606 (2010).
13. S. D. Noble, R. B. Brown, and T. G. Crowe, “Design and evaluation of an imaging spectrophotometer incorporating a uniform light source,” Review of Scientific Instruments 83(3), 033112 (2012).
14. M. Naeem, T. Imran, M. Hussain, and A. S. Bhatti, “Design simulation and data analysis of an optical spectrometer,” Optics 3(3), 304–312 (2022).
15. M. Czerny, A. F. Turner, “Über den astigmatismus bei spiegelspektrometern,” Zeitschrift für Physik 61, 792–797 (1930).
16. P. R. Bevington, D. K. Robinson, Data Reduction and Error Analysis for the Physical Sciences, McGraw-Hill Education, (2003). ISBN: 978-0-07-247227-1.
17. R. Storn, K. Price, “Differential evolution – a simple and efficient heuristic for global optimization over continuous spaces,” Journal of Global Optimization 11(4), 341–359 (1997).

Optical Coherence Tomography Angiography for Monitoring Sublingual Microcirculatory Changes: a Prospective Tool for Investigation of Tissue Hypoperfusion in Critical Care Medicine

Anton A. Plekhanov[1*], **Ivan A. Ryzhkov**[2], **Pavel A. Shilyagin**[3], **Elena B. Kiseleva**[1], **Konstantin N. Lapin**[2], **Lydia A. Varnakova**[2], **Yulia V. Korzhimanova**[1], **Anna I. Dementeva**[1,4], **Marina A. Sirotkina**[1], **Grigory V. Gelikonov**[3], **Evgeniy V. Grigoryev**[5], **and Natalia D. Gladkova**[1]

[1] Institute of Experimental Oncology and Biomedical Technologies, Privolzhsky Research Medical University, 10/1 Minin and Pozharsky sq., Nizhny Novgorod 603950, Russian Federation
[2] Laboratory of Experimental Research, V.A. Negovsky Research Institute of General Reanimatology, Federal Research and Clinical Center of Intensive Care Medicine and Rehabilitology, 25/2 Petrovka str., Moscow 107031, Russian Federation
[3] A.V. Gaponov-Grekhov Institute of Applied Physics of the Russian Academy of Sciences, 46 Ulyanov str., Nizhny Novgorod 603155, Russian Federation
[4] Lobachevsky University, 23 Gagarin av., Nizhny Novgorod 603022, Russian Federation
[5] Research Institute for Complex Issues of Cardiovascular Diseases, 6 Sosnoviy blvd., Kemerovo 650002, Russian Federation
*e-mail: strike_gor@mail.ru

Abstract. Using optical coherence tomography angiography (OCT-A), we demonstrate the feasibility of monitoring microcirculatory changes in the clinically important sublingual region, which reflects perfusion disturbances in internal organs of critically ill patients. We present the results of OCT-A monitoring of sublingual microcirculation alterations in both animals and humans induced by external stimuli (modeling massive blood loss and administration of a vasodilator drug). Our findings highlight the strong potential of OCT-A for addressing the challenges of early detection of tissue hypoperfusion in patients. We propose a signal intensity analysis for OCT-A images which might be an effective approach to predict multiple organ failure development, thereby enabling monitoring of the effectiveness of ongoing intensive care.

Keywords: optical coherence tomography angiography; sublingual microcirculation; tissue hypoperfusion; multiple organ failure.

Paper #9580 received 9 Apr 2026; revised manuscript received 1 May 2026; accepted for publication 4 May 2026; published online 29 Jun 2026. doi: 10.18287/JBPE26.12.020401.

1 Introduction

One of the key challenges in the intensive care of critically ill patients with systemic inflammatory response syndrome, sepsis, or shock is the lack of effective clinical and laboratory tools for direct assessment of microcirculatory disorders in organs and tissues [1]. It is worth noting that diagnostics and therapy of already existing macro-vascular complications do not guarantee recovery of microcirculation and sufficient regeneration of perfusion in hypoxic organs [2], which is reflected in current trends in maintaining high mortality rates in critically ill patients with the manifestation of shock and multiple organ failure (MOF) [3]. Therefore, it is necessary to develop new clinical tools for direct diagnostics of microcirculatory disorders to identify effective criteria for predicting the manifestation/progress of MOF and timely provision of targeted therapy.

This paper was presented at the Saratov Fall Meeting 2025 – International Symposium on Optics and Biophotonics, Saratov, Russian Federation, September 29 – October 3, 2025.

It has been repeatedly shown that sublingual microcirculation reflects the state of blood supply to internal organs, likely because these vascular beds share a common embryonic origin [4–6]. Direct visualization of sublingual blood vessels with the ability to quantify them can significantly surpass other criteria in understanding the severity of a patient's condition and help physicians make timely optimal decisions. Vital microscopy (orthogonal polarization spectral imaging / side-stream dark field imaging / incident dark field illumination imaging) is widely used for sublingual assessment [7]. However, it has not become standard clinical practice due to the frequent and inevitable occurrence of artifacts (microscope pressure on the tissue being studied, shifting of the scanning area, poor illumination, and uneven focus) [8]. These artifacts require continuous, real-time quality control of the recordings by a qualified specialist. The lack of such a specialist often leads to the rejection of most data due to unacceptable recording quality, even with manual processing. Another limitation of such methods is the time-consuming and labor-intensive manual post-processing of recordings, which is often required because existing automated analysis approaches frequently yield inaccurate estimates of microcirculatory parameters [9]. Furthermore, existing studies evaluating therapies for critical illness complicated by internal organ hypoxia / MOF demonstrated inconsistent results regarding the prognostic value of sublingual microcirculation parameters measured by vital microscopy and highlight the need for further research and for the development of effective criteria / methods for monitoring the treatment being administered [10, 11].

This Letter discusses the possibility of using optical coherence tomography (OCT) technology to monitor changes of sublingual perfusion and diagnose microcirculatory disorders in patients developing shock / MOF. OCT-Angiography (OCT-A), based on interferometric signal recording method [12], offers several advantages for the investigation of oral vascular architecture. The device's built-in beam focusing system shifts along the depth of the object, allowing for stable examination of the structure and microcirculation of biological tissue at various depths up to 2 mm with high spatial resolution up to 10 μm [13]. As previously shown using vital microscopy, the relatively limited visualization depth does not hinder the study of microcirculatory changes in sublingual vessels, which are located beneath the basement membrane of the lamina propria of the oral mucosa [14, 15]. Moreover, OCT-A is a label-free method with high scanning rate and enough fast signal filtration to localize micromovements of scatterers (erythrocytes) and visualize in real time of blood vessels down to the capillary level [16]. Most often OCT-A represents the blood vessel network as a 2D image in *en face* (top view) projection (Fig. 1). Having proven its high efficiency in ophthalmology [17, 18], the multimodal OCT/OCT-A has been widely developed to address problems in various clinical areas [19–21], including growing interest in the use of OCT for diagnosing the oral mucosa [22, 23]. In particular, the feasibility of studying sublingual microcirculation was demonstrated in volunteers (in a sitting position) using an adapted commercial ophthalmological OCT-A system [24]. The study demonstrated the effectiveness of OCT-A and its high agreement with incident dark field illumination microscopy (current gold standard) in assessing perfused vessel density (PVD), confirming the promising potential for OCT-A to address various clinical challenges in critical care medicine.

It is worth noting that the first OCT studies of the oral cavity carried out by our research group were focused primarily on examining the morphology of oral soft and hard tissues with qualitative image evaluation [25]. We subsequently expanded these studies by adding blood flow assessment using the OCT-A modality. To reduce motion artifacts and improve the quality of OCT-A monitoring of oral cavity vessels, we use a non-traumatic vacuum-assisted attachment [26]. This attachment significantly stabilizes OCT-A images even in the absence of dedicated OCT probe fixtures and during manual scanning.

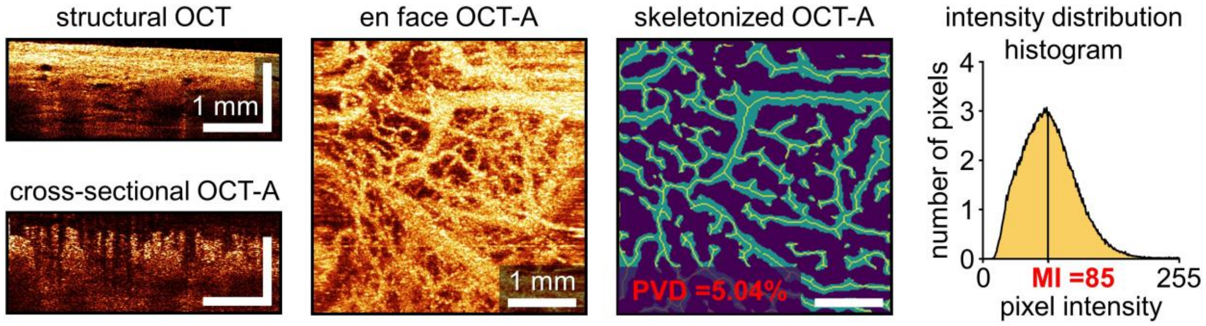

Fig. 1 A demonstration of standard OCT-A imaging via human sublingual vessel assessment. High-frequency filtration of sequential B-scans (structural OCT images) generates a 3D angiographic dataset (from cross-sectional OCT-A images), processing (manual depth selection and maximum intensity projection) of which produces a 2D *en face* OCT-A image of the tissue's vascular network [16]; scale bar size is indicated on images. Subsequent analysis of such images most often relies on skeletonization and characterization of the traced vascular branches; moreover, analysis of the signal intensity distribution spectrum is used less frequently.

In the paper [27], the capability of OCT-A for mapping the microcirculatory bed of oral cavity vessels in the cheek region was demonstrated. The resolution of the method allowed the detection of vascular loops in the papillary layer and a branched vascular network in the reticular layer of the lamina propria, as well as the cessation of blood flow in individual capillaries due to cold exposure. However, quantitative evaluation of OCT-A images, which involved skeletonization of vascular branches followed by PVD analysis, did not allow statistically significant confirmation of the visually observed changes, namely, a decrease in the signal intensity of vessels in the reticular layer during monitoring of cooling. The reduction of blood flow in the vascular loops of the papillary layer also supports the conclusion that there is a decreased blood flow velocity in the reticular layer, while the perfusion map remains preserved. Therefore, given that a drastic pathomorphological alteration of the tissue's vascular pattern (such as that seen in neoangiogenesis monitoring [28, 29]) is not anticipated, it is essential to validate novel analytical approaches capable of detecting subtle physiological changes in blood flow velocity using OCT-A monitoring data from the same oral mucosa regions.

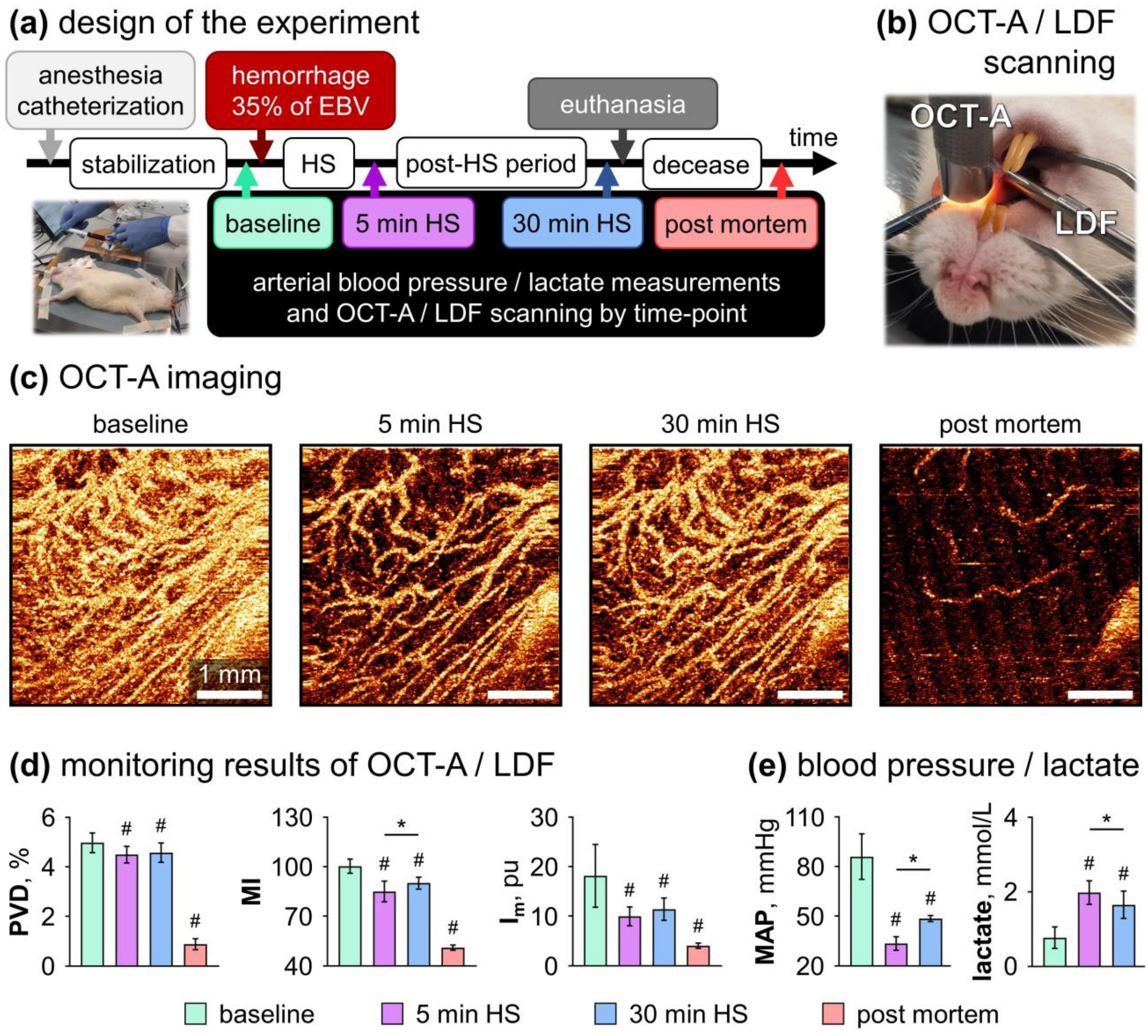

Fig. 2 Sublingual microcirculation changes during modeling of HS in rat: (a) schematic design of the experiment; (b) OCT-A and LDF probes placement for parallel monitoring of sublingual microcirculation; (c) representative OCT-A images before hemorrhage modeling (baseline), 5 min after losing 35% of estimated blood volume and HS onset (5 min HS), 30 min after HS onset (30 min HS), and immediately after animal euthanasia (post mortem); scale bar size is indicated on images; (d) analysis of sublingual microcirculation and diagrams of obtained values (mean ± SD) for PVD and MI according to OCT-A data, and I_m according to LDF data; # – statistical significance ($p < 0.05$) between the time points after hemorrhage modeling and baseline point, * – statistical significance ($p < 0.05$) between 5 and 30 min HS time points, Repeated Measures one-way ANOVA test; (e) analysis of hemodynamic and perfusion/oxygenation parameters – diagrams of MAP values and lactate concentration.

This study is the first to demonstrate OCT-A monitoring of sublingual microcirculatory changes in response to external stimuli. These stimuli were associated with changes in microhemodynamics commonly observed in routine intensive care practice [3]. In animal experiments, we assessed the sensitivity of OCT-A to alterations in sublingual blood flow during massive blood loss accompanied by hemorrhagic shock (HS). While the fact and etiopathogenesis of microcirculatory changes in HS are known [30, 31], OCT-A here allows for the first visualization and demonstration of this effect specifically in the sublingual area, which is of practical interest for subsequent clinical implementation. Furthermore, parallel monitoring of microcirculation using laser Doppler flowmetry (LDF), monitoring of the animal's arterial blood pressure, and biochemical analysis of arterial blood lactate confirmed hemodynamic disturbances and the development of organ ischemia in HS due to massive blood loss. Subsequently, we tested OCT-A monitoring of changes in sublingual microcirculation in volunteers under the influence of the vasodilator nitroglycerin (glyceryl trinitrate, GTN). Parallel blood pressure monitoring confirmed the observed hemodynamic changes upon local administration of the drug. Beyond demonstrating OCT-A's utility for monitoring sublingual microcirculation in both animals and humans, we propose a different approach of OCT-A data (was obtained as described in Ref. [32]) analyzing based on estimation of signal intensity (pixels' grey scale range from 0 to 255) histogram distributions and calculation the value of mean intensity (MI) of image (Fig. 1). This approach yields statistically significant differences (in contrast to PVD analysis) in cases where vascular maps show clear visual differences due to changed flow velocity, despite an unchanged vascular network architecture.

The experimental phase involved studies of sublingual blood flow changes in Wistar rats ($n = 5$) during modeled fixed-volume blood loss. The design of the experiment is presented in Fig. 2(a). The target blood loss volume was 35% of the estimated blood volume, corresponding to class III hypovolemic shock (HS) according to the Advanced Trauma Life Support classification [33]. This class of blood loss typically leads to pronounced tachycardia, hypotension, decreased pulse pressure, and increased respiratory rate, indicating significant tissue hypoperfusion / hypoxia of internal organs [34]. Changes in sublingual vascular perfusion were monitored in parallel using OCT-A (Biomedtech Ltd., Russia) [27] and LDF (LAZMA Ltd., Russia) [35] (probes' placements is demonstrated in Fig.2(b)) before modeling blood loss (time point "baseline"), 5 min after the completion of blood loss and the onset of HS ("5 min HS"), 30 min after the onset of HS ("30 min HS"), and immediately after animal euthanasia (via intra-arterial administration of a lidocaine solution) following the 30-min monitoring period ("post mortem").

Visual analysis of the OCT-A images revealed a sharp decrease in capillary blood flow while vascular architecture remained relatively preserved by the 5 min HS (Fig. 2(c)). By 30 min HS, some increase in signal intensity of blood vessels was observed. This small increase in sublingual perfusion can be explained by two factors: a simultaneous increase in mean arterial pressure (MAP) due to sympathetic activation, increased myocardial contractility and hemodilution (a compensatory response to bleeding); and microvascular vasodilation due to persistent metabolic acidosis [36]. In contrast, following animal euthanasia, a complete cessation of blood flow was observed in the majority of vessels.

Quantitative analysis of the PVD and MI parameters (by OCT-A) and the index of blood microcirculation (I_m; by LDF) revealed statistically significant differences ($p < 0.05$) between the time points "5 min HS" and "baseline" (Fig. 2(d)). Among the evaluated indices, only MI detected the visually observed change in microcirculation between the 5- and 30-min HS time points (85.01 ± 6.23 vs 90.09 ± 3.60, $p < 0.05$), whereas PVD (4.49 ± 0.34 vs 4.57 ± 0.39%, $p = 0.44$) and I_m (9.96 ± 1.90 vs 11.42 ± 2.25 perfusion units, $p = 0.46$) did not differ significantly. These changes are consistent with the statistically significant ($p < 0.05$) increase in MAP (33.50 ± 4.05 vs 48.58 ± 1.81 mmHg) and the decrease in arterial blood lactate concentration (1.98 ± 0.31 vs 1.65 ± 0.36 mmol/L), confirming the development of HS and tissue hypoxia (Fig. 2(e)). Similar trends in sublingual microcirculatory changes have been demonstrated using vital microscopy in critically ill patients with HS who developed MOF or mortality [37]. Finally, the results obtained at this experimental stage, on one hand, directly demonstrate the development of microhemodynamic disturbances in sublingual area during acute blood loss and HS; on the other hand, they establish the efficacy of OCT-A with MI estimation for monitoring sublingual microcirculation changes during the progression of critical conditions.

In the next phase, we evaluated the capability of OCT-A for monitoring changes of human sublingual microcirculation in healthy volunteers ($n = 9$) receiving GTN sublingually (to reduce drug burden and adverse effects half of the therapeutic dose was used). The OCT-probe was firmly fixed to the assessed tissue using a vacuum attachment [26], which prevented displacement of the scanning area during prolonged monitoring (Fig. 3(a)). The predictable pharmacokinetics of GTN (therapeutic vasodilatory effect following a full sublingual dose occurs within 2–4 min, with a mean duration of approximately half an hour [38]) enabled the design of an OCT-A monitoring protocol comprising measurements before GTN administration ("baseline"), and at 5 and 20 min after GTN application ("5 and 20 min post-GTN"). Parallel blood pressure measurements confirmed a decrease in systolic arterial pressure (SAP) at 5 min following GTN administration (111 ± 5 vs 122 ± 8 mmHg, $p < 0.05$), whereas by 20 min (118 ± 4 mmHg) no statistically significant differences compared to "baseline" were observed (Fig. 3(b)).

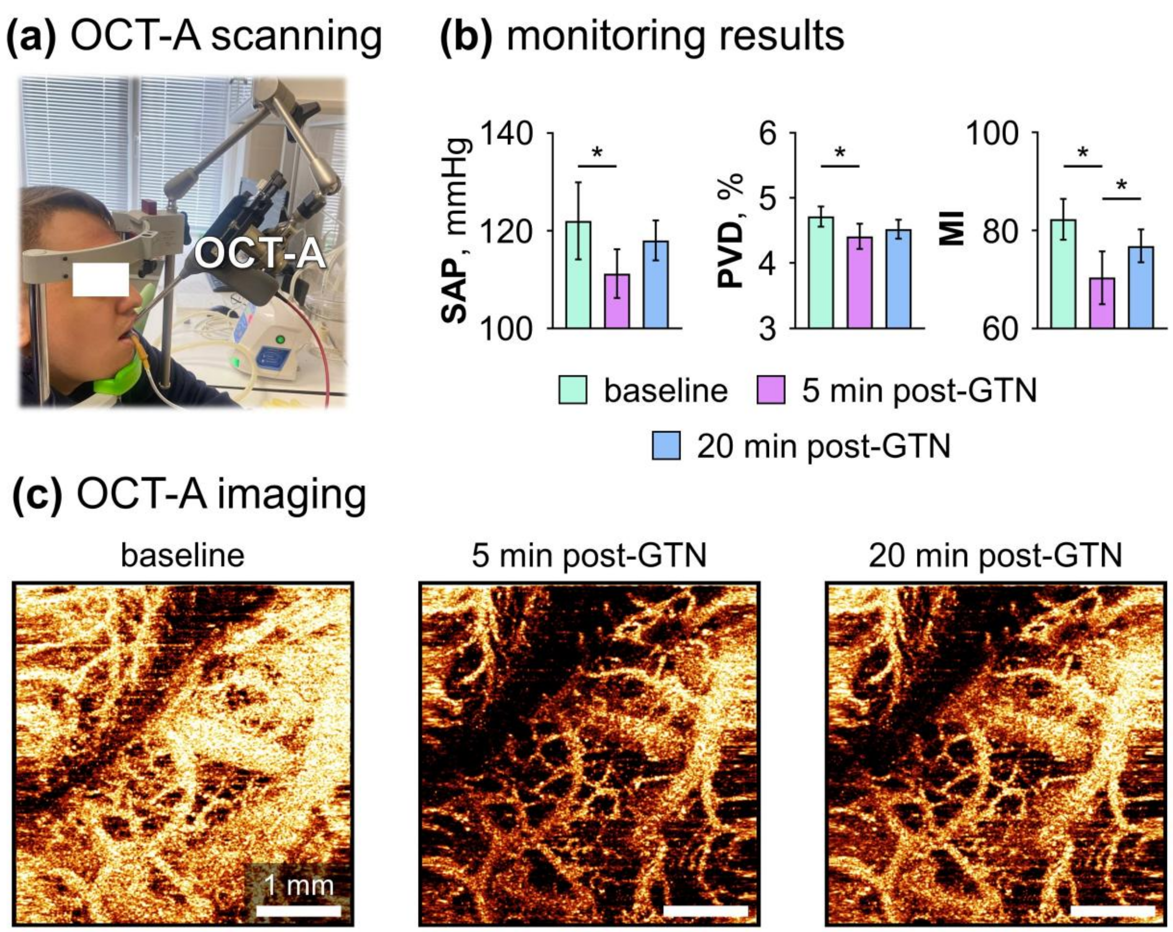

Fig. 3 Changes in human sublingual microcirculation following local GTN administration: (a) demonstration of sublingual OCT-A monitoring of volunteer; (b) diagrams of the obtained values (mean + SD) before GTN administration (baseline), by 5 and 20 min after GTN application (5 and 20 min post-GNT) for SAP, PVD and MI; * – statistical significance ($p < 0.05$) between the monitoring time points, Repeated Measures one-way ANOVA test; (c) representative OCT-A images; scale bar size is indicated on images.

Visual and quantitative (by PVD and MI) analyses of the OCT-A data (Fig. 3(b–c)) demonstrated a statistically significant ($p < 0.05$) decrease in sublingual microcirculation 5 min after GTN application (4.41 ± 0.19 vs 4.71 ± 0.16%; 70.34±5.38 vs 82.24±4.17). Furthermore, the use of intensity analysis and calculation of the MI parameter enables statistically significant confirmation of the restoration of vascular perfusion in the sublingual region when comparing the 5- and 20-min post-GTN time points (70.34 ± 5.38 vs 76.83 ± 3.35, $p < 0.05$). These results confirm the feasibility of longitudinal OCT-A monitoring of microcirculatory changes in the human sublingual region and underscore the need for further development of a novel approach to the analysis of OCT-A data (distinct from the widely used PVD estimation) for assessing physiological (hemodynamic) alterations in vascular network, which are frequently encountered in critically ill patients. This could provide a clear basis for assessing the effectiveness of sublingual microcirculation monitoring in critically ill patients, both for predicting complications and for guiding appropriate adjustments to critical care treatment [39].

It is only fair to note that the sole limitation of OCT-A compared to vital microscopy techniques is essentially the inability to assess the proportion of non-perfused and perfused vessels among their total number. Nevertheless, it should not be overlooked that vital microscopy methods (not yet entered into widespread clinical practice) remain susceptible to artifacts caused by microscope pressure on the tissue or displacement of the scanning area, require precise focusing and the involvement of a skilled operator to ensure correct image acquisition, and often necessitate labor-intensive and time-consuming manual processing of the recorded data [7–9]. In contrast, OCT-A at its current stage of development is substantially less dependent on the above-mentioned factors. Among the advantages of OCT-A are the mitigation of motion artifacts through the use of a vacuum attachment and real-time visual control of acquired images (with the ability to quickly reject and re-collect data), a straightforward and intuitive software interface, the absence of a need for focusing, and the capability for immediate interpretation and assessment of the obtained OCT-A data.

It is also fair to say that future studies of sublingual microcirculation will need to explore how to utilize or modify the OCT-A parameters used (possibly in combination with other detectable features) to achieve sufficient diagnostic power for practical clinical applications. Addressing the diagnostic aspect would require subsequent work dedicated to identifying the most informative combination of OCT-A and clinical parameters capable of high-accuracy state classification in critical care medicine. The development of such methods could involve machine learning and other advanced techniques, followed by rigorous evaluation of their performance metrics (e.g., ROC, AUROC, accuracy, sensitivity, and specificity).

In conclusion, considering recent advances in the development of OCT-A approaches for assessing tissue microcirculation and the results presented in this Letter, there is no doubt regarding the relevance and promise of OCT-A technology for addressing the challenges of early detection of tissue hypoperfusion in critically ill patients and for identifying predictive criteria of MOF development to monitor the effectiveness of ongoing intensive care.

Disclosures

The authors declare no conflict of interest.

Data Availability

Data underlying the results presented in this paper are not publicly available at this time but may be obtained from the authors upon reasonable request.

Acknowledgements

The study was supported by the Russian Science Foundation, grant # 25-75-10160, https://rscf.ru/project/25-75-10160/. The authors are grateful to Margarita Sysueva (Linguistics University of Nizhny Novgorod) for proofreading the manuscript.

References

1. D. De Backer, K. Donadello, Y. Sakr, G. Ospina-Tascon, D. Salgado, S. Scolletta, and J.-L. Vincent, "Microcirculatory Alterations in Patients With Severe Sepsis: Impact of Time of Assessment and Relationship With Outcome*," Critical Care Medicine 41(3), 791–799 (2013).
2. C. Ince, "Hemodynamic coherence and the rationale for monitoring the microcirculation," Critical Care 19(Suppl. 3), S8 (2015).
3. A. A. Plekhanov, I. A. Ryzhkov, E. B. Kiseleva, S. V. Panfilov, A. A. Mikhailova, M. A. Sirotkina, N. D. Gladkova, and E. V. Grigoriev, "Microcirculation in critical care: current pathophysiology and place in the strategy of monitoring critical conditions as a monitoring technology," Complex Issues of Cardiovascular Diseases 14(5), 139–159 (2025).
4. D. De Backer, J. Creteur, J. C. Preiser, M. J. Dubois, and J. L. Vincent, "Microvascular blood flow is altered in patients with sepsis," American Journal of Respiratory and Critical Care Medicine 166(1), 98–104 (2002).
5. C. L. Verdant, D. De Backer, A. Bruhn, C. M. Clausi, F. Su, Z. Wang, H. Rodriguez, A. R. Pries, and J. L. Vincent, "Evaluation of sublingual and gut mucosal microcirculation in sepsis: a quantitative analysis," Critical Care Medicine 37, 2875–2881 (2009).
6. J. Harki, M. Suker, M. S. Tovar-Doncel, L. J. van Dijk, D. van Noord, C. H. van Eijck, M. J. Bruno, E. J. Kuipers, and C. Ince, "Patients with chronic mesenteric ischemia have an altered sublingual microcirculation," Clinical and Experimental Gastroenterology 11, 405–414 (2018).
7. C. Ince, E. C. Boerma, M. Cecconi, D. De Backer, N. I. Shapiro, J. Duranteau, M. R. Pinsky, A. Artigas, J. L. Teboul, I. K. M. Reiss, C. Aldecoa, S. D. Hutchings, A. Donati, M. Maggiorini, F. S. Taccone, G. Hernandez, D. Payen, D. Tibboel, D. S. Martin, A. Zarbock, X. Monnet, A. Dubin, J. Bakker, J. L. Vincent, and T. W. L. Scheeren, "Second consensus on the assessment of sublingual microcirculation in critically ill patients: results from a task force of the European Society of Intensive Care Medicine," Intensive Care Medicine 44, 281–299 (2018).
8. E. Damiani, C. Ince, C. Scorcella, R. Domizi, A. Carsetti, N. Mininno, S. Pierantozzi, E. Adrario, R. Romano, P. Pelaia, and A. Donati, "Impact of microcirculatory video quality on the evaluation of sublingual microcirculation in critically ill patients," Journal of Clinical Monitoring and Computing 31, 981–988 (2017).
9. E. Damiani, A. Carsetti, E. Casarotta, R. Domizi, C. Scorcella, A. Donati, and E. Adrario, "Microcirculation-guided resuscitation in sepsis: the next frontier?," Frontiers in Medicine 10, 1212321 (2023).
10. W. Liu, H. He, C. Ince, and Y. Long, "The effect of blood transfusion on sublingual microcirculation in critically ill patients: A scoping review," Microcirculation 28(3), e12666 (2021).
11. Z. Yao, Y. Chen, D. Li, Y. Li, Y. Liu, and H. Fan, "Hemorrhagic Shock Assessed By Tissue Microcirculatory Monitoring: A Narrative Review," Shock 61(4), 509–519 (2024).
12. V. M. Gelikonov, V. N. Romashov, D. V. Shabanov, S. Yu. Ksenofontov, D. A. Terpelov, P. A. Shilyagin, G. V. Gelikonov, and I. A. Vitkin, "Cross-Polarization Optical Coherence Tomography with Active Maintenance of the Circular Polarization of a Sounding Wave in a Common Path System," Radiophys Quantum El 60(11), 897–911 (2018).

13. A. A. Plekhanov, M. A. Sirotkina, A. A. Sovetsky, E. V. Gubarkova, S. S. Kuznetsov, A. L. Matveyev, L. A. Matveev, E. V. Zagaynova, N. D. Gladkova, and V. Y. Zaitsev, "Histological validation of *in vivo* assessment of cancer tissue inhomogeneity and automated morphological segmentation enabled by Optical Coherence Elastography," Scientific Reports 10, 11781 (2020).
14. W. Groner, J. W. Winkelman, A. G. Harris, C. Ince, G. J. Bouma, K. Messmer, and R. G. Nadeau, "Orthogonal polarization spectral imaging: a new method for study of the microcirculation," Nature Medicine 5, 1209–1212 (1999).
15. D. De Backer, G. Ospina-Tascon, D. Salgado, R. Favory, J. Creteur, and J. L. Vincent, "Monitoring the microcirculation in the critically ill patient: current methods and future approaches," Intensive Care Medicine 36, 1813–1825 (2010).
16. L. A. Matveev, V. Yu. Zaitsev, G. V. Gelikonov, A. L. Matveyev, A. A. Moiseev, S. Yu. Ksenofontov, V. M. Gelikonov, M. A. Sirotkina, N. D. Gladkova, V. Demidov, and A. Vitkin, "Hybrid M-mode-like OCT imaging of three-dimensional microvasculature *in vivo* using reference-free processing of complex valued B-scans," Optics Letters 40(7), 1472 (2015).
17. J. Fujimoto, E. Swanson, "The Development, Commercialization, and Impact of Optical Coherence Tomography," Investigative Ophthalmology & Visual Science 57(9), 2536019 (2016).
18. R. Leitgeb, F. Placzek, E. Rank, L. Krainz, R. Haindl, Q. Li, M. Liu, M. Andreana, A. Unterhuber, T. Schmoll, and W. Drexler, "Enhanced medical diagnosis for dOCTors: a perspective of optical coherence tomography," Journal of Biomedical Optics 26(10), 100601 (2021).
19. A. A. Plekhanov, E. V. Gubarkova, M. A. Sirotkina, A. A. Sovetsky, D. A. Vorontsov, L. A. Matveev, S. S. Kuznetsov, A. Y. Bogomolova, A. Y. Vorontsov, A. L. Matveyev, S. V. Gamayunov, E. V. Zagaynova, V. Y. Zaitsev, and N. D. Gladkova, "Compression OCT-elastography combined with speckle-contrast analysis as an approach to the morphological assessment of breast cancer tissue," Biomedical Optics Express 14(6), 3037 (2023).
20. A. A. Plekhanov, M. A. Sirotkina, E. V. Gubarkova, E. B. Kiseleva, A. A. Sovetsky, M. M. Karabut, V. E. Zagainov, S. S. Kuznetsov, A. V. Maslennikova, E. V. Zagaynova, V. Y. Zaitsev, and N. D. Gladkova, "Towards targeted colorectal cancer biopsy based on tissue morphology assessment by compression optical coherence elastography," Frontiers in Oncology 13, 1121838 (2023).
21. A. A. Plekhanov, G. O. Grechkanev, E. A. Avetisyan, M. M. Loginova, E. B. Kiseleva, A. A. Shepeleva, A. A. Moiseev, A. A. Sovetsky, E. V. Gubarkova, A. A. Anina, A. M. Shutova, S. V. Gamayunov, G. V. Gelikonov, V. Y. Zaitsev, M. A. Sirotkina, and N. D. Gladkova, "Quantitative Assessment of Polarization and Elastic Properties of Endometrial Tissue for Precancer/Cancer Diagnostics Using Multimodal Optical Coherence Tomography," Diagnostics 14(19), 2131 (2024).
22. X. Y. Chen, G. Zhou, and J. Zhang, "Optical coherence tomography: Promising imaging technique for the diagnosis of oral mucosal diseases," Oral Diseases 30(6), 3638–3651 (2024).
23. A. A. Plekhanov, S. I. Gazhva, Y. S. Ibragimova, A. A. Sovetsky, N. V. Mishina, A. L. Potapov, L. A. Matveev, K. I. Kalinkin, A. A. Anina, A. L. Matveyev, M. A. Sirotkina, N. D. Gladkova, and V. Y. Zaitsev, "Compression optical coherence elastography as a new tool for non-invasive identification of precancerous lesions of the oral mucosa," Laser Physics Letters 22, 015602 (2025).
24. M. Hessler, P. Nelis, C. Ertmer, M. Alnawaiseh, F. Lehmann, C. Schmidt, T. G. Kampmeier, S. W. Rehberg, P. H. Arnemann, and A. Rovas, "Optical coherence tomography angiography as a novel approach to contactless evaluation of sublingual microcirculation: A proof of principle study," Scientific Reports 10, 5408 (2020).
25. F. I. Feldchtein, G. V. Gelikonov, V. M. Gelikonov, R. R. Iksanov, R. V. Kuranov, A. M. Sergeev, N. D. Gladkova, M. N. Ourutina, J. A. Warren, and D. H. Reitze, "*In vivo* OCT imaging of hard and soft tissue of the oral cavity," Optics Express 3(6), 239 (1998).
26. M. Ryabkov, M. Sizov, E. Bederina, P. Zarubenko, P. Peretyagin, A. Moiseev, A. Vorobiev, N. Gladkova, V. Zaitsev, and E. Kiseleva, "Optical Coherence Tomography Angiography of the Intestine: How to Prevent Motion Artifacts in Open and Laparoscopic Surgery?," Life 13(3), 705 (2023).
27. A. A. Plekhanov, N. A. Guseynov, E. B. Kiseleva, S. V. Bopkhoev, A. L. Potapov, A. B. I. Ali, A. A. Moiseev, V. M. Ryabova, S. Y. Ivanov, A. A. Muraev, N. D. Gladkova, and M. A. Sirotkina, "The Effect of Cryotherapy on Buccal Blood Vessels Evaluated by Optical Coherence Tomography Angiography: A Pilot Study," Journal of Biophotonics 17(11), e202400318 (2024).
28. A. V. Maslennikova, M. A. Sirotkina, A. A. Moiseev, E. S. Finagina, S. Y. Ksenofontov, G. V. Gelikonov, L. A. Matveev, E. B. Kiseleva, V. Y. Zaitsev, E. V. Zagaynova, F. I. Feldchtein, N. D. Gladkova, and A. Vitkin, "*In-vivo* longitudinal imaging of microvascular changes in irradiated oral mucosa of radiotherapy cancer patients using optical coherence tomography," Scientific Reports 7(1), 16505 (2017).
29. I. N. Druzhkova, A. G. Orlova, A. S. Fedulova, A. V. Avakiants, A. A. Isakova, E. V. Kukovyakina, Y. Zijian, E. A. Plotnikova, G. V. Trunova, A. A. Pankratov, A. A. Plekhanov, A. A. Kurnikov, P. V. Subochev, A. K. Shaytan, M. E. Gasparian, M. P. Kirpichnikov, D. A. Dolgikh, D. Razansky, and A. V. Yagolovich, "Multivalent fusion protein targeting VEGFR2 and DR5 receptors: assessing the antiangiogenic and antitumor effects via multimodal microangiography," Journal of Translational Medicine 23(1), 949 (2025).

30. N. Libert, A. Harrois, N. Baudry, E. Vicaut, and J. Duranteau, "Intestinal microcirculation and mucosal oxygenation during hemorrhagic shock and resuscitation at different inspired oxygen concentrations," The Journal of Trauma and Acute Care Surgery 83(3), 476–484 (2017).
31. M. Siegemund, A. Hollinger, E. C. Gebhard, J. D. Scheuzger, and D. Bolliger, "The value of volume substitution in patients with septic and haemorrhagic shock with respect to the microcirculation," Swiss Medical Weekly 149(0506), w20007 (2019).
32. A. Moiseev, S. Ksenofontov, M. Sirotkina, E. Kiseleva, M. Gorozhantseva, N. Shakhova, L. Matveev, V. Zaitsev, A. Matveyev, E. Zagaynova, V. Gelikonov, N. Gladkova, A. Vitkin, and G. Gelikonov, "Optical coherence tomography-based angiography device with real-time angiography B-scans visualization and hand-held probe for everyday clinical use," Journal of Biophotonics 11(10), e201700292 (2018).
33. S. Taghavi, A. K. Nassar, and R. Askari, Hypovolemia and Hypovolemic Shock, StatPearls[Internet], StatPearls Publishing (2025).
34. J. K. Parks, A. C. Elliott, L. M. Gentilello, and S. Shafi, "Systemic hypotension is a late marker of shock after trauma: a validation study of Advanced Trauma Life Support principles in a large national sample," The American Journal of Surgery 192, 727-731 (2006).
35. E. Zherebtsov, A. Zherebtsova, A. Doronin, A. Dunaev, K. Podmasteryev, A. Bykov, and I. Meglinski, "Combined use of laser Doppler flowmetry and skin thermometry for functional diagnostics of intradermal finger vessels," Journal of Biomedical Optics 22(4), 040502 (2017).
36. I. A. Ryzhkov, N. V. Golubova, K. N. Lapin, S. N. Kalabushev, V. V. Dremin, E. V. Potapova, A. V. Dunaev, V. T. Dolgikh, and V. V. Moroz, "Skin Microcirculatory Parameters as Diagnostic Markers of Central and Cerebral Circulatory Disorders in Hemorrhagic Shock," General Reanimatology 21(3), 11–25 (2025). [in Russian]
37. G. Tachon, A. Harrois, S. Tanaka, H. Kato, O. Huet, J. Pottecher, E. Vicaut, and J. Duranteau, "Microcirculatory alterations in traumatic hemorrhagic shock," Critical Care Medicine 42(6), 1433–1441 (2014).
38. M. J. Twiner, J. Hennessy, R. Wein, and P. D. Levy, "Nitroglycerin Use in the Emergency Department: Current Perspectives," Open Access Emergency Medicine 14, 327-333 (2022).
39. O. Dilken, B. Ergin, and C. Ince, "Assessment of sublingual microcirculation in critically ill patients: consensus and debate," Annals of Translational Medicine 8(12), 793 (2020).